FAKULTÄT FÜR MATHEMATIK UND NATURWISSENSCHAFTEN
FACHGRUPPE PHYSIK
BERGISCHE UNIVERSITÄT WUPPERTAL

Scintillator Calorimeters for a Future Linear Collider Experiment

Dissertation

by

Oskar Hartbrich

July 22, 2016

Contents

Introduction **7**

1. Particle Physics **9**
1.1. The Standard Model . . . 9
1.2. Future e^+e^- Experiments . . . 11
1.2.1. The International Linear Collider . . . 13
1.2.2. The International Large Detector . . . 15
1.2.3. Model Independent Determination of Higgs Parameters at the ILC . . . 17
1.3. Particle Interactions with Matter . . . 25
1.3.1. Electromagnetic Cascades . . . 25
1.3.2. Heavy Charged Particles . . . 27
1.3.3. Hadronic Cascades . . . 28
1.4. Simulation of Particle Showers . . . 31
1.4.1. Electromagnetic Cascades . . . 31
1.4.2. Hadron Cascade Simulations . . . 31
1.4.3. Physics Lists . . . 33
1.5. Calorimeters . . . 34
1.5.1. Particle Flow Calorimetry . . . 38

2. CALICE Physics Prototypes **41**
2.1. Silicon Photomultipliers . . . 41
2.2. The Scintillator Electromagnetic Calorimeter . . . 44
2.3. The Analog Hadron Calorimeter . . . 44
2.4. The Tail Catcher and Muon Tracker . . . 45
2.5. DAQ and Electronics of the Scintillator-SiPM Prototypes . . . 46
2.6. Calibration of the CALICE Scintillator-SiPM Prototypes . . . 47
2.6.1. Pedestal . . . 47
2.6.2. SiPM & Tile Properties . . . 48
2.6.3. MIP Calibration . . . 49
2.7. Digitisation Effects . . . 50
2.7.1. Hit Timing . . . 50
2.7.2. Optical Crosstalk . . . 50
2.7.3. Conversion to the MIP Scale . . . 51
2.7.4. Scintillator-SiPM Modelling . . . 51
2.7.5. Noise . . . 56

3. CALICE Engineering Prototypes **57**
3.1. The AHCAL Engineering Prototype . . . 57
3.1.1. The HCAL Base Unit . . . 58

3.1.2. The SPIROC2 ASIC . . . 58
3.1.3. Current Status of the AHCAL Engineering Prototype . . . 60
3.2. Considerations for a Full Scale Calorimeter System . . . 61
3.2.1. Tile Lightyield . . . 62
3.2.2. Trigger Threshold Validation . . . 64
3.2.3. SPIROC2 Readout Efficiency . . . 67

4. Energy Resolution of the Combined Scintillator Calorimeter System 71
4.1. The FTBF MTest Beamline . . . 71
4.2. Testbeam Setup . . . 72
4.3. Simulation Setup . . . 75
4.3.1. ScECAL Absorber Composition . . . 75
4.3.2. Beam Profiles . . . 76
4.3.3. Relative Alignment of the Subdetectors . . . 81
4.4. Reconstruction . . . 82
4.4.1. Deposited Energy . . . 82
4.4.2. Layer of First Interaction . . . 83
4.4.3. Track Reconstruction . . . 88
4.5. Event Selection . . . 90
4.5.1. MIP Selection . . . 92
4.5.2. Pion Selection . . . 92
4.5.3. Electron Selection . . . 97
4.5.4. Pion Event Contaminations . . . 103
4.6. Validation Studies . . . 107
4.6.1. MIP Calibration . . . 108
4.6.2. Hit Energy Spectra and Shower Profiles . . . 110
4.6.3. ScECAL Electron Response & Resolution . . . 111
4.7. Energy Reconstruction in a Combined Calorimeter System . . . 114
4.7.1. Standard Weighting . . . 116
4.7.2. Software Compensation Weighting . . . 116
4.8. Pion Analysis . . . 129
4.8.1. Pion Shower Profiles . . . 129
4.8.2. Energy reconstruction and linearity . . . 131
4.8.3. Energy resolution . . . 132
4.8.4. Applying the Software Compensation Weights from Simulation to Data 133
4.9. Summary and Outlook . . . 136

5. Validation of the HCAL Simulation for ILD 139
5.1. Simulation Setup . . . 139
5.1.1. Model Geometry Modifications . . . 139
5.1.2. ILDCaloDigi . . . 140
5.2. Digitisation Effects on Shower Measurement . . . 141
5.3. Testbeam Comparison . . . 145
5.4. Conclusions . . . 147

Summary 149

Acknowledgements **153**

Appendix **155**
A. Analytical Resolution of the Binomial SiPM-Model 155
B. Systematic Influence of the Observed Beam Contamination in Pion Runs . . 156
C. Event Selections 158
D. Additional Information FNAL Testbeam Analysis 161

Bibliography **173**

Introduction

Modern particle physics experiments measure the results of high energy particle collisions. The highest energy particle accelerator to date is the *Large Hadron Collider* (LHC) at CERN, colliding protons with center of mass energies up to $\sqrt{s} = 14\,\text{TeV}$. The discovery of the Higgs boson at two independent experiments at the LHC in 2012 completed the *Standard Model* of particle physics and marks a cornerstone in the research of fundamental particles and their interactions.

A high energy lepton collider would complement the results expected from LHC, both in achievable precision and projected discovery reach. One concept for such a facility is the *International Linear Collider* (ILC), colliding electrons and positrons with a planned center of mass energy up to $\sqrt{s} = 500\,\text{GeV}$. To achieve the best possible measurement precision in experiments at the ILC, unprecedented resolutions of the detector systems are required. Detector concepts planned for the ILC aim to measure jet energies to around 3 % to 4 % precision by applying *Particle Flow Algorithms* (PFAs). PFAs aim to combine the measurements of the tracking system and calorimeters into an optimal jet energy measurement by individually reconstructing every particle in a given jet and using the best resolution sub-detector measurement for each particle, requiring calorimeter systems with unprecedented spatial granularities.

This thesis discusses multiple aspects of the ongoing developments of such highly granular calorimeters within the CALICE collaboration, focusing on prototypes of scintillator based calorimeters with *Silicon Photomultiplier* (SiPM) readout. The discussed topics range from the testbeam analysis of a combined prototype calorimeter system, to considerations about the operation of fully integrated calorimeter prototypes in testbeam environments and a full ILC experiment, up to the performance of the hadronic calorimeter implemented in the full detector simulation of an ILC detector concept.

The first chapter gives a brief recapitulation of the Standard Model and a description of the ILC and its detector concepts. Furthermore, examples for precision measurements of properties of the Higgs boson are given. Finally an introduction to interactions of particles with matter, and calorimetry is presented, including a description of the particle flow concept and its requirements.

The second chapter describes the first generation calorimeter prototypes developed within the CALICE collaboration with a focus on the scintillator-SiPM technology, including a description of the calibration procedures developed for the scintillator-SiPM prototypes. The statistical models used to realistically include sensor effects into simulations are fully validated as part of this thesis.

The second generation of CALICE scintillator-SiPM calorimeters is discussed in chapter three. The goal of these prototypes is to demonstrate a hardware system that is scalable to the size and demands of a full calorimeter system at a future linear collider detector. The efficient operation of such self-triggered detectors demands careful considerations about

the design parameters of the whole readout chain. Some of the design parameters and their efficient validation, as well as general considerations about the expected readout efficiency of the engineering prototype system in testbeam environments and at a future linear collider experiment are investigated in this thesis. These studies are important in the current phase of continuously growing second generation CALICE prototypes, as problems identified and investigated in the current state can be mitigated and efficient solutions devised before scaling to the next larger prototypes.

The fourth chapter presents testbeam analysis results obtained as part of this thesis, using data from the combined scintillator-SiPM calorimeter system consisting of the *Scintillator Electromagnetic Calorimeter* (ScECAL), *Analogue Hadronic Calorimeter* (AHCAL) and *Tail Catcher & Muon Tracker* (TCMT) in the energy range 4–32 GeV, recorded during a testbeam campaign at the Fermilab testbeam facility in 2009. The sampling fraction and material composition of the ScECAL is very different from the AHCAL and TCMT, complicating the reconstruction of shower energies and potentially degrading the achievable energy resolution of hadronic showers. The main goal of the analysis is the extraction of the single pion energy resolution, to demonstrate the feasibility of a full scintillator-SiPM calorimeter system. The analysis includes longitudinal shower profiles as well as studies on the response linearity and energy resolution of single pions for two different methods of energy reconstruction, including a novel implementation of a software compensation algorithm. The results are compared to several GEANT 4 physics lists in software versions 9.6 and 10.1., and reference results obtained from an AHCAL+TCMT analysis without the ScECAL.

Chapter five discusses the performance of the hadronic calorimeter of the full simulation model of a future linear collider detector. In order to obtain realistic results from full detector simulations, each sub-detector performance is ideally validated with appropriate testbeam or lab measurements of prototypes. This validation of the hadronic calorimeter performance has been performed in comparison to testbeam data taken with the CALICE AHCAL as part of this thesis.

1. Particle Physics

Since the discovery of the atomic substructure in the famous scattering experiments by Geiger and Marsden [1], later interpreted theoretically by Rutherford [2], at the beginning of the 20$^{\text{th}}$ century, particle physics is striving to understand the fundamental constituents composing our universe. The currently best description of all fundamental particles and their interactions is the *Standard Model* (SM) of particle physics.

This chapter first gives a short overview of the Standard Model. Possible future high energy e^+e^--experiments are presented next. Precision measurements of the Higgs boson properties are one of the flagship physics measurements of such future collider experiments. The determination of the full Higgs decay width from Z recoil is discussed as an example of a measurement and analysis technique that is not at all accessible at hadron colliders. The specific measurement of the full model independent Higgs decay width from $e^+e^- \to hZ$ events with $Z \to jj$ is described as a showcase of the calorimeter system performance at planned future linear collider experiments. Finally the general interactions of high energy particles with matter, typically resulting in particle showers, the simulation of such interactions as well as a general introduction to measuring particle shower energies is given.

1.1. The Standard Model

The Standard Model of particle physics classifies all known subatomic particles and describes their interactions in terms of a consistent *quantum field theory* (QFT). Since its formulation around the 1960's [3–5], many of its predictions could be verified over the next decades in increasingly complex particle physics experiments, culminating in the discovery of the Higgs boson by the ATLAS and CMS experiments at the LHC accelerator based at CERN, presented in 2012 [6, 7].

The Standard Model consists of 17 fundamental particles, subdivided into twelve matter particles, the *fermions* with spin $1/2$, four fundamental force carriers, the *gauge bosons* with spin 1 and the Higgs boson with spin 0, as shown in Figure 1.1.

The fermions are further subdivided into six leptons and six quarks in three generations each. The mass of fermions generally increases with higher generations. For each fermion there is a corresponding anti-particle with opposite quantum numbers but otherwise identical behaviour.

The leptons consists of the electron (e), muon (μ) and tau (τ) with electric charge ± 1 and their respective electrically neutral neutrinos ν_e, ν_μ, ν_τ. Out of the leptons only the electron and the neutrinos are stable, muons and taus decay with mean lifetime 2.2×10^{-6} s and 290×10^{-15} s, respectively.

The quarks are divided in up-type quarks of electric charge $\pm 2/3$ and down-type quarks with electric charge $\mp 1/3$. Quarks are never observed in isolation and always come in multi-quark bound states, the *hadrons*. This experimentally observed *confinement* is described by

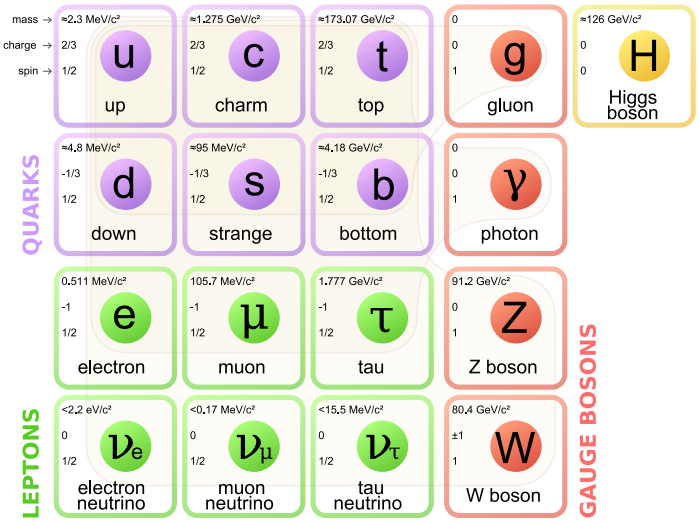

Figure 1.1.: *The elementary particles of the Standard Model, consisting of the 12 fundamental fermions and 4 fundamental gauge bosons plus the Higgs boson. Brown loops indicate which gauge bosons (red) couple to which fermions (purple and green). The Higgs boson couples to all massive particles shown. [8]*

introducing an additional *color charge* and imposing every possible bound state of quarks to have neutral net color charge. Bound states consisting of a quark-antiquark pair are termed *mesons* while bound states of three quarks are termed *baryons*. All known mesons are unstable, as are all known baryons except for the proton, consisting of two up-quarks and one down-quark (uud), and the neutron, consisting of one up-quark and two down-quarks (udd). As matter is exclusively made up of protons, neutrons and electrons, fermions of the second and third generations are observable exclusively in high-energy particle collisions, with the possible exception of muons, which are also produced from cosmic radiation in the earth's atmosphere.

Four known fundamental forces[1)] describe the interaction between all particles: The gravitational force, the electromagnetic force, the weak nuclear force and the strong nuclear force. Gravity is excluded from the Standard Model as it is assumed to be negligible on the scale of subatomic particles and no consistent description of gravity as a QFT has been devised yet. The Standard Model describes the remaining interactions as being mediated by force-carrying gauge bosons.

The electromagnetic force is mediated by the exchange of photons (γ) between electrically charged particles. As photons are massless the reach of electromagnetic interactions is infinite. However, its $1/r$ potential limits the effective range of the interaction.

The weak nuclear force is mediated by the exchange of $W^{\pm}$ and Z^0 bosons. All matter particles take part in the weak interaction, especially also neutrinos which do not interact in any other way. The weak gauge bosons are massive with $m_{W^{\pm}} = 80.4\,\text{GeV}$ and $m_{Z^0} = 91.2\,\text{GeV}$, limiting the effective range of the weak interaction to around $10^{-18}\,\text{m}$ due to the Yukawa potential [9].

[1)] A force is considered fundamental when it cannot be described in terms of other interactions.

The strong nuclear force is carried by gluons, which couple to color charge and thus exclusively to quarks. As gluons mediate the exchange of color charge between quarks, they carry color charge themselves, making them self-interacting. This leads to an increase of the potential between two color-charged objects with increasing distance and causes quark-antiquark pair production once the potential energy goes above the pair production threshold, effectively limiting the range of the nuclear interaction even though the mediating gluons are massless. This *hadronisation* generates a cascade of mixed particles termed *jets*, sharing the initial quark momentum. The only way to reconstruct the energy and momentum of quarks is through the reconstruction of the resulting jet.

The Higgs mechanism [10, 11] introduces a Higgs field with nonzero vacuum expectation value which couples, and thus gives mass, to all SM particles[2)]. The coupling of a given particle to the Higgs field g_{hXX} is proportional to the respective particle mass m_X. The SM Higgs boson (h) is the fundamental excitation of the Higgs field manifesting as a spin 0 particle with $m_h = (125.7 \pm 0.4)\,\text{GeV}$, which should decay into all SM particles in fractions proportional to their squared Higgs couplings. The exact measurement of the Higgs coupling strengths and the total Higgs decay width are important cornerstones of the physics programme of current and future particle physics experiments.

1.2. Future e^+e^- Experiments

The highest energy collider experiment currently in operation is the *Large Hadron Collider* (LHC) [12] at CERN in Switzerland and France. The LHC is colliding protons with center of mass energies up to 14 TeV, probing the Standard Model at previously unreached energy scales and searching for yet unknown particles beyond the Standard Model. However, as protons are composite particles, only a random fraction of the center of mass energy is available in each collision, while the complexity of such collisions is very high. Such effects make certain measurements practically impossible at the LHC.

The *International Linear Collider* is a proposed particle physics accelerator complementary to the LHC. It is designed to collide electrons and their antiparticles, positrons, at center of mass energies of 250 GeV to 500 GeV, with a potential energy upgrade to 1 TeV. The reduced backgrounds and cleaner events compared to a hadron collider allow for highest precision measurements.

Exemplary event displays for the associated production of a Higgs boson decaying to a pair of b-quarks and a Z boson decaying to two leptons are shown in Figure 1.2, both from the ATLAS experiment at LHC and a simulated ILC event. The LHC event shows the products of multiple additional background collisions in the same event, as is typical in LHC events. The ILC event is visibly cleaner with less additional activity in the event.

The descriptions of the ILC accelerator and its detector concepts in this section are based on the ILC Technical Design Report [14–18], if not stated otherwise.

[2)] However, the Higgs field is not responsible for the largest part of the mass of baryonic matter, which is mostly generated from the binding energy of its constituting protons and neutrons.

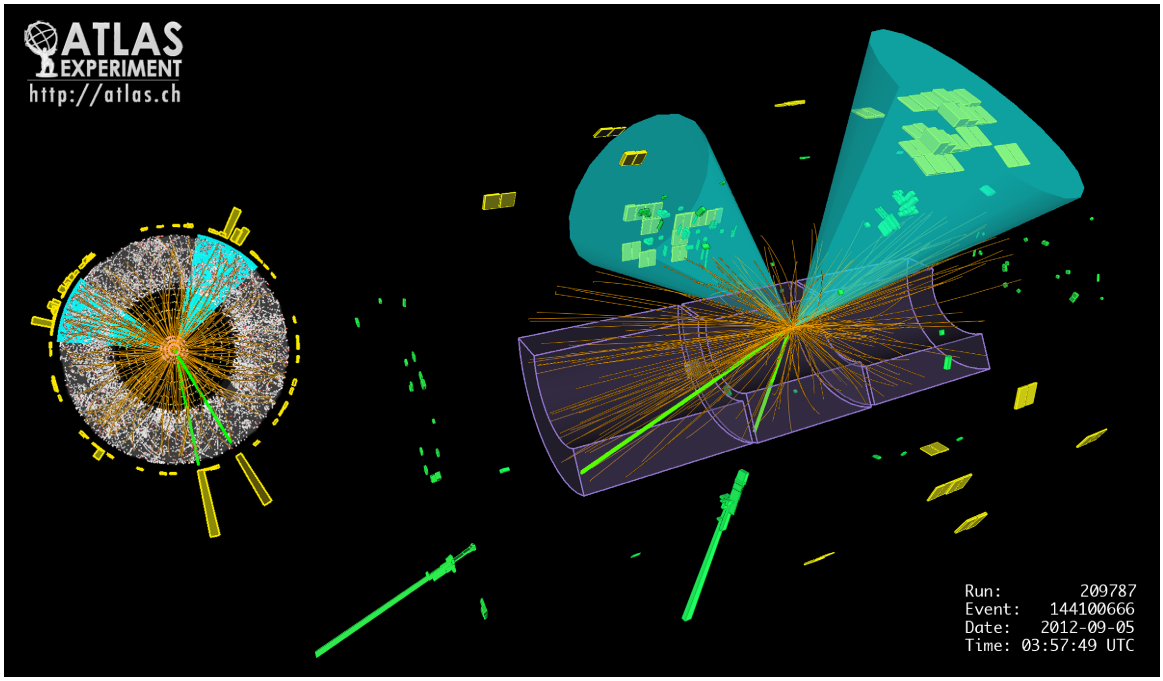

(a) *ATLAS ZH Event Candidate:* $Zh \to l\bar{l}jj \quad (Z \to e^+e^-, h \to b\bar{b})$ *[13]*

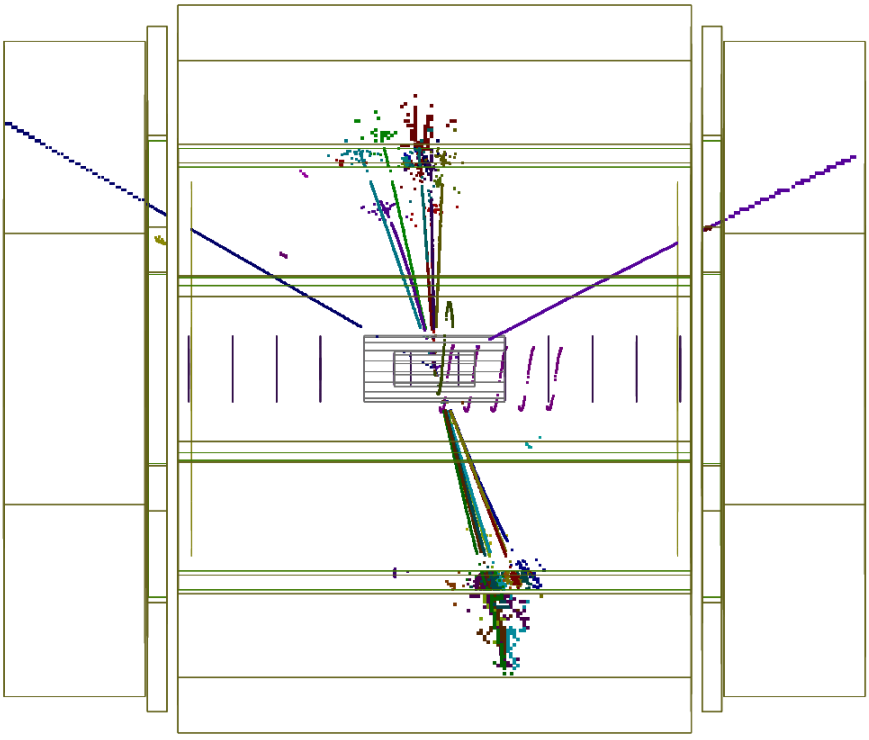

(b) *Simulated ZH ILD Event:* $Zh \to l\bar{l}jj \quad (Z \to \mu^+\mu^-, h \to b\bar{b})$ *[14]*

Figure 1.2.: *Candidate event displays of associated ZH production at the LHC and the ILC.*

1.2.1. The International Linear Collider

The *International Linear Collider* (ILC) is a mature concept for a future linear e^+e^--accelerator experiment of around 31 km total length with a planned center of mass energy $\sqrt{s} = 250\,\text{GeV}$ to $\sqrt{s} = 500\,\text{GeV}$. The main linear accelerators are based on 1.3 GHz *superconducting radio-frequency* (SCRF) acceleration technology with an average accelerating gradient of $\geq 31.5\,\frac{\text{MV}}{\text{m}}$. A schematic view of the accelerator layout is given in Figure 1.3.

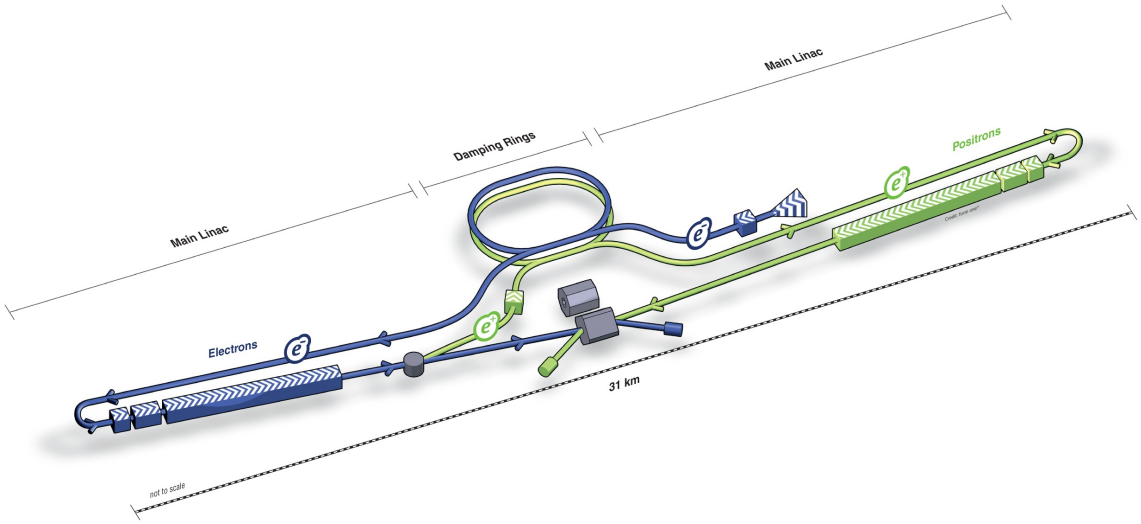

Figure 1.3.: *Schematic depiction of the International Linear Collider (not to scale). [14]*

The ILC is expected to collide longitudinally polarised beams with mean polarisations $P_- \approx \pm 0.8$ and $P_+ \approx \pm 0.3$. Electrons are generated with up to 90 % polarisation by illuminating a strained GaAs photocathode with a polarised laser. To generate polarised positrons, the primary electron beam is transported through a superconducting helical undulator, generating polarised photons in the energy range around 10 MeV to 30 MeV. These photons are directed onto a Ti-alloy target, producing a beam of polarised e^+e^--pairs, out of which the electrons are dumped and the positrons are extracted for use as the positron beam. Both electrons and positrons are pre-accelerated to 5 GeV and injected into a 3.2 km circumference damping ring, which reduces the nominal emittance of the beams within the 200 ms circulation time available between bunch trains. The beams are then injected into the main accelerator structure and boosted up to the full design energy.

One ILC bunch train consists of 1312 bunches of 2×10^{10} particles each. The repetition frequency of bunch trains is 5 Hz (Up to 10 Hz at $\sqrt{s} = 250\,\text{GeV}$, depending on the running scenario). Both beams are focused to down to 474 nm × 5.9 nm at the interaction point, leading to an average delivered instantaneous luminosity of $0.8 \times 10^{34}\,\frac{1}{\text{cm}^2\,\text{s}}$ to $1.8 \times 10^{34}\,\frac{1}{\text{cm}^2\,\text{s}}$, depending on the center of mass energy.

Possible planned upgrades from the ILC baseline design include a luminosity upgrade doubling the number of bunches per bunch train, which does not need major changes to the accelerator except for the installation of new klystrons and modulators, and the option of

an energy upgrade to 1000 GeV center of mass energy, requiring an extension of the main accelerators to around 50 km length and other major changes to the accelerator layout.

A dedicated study has been conducted to investigate the ideal running scenario in terms of center of mass energies and luminosities to optimise the precision of Higgs measurements and top physics while searching for new particles beyond the Standard Model [19]. The currently preferred running scenario *H-20* seeks to operate the ILC for at least 20 years, initially recording a total of 500 fb^{-1} at 500 GeV, then 200 fb^{-1} at 350 GeV and then 500 fb^{-1} at 250 GeV. After a shutdown for the luminosity upgrade after eight years of operation, recording further 3500 fb^{-1} at 500 GeV and finally another 1500 fb^{-1} at 250 GeV is foreseen. The planned schedules with recorded integrated luminosities are shown in Figure 1.4.

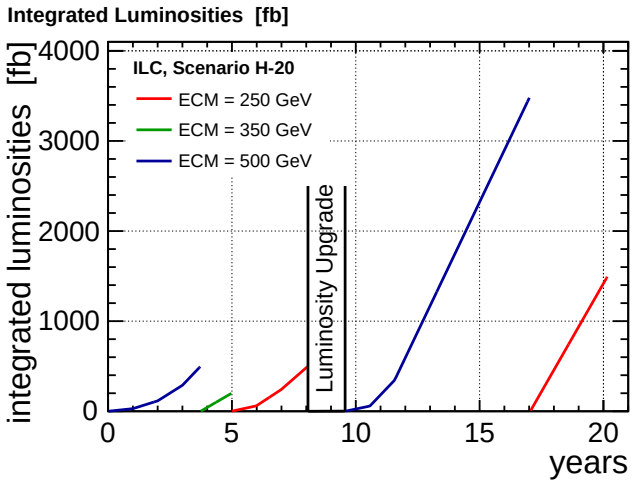

Figure 1.4.: *Accumulation of integrated luminosity vs. real time in the currently preferred ILC running scenario H-20 [19].*

All key points and technologies needed to build the ILC have been demonstrated and documented in the ILC Accelerator Technical Design Report [16, 17]. Especially the mass production and operation of SCRF cavities has been demonstrated at the linear SCRF-driven synchrotron sources FLASH [20] and XFEL [21] at DESY. Construction of the ILC could thus commence with minimal delay once a positive decision on its realisation is made. The Japanese government is investigating hosting the ILC in northern Japan, however no final decision has been taken yet.

A separate concept for a future linear collider is the *Compact Linear Collider* (CLiC) concept [22]. CLiC is based on normal-conducting copper structures, which are operated at 12 GHz radio frequency, significantly higher than at the ILC. Instead of a classic RF generation with klystrons, a two-beam operation scheme is planned in which a low energy but high current drive beam excites RF waves that are used to accelerate a low current, high energy main beam. With the CLiC concept higher center of mass energies up to 3 TeV are thought to be realisable, albeit at a higher power consumption than ILC. The CLiC technology is currently not yet as mature as the ILC concept and will need several more years of research and development before a full CLiC-like accelerator could be constructed.

1.2.2. The International Large Detector

In order to realise the ambitious physics programme of the ILC, significant advances in detector performance compared to previously operated experiments are essential. The detector concepts developed for the ILC are focused on *Particle Flow* reconstruction, aiming to individually reconstruct all particles in each event. To efficiently separate charged and neutral particles even within jets, the detectors need to provide three dimensional imaging capabilities, requiring unprecedented spatial resolution in all subdetectors. The particle flow approach is discussed in more detail in subsection 1.5.1.

It is planned to operate two separate detector experiments at the ILC. The detectors are foreseen to share the ILC interaction point using a *push-pull* approach, in which only one detector is occupying the interaction region at a time, while the other detector is moved out of the beam and into a parking position in the detector hall. Both detectors would then be moved in and out of the interaction point periodically, alternating every few weeks.

Two detector concepts have been developed and described in detail in the detector volume of the ILC Technical Design Report [18], the *Silicon Detector* (SiD) and the *International Large Detector* (ILD). Detailed full detector simulations are available for both these concepts and have been used extensively in the evaluation of the ILC physics potential. These detector models contain realistic implementations of all subsystems, which have been crosschecked with prototype data where possible (see chapter 5). The ILD concept is broadly described here.

The ILD is planned in a close to cylindrical shape of 13 m length and 7.8 m radius. Both the tracking system and the calorimeters are located within a superconducting solenoid coil of 3.4 m inner radius, creating a 3.5 T magnetic field oriented in parallel to the beam axis. Schematic views of the ILD layout are given in Figure 1.5.

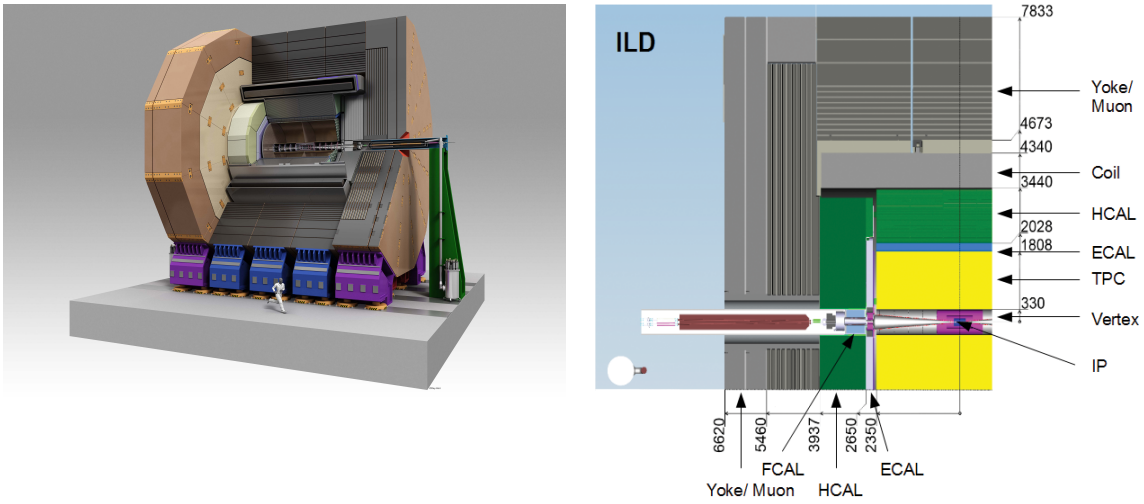

(a) *Full ILD Rendering* **(b)** *Schematic ILD Cross-section*

Figure 1.5.: *Views of the ILD detector concept. Dimensions are given in mm. [14]*

ILD Tracking System

The innermost part of the ILD tracking system consists of a vertex detector built of either three double-layers or five single layers of silicon pixel detectors as close as 16 mm to the beam axis, offering hit position resolutions of $<6\,\mu m$ with a material budget of $<0.0015\,X_0$ per layer. Outwards of the vertex detector, two double layers of silicon strip sensors are located at 153 mm and 300 mm radius, measuring hit positions with 7 µm resolution with a material budget of $<0.0065\,X_0$ per layer. The high spatial resolution and proximity to the interaction point offers ideal performance in the reconstruction of secondary vertices for identification of b-jets.

The main tracking detector in ILD is a large *time projection chamber* (TPC), covering 330 mm to 1808 mm in radius. Traversing charged particles ionise the gas within the TPC volume along their trajectory. The resulting free electrons are accelerated towards the barrel endcaps by an electric field applied parallel to the beam axis. These ionisation electrons are detected by a *gas electron multiplier* (GEM) or *micro-mesh gaseous structure* (Micromegas) based readout in the endcaps, measuring up to 224 points per track. The spatial point resolution of the TPC around 100 µm is worse than what silicon sensor could offer. This is offset by the low material and continuous tracking of the TPC, enabling excellent reconstruction of non-pointing tracks due to kinks from multiple scattering. Additionally the TPC offers particle identification via deposited energy density $\frac{dE}{dx}$ from the measured ionisation strength (see subsection 1.3.2).

The combined ILD tracking system is designed to achieve a momentum resolution of $\frac{\sigma}{p} = 5 \times 10^{-5} \times p\,[\mathrm{GeV}/c]$.

ILD Calorimeter System

The ILD calorimeter system is optimised for Particle Flow jet energy reconstruction (see subsection 1.5.1), aiming to achieve a relative jet energy resolution of $\leq 3\,\%$ across the whole relevant jet energy range from 45 GeV to 250 GeV. Apart from the needed unprecedented track reconstruction, this necessitates calorimeters with previously unheard of readout granularity in all three spatial dimensions.

To enable an optimal association of tracks to calorimeter depositions, the calorimeters are located within the magnet coil, effectively limiting the depth of the calorimeter system. The ILD calorimeter system thus presents a reasonable trade-off between imaging capabilities and intrinsic energy resolution, which are both important ingredients to the full Particle Flow jet energy resolution [23].

The baseline configuration of the electromagnetic calorimeter in ILD consists of a silicon readout based electromagnetic calorimeter with 5 mm × 5 mm readout segmentation and the *Analog Hadronic Calorimeter* (AHCAL) which is discussed in more detail in chapter 2.

The magnetic field return yoke surrounding the ILD is planned to be instrumented with scintillators or *resistive plate chambers* (RPCs) to serve as a muon tagging system with the potential of being useful as a hadron shower tail catcher for very high energy jets.

The Silicon Detector (SiD) Concept

The current SiD design is generally similar to the ILD concept. The main differences are the slightly smaller overall dimensions at 11 m length and 6.6 m radius, a stronger magnetic field within the detector of 5 T and a full silicon tracking system instead of the ILD TPC. The SiD design has recently been changed to also include a scintillator-SiPM hadronic calorimeter as its baseline option. The overall expected performance numbers of the SiD concept are similar to ILD.

1.2.3. Model Independent Determination of Higgs Parameters at the ILC

The compelling ILC physics case is well documented in the ILC TDR [15], in a recent update paper of the main points of the TDR [24] and in an extensive review article [25], apart from various other publications.

Experiments at the ILC will provide a precise and model independent determination of the Higgs boson parameters such as its mass, full decay width and absolute couplings to many Standard Model particles. The respective precisions achievable with the full LHC dataset are typically significantly worse. Certain quantities such as the full Higgs decay width, and thus absolute Higgs couplings, are not at all accessible in a model independent way at LHC.

This section gives a short overview about Higgs production in electron-positron collisions as well as Higgs precision measurements at the ILC, with a focus on the model independent determination of the full Higgs width, as is needed for the extraction of the absolute Higgs coupling strengths, as one of the key results of a future lepton collider experiment.

Higgs Production and Decay at the ILC

The two main production modes of Higgs bosons at the ILC are *Higgsstrahlung* and *vector boson fusion* (VBF). In the Higgsstrahlung process, the Higgs boson is produced in association with a Z boson, as shown in the corresponding Feynman diagram in Figure 1.6(a). In VBF Higgs production, either two W bosons or two Z bosons fuse into a Higgs boson, producing the Higgs in association with either two electron-neutrinos or an electron-positron pair, as given in Figure 1.6(b, c).

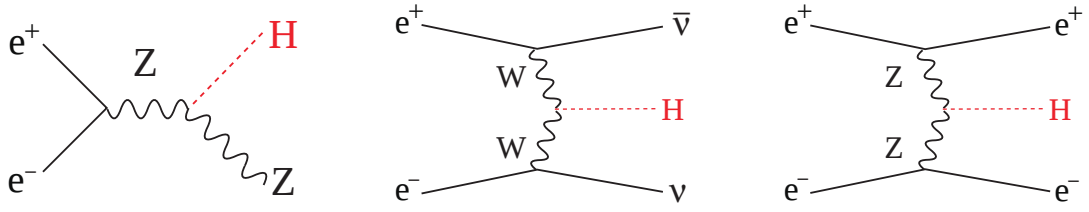

(a) *Higgsstrahlung* **(b)** *W Fusion* **(c)** *Z Fusion*

Figure 1.6.: *Tree level Feynman diagrams for the dominant Higgs production processes at an electron-positron collider [15].*

The Higgs production cross sections for these two processes as a function of center of mass energy are given in Figure 1.7(a). The production cross section of the Higgsstrahlung process peaks around 250 GeV center of mass energy, while the W fusion process slowly turns on from above 200 GeV, becoming dominant only at 450 GeV and higher. The cross section of Z fusion Higgs production is around a factor 30 smaller than for the W fusion process.

The Standard Model Higgs boson decays primarily to pairs of bottom quarks with around 60 % branching ratio. The next likely Higgs decay is into a pair of W bosons at around 20 % branching ratio. The branching ratio into a pair of Z bosons is around a factor ten smaller than for W pairs. The most important Higgs decay branching ratios are shown in Figure 1.7(b). In Higgs decays to massless final states ($h \to \gamma\gamma, h \to gg$), the final state particles are radiated off of virtual heavy-quark loops.

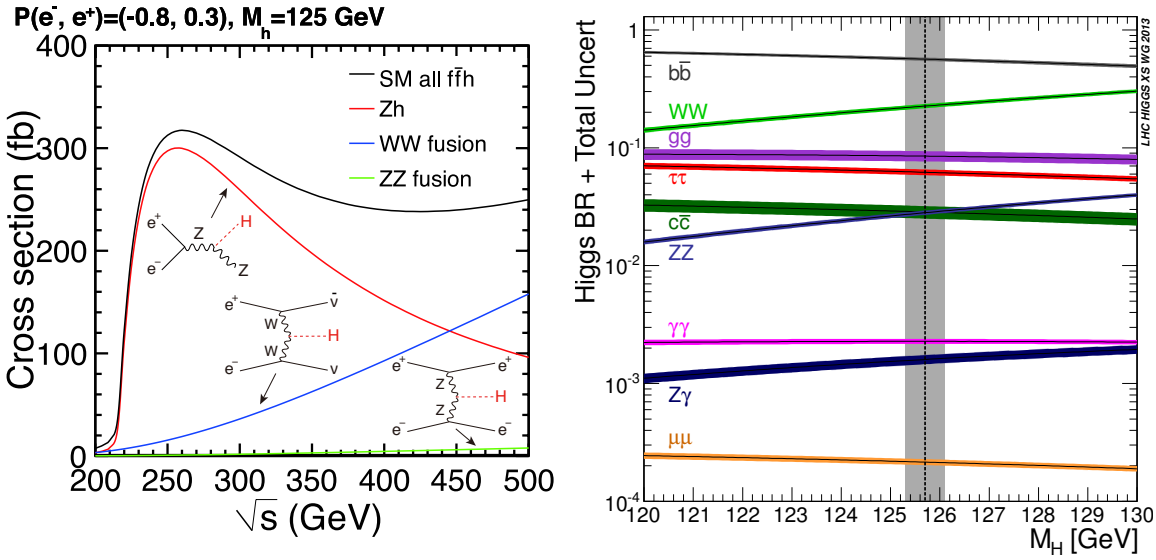

(a) *ILC Higgs production cross sections* **(b)** *SM Higgs decay branching ratios*

Figure 1.7.: *(a): ILC Higgs production cross sections [24]. (b): Higgs decay branching ratios as a function of the Higgs mass in the Standard Model, including the current world average Higgs mass measurement and its uncertainty [26]. Figure adapted from [27].*

Although the masses of Z and W bosons, and thus their Standard Model couplings to the Higgs, are similar within around 10 %, both Higgs decays to Z pairs and the Z fusion Higgs production are at least one order of magnitude less frequent than their respective equivalents with W bosons. At least one of the two vector bosons is necessarily off-shell, as $m_h \ll 2 \times m_W < 2 \times m_Z$. The virtual Z boson in $h \to ZZ^*$ decays is thus further off-shell than a the virtual W boson in $h \to WW^*$, relatively suppressing the Z branching ratio.

Higgs Recoil Measurement

At lepton colliders, the production of a Higgs boson via the Higgsstrahlung channel offers a unique method of measuring Higgs properties. As the initial state of the collision, the

four-momenta of the colliding electron and positron, is known precisely, reconstructing the Z boson recoiling against the Higgs makes identification of such events possible without reconstructing the Higgs boson at all.

This enables the model independent determination of the total Higgs decay width, measurement of the Higgs branching ratio to invisible particles to below 1 % as well as high precision Higgs mass measurements.

Using events in which the Z boson decays to a pair of charged leptons, the mass of the Higgs boson produced in association with the Z boson can be calculated as

$$m^2_{\text{rec}} = \left(p_{\text{CM}} - (p_{l^+} + p_{l^-})\right)^2, \tag{1.1}$$

with p_{CM} the sum of the four-momenta of the initial collision particles, and $p_{l^\pm}$ the measured four-momenta of the Z decay products [24]. Such events can be selected by requiring the invariant mass of the di-lepton system to be consistent with the known Z mass.

Counting of such events yields the full model independent Higgsstrahlung cross section $\sigma(\text{e}^+\text{e}^- \to \text{hZ})$. The expected precision of this measurement is optimal for $\sqrt{s} = 250\,\text{GeV}$ and degrades quickly for higher center of mass energies, due to a reduced production cross section and the resolution scaling of the tracking system. The determination of the total Higgsstrahlung production cross section via leptonic Z-decays is thus strongly preferring $\sqrt{s} = 250\,\text{GeV}$, reaching a precision of 2.6 % with $250\,\text{fb}^{-1}$ integrated luminosity.

A simulated spectrum of reconstructed recoil masses for Higgsstrahlung events with $Z \to \mu^+\mu^-$ is shown in Figure 1.8, including a fit of the background and peaking signal. The apparent tail of the signal towards higher reconstructed recoil masses is identified as events in which initial state radiation altered the four momentum of the collision system. However this can be accounted for in the event reconstruction and does not systematically shift the measured Higgs mass. With the full luminosity foreseen for the ILC programme, a Higgs mass resolution of 32 MeV is achievable by combining the muon and electron decay channels of the Z boson. This resolution is not improved further by including events in which the Z boson decays to jets.

Higgs Couplings

The precise measurement of the Higgs coupling strengths is of high interest, as deviations to the SM Higgs couplings in the order of 1 % are expected in many generic models of new physics beyond the Standard Model [28, 29].

In the Standard Model, the coupling $g_{\text{h}XX}$ of the Higgs boson to any given SM particle X is expected to be proportional to m_X[3)] . The squared Higgs coupling enters both the production cross sections and the decay branching ratios of the Higgs boson. The measured quantity at a collider is typically the event rate of a given final state, which corresponds to the product of the production cross section and the branching ratio. At hadron colliders it is not possible to accurately measure the full production cross section of a given Higgs production process, especially not without model dependent assumptions, as invisible Higgs decays cannot be disentangled from background processes. At the ILC the full inclusive Higgsstrahlung

[3)] The effective dependence of the Higgs coupling to vector bosons is proportional to the squared boson mass, as the m_{W}, which is directly proportional to m_{Z} via the Weinberg angle $\cos\theta_{\text{W}} = \frac{m_{\text{W}}}{m_{\text{Z}}}$, enters the coupling both as the scale parameter of the electroweak interaction and as a scaling factor of the coupling.

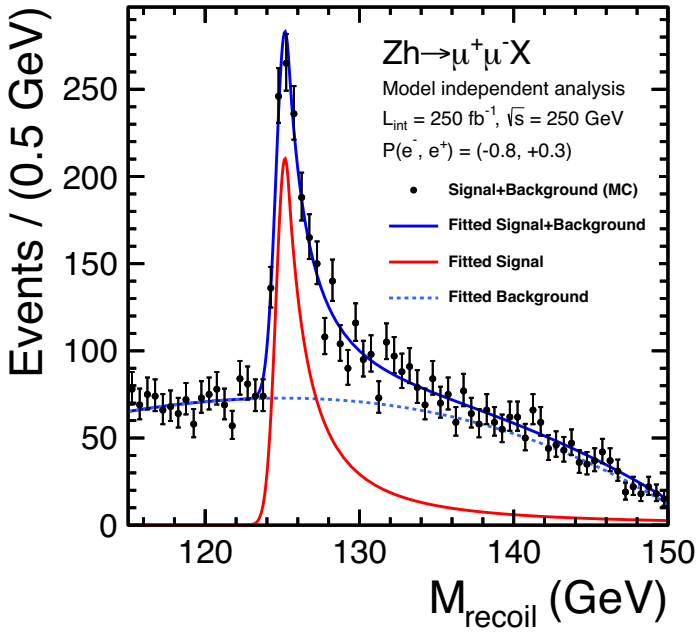

Figure 1.8.: *Recoil mass distribution for $Zh \to l\bar{l}jj$ $(Z \to \mu^+\mu^-)$ events. Simulated for $m_h = 125\,\mathrm{GeV}$. [24].*

production cross section $\sigma(\mathrm{e^+e^-} \to \mathrm{hZ})$, and thus the coupling g_{hZZ} can be measured in a model independent way as explained in the previous section. This can be leveraged into a fully model independent determination of all Higgs couplings.

First the branching ratio $BR(\mathrm{h} \to \mathrm{b\bar{b}})$ is measured in Higgsstrahlung events by dividing the measured event rate by $\sigma(\mathrm{e^+e^-} \to \mathrm{hZ})$. The full W fusion Higgs production cross section and thus g^2_{hWW} can then be calculated from dividing the measured event rate of the W fusion process

$$e^+e^- \to h\nu_e\nu_e \quad (h \to b\bar{b}) \tag{1.2}$$

by the previously measured $BR(\mathrm{h} \to \mathrm{b\bar{b}})$ [30].

The branching ratio of a decay channel $BR(\mathrm{h} \to X\bar{X})$ is related to the partial decay width $\Gamma(\mathrm{h} \to X\bar{X})$ and the full Higgs decay width Γ_{h} as

$$BR(\mathrm{h} \to X\bar{X}) = \frac{\Gamma(\mathrm{h} \to X\bar{X})}{\Gamma_{\mathrm{h}}}, \tag{1.3}$$

with

$$\Gamma(\mathrm{h} \to X\bar{X}) \propto g^2_{\mathrm{h}XX}. \tag{1.4}$$

So in order to obtain the coupling of the Higgs to a given particle, the partial decay width of the corresponding Higgs decay can be calculated from its measured branching ratio, if the full Higgs decay width is known.

As g^2_{hWW}, and thus $\Gamma(\mathrm{h} \to W^+W^-)$, is already known, all that is needed to calculate Γ_{h} is the branching ratio $BR(\mathrm{h} \to \mathrm{W^+W^-})$. This branching ratio can be measured from either

Higgsstrahlung or W fusion processes, as both full production cross sections are known at this point.

The measurement uncertainty on Γ_h directly propagates into the precision of each absolute coupling measurement. Thus, in order to optimise uncertainty on Γ_h, the measurements of all cross sections $\times$ branching ratios are included into the measurement in a global fit.

The relative precisions achievable with both the initial and full statistics of the ILC programme, in comparison to the projected LHC precisions and possible combination results are shown in Figure 1.9. For most couplings the ILC measurements are ten times more precise than what is expected from the full LHC dataset.

Extracting the Full Higgs Width from Z→jj

The extraction of the full Higgs decay width as described in the previous paragraphs relies on the measurement of the full Higgsstrahlung cross section with events where the Z bosons decays to two leptons, which is most precise at $\sqrt{s} = 250\,\text{GeV}$. A recent paper [31] shows that the measurement of the full Higgsstrahlung cross section is feasible at $\sqrt{s} = 350\,\text{GeV}$ when utilising the much higher statistics of $Z \to q\bar{q}$ with roughly ten times increased branching ratio over the di-lepton decay. Spending less time measuring at 250 GeV center of mass energy could improve the integrated luminosity recorded at higher beam energies, where even more processes such as top-pair production are kinematically accessible.

As will be explained in this section, an excellent jet energy resolution is a key requirement to extract Γ_h from hadronic recoil events with sufficient accuracy.

The main challenge of using the Z to jets decay channel to determine $\sigma(e^+e^- \to hZ)$ is devising an event selection that efficiently suppresses Standard Model backgrounds as $e^+e^- \to q\bar{q}$ but does not introduce a bias towards specific Higgs decays. Ideally the selection efficiency for each SM decay channel would thus be similar, with an equal efficiency also on potential invisible Higgs decays. Events are classified into possible visible and invisible Higgs decays by their topology, where invisible Higgs decays should show a clear di-jet topology and nothing else. In the invisible Higgs channel, the two reconstructed jets are used for the recoil mass reconstruction. In events classified as a visible Higgs decay, the di-jet combination with invariant mass closest to the Z mass is used for the recoil mass reconstruction. The resulting recoil mass spectra for the Higgs decays to invisible and several decays of Higgs into jets is given in Figure 1.10. All shown m_{rec} spectra show clear peaks around the Higgs mass, with very similar shapes of the recoil mass distribution despite the very different final states.

The cross section $\sigma(e^+e^- \to hZ)$ is extracted from fitting signal and background templates to the measured likelihood distributions of several variables. One of these variables is the two-dimensional distribution of the recoil mass of the selected di-jet system m_{rec} versus the invariant mass of the di-jet system m_{qq}. Signal events should peak around $m_{\text{rec}} = m_H, m_{qq} = m_Z$, with an inherent width of the signal peak corresponding to the jet energy resolution in both dimensions, as the natural widths of the Z and Higgs are comparably narrow. The obtained distributions for signal and background events are given in Figure 1.11, showing clearly how a reduced jet energy resolution would significantly decrease the separation of signal and background in this variable, potentially degrading the achievable resolution in $\sigma(e^+e^- \to hZ)$.

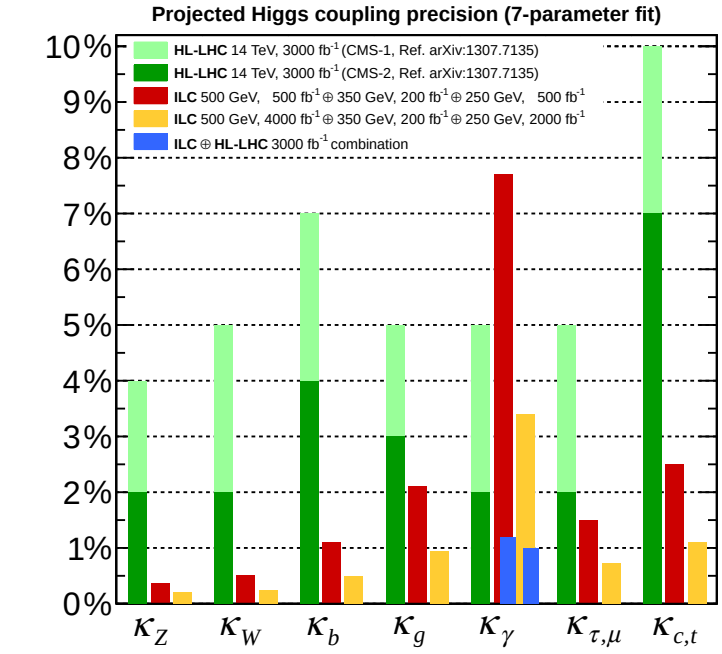

(a) *Model Dependent Analysis*

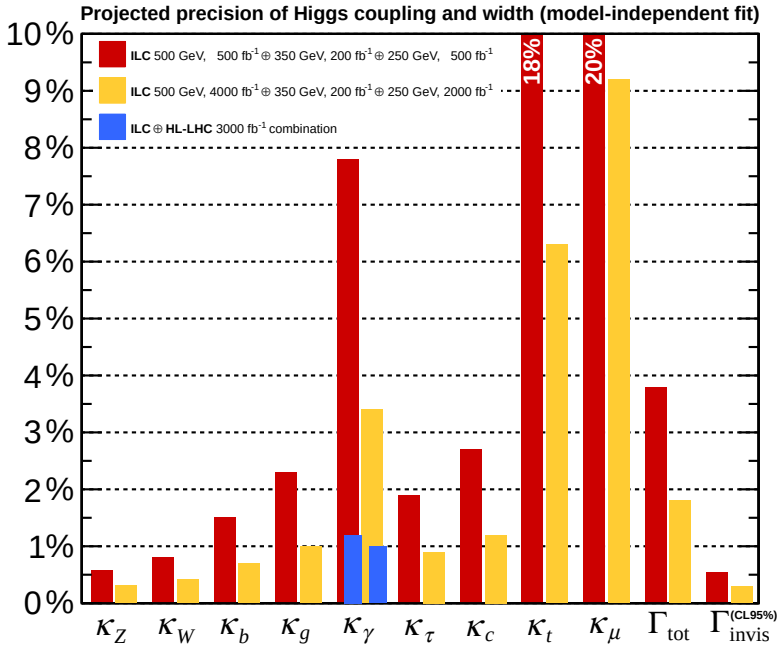

(b) *Model Independent Analysis*

Figure 1.9.: *Expected precisions on the ratio of the measured Higgs couplings to the Standard Model expectations for the initial and full ILC dataset, for both model dependent and model independent analyses. In model dependent analyses, projections on the achievable resolution with the full HL-LHC dataset are shown as well, for pessimistic (CMS-1) and optimistic (CMS-2) assumptions about achievable systematic uncertainties. [24].*

The obtained precision on $\sigma(e^+e^- \to hZ)$ is 1.8 % from 350 fb^{-1} at $\sqrt{s} = 350$ GeV, corresponding to a similar running time as the 250 fb^{-1} at $\sqrt{s} = 250$ GeV given in the leptonic recoil measurement[4)].

[4)] Assuming a 5 Hz operation scheme at $\sqrt{s} = 250$ GeV

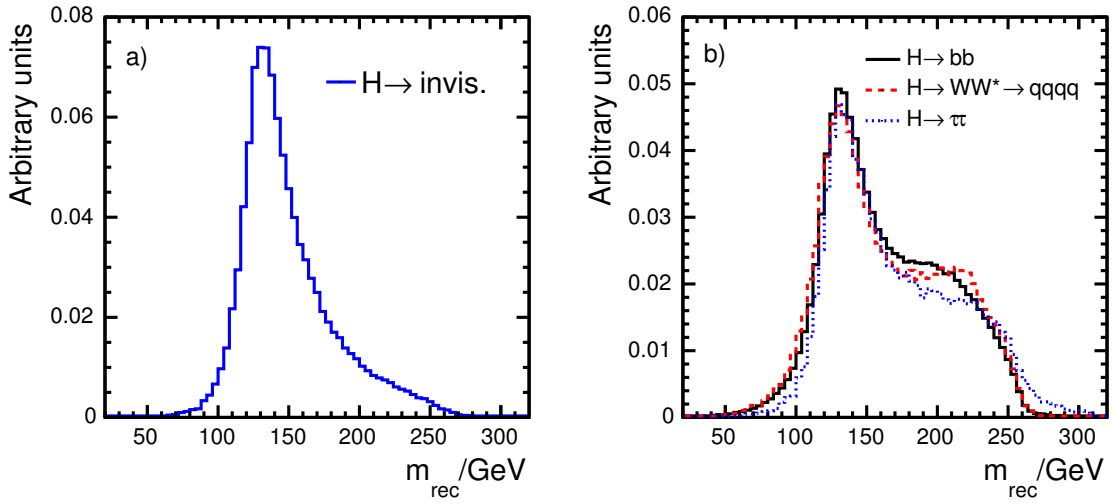

(a) $h \rightarrow$ *invisible* **(b)** $h \rightarrow$ *jets*

Figure 1.10.: *Reconstructed Higgs mass spectra from Z to jets recoil, both for Higgs decays to jets and to invisible particles [31].*

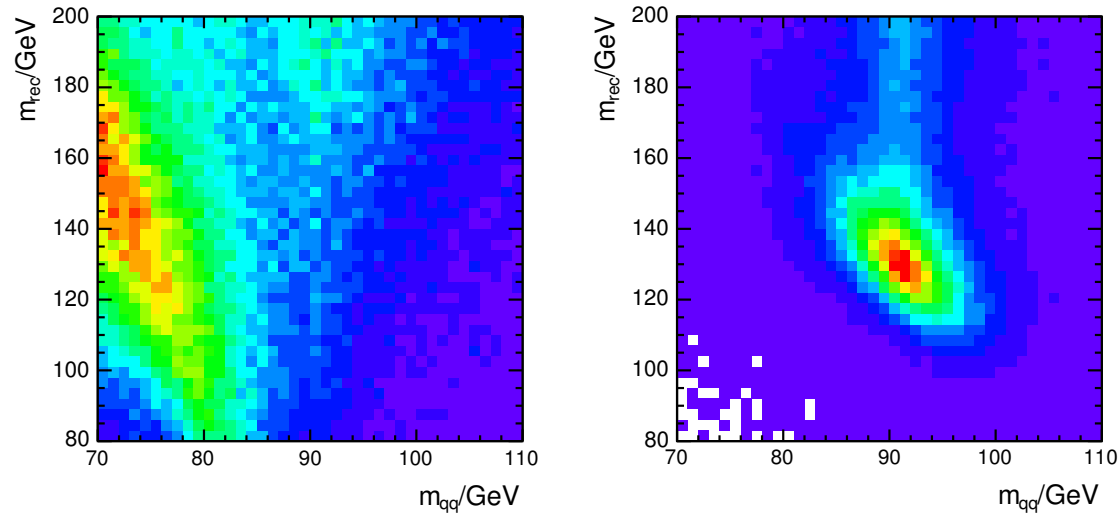

(a) *SM Background* **(b)** $e^+e^- \rightarrow Zh(Z \rightarrow jj)$

Figure 1.11.: *Signal and background distributions of the reconstructed recoil mass m_{rec} versus the invariant mass of the di-jet system used to calculate the recoil mass m_{qq} [31].*

1.3. Particle Interactions with Matter

Out of the hundreds of known elementary and composite particles that can be created in a particle collision, almost all decay into more stable particles before reaching any detectors. By far most particles that ever reach the detectors are one of the following: $e^{\pm}, \mu^{\pm}, \gamma, \pi^{\pm}, K^{\pm}, K^0, p^{\pm}, n, \nu$. These can be broadly categorised into charged particles which generate signals in the tracking detectors and neutral particles which typically do not. A further categorisation divides particles that induce electromagnetic showers, $e^{\pm}$ and γ, and particles that induce hadronic showers, $\pi^{\pm}, K^{\pm}, K^0, p^{\pm}, n$. Muons typically do not induce showers at all. Neutrinos almost never interact with matter and thus pass through the detectors without generating any signals.

This section describes the interactions of these particles with matter, including electromagnetic shower processes of electrons and photons, the electromagnetic energy loss of heavy charged particles in matter as well as the initiation and development of hadronic showers.

1.3.1. Electromagnetic Cascades

High energy electrons traversing matter lose their energy mainly due to *Bremsstrahlung*. Bremsstrahlung is radiation generated during the deflection, and thus acceleration, of an incident electron in the electric field of one of the surrounding nuclei. The electron is radiating off some of its energy as a photon. The emitted photons follow a $\frac{1}{E}$ spectrum, with typically only a small fraction of the initial electron's energy radiated per interaction [32]. The electron energy loss due to Bremsstrahlung is roughly proportional to the electron energy

$$-\left[\frac{dE}{dX}\right]_{\text{Brems}} = \frac{E}{X_0}, \tag{1.5}$$

with the *radiation length* X_0 defined as the amount of traversed material in which an electron reduces its energy to $\frac{1}{e}$ of the initial energy by Bremsstrahlung. X_0 is measured either in cm as the depth of traversed material, or more commonly in $\frac{g}{cm^2}$ as the area density of the traversed material. The value of X_0 is material dependent. A common parametrisation as a function of the atomic number Z and the mass number A is given in [26] as

$$X_0 = \frac{716.4\,\frac{g}{cm^2} A}{Z\,(Z+1)\ln 287/\sqrt{Z}}. \tag{1.6}$$

The energy loss of electrons per X_0 as a function of the electron energy is given in Figure 1.12(a). At low electron energies, the ionisation of surrounding atoms is the primary source of energy loss, while the almost constant energy loss due to Bremsstrahlung is dominating at higher electron energies.

High energy photons passing through matter will undergo electron-positron pair production if their energy is above the production threshold $E_\gamma \geq 2m_e \approx 1\,\text{MeV}$. The photon energy above the threshold is distributed into the momenta of the electron-positron pair. The mean free path of such a high energy photon before pair production takes place is $9/7\,X_0$.

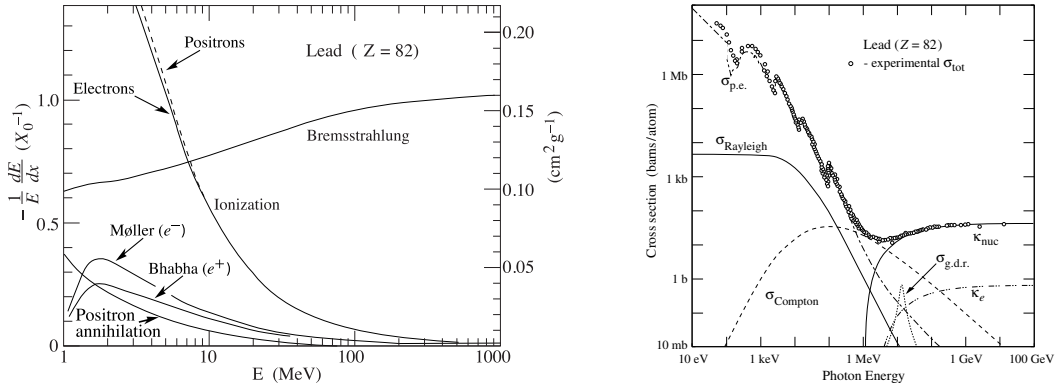

(a) *Electron Energy Loss* ***(b)*** *Photon Interaction Cross Section*

Figure 1.12.: *Energy loss and specific interaction cross sections for electrons and photons in Pb. Figures adapted from [26].*

The cross section of different photon processes as a function of photon energy is shown in Figure 1.12(b). At energies below the pair production threshold, photons dominantly cause photo-electric nuclear excitations.

When a high energy photon or electron enters a dense material, the combination of bremsstrahlung by electrons and pair production by photons generates an electromagnetic cascade. The number of particles in such *electromagnetic showers* roughly doubles for every X_0 of traversed material. Individual branches of the cascade stop evolving when the electron energy gets low enough that energy loss by ionisation becomes dominant. This *critical energy* threshold E_c is defined as the energy at which the energy losses from Bremsstrahlung and ionisation are equivalent. The critical energy is material dependent, and for solids can be parametrised as

$$E_c = \frac{610\,\mathrm{MeV}}{Z + 1.24} \tag{1.7}$$

as a function of the atomic number Z [26]. The number of generated particles in an electron shower is thus

$$N \approx E_0 / E_c. \tag{1.8}$$

The mean longitudinal profile of an electron shower is characterised by an exponential rise of the deposited energy in the early shower development, an exponential falloff towards the end of the shower with a shallow maximum in between. An example of a simulated electron shower profile, including the mean number of electrons and photons throughout the shower depth is given in Figure 1.13.

The mean shower maximum depth X_{max} is parametrised as

$$\frac{X_{\mathrm{max}}}{X_0} = \ln N + C, \tag{1.9}$$

with $C = -0.5$ for showers induced by electrons and $C = 0.5$ for photon induced showers, and thus scales with the logarithm of the shower energy [26].

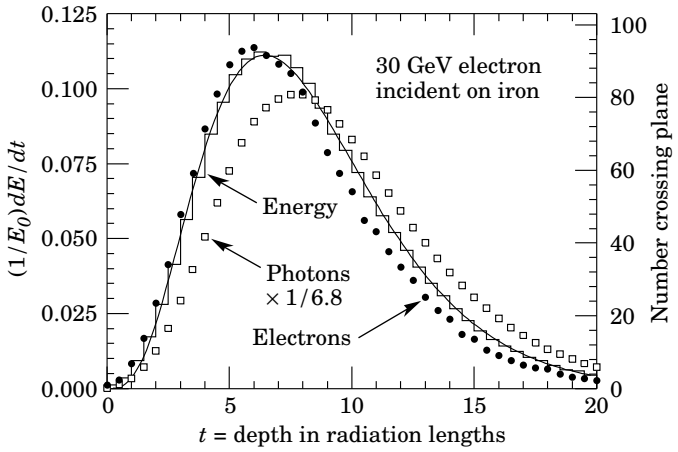

Figure 1.13.: *Averaged longitudinal profile of simulated 30 GeV electron showers in iron. The histogram shows the longitudinal energy deposition profile of the shower, fitted with a gamma-function. The number of electrons (closed circles) and photons (open squares) above* 1.5 MeV *energy is given as well. [26].*

The mean longitudinal containment similarly scales with the logarithm of the shower energy. On average 99 % of the deposited energy of a 1 GeV electron is contained within $16\,X_0$ of material, while only $27\,X_0$ are needed to achieve the same average containment for 1 TeV electrons [32].

The transverse extension of electromagnetic showers is characterised by the Molière radius R_M. On average 90 % of the shower energy are deposited within a cylinder of radius $1\,R_M$. A parametrisation of R_M as a function of the critical energy E_c is given in [26] as

$$R_M = 21.2\,\text{MeV}\frac{X_0}{E_c}. \tag{1.10}$$

1.3.2. Heavy Charged Particles

The energy loss of charged particles due to Bremsstrahlung is suppressed by the particle mass as

$$-\left[\frac{dE}{dX}\right]_{\text{Brems}} \propto \frac{1}{m^4}. \tag{1.11}$$

Ionisation is thus the main electromagnetic process for energy loss of charged hadrons and muons in a wide momentum range of around 0.1 GeV to 1000 GeV. The mean energy loss of a heavy charged particle as a function of its momentum is given by the Bethe-Bloch formula [26] as:

$$-\left\langle\frac{dE}{dx}\right\rangle = Kz^2\frac{Z}{A}\frac{1}{\beta^2}\left(\frac{1}{2}\ln\frac{2m_ec^2\beta^2\gamma^2T_{\max}}{I^2} - \beta^2 - \frac{\delta(\beta\gamma)}{2}\right), \tag{1.12}$$

with a constant K[5)], the projectile charge z, the atomic number of the absorber Z, its atomic mass A, the maximum single collision energy transfer (see [26]) $T_{\max}$ and the mean absorber excitation energy I. $\delta(\beta\gamma)$ is a function correcting for relativistic effects. The combined energy loss of positively charged muons as a function of momentum is given in Figure 1.14, showing a wide minimum around $\beta\gamma \approx 4$, the *minimum ionising particle* (MIP) region, with only a shallow increase for higher momenta.

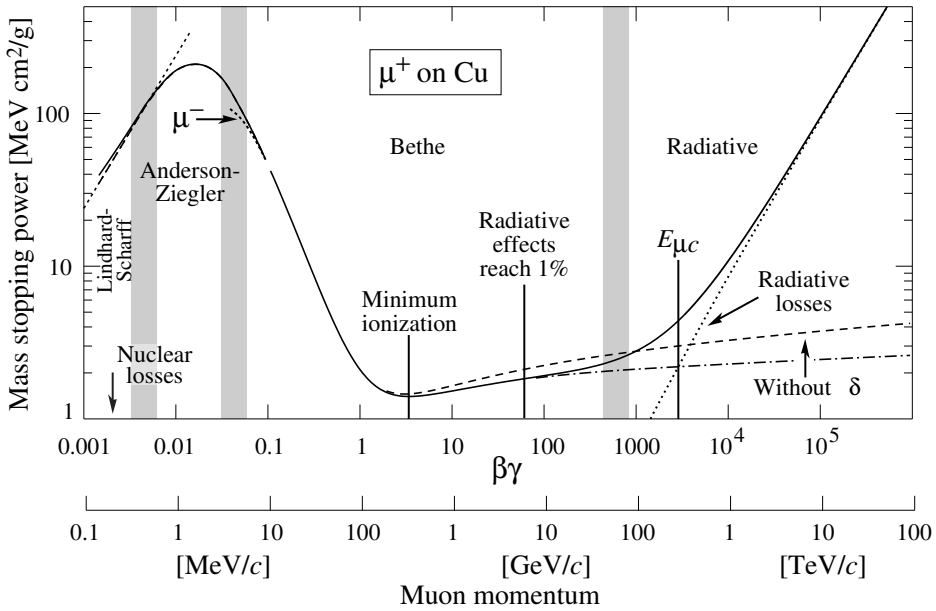

Figure 1.14.: *Mean energy loss of muons in copper as a function of the muon momentum. The shaded areas indicate model transitions. Figure adapted from [26].*

The distribution of energy deposited by charged particles in layers of "moderate thickness" [26] follows a Landau distribution as shown in Figure 1.15. Due to the skewness of the distribution, the most probable energy deposition is around 60 % of the mean energy deposition in this example. The most probable energy deposition is less dependent on the particle momentum than the mean energy loss, enabling the use of the most probable energy deposition of single charged particles as a natural, easily accessible deposition scale.

In the case of a very high energy deposition in a thin layer, the momentum transferred to an electron in the material can reach large enough values to make the secondary electron travel macroscopic distances before being stopped. In very rare cases, the energy of such δ-electrons is enough to induce a small electromagnetic shower on its own.

1.3.3. Hadronic Cascades

Besides ionisation, charged hadrons lose energy from inelastic scattering on nuclei termed *hadronic interactions*. The *nuclear interaction length* λ_n is defined as the mean free path between such hadronic interactions. For any given material, λ_n is typically much larger than the

[5)] $K = 4\pi N_A r_e^2 m_e c^2$, with Avogadro's number N_A, the classical electron radius r_e and the electron mass m_e

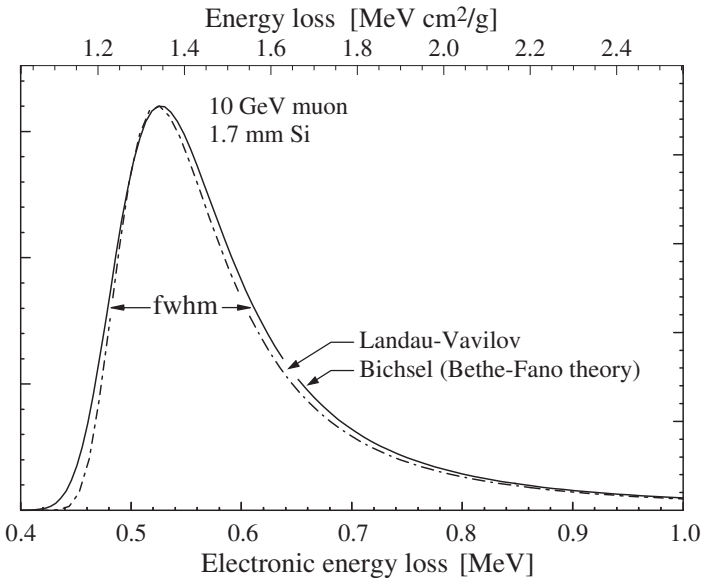

Figure 1.15.: *Distribution of deposited energy of a 10 GeV muon in a 1.7 mm Si layer in two slightly different parametrisations. Figure adapted from [26].*

corresponding value of X_0. For materials with $A > 7$, λ_n can be parametrised [33] as

$$\lambda_n = \left(20A^{0.4} + 32\right) \frac{g}{cm^2}. \tag{1.13}$$

According to the cross section ratio of protons and pions for inelastic scattering on target protons, the *pion interaction length* λ_π is typically increased by a factor of $\frac{3}{2}$ compared to λ_n.

In inelastic hadronic interactions, the incident hadron interacts with one or several nucleons inside the target nucleus, transferring significant fractions of its momentum. This energy transfer into the nucleus can lead to a variety of nuclear reactions, including spallation, fission and nuclear breakup, typically generating secondary mesons ($\pi^\pm, \pi^0, \eta$), ejecting protons and neutrons from the target and potentially leaving behind excited fragments of the struck nucleus. The composition, number and momenta of the secondary particles fluctuate strongly from interaction to interaction, depending on the impact parameter and total momentum transfer as a measure of the hardness of the interaction. Depending on the projectile energy, 2 % to 5 % of charged hadrons undergo full charge conversion in quasi-elastic interactions (e.g. $\pi^- + p^+ \to n + \pi^0$, $\pi^+ + n \to p^+ + \pi^0$) with minimal energy transfer to the interacting nucleon[6)].

Secondary hadrons of sufficient energy may continue their way through the absorber material, inducing further hadronic interactions, leading to a hadronic shower cascade. Secondary π^0 and η particles immediately decay into two (or more) photons[7)], initiating a local electromagnetic sub-shower. On average around 20 % of the energy transferred into the target nucleus are *invisible*, going into excitation or recoil of the target nucleus, or nuclear binding energy of secondary particles. Additional energy might be lost to neutrinos from

[6)] Private communication with Sergej Schuwalow (DESY)
[7)] $BR(\eta \to \geq 2\gamma) = 72\,\%$

the decay of charged hadrons in the cascade. The hadron cascade dies out eventually, when the secondary particles do not have enough energy to induce further hadronic interactions. A schematic view of a hadronic cascade is shown in Figure 1.16.

Compared to electromagnetic showers, hadron showers are typically larger in extension due to $\frac{\lambda_n}{X_0} \gg 1$. The possible processes in hadronic showers are much more complex than in electromagnetic showers. Hadron showers are characterised by only a few hard hadronic interactions with a strongly variable number of secondaries per interaction. There are thus large statistical fluctuations in the longitudinal and transverse shower extensions, invisible energy fraction and the fraction of energy in purely electromagnetic sub-showers.

To longitudinally contain an average of 95 % of the energy deposited by a 100 GeV charged pion, a calorimeter of around $8\,\lambda_\pi$ depth is needed. In transverse direction a cylinder of radius $1\,\lambda_\pi$ contains around 90 % of the full shower energy on average [32].

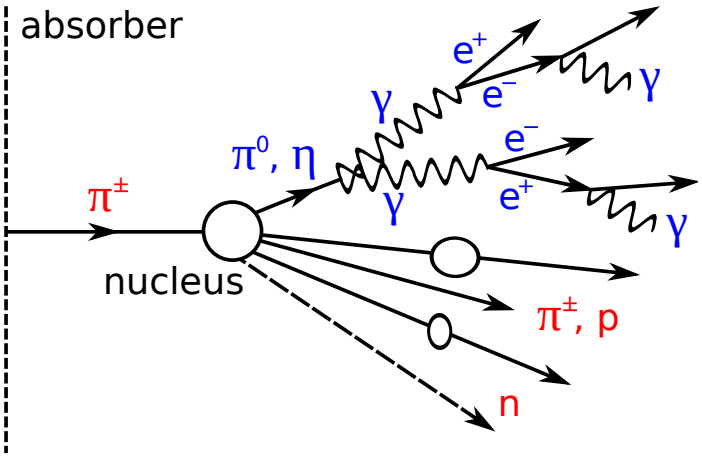

Figure 1.16.: *Schematic depiction of a hadronic cascade. The purely electromagnetic fraction is depicted in blue, the hadronic fraction is shown in red [34].*

1.4. Simulation of Particle Showers

GEANT 4 [35] is a toolkit to simulate particle interactions with matter in a wide range of energies, making it a widely used simulation tool even outside of high-energy physics. Within the context of simulations for CALICE calorimeter prototypes and the full ILD detector, it is used in conjunction with MOKKA, which provides detailed implementations of detector geometries [36].

GEANT 4 offers diverse tools and models for simulating the physics processes occurring in particle showers.

1.4.1. Electromagnetic Cascades

Electromagnetic showers are generally considered well understood due to their simple interactions between only electrons, positrons and photons. All electromagnetic interactions in GEANT 4 are simulated with a standard EM package [37], typically reproducing observables in sampling calorimeters to around $\leq$1 % [38].

The recently introduced _EMY physics list suffix enables a more accurate description of the electromagnetic ionisation processes in active media, effectively generating more ionisation clusters with less deposited energy each, which is needed to correctly simulate thin active layers with detection methods that are sensitive to the position of the first ionisation, like RPC gas detectors. The use of the _EMY physics lists is greatly improving the agreement of simulation and data in the RPC based CALICE calorimeter prototypes [39].

1.4.2. Hadron Cascade Simulations

The simulation of hadron cascades is decidedly more complex than the simulation of electromagnetic showers due to the compositeness of both the projectile hadron and the struck target nuclei. High energy interactions between these hadrons have very large final state phase spaces governed by the strong force, which typically cannot be solved analytically. Instead, models, approximations and parametrisations of such processes are employed. At the present day no ultimate model of hadron cascade development, which would describe measured hadronic shower observables to the same accuracy as what has been established in electromagnetic shower simulations, has been devised. Significant advances have however been made in recent years.

The general assumption in hadronic interaction models is that the deBroglie wavelength of the projectile $\lambda = \frac{h}{p}$ defines the scale of target and projectile substructures to be considered in the modeling of the interaction. At lower energies it is sufficient to model individual nucleons in the target, while at higher energies the quark content of the projectile and target nucleon have to be taken into account. Different models thus aim to describe interactions at different energies.

In typical hadronic interaction models, first the direct interactions of the projectile and target nucleus are calculated, yielding an excited nucleus and possible secondary particles. In a second step the de-excitation of the nucleus, possibly ranging from yielding more secondary particles to its full fragmentation, is modelled.

Intra-nuclear Cascade Models

In energies up to a few GeV λ is around the distance between nucleons, but larger than the quark sub-structure. Thus an interaction model based on individual nucleons is expected to give reasonable results.

Typically the projectile hadron is tracked through the target nucleus, where it is interacting with the nucleons. The mean free path between such interactions is calculated from modelled nucleon densities and parametrised interaction cross sections. Secondary particles generated in intra-nuclear interactions are tracked in the same way. This *intra-nuclear cascade* (INC) concludes when all tracked particles are either absorbed in the nucleus (by means of a minimum energy threshold), or have left the nucleus as a secondary particle. A schematic sketch of an INC is shown in Figure 1.17.

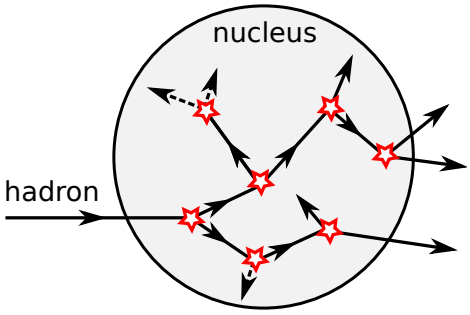

Figure 1.17.: *Schematic sketch of an intra-nuclear cascade [34].*

In the Bertini cascade model [40], the nucleus is modelled as three spherical shells of respectively constant nucleon density. Nucleons and their momentum distributions in each shell are treated as Fermi gas, occupying all energy states up to the Fermi energy. In each INC collision the struck nucleon, the type of interaction taking place and the reaction products and their four-momenta are calculated while the energy of the tracked particle is $>2\,\mathrm{MeV}$.

The Bertini model includes a de-excitation model. First pre-equilibrium evaporations as the emission of neutrons and protons from the excited nucleus are computed. Then a full de-excitation is modelled, including Fermi-breakup of light ($A < 17$) excited nuclei into multiple fragments, a simple explosion model, in which all nucleons are released from the nucleus, and a phenomenological fission model for heavier nuclei.

A more detailed description of the Bertini cascade model implemented in GEANT 4 is given in the GEANT 4 Physics Reference Manual [41].

Parton String Models

Parton string models are applied in the energy range of typically $>5\,\mathrm{GeV}$, where a description of the interaction in terms of the constituent quarks of the projectile and the target nucleon becomes crucial. The projectile is assumed to initially interact with a single target nucleon, which is assigned a random momentum up to the Fermi momentum. The type of interaction is predicted from the impact parameter and center of mass energy between projectile and target, based on the cross sections of inelastic and diffractive interactions.

A gluon string is established between one quark of the projectile and one quark from the target nucleon, which fragments within the nucleus, causing excitation of the nucleus and the generation of secondary particles within the nucleus [42]. Schematic sketches of the string formation and fragmentation are shown in Figure 1.18.

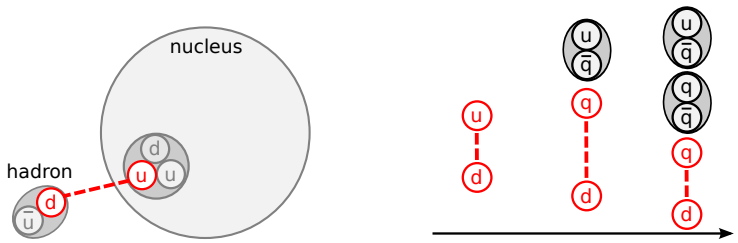

Figure 1.18.: *Schematic working principle of string models implemented in GEANT 4. (a): Gluon string formation between one quark from the projectile and one quark from the nucleon. (b): Gluon string fragmentation via the generation of quark-antiquark pairs and subsequent hadronisation. [34].*

Two different models for this are implemented in GEANT 4, the *Fritiof* model and the *quark-gluon string* model, which differ in their treatment of gluon string formation and fragmentation. The Fritiof model considers only momentum exchange between projectile and nucleon in diffractive hadronic interactions [43]. The quark-gluon string model additionally includes inelastic scattering processes mediated by pomerons [44, 45].

After the parton string model calculations, the excited nucleus and possible secondary particles within the nucleus remain. The secondaries are propagated through the nucleus in cascade models. The de-excitation is calculated with the standard GEANT 4 de-excitation model [41, 46].

More simple parametrised models are based on fits to experimental data to predict the production of secondaries in hadronic interactions. In such models no detailed interactions are modelled and energy is only conserved on average, but not necessarily in each interaction. GEANT 4 provides the *low energy parametrisation* (LEP) and high energy parametrisation (HEP) models adapted from the GHEISHA package [47]. Parametrised models are not anymore considered state of the art, but used occasionally to fill gaps in energy coverage of other models in certain physics lists.

1.4.3. Physics Lists

In GEANT 4, physics lists are combinations of interaction models, each active in different energy ranges [48]. A smooth transition between models is achieved by overlapping their energy regions and randomly selecting one of both models per interaction.

In this thesis, the physics lists QGSP_BERT_HP and FTFP_BERT_HP are used in GEANT 4 version 10.1p2 and 9.6p3, as those are considered most mature, stable and well tuned [49]. The model composition of these physics lists is shown in Figure 1.19.

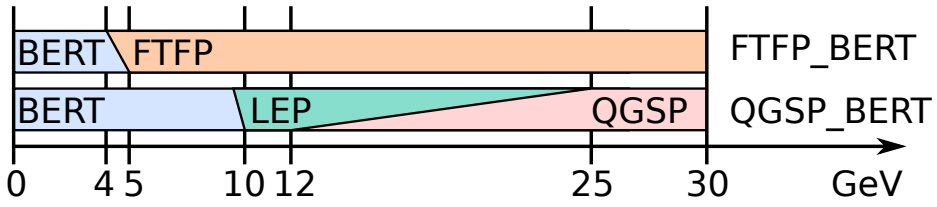

Figure 1.19.: *Schematic G4 physics lists parametrisation vs. energy. Adapted from [34].*

QGSP_BERT

The QGSP_BERT physics list uses the Bertini cascade model in the low energy range up to 10 GeV. The energy range 9 GeV to 25 GeV is covered by the LEP parametrisation. The high energy range >12 GeV uses the *Quark-Gluon String Precompound* (QGSP) modeling.

FTFP_BERT

The FTFP_BERT physics list also uses the Bertini cascade model in the low energy range, but only up to 5 GeV. The full energy range >4 GeV is covered by the *Fritiof Precompound* (FTFP) model.

In the version change of GEANT 4 9.6p3 to 10.1p2 the π^0 production rate in hadron showers was re-tuned [50]. Most hadron shower simulations in this thesis have been carried out in both GEANT 4 versions for this physics list to judge the influence of this change on the hadron shower description.

_HP Neutron Tracking

The _HP versions of the QGSP_BERT and FTFP_BERT lists improve the accuracy in the neutron tracking at low neutron energies, improving the simulated response and deposition timings, especially in high-Z absorbers.

1.5. Calorimeters

Calorimeters in high energy physics determine the energy of incident particles by total absorption and subsequent detection of the deposited energy. The concept of a fully absorbing calorimeter is only feasible in dense absorbing materials to limit the overall shower dimensions and due to the logarithmic scaling of the shower depth with the shower energy. The energy deposited by a particle shower is generally proportional to the energy of the incident particle. The measurement of deposited energy is possible with scintillating materials which emit visible photons from atomic de-excitation, or with charge sensitive media that allow the amplification and collection of the free charges generated from ionisation in the material, such as silicon diodes, liquid argon or certain gas mixtures.

In *homogeneous* calorimeters the absorber material itself is sensitive to energy depositions. In order to constrain the required size of such calorimeters, dense scintillating crystals such as $PbWO_4$ ($\rho = 8.2\,\frac{g}{cm^3}$) are used. The generated photons are detected either with photomultiplier tubes or modern semi-conductor photon detectors (see section 2.1).

Sampling calorimeters interleave dense but passive absorber materials with sensitive detectors. Most of the shower energy is deposited in the absorber materials and thus not measured, so the measured energy deposited in the active material is used to extrapolate to the full shower energy. Sampling calorimeters enable a largely free choice of absorber material and detection technology as well as geometric layout of the detector. As absorber materials are more dense and less expensive than sensitive materials, sampling calorimeters can reduce both the cost and the total detector volume. *Sandwich* geometries, in which layers of absorbing and sensitive material are alternated, allow for readout granularity along the longitudinal shower axis. Compared to homogeneous calorimeters, the energy resolution of sampling calorimeters is degraded due to the fluctuations in the fraction of the total energy deposited in the sensitive material. In order to quantify the fraction of energy measured in the active layers, the *electromagnetic sampling fraction* f_s is used, defined as the fraction of the full shower energy deposited in the sensitive material by a purely electromagnetic shower, which to first order is equivalent to

$$f_s \approx \frac{\left[\mathrm{X}_0/\mathrm{layer}\right]_{\mathrm{sens.}}}{\left[\mathrm{X}_0/\mathrm{layer}\right]_{\mathrm{abs.}} + \left[\mathrm{X}_0/\mathrm{layer}\right]_{\mathrm{sens.}}}, \tag{1.14}$$

with the radiation length of one layer of sensitive material $\left[\mathrm{X}_0/\mathrm{layer}\right]_{\mathrm{sens.}}$ and the radiation length of one layer of absorber $\left[\mathrm{X}_0/\mathrm{layer}\right]_{\mathrm{abs.}}$.

Most given calorimeters are specifically optimised for the measurement of either electromagnetic or hadronic showers. Electromagnetic calorimeters (ECALs) are designed as homogeneous calorimeters or as sampling calorimeters, typically using high density absorbers (Pb, W) and sampling fractions of at least 5 %, for a depth of $20\,\mathrm{X}_0$ to $25\,\mathrm{X}_0$ in 25 cm to 50 cm [51].

Hadron calorimeters (HCALs) are often constructed as sandwich calorimeters in which the absorber is simultaneously providing mechanical support, typically using steel plate absorbers. HCALs need to be of significantly larger dimensions than ECALs due to the extensions of hadron showers. A depth of 160 cm Fe absorber is needed to ensure 95 % average containment of a 100 GeV charged pion [26, 32]. The sampling fractions of HCALs are typically only around few percent, as sampling fluctuations are not the primary driver of the hadron energy resolution. HCALs are still capable of measuring electromagnetic showers, but at generally worse energy resolution than ECALs.

In the design of hermetic particle physics detectors, the HCAL system is fully surrounding the outside of the ECAL system. Any hadron reaching the HCAL has thus necessarily passed through the ECAL, where it potentially deposited significant amounts of energy. To reconstruct the full energy of a given hadron shower, it is thus necessary to combine the depositions from the ECAL and HCAL, as is described in more detail in section 4.7.

The measured response of a calorimeter to an electromagnetic shower is proportional to the number of generated particles N and thus the total shower energy E_0 (see Equation 1.8). Statistical fluctuations in the measured response lead to an absolute energy resolution $\sigma_E \propto \sqrt{E_0}$, which yields the well known stochastic term A of the relative calorimeter resolution $\frac{A}{\sqrt{E_0}}$. For a full description of the relative calorimetric energy resolution a noise

term $\frac{B}{E}$ and a constant term C are added in quadrature, yielding

$$\frac{\sigma}{E} = \underbrace{\frac{A}{\sqrt{E}}}_{\text{stochastic}} \oplus \underbrace{\frac{B}{E}}_{\text{noise}} \oplus \underbrace{C}_{\text{constant}} . \tag{1.15}$$

The noise term B describes resolution effects due to the fluctuating pedestal level of individual readout channels. It is measured from empty events and, if at all, only relevant at very low particle energies and thus often omitted from reporting. The constant term C describes the minimum achievable energy resolution due to detection inefficiencies and calorimeter inhomogeneities.

In sampling calorimeters, the number of measured shower particles is reduced to $N_{\text{meas}} \approx f_s N$, which degrades the electromagnetic energy resolution by a factor around $\frac{1}{\sqrt{f_s}}$. This sampling uncertainty is increased further by the long non-Gaussian tail in the energy deposition of single particles traversing a sensitive layer (see Figure 1.15).

As an example for currently operating electromagnetic calorimeters, the homogeneous crystal ECAL of the CMS experiment reaches a resolution of $\frac{\sigma}{E} \approx \frac{2.8\,\%}{\sqrt{E[\text{GeV}]}} \oplus 0.3\,\%$ for electromagnetic showers [52]. The ATLAS ECAL is a liquid argon-Pb sampling calorimeter with around 4 % to 6 % sampling fraction, reaching a testbeam energy resolution of $\frac{\sigma}{E} \approx \frac{9.2\,\%}{\sqrt{E[\text{GeV}]}} \oplus 0.2\,\%$ for electromagnetic showers [53, 54].

Due to a mean energy fraction of around 20 % going to invisible processes in hadron showers, the measured response for a hadron shower of a given energy is typically significantly smaller than the measured response of an electromagnetic shower of the same energy. This $\frac{e}{h}$ ratio is larger than unity for typical calorimeters and may increase beyond the invisible energy fraction from inefficiencies in detecting neutrons generated in hadronic processes. Calorimeters with effective $\frac{e}{h} > 1$ are termed under-compensating, while calorimeters with effective $\frac{e}{h} < 1$ are termed over-compensating.

As the energy fraction going into purely electromagnetic sub-showers fluctuates strongly from shower to shower, the measured energy fluctuates due to $\frac{e}{h} \neq 1$, degrading the energy resolution. The mean energy fraction in electromagnetic sub-showers increases with the shower energy, as the π^0/η production depends on the number of hadronic interactions in the shower. In a simplified hadron shower model, in which each hadronic interaction generates secondary π^+, π^-, π^0 particles in equal fractions of $\frac{1}{3}$, the mean total energy fraction in electromagnetic subshowers is $f_{\text{EM}} \approx 1 - \left(\frac{2}{3}\right)^n$ with the number of occurred hadronic interactions n. Due to the cascading nature of particle showers number of hadronic interactions scales as $n \propto \log E_0$ and thus increases with energy, resulting in a non-linear response for non-compensating calorimeters. The fluctuations in electromagnetic and invisible energy fraction typically dominate the resolution of hadron calorimeters over sampling fluctuations.

The generation of low energy ($E_n \lesssim 20\,\text{MeV}$) neutrons is abundant in hadronic interactions and thus correlated to the invisible energy fraction. Low energy neutrons mostly undergo elastic interactions in which the energy transfer is maximised when $\Delta m = \left|m_n - m_{\text{target}}\right| = 0$. Such neutrons will thus deposit very low energy in very high Z absorber materials. If the active material is rich in hydrogen (e.g. plastic scintillators), the

momentum of low energy neutrons will be mostly transferred into these hydrogen nuclei. As the range of MeV protons is small in plastic scintillators (tens of µm [51]), the neutron fraction of the full shower energy is not sampled according to f_s, but deposited almost exclusively in the scintillator. By optimising the used absorber material, the used active material, their respective thicknesses and thus the sampling fraction of the calorimeter, the deposition loss due to invisible energy can be offset by the enhanced depositions of low energy neutrons. There are additional dependencies on the surface area between absorber and sensitive material as well as their geometric depth ratio [55, 56].

The ZEUS hadron calorimeter, which is widely regarded as the best energy resolution hadron calorimeter ever operated, was designed as a compensating sandwich sampling calorimeter, using U ($Z = 82$) absorbers and plastic scintillator readout. The respective thicknesses of absorber and scintillator were carefully optimised to achieve near perfect compensation. Finally, 3.2 mm U absorber plates were interleaved with 3.0 mm plastic scintillator tiles, achieving a single charged pion energy resolution of $\frac{\sigma}{E} \approx \frac{35\,\%}{\sqrt{E\,[\mathrm{GeV}]}} \oplus 2\,\%$ with $\frac{\mathrm{e}}{\mathrm{h}} = 1.00 \pm 0.03$ [57].

As an example of an HCAL currently in active operation, the ATLAS hadronic tile calorimeter is constructed as a scintillator steel sampling calorimeter built of radially staggered scintillator tiles and steel plates, pointing towards the beam axis. It is clearly undercompensating at $\frac{\mathrm{e}}{\mathrm{h}} = 1.36$, yielding a single hadron energy resolution of $\frac{\sigma}{E} = \frac{52.9\,\%}{\sqrt{E\,[\mathrm{GeV}]}} \oplus 5.7\,\%$ in testbeam measurements [58].

To improve the resolution of hadron calorimeters apart from implementing sampling configurations that result in near compensation, other approaches are used and actively investigated:

In *dual readout* calorimeters, two separate active media are read out to estimate the electromagnetic energy fraction of hadronic showers on an event-by-event basis. In addition to the ionisation generated by charged particles, the Cherenkov radiation (see section 4.2) generated by relativistic charged particles in dense media is typically measured in non-scintillating quartz fibers. As the hadrons generated in hadron showers are mostly non-relativistic ($m_\mathrm{h} \gg p_\mathrm{h}$), the obtained Cherenkov signal is strongly correlated to the electromagnetic fraction of the hadron shower. This enables reweighting of individual showers according to their estimated electromagnetic energy fraction. Prototypes of such calorimeters have been constructed and tested, but currently still suffer from low Cherenkov light yields and possible leakage effects due to limited prototype size [59]. Preliminary energy resolutions of 11.0 % for 20 GeV pions and 7.7 % for 60 GeV pions have been achieved with a prototype of around 30 cm × 30 cm × 250 cm size [60].

In calorimeters with fine spatial segmentation, it is possible to statistically identify electromagnetic sub-showers within hadron showers from the measured shower topology. Either the whole shower or single hits of the shower can then be re-weighted to compensate for $\frac{\mathrm{e}}{\mathrm{h}} \neq 1$. This has been demonstrated to significantly improve the hadron energy resolution of the H1 hadron calorimeter, which is utilising the local hit deposition density to distinguish electromagnetic sub-showers from hadronic shower depositions [61]. In the ATLAS forward calorimeter (FCAL), a similar approach uses the distance of each deposition to the reconstructed shower axis to discern electromagnetic sub-showers in hadron showers. An

independent implementation of such a *software compensation* reconstruction developed as part of this thesis is presented in subsection 4.7.2.

1.5.1. Particle Flow Calorimetry

Particle jets generated in high energy particle physics processes can carry large fractions of their energy in hadrons. Thus measuring jet energies using classical calorimeter systems is limited by the hadronic energy resolution of the calorimeter system.

A modern approach to jet energy reconstruction was made possible due to the significant advances in tracking detectors and high granularity calorimeters over the past 15 years. The goal of *Particle Flow Algorithms* (PFAs) is to reconstruct every single particle in a jet, using the subdetector measurement yielding the best resolution for each particle individually. PFA implementations have been used at previous experiments dating back to ALEPH at LEP [62], H1 at HERA [63, 64] up to the currently operating CMS at LHC [65]. However, none of these detectors were designed specifically for particle flow reconstruction, in parts because the calorimeter granularities needed for this were simply not achievable at the time. The detectors planned for ILC are designed to offer the best possible instrumentation for the application of PFAs.

Assuming the projected subdetector performances at the ILD (tracking: $\frac{\sigma}{p} \approx 5 \times 10^{-5} \times\ p\,[\mathrm{GeV}/c]$, ECAL: $\frac{\sigma}{E} \approx \frac{17\,\%}{\sqrt{E[\mathrm{GeV}]}}$, HCAL: $\frac{\sigma}{E} \approx \frac{60\,\%}{\sqrt{E[\mathrm{GeV}]}}$), the resolution crossover point between tracking and calorimeter resolution is around 200 GeV in the ECAL and around 500 GeV in the HCAL for single particles. As jets typically consist of many particles, the tracking momentum resolution is practically always better than the calorimetric resolution for any charged particle of the jet.

An average of $f_{\pm} \approx 60\,\%$ of particles in a jet is charged and their momentum thus precisely measured by the tracking system. The energy of these charged particles can be calculated from the energy-momentum relation $E = (pc)^2 + (m_0c^2)^2$, using an educated assumption about the particle type and thus its mass. The $f_\gamma \approx 30\,\%$ photons in a jet can be measured to good accuracy in the electromagnetic calorimeter system. This leaves only $f_{h^0} \approx 10\,\%$ of all particles to be neutral hadrons which are limited by the hadronic energy resolution of the calorimeter system. A schematic depiction of particle flow reconstruction given in Figure 1.20. Due to their ability to reconstruct single particles within a jet, PFAs naturally yield precise and efficient object definitions for the general reconstruction of high energy collision events.

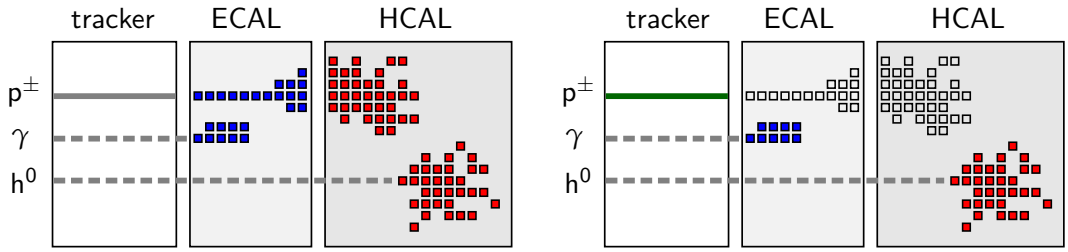

Figure 1.20.: *Schematic depiction of purely calorimetric and Particle Flow jet energy reconstruction. In the calorimetric reconstruction (left), depositions in the calorimeters are simply added up to yield the full jet energy, regardless of particle type and without using the measured momentum information from the tracking system. In Particle Flow reconstruction schemes (right), the tracker momentum measurement is used to measure the energy of charged particles instead of their calorimeter depositions. [34]*

To use PFAs to their full potential, the detector system has to fulfill unprecedented requirements:

The tracking system needs to have a high track reconstruction efficiency of $>99\,\%$. The mis-reconstruction of two close tracks as one single track potentially causes the full loss of the energy of one of both particles. The possibility to measure the ionisation power of tracks potentially helps to identify the particle type of each track to calculate the particle energy from the measured momentum.

The calorimeter readout needs to be finely segmented spatially to be able to reliably assign calorimeter depositions to tracks and to identify neutral hadron depositions that are not connected to any track. Overlapping calorimeter depositions of a neutral and a charged particle may lead to a loss of reconstructed energy due to the (partial) assignment of the neutral depositions to the charged particle cluster. Similarly energy is double-counted when fragments of a charged hadron shower are mis-identified as a separate neutral particle deposition. The calorimeter requirements to minimise this *confusion* are thus very thin active layers to minimise the effective Molière radius of the calorimeter, yielding the most compact possible sub-showers, and lateral readout segmentation around one R_M combined with a longitudinal readout granularity around one X_0, to be able to spatially resolve electromagnetic sub-showers as the smallest features of hadron showers.

The jet energy resolution achieved by an ideal PFA would be composed of the individual resolutions of the tracking system, ECAL and HCAL, weighted with their respective mean measured jet energy fraction. In realistic implementations, such as *PandoraPFA* [23], the achieved jet energy resolution is dominated by the calorimeter resolution for jet energies $<100\,\mathrm{GeV}$, while the confusion term is the driving the resolution for higher jet energies, as is shown in the breakdown of the jet energy resolution in its components in Figure 1.21(a). This is due to the reduced separation of tracks and calorimeter clusters as well as slightly larger shower extensions at higher jet energies, leading to more overlap of the calorimeter depositions and thus worse differentiation between neutral and charged hadron shower clusters. At very high jet energies the loss of resolution from shower leakage due to the relative small HCAL radius in ILD is visible, but by far not dominating. Most importantly, PandoraPFA improves the jet energy resolution over the raw calorimetric resolution at all jet energies.

The parametrised full jet energy resolution obtained from PandoraPFA in realistic simulations of the full ILD detector concept is given in Figure 1.21(b), reaching around 3 % in the jet energy range 45 GeV to 250 GeV as is the design goal of ILD, demonstrating the feasibility and performance of a detector design optimised for particle flow reconstruction

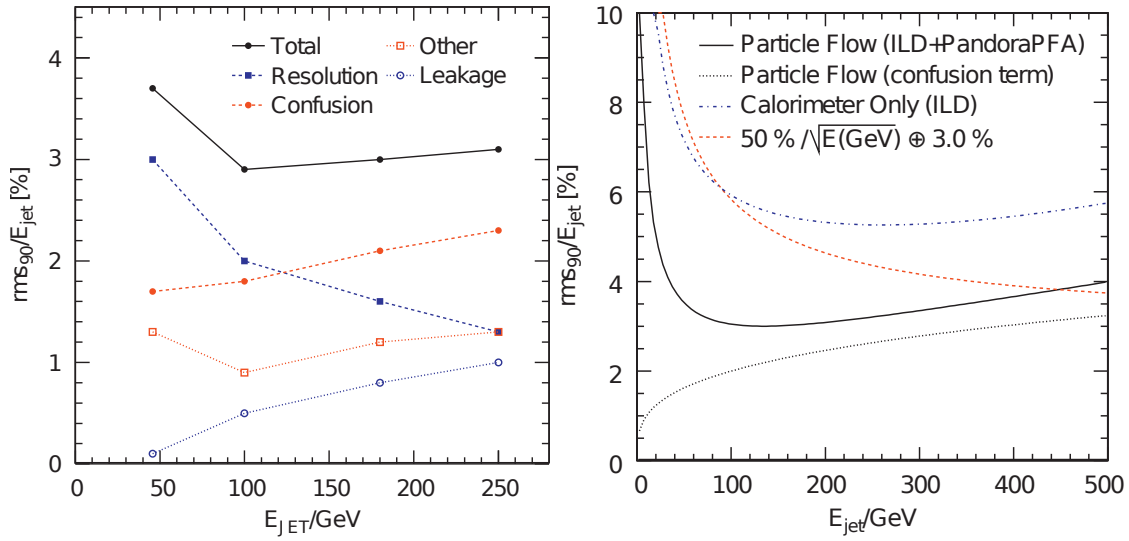

(a) *Single Point Jet Energy Resolution Contributions*

(b) *Parametrised Jet Energy Resolution*

Figure 1.21.: *Jet energy resolutions obtained for the ILD full detector simulations with the PandoraPFA Particle Flow implementation. The jet energy resolution of the ILD detector is significantly improved across the whole energy range. [23]*

2. CALICE Physics Prototypes

The CALICE collaboration develops and validates concepts of highly granular electromagnetic and hadronic sandwich calorimeters designed for the application of particle flow algorithms at a future e^+e^--collider experiment. The collaboration currently has 336 members in 57 institutes and 17 countries [66]. Several calorimeter concepts with different absorber materials, granularities and readout technologies are under active investigation and have been realised in various prototypes.

All CALICE electromagnetic calorimeter designs are based on tungsten absorbers. The investigated readout options span from fine-pitched *monolithic active pixel sensors* (MAPS) with down to 50 µm × 50 µm readout segmentation, to 5 mm × 5 mm silicon diodes, to thin scintillator strips with silicon photomultiplier readout (see section 2.2).

The CALICE hadronic calorimeters are foreseen to use steel absorbers in the baseline configuration, with tungsten absorber structures under investigation for higher energy e^+e^--colliders as CLiC. Gaseous active layers with 1 cm × 1 cm transverse granularity are considered using either *resistive plate chamber* (RPC) readout or *micro-mesh gaseous structures* (Micromegas) [67]. RPC based concepts are available with binary [68, 69] or 2 bit hit amplitude measurement [70]. Another concept utilising scintillator tiles with silicon photomultiplier readout is described in detail in section 2.3.

This chapter describes the technology, hardware and calibration procedures of the CALICE scintillator-SiPM calorimeter physics prototypes. The described methods used to accurately model the intrinsic readout effects of such calorimeters were validated as part of this thesis.

2.1. Silicon Photomultipliers

Silicon photomultipliers (SiPMs) are semiconductor devices capable of measuring light amplitudes down to single photon intensities. Gains[1)] up to around 10^6 are achievable with SiPMs, similar to classic *photomultiplier tubes* (PMTs). The advantages of SiPMs over PMTs are their small size in the range of mm^2, easy mass production and hence significantly reduced cost per unit, lower required bias voltage of only around $\lesssim$100 V and full insensitivity to even strong magnetic fields [71, 72]. The whole concept of a scintillator calorimeter with sufficient readout granularity for the effective application of particle flow algorithms is only feasible because SiPMs allow the integration of the sensors into the active detector layers [73].

Silicon photomultipliers consist of an array of PiN-diode pixels with serial quenching resistors on a common semiconductor substrate. Microscope pictures of a typical SiPM are shown in Figure 2.1. All pixels are connected in parallel to common anode and cathode leads. Typical SiPMs integrate thousands of pixels on a few mm^2 area.

[1)] The gain of photo detectors is defined as the number of output electrons per detected photon.

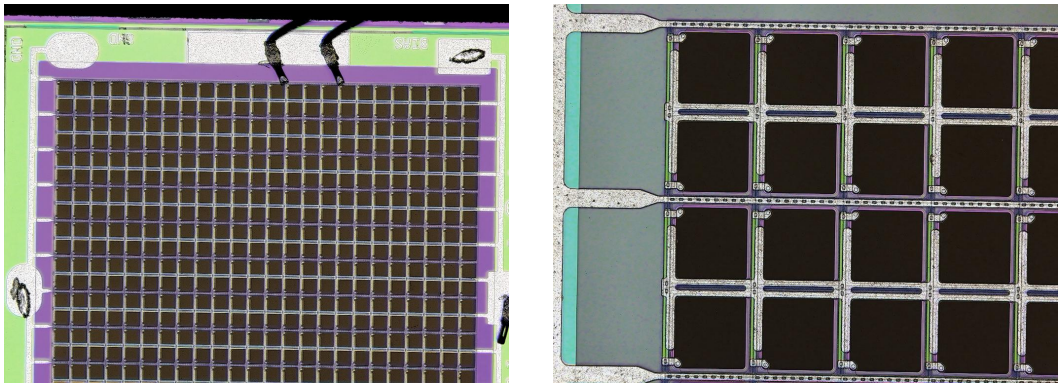

(a) SiPM Surface **(b)** SiPM Pixel Detail

Figure 2.1.: *Microscope pictures of a SiPM. The overview picture shows the grid of pixels, ground and bias voltage distribution traces and the bonding wires at the top. The detail picture shows the structure of each individual pixel, including the polysilicon quenching resistor in green. Images kindly provided by Michael Matysek, Sebastian Laurien and Erika Garutti (Universität Hamburg).*

The reverse bias voltage U_{bias} applied to each pixel is larger than its breakdown voltage U_{bd}, operating the diodes in *Geiger mode*. A single incident photon can generate a free electron-hole pair in the depletion region of the PiN-diode. Because of the high electric field in the depletion region, the electron and hole have a high probability (the SiPM *quantum efficiency*) of drifting apart instead of recombining immediately. They are then further accelerated by the electric field in the depletion region, generating more electron-hole pairs on their path via impact ionisation. This triggers a self-sustaining avalanche, the *Geiger discharge* or *firing*, effectively rendering the diode conductive. Due to the arising current, the quenching resistor with resistivity R_{q} reduces the effective voltage across the diode to below U_{bd}, stopping (or *quenching*) the avalanche. The charge expelled by the diode when firing Q depends on the capacitance of the biased diode C_{px}, and the over voltage $U_{\text{ov}} = U_{\text{bias}} - U_{\text{bd}}$ as

$$Q = U_{\text{ov}} \cdot C_{\text{px}}, \tag{2.1}$$

which corresponds to the pixel gain when expressed in units of elementary charge. C_{px} depends on the size and geometry of the diode as well as doping profile of the substrate. As Q is independent of the number of initially generated electron-hole pairs, each pixel acts as a binary device. Once the electron avalanche has stopped, the effective voltage across the diode returns to U_{bias} with the time constant $\tau = R_{\text{q}} \cdot C_{\text{px}}$, typically around hundreds of nanoseconds, and the pixel is ready to fire again.

Following Equation 2.1, the gain of a SiPM pixel is proportional to $U_{\text{bias}} - U_{\text{bd}}$. U_{bd} effectively increases with temperature, stemming from thermal excitation of vibrational modes in the semiconductor lattice. Thus SiPMs show a negative correlation with temperature in the range of $-1\,\frac{\%}{\text{K}}$, depending on the chosen U_{ov} operation point.

The quantum efficiency, the probability of a single electron-hole pair initiating a Geiger discharge, increases with U_{ov} and thus also shows negative temperature dependence, similar to the SiPM gain.

The signal of a SiPM is the sum of the charges expelled by all fired pixels. With near uniform pixel capacities and amplifications high enough to resolve single fired pixels with cheap electronics at room temperature, the gain of a SiPM can be measured in-situ from the separation of the peaks in *single photon spectra* (SPS). Such spectra are obtained by illuminating the SiPM with short, low amplitude light pulses which do not need to be calibrated or repeatable in intensity. An example SPS taken with the current AHCAL engineering prototype using the integrated LED calibration system is shown in Figure 2.2.

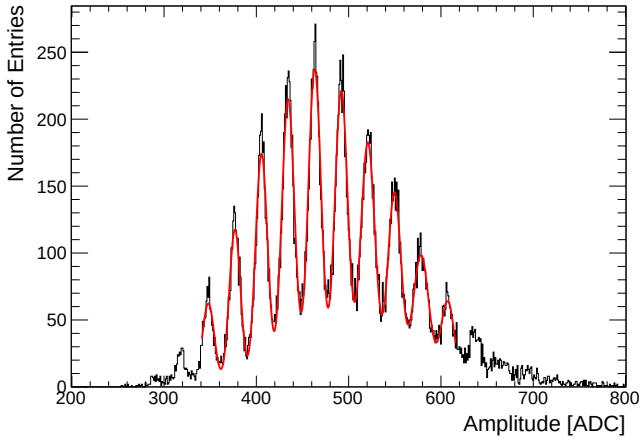

Figure 2.2.: *Raw single photon spectrum acquired with a SensL MicroFB-10020-SMT SiPM, read out by a SPIROC2b ASIC mounted on a HBU3 AHCAL engineering prototype board at room temperature. Each consecutive peak corresponds to one more photon being detected. The spectrum is fitted with a multi-Gaussian function. The distance of the fitted peaks corresponds to the SiPM gain in hardware specific units. The width of the fitted peaks does not visibly increase for higher numbers of fired pixels, indicating a good pixel capacity uniformity of the sensor.*

Because of the finite number of pixels on a SiPM and the pixel recovery time scale τ usually being longer than the typical timescale of incoming photons, the response of a SiPM is inherently non-linear, as shown for a simplified simulation model in Figure 2.5. However the number of incoming photons can be reconstructed from the number of fired pixels, requiring knowledge of the effective number of SiPM pixels, as described in subsection 2.7.4.

Thermal excitations and quantum tunnelling continuously generate electron hole pairs in the depletion zone of each pixel, independent of incident signal photons. The rate of this *dark noise* increases with U_{ov} and temperature. The dark noise frequency for single pixel amplitudes is in the order of 100 kHz for typical SiPMs [74]. Noise amplitudes above the single pixel level are mediated by photons emitted during the avalanche in one pixel, firing one of the neighboring pixels [75]. The dark noise frequency at n_{px} pixel amplitude $r(n_{\mathrm{px}})$ with pixel crosstalk probability p_{x} and overall dark noise rate r_{dark} is well described by a geometric distribution

$$r(n_{\mathrm{px}}) = r_{\mathrm{dark}} \cdot p_{\mathrm{x}}^{n_{\mathrm{px}}}. \tag{2.2}$$

Typical SiPMs show pixel crosstalk probabilities of around 10 % [74].

The batch of prototype SiPMs used in the construction of the AHCAL physics prototype was operated at $U_{\mathrm{bias}} \approx 50\,\mathrm{V}$, yielding a gain of around 1×10^6. The dark noise rate at

0.5 px threshold of these devices is around a few MHz with an average pixel crosstalk probability of about 25 %, leading to an effective noise rate of few kHz at a threshold of 0.5 MIP corresponding to around 7.5 px [76].

The latest generations of SiPMs available from commercial manufacturers offer significant improvement in performance compared to previous models. Dark noise rates as low as 20 kHz have been achieved at room temperature. By introducing etched trenches in the substrate between individual SiPM pixels, the pixel crosstalk was reduced down to $\lesssim$1 % in some SiPM models [77]. The parameter uniformity within one production batch improved enough that channel individual bias adjustment (see section 3.1) is not anymore considered mandatory. SiPMs with very high number of pixels $\geq$10 000 are also available now, offering an improved range of linear response and dynamic range, although with worse noise figures and detection efficiencies due to the small pixel sizes of such devices.

2.2. The Scintillator Electromagnetic Calorimeter

The CALICE scintillator electromagnetic calorimeter (ScECAL) is an ECAL concept based on plastic scintillator strips with SiPM readout. After construction of a small scale prototype, successfully tested in the DESY testbeam in 2007 [78], a larger prototype was built for use in the combined CALICE testbeam at the *Fermilab Testbeam Facility* (FTBF) 2008 & 2009, of which data is analysed in this thesis.

This second prototype instruments an area of $18 \times 18\,\mathrm{cm}^2$ with a depth of 26 cm. 30 layers of 3.5 mm thick tungsten absorber plates, corresponding to around 20 X_0, are instrumented with 72 scintillator strips in alternating horizontal and vertical strip orientations per layer, for a total of 2160 channels. Each extruded plastic scintillator strip of size $45 \times 10 \times 3\,\mathrm{mm}^3$ is individually wrapped in reflective foil. A centrally implemented *wavelength-shifting-fiber* (WLS)[2)] is guiding the scintillation photons onto a 1600 pixel SiPM manufactured by Hamamatsu. The used SiPMs have an exceptionally short pixel recovery time constant, enabling the same pixel to fire more than once per event. This can generate signal amplitudes higher than the number of pixels of the SiPM [79].

The electromagnetic sampling fraction of the ScECAL is around $1/17$.

Preliminary results of the electromagnetic energy resolution of the ScECAL, obtained from data taken at FTBF in 2008-2009, including a more detailed description of the prototype are given in [79–82].

2.3. The Analog Hadron Calorimeter

The CALICE analog hadron calorimeter (AHCAL) was the first large scale particle physics detector utilising SiPMs, pioneering their use in high energy physics. After a small scale prototype, the MiniCal [73], was successfully tested and validated in the DESY electron testbeam in 2003, a $1\,\mathrm{m}^3$ AHCAL physics prototype was built and operated in various CALICE testbeam campaigns from 2006–2012 [76]. From 2010 on the AHCAL was used to study hadron showers with tungsten absorbers, using a separate absorber structure equipped with tungsten plates.

[2)] Kuraray Y-11 [79]

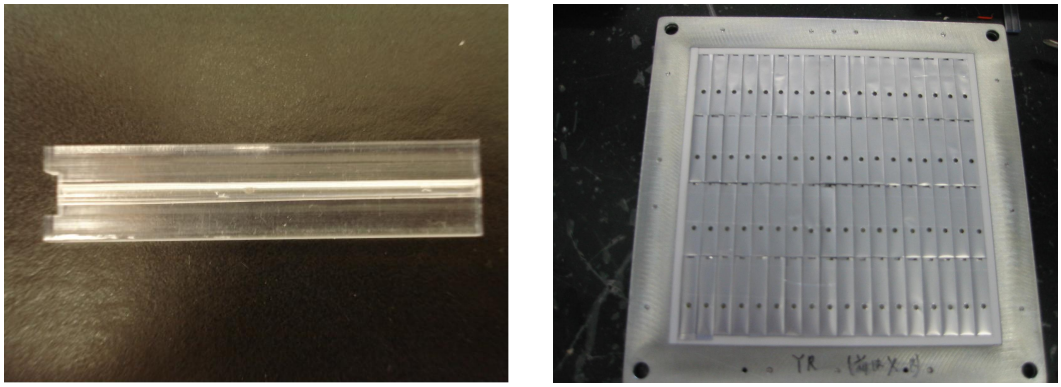

(a) ScECAL strip **(b)** ScECAL active layer

Figure 2.3.: ***(a)****: Raw ScECAL scintillator strip without SiPM, WLS fiber and wrapping.* ***(b)****: Active ScECAL layer with* 4×18 *ScECAL strips wrapped in reflective foil.*

The AHCAL physics prototype is a 100 cm × 100 cm × 120 cm scintillator-steel sampling calorimeter [76]. It is constructed of 39 steel absorber layers of 19.4 mm average thickness for a depth of 5.3 nuclear interaction lengths λ_n corresponding to 4.3 pion interaction lengths λ_π.

The 38 active layers inserted into the slots between absorber plates consist of 7608 plastic scintillator tiles of 5 mm thickness, for an electromagnetic sampling fraction of $1/33$.The central region of each layer is instrumented with 100 tiles of 3 cm × 3 cm, followed by three rings of 6 cm × 6 cm tiles (96 total) and one outer ring of 20 tiles of 12 cm × 12 cm, for a total of 216 tiles per layer. The last eight layers are instrumented with less granularity, only using 141 tiles of the two larger types. A picture of the used tile types and their layout within one layer is shown in Figure 2.4.

A WLS fiber is inserted into a milled groove in each plastic scintillator, directing the scintillation light signal to a 1186 pixel SiPM, manufactured by a collaboration of the *National Research Nuclear University MePhI* (Moscow) and *Pulsar Enterprise*. The edges of each tile are chemically passivated to minimise light crosstalk to adjacent tiles. To simplify installation and maintenance, all tiles of one layer are mounted inside of a steel cassette built from 2 mm thick steel sheets. The insides of the cassettes are lines with reflective foil to improve the lightyield of the tiles.

2.4. The Tail Catcher and Muon Tracker

The tail catcher and muon tracker (TCMT) is a coarse granularity steel scintillator-SiPM sandwich calorimeter mainly used to measure hadron shower leakage and to identify muons in testbeam events [83]. The 100 cm × 100 cm × 140 cm TCMT absorber structure consists of 16 steel plates of varying thickness for a total depth of 5.5 λ_n or 4.4 λ_π. The first eight plates are 19 mm thick, corresponding to the AHCAL sampling, while the other eight plates are 105 mm thick.

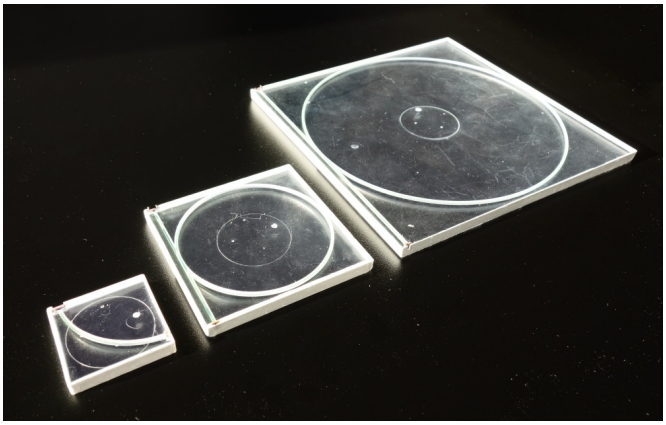

(a) AHCAL Tiles

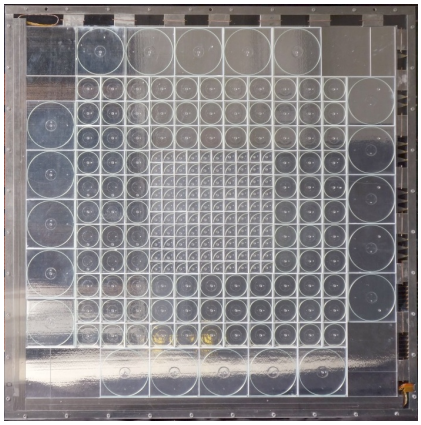

(b) Tile Layout

Figure 2.4.: ***(a)****: Tiles of all three sizes used in the AHCAL prototype (left to right: 3 cm × 3 cm, 6 cm × 6 cm, 12 cm × 12 cm). The sensors glued to the tiles are visible in the top left corner of each tile.* ***(b)****: Active layer of the AHCAL prototype showing the arrangement of differently sized tiles.*

Each of the 16 active layers is instrumented by 20 extruded scintillator strips with embedded WLS fiber sized 50 mm × 1000 mm × 5 mm, for a total of 320 channels. The first active layer is mounted in front of the first absorber plate to maintain an equal sampling ratio when operated behind the AHCAL. The orientation of scintillator strips is alternated between layers.

The electromagnetic sampling fraction of the TCMT is very similar to the AHCAL in the first eight layers, around $1/33$, reducing to $1/165$ in the rear part.

The absorber structure of the TCMT can be equipped with other active layers to increase the effective depth of other calorimeter prototypes, as has been done with additional layers in RPC calorimeter testbeams [69, 70].

2.5. DAQ and Electronics of the Scintillator-SiPM Prototypes

The CALICE scintillator-SiPM calorimeter physics prototypes are operated in a common *data acquisition system* (DAQ), using near identical front-end electronics for all subdetectors.

All SiPMs are connected to charge sensitive preamplifiers attached to each readout layer. These *application specific integrated circuits* (ASICs) have an adjustable input gain of 1 $\frac{\text{mV}}{\text{pC}}$ to 100 $\frac{\text{mV}}{\text{pC}}$ and shaping times between 40 ns to 180 ns [76]. In *physics mode* (PM) the amplification is set up such that the dynamic range spans from single MIPs up to SiPM saturation. The shaping time in physics mode is 150 ns to integrate over the most important hadron shower contributions and to delay the signal until slow beam instrumentation signals can be incorporated into the trigger decision. In *calibration mode* (CM) the amplification is increased by around a factor 10 and the shaping time reduced to 40 ns to resolve single photon peaks.

The amplified signals from the very-front-end electronics are transferred to *CALICE Readout Cards* (CRCs) with 16 bit analog-to-digital (ADC) converters, which are mounted in

VME racks next to the setup. Sampling and digitisation of the signal is triggered by external inputs such as beam scintillator paddles, beamline Cherenkov counters, random (pedestal) oscillators or logic combinations thereof. Trigger decisions are synchronously propagated to each CRC through the VME backplane. The readout data of the triggered event, consisting of one digitised hit amplitude for each calorimeter cell plus the readout from the beam instrumentation, is then transferred to local disk storage.

An attached LED calibration system can provide $\approx 10\,\text{ns}$ light pulses of variable amplitudes to each scintillator cell, ranging from single photons to full SiPM saturation. Low light amplitudes are used to calibrate the gain of each SiPM individually from single-photon-spectra (see section 2.1), while optical crosstalk and SiPM saturation measurements can be performed with higher light intensities. The calibration system also reads out the temperature sensors distributed in the active AHCAL layers. The ScECAL uses a standalone system for temperature measurement which is synchronised to the DAQ system via timestamps in the offline reconstruction.

2.6. Calibration of the CALICE Scintillator-SiPM Prototypes

The raw measurements taken in testbeam campaigns have to be calibrated into a common physics signal scale before being used in analyses. CALICE Calorimeter studies typically use the MIP scale based on the most probable deposition of a minimum ionising particle (see subsection 1.3.2) traversing one calorimeter cell perpendicular to the absorber structure, which is easily calibrated in data and simulation.

To perform this conversion, various calibration factors and diagnostics based on previous laboratory measurements and in-situ procedures are used. Most of these calibration parameters are extracted once from specific runs and made available in CALICE databases for use in the event reconstruction and simulation digitisation. Channel specific calibration factors cannot always be determined for all cells. In this case default values, typically the mean of the parameter extracted from other channels, are utilised.

For each cell i, the ADC readout a_i is pedestal subtracted using the current pedestal value P_i for the channel. The amplitude measured in each channel is converted into the corresponding number of fired SiPM pixels using the SiPM gain $G_i^{\text{CM}}(T)$ and the intercalibration factor IC_i. The SiPM response saturation is linearised by applying the inverse of the SiPM saturation function ${f_{\text{sat}}^i}^{-1}$, yielding the reconstructed number of photons hitting the SiPM. The reconstructed number of photons is converted to the MIP scale using the cell's lightyield LY_i. The full formula to reconstruct the measured cell amplitude a_i into the hit amplitude in MIP units A_i is thus

$$A_i = \frac{{f_{\text{sat}}^i}^{-1}\left((a_i - P_i) \cdot \frac{IC_i}{G_i^{\text{CM}}(T)}\right)}{LY_i}. \tag{2.3}$$

2.6.1. Pedestal

The ADC pedestal P_i for each channel is extracted from random triggers uncorrelated to incident particles. At the beginning of each data run typically 500 such triggers are

generated and used for an initial estimate of the pedestal positions. The pedestal values are then continuously updated from further random triggers generated throughout the run.

The spectrum of pedestal amplitudes, especially its width measured by the standard deviation, is used to determine dead and noisy channels to be excluded in the analysis. Cells with too narrow pedestal distribution are considered dead, usually due to sensor connectivity problems. Cells with too wide pedestal distribution are considered noisy or unstable, usually due to SiPMs with very long discharge times. The thresholds used to classify cells as dead or noisy vary between the subdetectors. During the 2008–2009 testbeam period at Fermilab only three ScECAL cells ($\approx 1‰$) are identified as dead or noisy. In the AHCAL 3.5% of the cells are not used for analysis [34]. Out of the 320 TCMT strips eight do not give usable signals, amounting to 2.5% of the channels [83].

2.6.2. SiPM & Tile Properties

At the beginning of each beam data run, and in dedicated gain calibration runs, the LED system is used to inject light signals of few detected photons into each scintillator cell to record single-photon spectra (see section 2.1), using the calibration mode of the front-end chip. Ideally the SiPM gain $G_i^{\mathrm{CM}}(T)$ is extracted for each channel in units of $\frac{\mathrm{ADC_{CM}}}{\mathrm{px}}$ as a function of temperature T. Correlating gain measurements at different temperatures yields the temperature dependence of SiPM gains, measured to be $-1.7\,\frac{\%}{\mathrm{K}}$ for the AHCAL [76] and around $-0.8\,\frac{\%}{\mathrm{K}}$ in the ScECAL [81].

In order to use the measured gain value to translate recorded shower hit amplitudes into the number of fired SiPM pixels, the ratio of effective gains between the calibration mode and the physics mode has to be determined. This *intercalibration factor* is different from the ratio of configured preamplifier gains because of the different shaping times used in each gain mode. The LED system is used to inject several fixed light intensities into each cell and the intercalibration factor IC_i is extracted for each channel as the fitted slope of the correlation of measured amplitudes in calibration mode and physics mode in units of $\frac{\mathrm{ADC_{CM}}}{\mathrm{ADC_{PM}}}$ [84].

The saturation curve $f_{\mathrm{sat}}^i(a)$ for each SiPM in the AHCAL was measured on a test bench without attached scintillator tile. To take into account the geometric illumination of the SiPM by the WLS fiber, these saturation curves are scaled with a factor ≤ 1. This saturation curve scaling factor is individually determined from LED system measurements [84] for around 75 % of the channels. For all other channels a constant scaling factor of 0.8 is used.

In the ScECAL the saturation curves were measured for 72 wrapped ScECAL strips with attached SiPMs taken from the prototype, using a pulsed laser and reference PMT [81]. The resulting response curves do not saturate towards the number of pixels of the specific SiPMs, but show amplitudes corresponding to beyond 50 % more fired pixels than pixel are present on the SiPMs. This is explained by the short recovery time of the used SiPMs, enabling each SiPM pixel to fire more than once per injected light pulse. This behaviour is not well modelled by the simple SiPM saturation model described in subsection 2.7.4. The model saturation curve is thus fitted to a subrange of the injected light amplitudes, disregarding the measurements for very high measured amplitudes. The number of effective pixels needed to correct for saturation correction is used as the mean of the measured 72 strips. A refined model of SiPM saturation behaviour including pixel recovery effects has been developed

in the meantime [85], but is not yet included in the ScECAL calibration or reconstruction software.

To reconstruct the number of incoming photons, the inverse of the saturation function ${f_{\text{sat}}}^{-1}$ is applied to the measured number of fired pixels. The inverse of an idealised SiPM response function (as described in subsection 2.7.4), is however not defined for values larger than the number of assumed SiPM pixels, leading to mathematical instabilities in the reconstruction of hit amplitudes in channels with miscalibrated number of effective SiPM pixels. To extend its function domain to $[0, \infty[$ the inverse saturation function is approximated by its continuous linearly continuation for hits above a certain fraction of fired SiPM pixels.

The LED system is also used to determine the optical crosstalk between AHCAL tiles as 3.5 % to 4.5 % per tile edge, depending on measurement procedure and tile size [84].

2.6.3. MIP Calibration

For physics analysis and energy reconstruction, all measured cell amplitudes are normalised to the MIP scale. For this the MIP constant $M_i(T)$, the most probable deposition of a single MIP on the ADC_{PM} scale, is extracted for each channel. In data this is calibrated from selecting hits on tracks out of events from muon runs and fitting the pedestal corrected ADC spectrum with the convolution of a Landau and Gaussian function [34, 76, 84]. The MIP constant is extracted from the fit for each channel individually, either as the most probable value of the fit function in the AHCAL or as the position parameter of the Landau distribution in the ScECAL. The different in definitions of the MIP position correspond to 10 % to 20 % difference in extracted calibration factor when applied to the same spectrum. This does not further influence the analysis of reconstructed energies as the differences are absorbed in the optimised weighting factors. The consequent difference in lightyield determination has a small difference in the digitisation step and thus width of a simulated and digitised MIP spectrum. This effect is practically irrelevant, as MIP spectra still show very similar shapes in data and simulation (see Figure 4.26) and the general influence of SiPM digitisation effects on simulated energy resolutions and responses is small (see chapter 5).

The temperature dependence of the MIP constant is caused by the combined influences of temperature on the SiPM gain and the SiPM quantum efficiency. In the AHCAL, the measured mean value of $-3.7\,\frac{\%}{\text{K}}$ is assumed as the temperature slope of the MIP constant for runs taken at FTBF [34, 84]. In the ScECAL the temperature dependence of the MIP constant is measured for each channel individually, resulting in a mean slope of $-5.1\,\frac{\text{ADC}_{\text{PM}}}{\text{K}}$, corresponding to around $-3\,\frac{\%}{\text{K}}$ [80].

From the combination of the MIP constant, gain constant and the intercalibration factor the *lightyield*, defined as most probable number of fired SiPM pixels per incident MIP, of each cell can be extracted as $LY_i = \frac{M_i(T) \cdot IC_i}{G_i^{\text{CM}}(T)}$.

2.7. Digitisation Effects

The output of particle interaction simulations as GEANT 4 typically consists of a list of energy depositions in the volumes marked as active material in the simulation geometry. In contrast, raw output of a modern particle physics detector usually consists of a list of digitised measured voltages or charges in hardware units (ADC), which are reconstructed into energy depositions or higher level objects before analysis (see section 4.4). The software chain used for reconstruction should be identical for data and simulation, requiring a transformation of the raw simulation results into a structure that resembles the raw data format. In order to obtain as realistic results as possible from the simulation, this should include an appropriate modelling of all readout effects arising from the combination of used active material, sensors and electronics.

This section describes the digitisation procedures for scintillator-SiPM calorimeters that are part of the CALICE AHCAL and CALICE ScECAL simulation models: Excluding late energy depositions, accounting for optical crosstalk between cells, modeling the statistical features of the scintillator-SiPM system, converting the result to the ADC scale used in the electronics and finally overlaying noise extracted from data. Note that this does not include application of any hit energy threshold, as this is part of the later offline reconstruction in the CALICE physics prototypes considered here.

2.7.1. Hit Timing

Depending on the shaping time of the used readout electronics, effectively only energy deposition within a specific time window around the trigger decision are included in the cell amplitude measurement. This has to be included in the digitisation, as especially slow neutrons generated in hadronic showers can deposit significant amounts of energy on much longer time scales up to seconds after the initial particle shower has developed [86].

In the CALICE testbeam simulation, the shaping time of the used readout electronics is accounted for already during the simulation, where energy depositions later than 150 ns after the generation of the primary particle are not included in the output.

2.7.2. Optical Crosstalk

A fraction of the scintillation light generated by a particle in one cell might propagate into adjacent scintillator tiles and thus add to the measured signal of the neighboring cell. This optical crosstalk is simulated by adding a fraction of the deposited energy in a primary cell into its neighboring secondary cells. The intuitive procedure would be to reduce the deposited energy in the primary cell by the amount of energy transferred into the secondary cells. In practice this couples the MIP2GeV factor to the crosstalk fraction parameter, impeding independent studies of these two parameters. Instead the energy deposition in the primary cell is not reduced by the energy spread into the secondary cells. This makes the MIP2GeV calibration independent of the crosstalk parameter but introduces a proportional relation between the total deposition sum and the crosstalk parameter.

Optical crosstalk between cells in the AHCAL is measured in-situ to be between 3.5 % to 4.5 % per tile edge for the 3 cm $\times$ 3 cm tiles. Light transfer via the corners of two AHCAL tiles is found to be irrelevant [84].

The optical crosstalk between ScECAL scintillator strips is assumed to be negligible, as each cell is individually wrapped in reflective foil [79].

2.7.3. Conversion to the MIP Scale

The simulated deposited energies are converted to the MIP scale. The applied *MIP2GeV* factor is obtained from a sample of simulated muons traversing the calorimeter cells perpendicular to the absorber structure and depends on the thickness of simulated scintillator with practically no influence of the used absorber material [84]. As the MIP2GeV value depends on other digitisation parameters, especially tile lightyield, it is extracted from the raw simulated depositions first and later adjusted such that the distribution of fitted MIP positions is centered around unity, see subsection 4.6.1.

2.7.4. Scintillator-SiPM Modelling

The finite number of pixels on SiPMs and the relatively small number of scintillation photons detected from single particles traversing a scintillator tile give rise to statistical effects on the energy resolution of single scintillator tiles. Statistical fluctuations are generally largest when operating on small numbers. Here this applies either to the small number of photons detected or to the small number of non-fired SiPM cells, governing the amplitude resolution of single scintillator cells. A statistical model incorporating these effects is implemented in the digitisation procedure. Apart from the external calibration parameters from data, the input of this scintillator-SiPM model is the deposited energy on the MIP scale. The output of the modeling procedure is the number of fired SiPM pixels. A detailed discussion and validation of two scintillator-SiPM models is given below.

After application of the scintillator SiPM modeling, the deposition is converted from the SiPM pixel scale to the hardware ADC scale using the gain calibration and gain intercalibration factors obtained for each channel individually from data, or their defaults if no calibration factor is available.

Statistical Models of the Scintillator-SiPM System

A MIP-like particle traversing a 3 mm AHCAL tile generates around 5000 scintillation photons inside the tile[3)], of which only 10 to 15 are detected by the SiPM. The distribution of number of registered photons given a fixed number of generated scintillation photons is thus well modelled by a Poisson distribution, leading to a relative resolution contribution of $\frac{1}{\sqrt{a}}$ for a number of incident photons a. The generation of scintillation photons itself is subject to Poissonian statistics, but the contribution to the resolution is considered negligible compared to the detection efficiency.

The main sensor contribution on the single channel amplitude resolution results from the finite number of SiPM pixels, especially statistical fluctuations of the fraction of fired SiPM pixels for very high amplitude hits. Such hits lead to large correction factors to the saturated SiPM response, amplifying these fluctuations. It is expected that this effect is

[3)] Private communication (27.01.2015) Lennart Adam, JGU Mainz. Based on simulations by Yong Liu, JGU Mainz

relevant mostly for hits in which the number of incoming photons is higher than the number of effective SiPM pixels.

These effects are easily modelled numerically for an idealised SiPM, assuming no pixel-crosstalk, afterpulsing and pixel recharging effects (see section 2.1). Two such models are discussed here: The *photon-by-photon* model treats each photon hitting the SiPM separately, while the *binomial* model utilises a more stochastic approach. This study of comparing the output of the two SiPM models was performed as part of the efforts to homogenise the ILD HCAL and AHCAL testbeam simulations discussed in chapter 5, as initially the ILD digitisation was using the photon-by-photon model while the CALICE testbeam digitisation was utilising the binomial model.

The parameters of both models are the cell energy deposition on the pixel scale a and the number of effective pixels of the SiPM m. The output of both algorithms is the number of fired SiPM pixels n and the resulting reconstructed number of incoming photons a_{rec}. Note that a and n (and thus a_{rec}) are random variables, sampled according to their probability density functions defined by the digitisation model for each hit.

In the photon-by-photon model first the number of photons hitting the SiPM is randomly chosen from a Poisson distribution $P(\lambda_P)$ with expectation value $\lambda_P = a$. For each incoming photon a random number is chosen from the uniform distribution of integers in the range 1 to m, representing the specific SiPM pixel hit by that photon. The number of distinct generated integers is used as the number of fired SiPM pixels n.

The mean number of fired pixels $\langle n \rangle$ as a function of the number of incoming photons a and the effective number of SiPM pixels m is calculated analytically for this model in [87] as

$$\langle n \rangle = f_{\text{sat}}(a, m) = m \left(1 - e^{-\frac{a}{m}}\right). \tag{2.4}$$

To reconstruct the initial number of incoming photons a_{rec}, the inversion of this saturation function can be calculated to be

$$a_{\text{rec}} = f_{\text{sat}}^{-1}(n, m) = -m \log\left(1 - \frac{n}{m}\right). \tag{2.5}$$

The relative resolution on the reconstructed number of incoming photons is calculated in [87] as

$$\frac{\sqrt{\text{Var}\left[a_{\text{rec}}\right]}}{a} = \sqrt{\underbrace{\left(\frac{1}{\sqrt{a}}\right)^2}_{\text{Poisson term}} + \underbrace{\left(\frac{\sqrt{m}}{a}\sqrt{e^{\frac{a}{m}} - 1 - \frac{a}{m}}\right)^2}_{\text{saturation term}}} \qquad = \frac{1}{a}\sqrt{m\left(e^{\frac{a}{m}} - 1\right)}. \tag{2.6}$$

The expanded formula shows the Poissonian resolution term from the incoming photons and the saturation term from the finite SiPM pixel statistics added in quadrature.

An alternative to the photon-by-photon model described in the previous paragraphs is the *binomial* model, which is used in the standard digitisation of the AHCAL prototype simulation model [34, 84, 88]. The binomial model does not rely on generating a random number for each incoming photon and is thus expected to show better runtime performance.

The first step in the binomial model calculates the mean number of fired SiPM pixels $\langle n \rangle$ from the number of incoming photons a using the saturation function Equation 2.4. The

number of fired SiPM pixels n is then randomly generated from a binomial distribution $B(n_B, p_B)$ with the parameters $n_B = m$ and $p_B = \frac{\langle n \rangle}{m}$.

The mean response and resolution of the binomial model are shown to be identical to the photon-by-photon model in Appendix A. It is remarkable that the binomial model reproduces the Poissonian photon statistics as well as the SiPM saturation contribution to the resolution in only one random number generation.

Figure 2.5 shows the response as the mean number of fired SiPM pixels $\langle n \rangle$ as a function of a from a toy simulation of an $m = 2000$ pixel sensor. The saturated response of both simulation models is identical to the analytic prediction, strongly deviating from linearity even for small fractions of fired SiPM pixels, asymptotically saturating towards m fired SiPM pixels.

The amplitude resolution of a single cell is shown for both simulation models in comparison to the analytical calculation in Figure 2.6. Both models show the same resolution behaviour which is well described by the analytical resolution. It is notable that the minimum point of ideal resolution is reached at a number of incident photons higher than the number of pixels of the simulated SiPM.

As the higher central moments are not as accessible analytically, the resulting distributions for n as a function of a from toy simulation runs are compared directly for both SiPM models. Figure 2.7.(a) shows the normalised distribution of a_{rec} (calculated from applying Equation 2.5 to n) as a function of a for the binomial model. Figure 2.7.(b-d) shows the normalised distribution of a_{rec} at fixed values of a (as indicated in Figure 2.7.(a)) for both discussed scintillator-SiPM models. No significant differences are observed in the shape of spectra obtained for the photon-by-photon model and the binomial model.

The computational complexity of both models differs substantially. The photon-by-photon model is generating one Poissonian random number for each hit, which in its naive implementation corresponds to an average λ_P uniform random numbers but can be done more efficiently [89, 90], and a uniform random numbers.

In the binomial model, for each hit the saturation function has to be evaluated once and a single random number has to be generated from a binomial distribution. Binomial random distribution is bounded to a maximum of $n_B \propto a$ uniform random number generations in its naive implementation, but can be performed more efficiently [91]. In the limit of large a, where the evaluation of the saturation function marginalises, the binomial model thus needs at most half of the uniform random number generations as the photon-by-photon model.

Assuming there are equally efficient implementations of time complexity class lower than $\mathcal{O}(a)$ for both Poissonian and binomial random number generations, the photon-by-photon model will still have time complexity $\mathcal{O}(a)$, while the binomial model will have the time complexity of the efficient binomial implementation. The binomial model is thus expected to show better computational performance in any realistic scenario.

Out of the two scintillator-SiPM models described in this section, the photon-by-photon model follows a more intuitive approach of calculation at the price of higher computational complexity. As the results are shown to be fully consistent between the photon-by-photon and the binomial model, the binomial model is used in all simulation studies presented in this thesis, as has been done in all earlier AHCAL testbeam simulation studies.

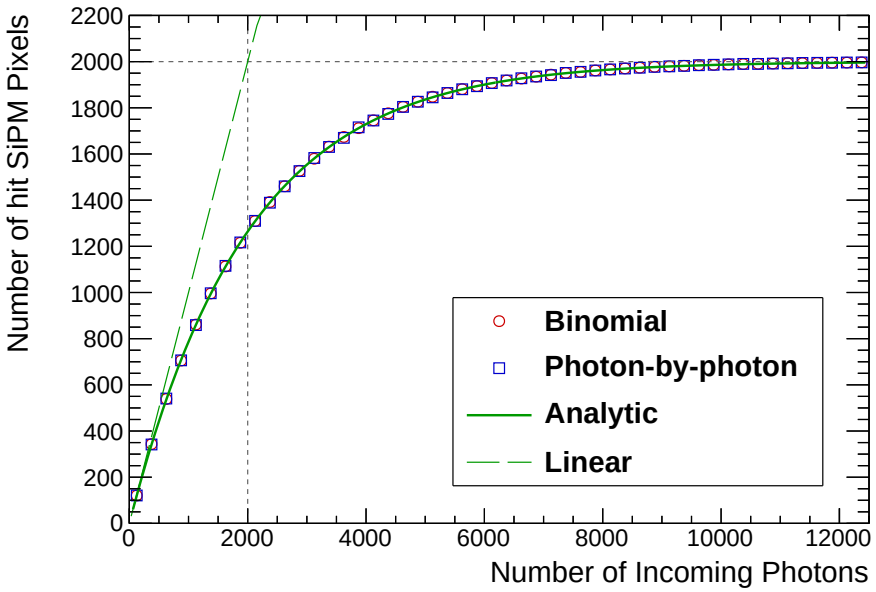

Figure 2.5.: *Mean number of fired SiPM pixels $\langle n \rangle$ as a function of the number of incoming photons a for toy Monte-Carlo simulations of both SiPM models and their analytical value. The dashed grey lines indicate the number of effective pixels of the simulated SiPM $m = 2000$.*

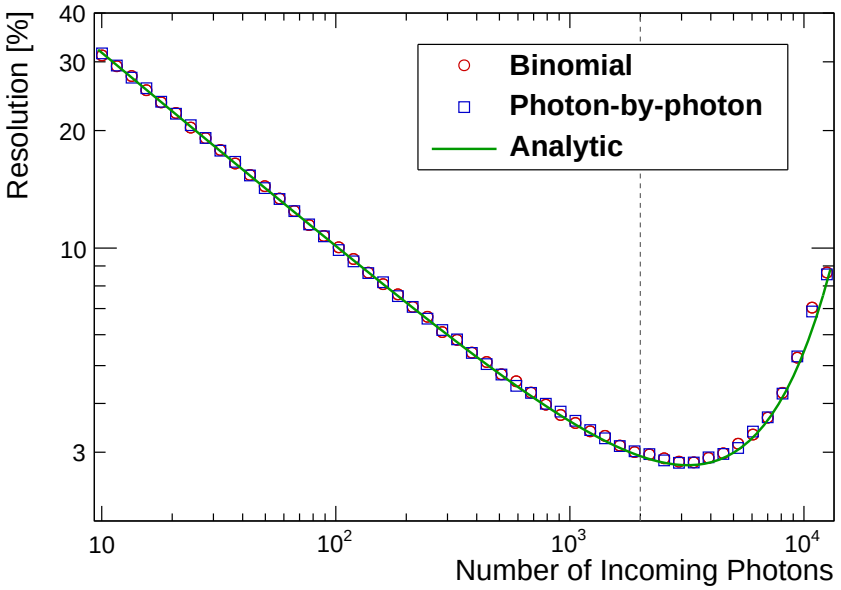

Figure 2.6.: *Amplitude resolution for toy Monte-Carlo simulations of both SiPM models and its analytic calculation. The dashed grey line indicates the number of effective pixels of the simulated SiPM $m = 2000$.*

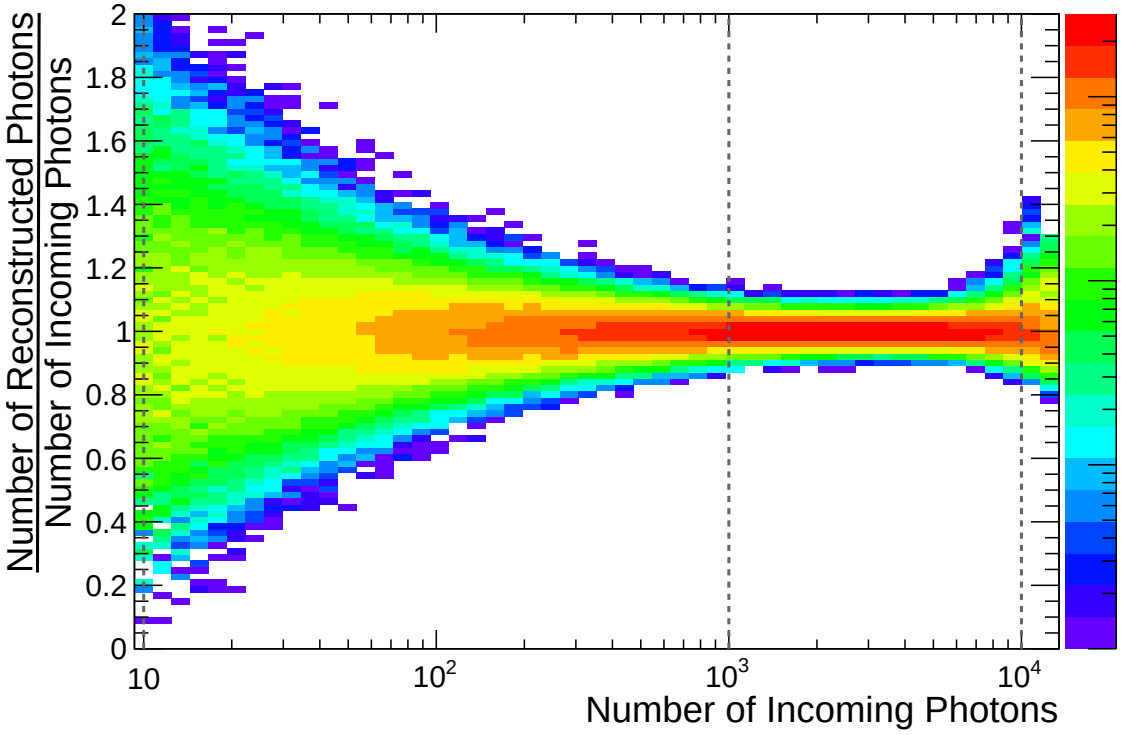

(a) *Full Distribution*

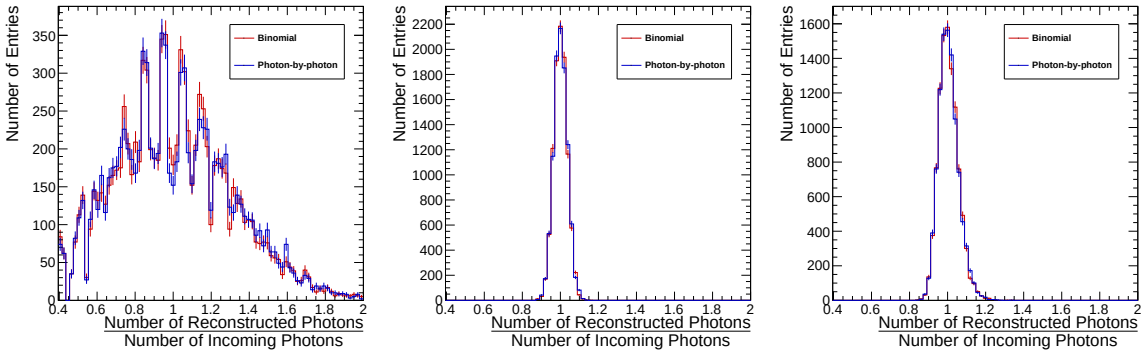

(b) $a = 10$ **(c)** $a = 1000$ **(d)** $a = 10000$

Figure 2.7.: *Distribution of normalised reconstructed amplitudes $\frac{a_{rec}}{a}$ as a function of number of incoming photons a on a SiPM with $m = 2000$ effective pixels from a toy Monte-Carlo simulation of the binomial SiPM model and slices of that distribution for both binomial and photon-by-photon model. The dashed grey lines indicate the number of incoming photons of the slices shown below. The slice distributions are identical within the statistical uncertainties, indicating that both SiPM models are equivalent.*

2.7.5. Noise

The noise frequency and amplitude of SiPMs dependends strongly on the specific sensor model and type as well as external parameters such as temperature and operation voltage. Even within one production batch of the same type of sensor, significant spreads in behaviour have been observed [76]. It is thus very difficult to accurately model noise behaviour for individual SiPMs in large scale installations as the CALICE prototypes or even a full scale detector.

To achieve a realistic simulation of noise in the CALICE testbeam prototypes, pure SiPM noise events are extracted from data for each run and overlaid onto simulated events. During data runs with the CALICE physics prototype setups, an external oscillator is generating random triggers uncorrelated to the incident testbeam particles. Selecting for events with active random trigger in offline processing, while rejecting events with active beam trigger or calibration trigger, yields a clean sample of around 5000 to 10 000 pure pedestal events per data run. This noise event sample is pedestal corrected, but no further reconstruction is applied. The noise amplitudes in ADC units are added to the digitised hits from the simulation for each hit event by event. As there are typically far less extracted noise events available than there are simulated events for a given run, the noise events are reused cyclically in one simulated run.

Due to inefficiencies in the triggers used to select noise events, a very small fraction around 1 ‰of overlaid noise events contains particle showers or fragments thereof. As all simulated runs are subject to the same reconstruction and event selection as data, such events are typically excluded from the analysis by the applied multi-particle rejection cuts and do not bias the simulation results.

3. CALICE Engineering Prototypes

The CALICE physics prototypes described in the previous chapter demonstrated the general feasibility and performance of high granularity scintillator-SiPM calorimeters. However, the design of the physics prototypes does not allow scaling of the system to a full 4π calorimeter system in a multi-purpose particle physics detector for a future accelerator experiment such as ILD. This is due to the readout electronics and power supplies of the physics prototype being fully separated from the active layers, taking up at least as much volume as the calorimeter prototype itself in external electronics and cabling.

Apart from the physics performance goals, the technical requirements of a hadronic calorimeter in the currently proposed design of the ILD [18, 92] are thus:

- Due to the high channel density within the AHCAL, all signal digitisation, readout electronics, calibration systems and voltage regulators must be fully integrated into the active detector layers.
- All recorded hit amplitudes and hit timing information must be buffered in the active layers until the end of each ILC bunch train.
- The power dissipation of the readout electronics is limited to 25 µW per readout channel (40 µW including the SiPM power consumption), averaged over one ILC bunch train cycle, in order to operate without active cooling within the calorimeter volume [93].
- The thickness of the active layers must be minimal in order to maximise the effective calorimeter depth of the AHCAL in the available space defined by the inner radius of the ILD solenoid coil.

This chapter briefly describes the current hardware design of the second generation AHCAL prototype seeking to fulfill the requirements of a hadronic calorimeter for ILD and to demonstrate the scalability of the AHCAL concept to a full size detector. In addition, general considerations on the efficient operation of such a prototype, which have been devised as part of this thesis, are presented.

3.1. The AHCAL Engineering Prototype

The AHCAL *engineering prototype* (EPT) aims to demonstrate the scalability of the AHCAL concept to a full size hadronic calorimeter for ILD. In the engineering design of the ILD AHCAL, the AHCAL barrel is built out of two separate rings of 16 calorimeter segments each, as shown in Figure 3.1(a). Each segment consists of 40 to 48 active layers with 20 mm steel absorbers in between. Each active layer consists of up to 18 PCBs, see Figure 3.1(b). No active cooling will be possible inside the calorimeter barrel, only the power converters

and readout boards at one end of each layer will be water cooled. The readout data from all active layers in two neighboring segments is aggregated, so only 16 data cables are foreseen to read out the whole AHCAL barrel. The full ILD AHCAL is expected to have eight to ten million individual cells in the barrel and endcaps combined.

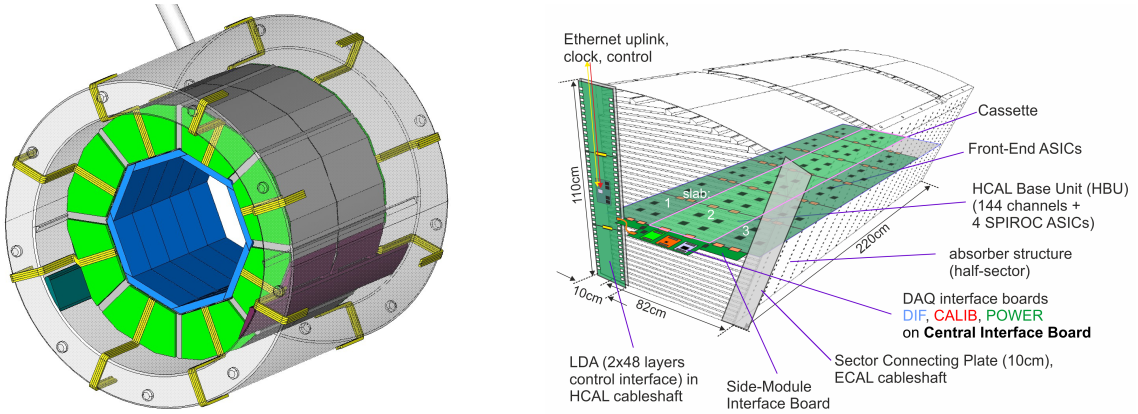

(a) *ILD barrel and magnet* **(b)** *ILD AHCAL barrel segment*

Figure 3.1.: *Schematic drawings of the mechanic setup of the ILD HCAL design. (a) kindly provided by Karsten Gadow (DESY), (b) kindly provided by Mathias Reinecke (DESY).*

3.1.1. The HCAL Base Unit

The *The HCAL Base Unit* (HBU) is a 36 cm × 36 cm printed circuit board, each housing 4 *application specific integrated circuits* (ASICs) reading out 144 SiPMs coupled to 30 mm × 30 mm × 3 mm plastic scintillator tiles mounted on its bottom side. The thickness of a fully assembled HBU including scintillator tiles is less than 5 mm. Pictures of the top and bottom side of an HBU are shown in Figure 3.2. Up to six HBUs are connected and read out in series as a *slab*. Up to three slabs are connected in parallel to one common set of readout, power and calibration modules, forming one ILD AHCAL layer. An integrated LED calibration system can deliver nanosecond-width light pulses with amplitudes from few photons up to the full SiPM saturation scale[94–96]. More detailed descriptions of the HBU hardware are available in [94, 97]. Several variants and iterations of the HBU design have been produced to accommodate both SiPMs with soldering pins and *surface mounted device* (SMD) type SiPMs. Furthermore a smaller version accommodating 144 scintillator strips of 45 mm × 5 mm, the *ECAL Base Unit* (EBU), has been produced and operated as an ScECAL engineering prototype.

3.1.2. The SPIROC2 ASIC

The readout chips used in the current modules of the AHCAL engineering prototype are iterations of the *SiPM Integrated Read-Out Chip 2* (SPIROC2) family designed by OMEGA, a mixed signal ASIC offering readout and signal digitisation of 36 SiPM channels [98, 99]. For each channel, the bias voltage of the connected SiPM can be tuned within ±2 V with

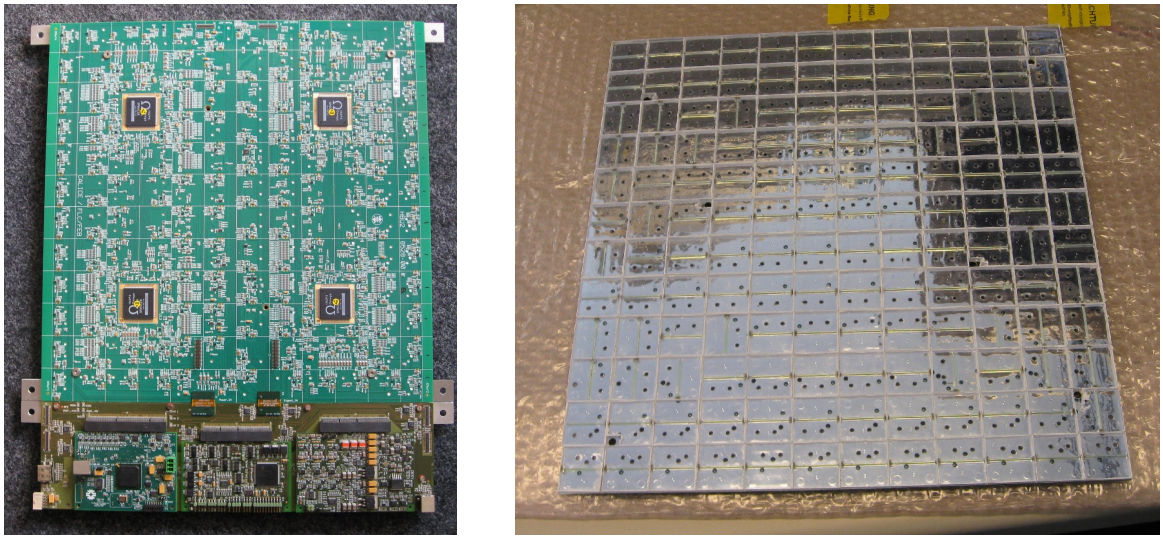

(a) Top side **(b)** Bottom side

Figure 3.2.: *HBU2 PCB equipped with four SPIROC2b ASICs and 144 scintillator tiles. The top view includes the readout and calibration modules at the bottom of the picture.*

around 50 mV resolution. Each channel has a configurable shaping preamplifier and 12 bit amplitude resolution, covering a dynamic range of up to around 2000 SiPM pixels, with a high precision calibration mode to separate single SiPM-pixel peaks for gain calibration measurements. The hit timing of each hit is stored with up to 100 ps precision if operated in ILC-like conditions. Most parts of the chip that are not needed in any given state of operation can be switched off to reduce its power consumption (*power pulsing*). A more detailed description of the chip is given in [94, 97].

A schematic representation of the signal path of a single channel in the SPIROC2 chip is given in Figure 3.3. The signal sampling can be operated either in *external trigger* (ET) mode, or in *auto trigger* (AT) mode. In external trigger mode, all channels are sampled synchronously based on an external signal. In auto trigger mode, the signal amplitude of each cell is continuously compared to an internally generated threshold. If the input signal of a given channel is above the configured threshold, the signal of the specific channel is sampled.

Regardless of the trigger mode, the sampled amplitudes are first collected in analog buffers, sequentially storing up to 16 signal amplitudes. No further hits can be stored once the buffers are filled. Only when a readout command is sent to the chip (typically when the first readout chip of the system has filled all its buffers), these buffers are digitised sequentially and transferred out of the chip. This scheme reflects the needs of a readout chip for an ILC experiment, where individual events come in short, high frequency bursts during the bunch train with relatively long time between the bunch trains. This way the analog part of the chip can be powered only during the bunch train, while the digital part needs to be switched on only during the amplitude to digital conversion phase.

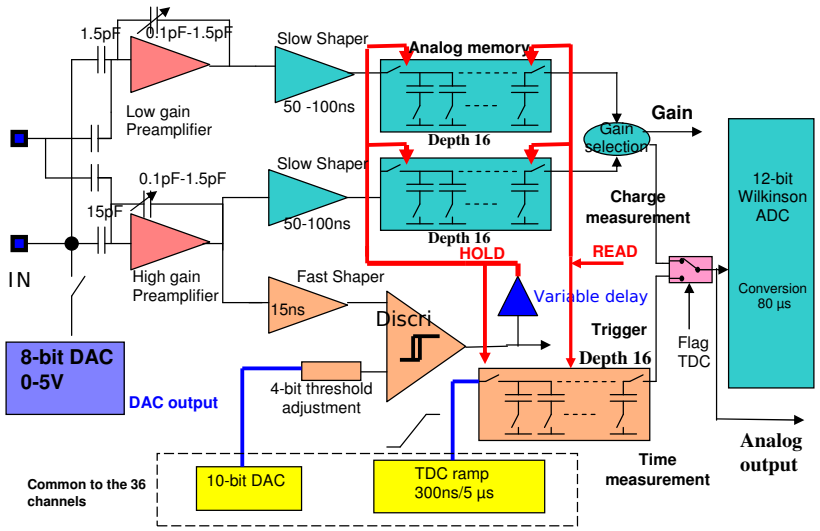

Figure 3.3.: *Schematic of the signal path of the SPIROC2 family for a single channel. [100]*

As all channels are sampled synchronously in external trigger mode, all channel buffers fill up simultaneously. In auto trigger mode this would not have to be the case, as buffers could be managed individually in each readout channel. However, to simplify the design of the SPIROC2, also in auto trigger mode all channel buffer pointers are always incremented synchronously. This means that even if in a given event only one single cell shows an amplitude above threshold, all channels switch to the next buffer. This behaviour is termed *OR36*, referencing the logic relation of the buffer pointer always being incremented for all channels. Channels in which the amplitude was measured above the threshold in a given event are marked with a *HitBit* in the readout data stream.

3.1.3. Current Status of the AHCAL Engineering Prototype

Various HBUs have been operated with many different types of SiPMs from different manufacturers, serving as a test bench for the ongoing development of scintillator tile concepts. The assembly of the electronics components on an HBU is already fully industrialised. The automated assembly of scintillator tiles is currently under investigation and will be demonstrated in the production of the next production batch of HBUs [101].

First tests of the power pulsing with single HBUs have been promising [97], although the average power consumption goal of 25 µW per channel is still missed by at least one order of magnitude. Further tests with an assembled slab of up to six sequentially connected HBUs with improved hardware are ongoing, however due to the inherent power consumption of the readout chips, the 25 µW per channel target is most likely not reachable with the current SPIROC2b generation.

The design of the AHCAL engineering prototype DAQ system is capable of efficiently operating from single layers for lab measurements up to full scale testbeam setups in variable configurations and is currently extended to integrate with the DAQ systems of other detector prototypes and testbeam instrumentation through the common EUDAQ framework [102, 103].

Over the recent years several iterations (SPIROC2 up to SPIROC2d) of the SPIROC2 ASIC have been designed, produced and tested. However, since all of the iterations after SPIROC2b show issues which fundamentally limit their use in testbeams, all currently used HBUs are still equipped with the SPIROC2b chip. The next version SPIROC2e is supposed to correct all known problems and will be the first SPIROC revision to be assembled in a *ball grid array* (BGA) package.

The current testbeam setup of the AHCAL engineering prototype integrates a full ILD-like power distribution, cooling and DAQ into an ILD HCAL absorber prototype of one third of the size of an ILD HCAL barrel segment. The readout layers consist of three single EBU layers, eight single HBU layers and four large layers of 2×2 HBUs each. This testbeam prototype has been operated with electron, pion and muon testbeams at DESY and CERN PS and SPS. A picture of the testbeam prototype setup as well as an example event is shown in Figure 3.4.

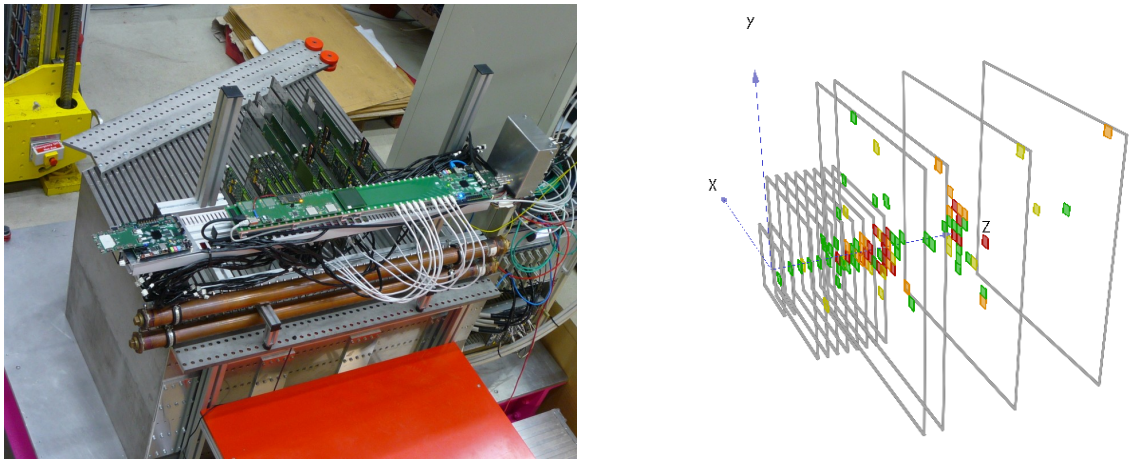

(a) *AHCAL Engineering Prototype Testbeam Setup* ***(b)*** *50 GeV Pion Event Display*

Figure 3.4.: *The CALICE AHCAL engineering prototype testbeam setup and an event display from a 50 GeV π^- run recorded at CERN SPS.*

The next milestone will be a smaller size steel absorber stack instrumented with about 15 single HBU layers, fully equipped with current SiPMs and tiles for an electron testbeam with full power pulsing.

3.2. Considerations for a Full Scale Calorimeter System

The operation of a fully self-triggering calorimeter system, such as the AHCAL engineering prototype or even a full ILD AHCAL with an unprecedented number of readout channels, poses new challenges in ensuring the quality of the recorded data. Especially in the case of the AHCAL engineering prototype, operating a readout chip that is specifically designed for the planned ILC bunch structure in testbeam environments requires careful consideration of all relevant parameters.

This section summarises studies prepared in the context of this thesis, concerning the readout efficiency of the AHCAL engineering prototype from the tile design, to trigger threshold setting and validation, up to the expected readout efficiency of a testbeam setup read out by SPIROC2 chips.

3.2.1. Tile Lightyield

The *lightyield* of a scintillator-SiPM tile, measured in $\frac{\text{px}}{\text{MIP}}$, is defined as the most probable number of fired SiPM pixels from a single MIP traversing the tile as given in subsection 2.6.3. The lightyield of a tile results from its optical properties defined by its geometry, the used scintillator material and possible reflective wrapping as well as the size and quantum efficiency of the used SiPM.

In order to define the optimum lightyield for a tile in the AHCAL engineering prototype, several boundary conditions, resulting from the expected photon statistics, the used readout chip and cost considerations, have to be examined.

The hit energy threshold below which measured depositions are dismissed in the reconstruction is typically 0.5 MIP in CALICE AHCAL analyses. To retain the shower imaging quality of the AHCAL even for MIP tracks in the AHCAL (as has been demonstrated and published with AHCAL physics prototype data [104]), the efficiency for MIP hits above this threshold should be better than 95 %. The lightyield of a given tile has a direct influence on the MIP efficiency at a given threshold, as its measured MIP spectrum is widened from the Poisson statistics of the detected photons (see subsection 2.7.4). A too low lightyield thus decreases the MIP efficiency at 0.5 MIP below the target of 95 %. Additionally the effective noise rate at 0.5 MIP increases due to the threshold in SiPM pixels decreasing. The general effect of a widened MIP spectrum, apart from the reduced MIP efficiency, is found to be negligible for the energy resolution of the AHCAL, see section 5.2.

Apart from the improved detection efficiency for single MIPs, increasing the lightyield of an AHCAL tile leads to an earlier onset and stronger influence of SiPM saturation effects. In an idealised picture this is no issue, as the single cell energy resolution is degraded only for extremely high amplitude hits with the number of incoming photons much larger than the number of effective SiPM pixels (see subsection 2.7.4), if an appropriate correction of the SiPM saturation effects is applied. However, in practice the parameter needed to correct for the saturation will never be known with perfect accuracy. As the desaturation function f_{sat}^{-1} rises very steeply for hits close to full SiPM saturation, small uncertainties in the number of effective pixels will have a large impact on the reconstructed energy.

To remedy the problem of stronger saturation effects with higher lightyield tiles, SiPMs with a higher number of pixels could be used. However for the AHCAL this is not preferred, as SiPMs with significantly higher number of pixels generally have larger active area and are thus more expensive. Such SiPMs also typically show worse noise figures, as no trenches between the individual pixels can be included in the design. Additionally the dynamic range of the currently mainly used SPIROC2b readout chip is not sufficient to resolve both single pixel spectra and the full SiPM response of such high-pixel SiPMs with the same configuration, necessitating more complex intercalibration schemes [105].

The ideal tile lightyield for the AHCAL engineering prototype is thus as low as possible while achieving the stated goal of 95 % single MIP efficiency above a threshold of 0.5 MIP,

with a reasonable safety margin to account for the expected spread in lightyields when operated on an HBU.

To study the dependence of the MIP efficiency on tile lightyield, a toy model is implemented. It uses the Landau shaped raw deposited energy in 3 mm plastic scintillator from simulated muons (as generated for chapter 5) with added Poissonian fluctuations as given in subsection 2.7.4. MIP spectra are generated for different lightyields and the fraction of hits below the threshold is extracted.

Figure 3.5(a) shows MIP spectra in units of fired SiPM pixels for three different lightyield values. The shaded areas below the given curves correspond to the fraction of events below threshold, which are decreasing for higher lightyields. The dependence of the MIP efficiency on tile lightyield is given in Figure 3.5(b) for two different thresholds. The blue points correspond to a 0.5 MIP threshold as used in current analyses while the red points correspond to a minimum viable fixed threshold of 2.5 px[1)].

Tile lightyields higher than $\geq 9\ \frac{\text{px}}{\text{MIP}}$ result in MIP efficiencies above the demanded 95 %. However, the lightyield spread of current tiles mounted to HBUs is observed to be around 20 % in testbeam measurements [106]. In order to ensure that only a minimal fraction of cells miss the MIP efficiency goal, the mean of the lightyield should be at least $2\,\sigma$ separated from the $9\ \frac{\text{px}}{\text{MIP}}$ 95 % efficiency threshold, leading to the target lightyield of AHCAL engineering prototype scintillator tiles of $15\ \frac{\text{px}}{\text{MIP}}$.

The mean lightyield measured on current tiles mounted to HBUs in the testbeam comes close to this value with $12\ \frac{\text{px}}{\text{MIP}}$ to $15\ \frac{\text{px}}{\text{MIP}}$, depending on the type of tile and SiPM used [106].

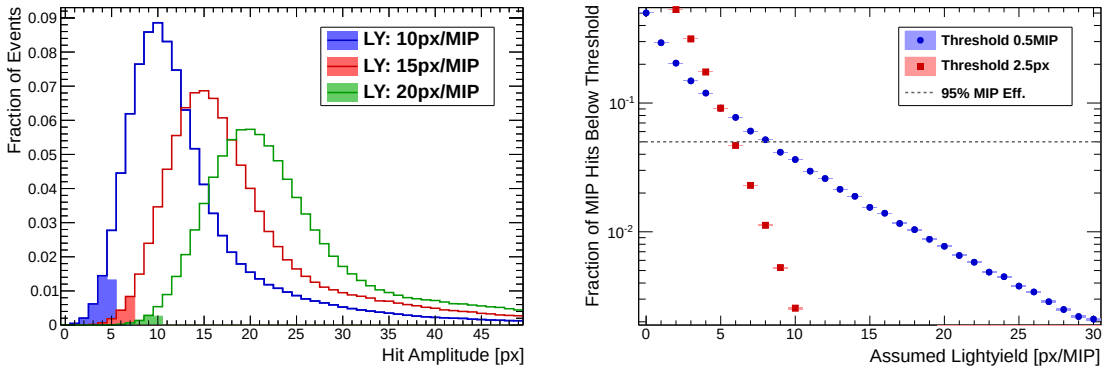

(a) *Toy MIP Spectra* **(b)** *Toy Efficiencies*

Figure 3.5.: *Results for MIP spectra and MIP efficiencies for different assumed tile lightyields generated from a toy simulation, taking into account the raw deposition spectrum of a MIP and the additional widening of the MIP spectrum from the Poisson statistics of the detected photons.*

[1)] Current SiPMs give noise frequencies in the 10 kHz range at 0.5 px threshold [77]. Thus even for low pixel crosstalk devices a threshold below 2.5 px seems unreasonable for operation in a calorimeter environment.

3.2.2. Trigger Threshold Validation

As the AHCAL engineering prototype is operated fully self-triggered in testbeam measurements, the setting of the trigger thresholds is of greatest importance for the quality of the acquired data. Setting the trigger threshold of a given channel too high causes an irrecoverable loss of information in that channel. Setting the trigger threshold too low possibly causes this channel to be overwhelmed by noise events. This is especially problematic considering the readout scheme of the SPIROC2 chip described in subsection 3.1.2, as a single noisy channel will fill up the chip's buffers quickly, forcing an interruption of the acquisition of the whole prototype and a full readout of all ASICs. In the worst case this makes the whole detector insensitive to beam events, in any case it will drastically reduce the data taking efficiency. The general readout efficiency of a HBU based calorimeter prototype is discussed in subsection 3.2.3.

The SPIROC2b offers one global trigger threshold per chip, adjustable via a 10 bit configuration parameter T. The corresponding threshold position on the ADC scale depends on the configured preamplifier gain of each channel, and has been measured manually for a limited number of channels [97]. A 4 bit channel-wise fine tuning of the trigger threshold is integrated into the chip, but setting individual thresholds for each channel induces a shift to the global threshold and is thus presently not used [97].

To ensure a proper setup of the configured trigger thresholds, a quick and efficient method to measure the trigger threshold position on all channels is needed. From the extracted threshold on the channel ADC scale, the corresponding threshold in MIP units can be calculated via the MIP calibration constant (see subsection 2.6.3). The needed accuracy of this online trigger threshold extraction is not very high, 5 % to 10 % are sufficient to maintain whether the threshold of a given channel is in the acceptable range <0.4 MIP or not. Ideally the thresholds would be set as low as possible to simplify fits to the acquired MIP spectra. Such a method could also be used to extract precise information about the trigger position when operated with higher statistics, in order to obtain a full characterisation of the trigger threshold dependencies for all channels of a whole chip at once.

The proof-of-concept of a method that seems to fulfill both of these requirements is presented here. The method utilises the LED calibration system integrated onto the HBU, recording a number of runs with increasing LED pulse amplitude. For each setting of the LED amplitude, one run is taken in external trigger mode, immediately followed by a run in auto trigger mode. This is needed to ensure comparable LED amplitudes between the ET and AT run, as the pulse amplitudes generated by the calibration system are not stable over time [94–96]. In the ET run all 16 amplitude buffers are filled with LED calibration events in each readout cycle. To maintain the normalisation to the ET run, exactly 16 LED pulses are generated in each readout cycle of the AT run before the acquisition is stopped and the readout is enforced. The summed up ADC spectra of all ET runs show a reasonably flat distribution of measured amplitudes. The runs taken in AT mode should show no events below the trigger threshold, a steep increase in statistics around the trigger threshold position and a similarly continuous spectrum as the ET measurement above the trigger threshold. Example spectra and the corresponding ratios obtained for a single channel for three different trigger thresholds from 300 readout cycles[2)] and nine different LED

[2)] 300 readout cycle amount to around one minute of acquisition time with the DAQ version used in this study.

amplitudes are given in Figure 3.6, showing a clear dependence of the trigger threshold position on the trigger parameter T.

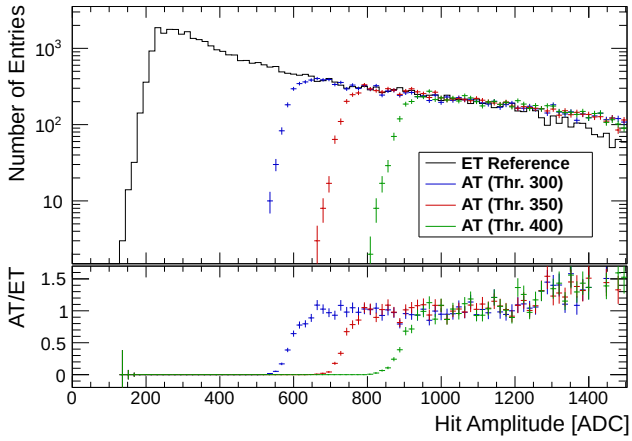

Figure 3.6.: *ET reference spectrum and AT spectra of a single channel for different threshold setups of $T = 300$, $T = 350$ and $T = 400$. A clear dependence of the trigger threshold position on T is seen.*

It is apparent that the bin-wise division of the ET and AT spectra yields a normalised efficiency curve out of which the trigger position and onset behaviour can be extracted. For this the extracted efficiency points are fitted with an *error function* $\mathrm{erf}(x)$ with the width parameter σ and the position parameter μ. In order to obtain a reasonable and unbiased fit, the statistical treatment of the errors on the extracted efficiency ratios has to be considered. Each bin content ET_i, AT_i of the respective external trigger and auto trigger spectra constitutes an individual counting experiment obeying Poisson statistics. The statistical uncertainties on ET_i, AT_i and their ratio $\frac{\mathrm{AT}_i}{\mathrm{ET}_i}$ are thus

$$\sqrt{\mathrm{Var}\left[\mathrm{ET}_i\right]} = \sqrt{\mathrm{ET}_i} \tag{3.1}$$

$$\sqrt{\mathrm{Var}\left[\mathrm{AT}_i\right]} = \sqrt{\mathrm{AT}_i} \tag{3.2}$$

$$\sqrt{\mathrm{Var}\left[\frac{\mathrm{AT}_i}{\mathrm{ET}_i}\right]} = \frac{\mathrm{AT}_i}{\mathrm{ET}_i}\sqrt{\frac{1}{\mathrm{AT}_i} + \frac{1}{\mathrm{ET}_i}}. \tag{3.3}$$

This standard description of Poissonian statistical uncertainties assigns ratios with $\mathrm{AT}_i = 0$ an uncertainty of zero, which makes χ^2-fits impossible if such points are not excluded from the fit. However, such bins do carry statistical information in form of an upper limit on the efficiency in this bin. Thus, for bins in which the measured ratio is zero, instead of the Poissonian error, the $1\,\sigma$ upper limit on the efficiency is used as an approximate uncertainty, leading to

$$\sqrt{\mathrm{Var}\left[\frac{\mathrm{AT}_i}{\mathrm{ET}_i}\right]} = \begin{cases} \frac{\mathrm{AT}_i}{\mathrm{ET}_i}\sqrt{\frac{1}{\mathrm{AT}_i} + \frac{1}{\mathrm{ET}_i}}, & \text{if } \mathrm{AT}_i \neq 0 \\ \frac{1}{\mathrm{ET}_i}\sqrt{1 + \frac{1}{\mathrm{ET}_i}}, & \text{if } \mathrm{AT}_i = 0. \end{cases} \tag{3.4}$$

Bins with $ET_i = 0$ carry no information and are not included in the fit. As the ET and AT measurements are independent measurements, the measured efficiency for a given bin is not bounded to unity.

An example fit for a single channel and one auto trigger setup, including the modified errors is shown in Figure 3.7(a). The efficiency is well normalised to unity due to the measurement method. The resulting statistical uncertainty on the trigger threshold mean position is $<1\,\%$ in this case, much better than the accuracy needed for a validation of configured trigger thresholds. Figure 3.7(b) shows the extracted threshold position dependence on the threshold setup parameter T. The dependence is close to linear, as expected from previous manual measurements on single channels [97].

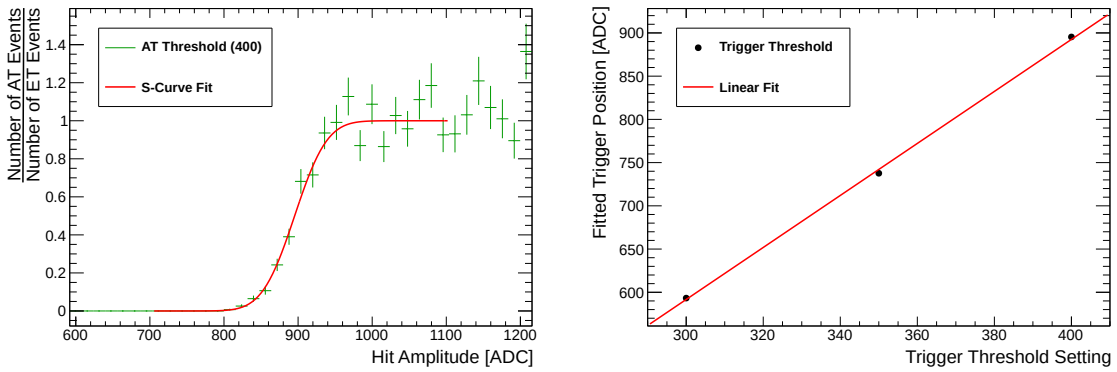

(a) *Efficiency curve with Fit* **(b)** *Trigger Position*

Figure 3.7.: *(a): Observed trigger efficiency with S-curve fit of an exemplary channel for $T = 400$. $\mu_{fit} = 895.4 \pm 2.2$, $\sigma_{fit} = 48.8 \pm 3.0$. (b): Extracted trigger threshold position as a function of T, showing a linear behaviour. The statistical errors are smaller than the used markers.*

The described method has been run on 14 fully equipped HBUs as a summer student project [107]. Threshold positions were obtained for most channels on most HBUs, proving the versatility of the approach. The method has been adapted for the standard commissioning and operation procedures of the AHCAL engineering prototype and the appropriate auto trigger runs are recorded as part of the gain calibration routine with only small additional runtime compared to the higher statistics needed for gain calibration. In principle the number of needed extra runs could even be decreased significantly if an online feedback of the last acquired ET gain calibration run was available. In that case, the needed AT run for threshold validation could only be acquired for LED amplitudes around the expected trigger thresholds position.

This method improves the previously used threshold extraction scheme [97] in several important ways. It does not rely on a precisely defined signal amplitude, as is generated from external charge injection, and thus does not need manual soldering operations to the HBU. It has been shown to work for all channels of a testbeam setup at the same time without any modification of the hardware, needing only minimal extra time in addition to the high statistics gain calibration runs taken anyway during testbeams. In the future this method can be used to do a full characterisation of the global trigger threshold dependency

as well as the channel-wise threshold tuning. A full understanding of trigger threshold behaviour in the SPIROC2 chip would possibly greatly simplify the threshold tuning phase of future AHCAL engineering prototype testbeam campaigns.

3.2.3. SPIROC2 Readout Efficiency

The acquisition of testbeam data with the AHCAL engineering prototype is governed by the readout scheme of the SPIROC2 chip when operated in the self-trigger mode. The data acquisition is started synchronously for all readout chips of the given setup. Once one of the readout chips has filled all of its 16 buffers (or a predefined timeout is reached), the acquisition is stopped for the whole system and the signal digitisation and readout of all chips is started. Once all chips have finished transferring their data to the DAQ system, the acquisition is restarted for all chips by a synchronous signal. Each time a readout of the full setup is performed, at least one chip has all of its 16 buffers filled. In an idealised environment each buffer would always only contain beam events, but in practice some of these buffers will be filled with SiPM noise. The influence of noise hits on the readout efficiency is studied here using a model of the SPIROC2 readout scheme including its OR36 trigger logic and a hypothetical chip with the same general behaviour but without the OR36 trigger logic. The beam event efficiency is defined as the fraction of number of beam events N_{beam} out of the 16 possible beam events acquired per readout cycle $\epsilon = \frac{N_{\text{beam}}}{16}$.

The implemented toy simulation assumes an exponential distribution of time between noise hits with a given mean frequency f_{noise} for each channel, which is assumed identical for all channels. Beam events are assumed to occur equidistant in time with a frequency f_{beam}. For each beam event one hit in each calorimeter cell is assumed. In the case of a testbeam prototype calorimeter, this is a realistic assumption for a readout chip with the OR36 trigger logic, as there is no difference in beam event efficiency whether only one channel has triggered on a given chip or all of the channels have triggered. For a readout chip without the OR36 logic, this assumption yields a slightly conservative estimate of the beam event efficiency. A more detailed analysis of expected cell occupancies would be needed to estimate a realistic behaviour for an ILC HCAL. However, as is discussed at the end of this section, SiPM noise is expected to be fully negligible in an ILD HCAL.

In the toy simulation, noise hits and beam events are generated ordered in time. The number of buffers filled by beam and noise hits in each chip and channel are counted until one of the chips has registered 16 hits, filling all buffers, in one of its channels, which terminates the simulation of a single acquisition cycle.

The input parameters of the toy model are the number of simulated chips N_{chips} and the ratio of the combined noise frequency and the beam event frequency $r = \frac{f_{\text{noise}}^{\text{ASIC}}}{f_{\text{beam}}}$. For convenience $f_{\text{noise}}^{\text{ASIC}}$ is defined as 36 times the noise frequency of a single channel. The output of one simulated readout cycle is the number of recorded beam events at the time of the readout. In all simulations shown here, 1000 readout cycles are simulated per parameter configuration.

The distribution of simulated readout efficiencies for an assumed noise-to-beam ratio of $r = 1$ as a function of N_{chips}, in the range from one to 640 ASICs (as an estimate of the number of readout chips in a fully equipped AHCAL engineering prototype of 40 layers $\times$ 4 HBUs $\times$ 4 ASICs), is given in Figure 3.8 for simulations with and without the OR36 logic.

It is shown that for a SPIROC with the OR36 logic, the naïve expectation of a 50 % beam event efficiency at $r = 1$ is true only if the whole system consists of exactly one ASIC. For larger setups, the statistical fluctuations of noise events on single chips cause a decrease in beam event efficiency which scales roughly as $\langle \epsilon \rangle \propto -\log N_{\text{chips}}$, resulting in a beam event efficiency of only around 25 % for a full 1 m^3 HBU prototype. For a readout chip without OR36 logic, the resulting readout efficiencies would be significantly improved, with 80 % beam event efficiency for a single HBU and around 70 % for a large prototype.

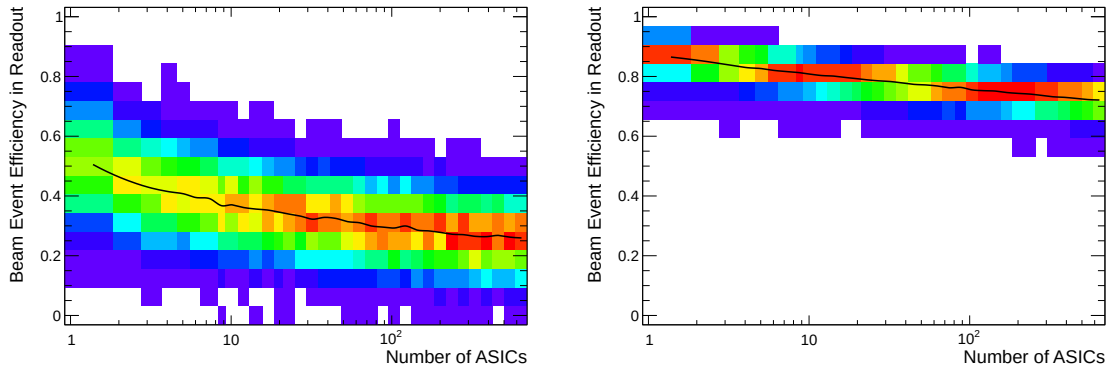

(a) *With OR36 Logic* **(b)** *Without OR36 Logic*

Figure 3.8.: *Simulated beam event efficiencies for a fixed noise-to-beam ratio $r = 1$, scanned over the simulated number of chips for a simulation with and without the OR36 trigger logic of the SPIROC2 ASIC. The colored boxes indicate the number of results per simulation configuration on a linear scale. The black curve indicates the mean beam event efficiency for a given number of readout ASICs.*

Scanning the noise-to-beam ratio r in the range 0.01 to 100 for a single readout chip yields the distributions given in Figure 3.9. As expected (and already visible in Figure 3.8) the beam event efficiency for a single chip is estimated to be 50 % at $f = 1$ for a readout chip with the OR36 trigger logic . The readout efficiency roughly scales as $\langle \epsilon \rangle = \frac{1}{1+r}$ with $\epsilon \approx 10\,\%$ at $r = 10$ and $\epsilon \approx 90\,\%$ at $r = 0.1$. The observed behaviour for a simulation without the OR36 logic is similar except for a general shift on the r axis, corresponding to the 36 channels $\times$ the observed readout efficiency. Thus, a chip without the OR36 logic would be able to handle $36 \times 0.5 = 18$ times higher SiPM noise rates to maintain a 50 % beam event efficiency.

Full scans of the r-N_{chips} parameter space are given in Figure 3.10. The maximum allowed SiPM noise ratio per ASIC can be read off these parameter scan diagrams for a given size of the prototype and desired beam event efficiency. For example, a 1 m^3 AHCAL engineering prototype consisting of 640 SPIROC2b readout chips requires around $r = 0.2$ for a beam event efficiency of around 50 %. To reach 90 % beam event efficiency, $r < 0.01$ is needed. In contrast, a future readout chip without the OR36 trigger logic would greatly improve the testbeam performance with otherwise identical sensors and general hardware setup.

These considerations about the readout efficiency could in principle also be scaled to the expected number of chips of a full ILD AHCAL. However, in the implementation of the simulation used above, the computation time to achieve reasonable statistics would

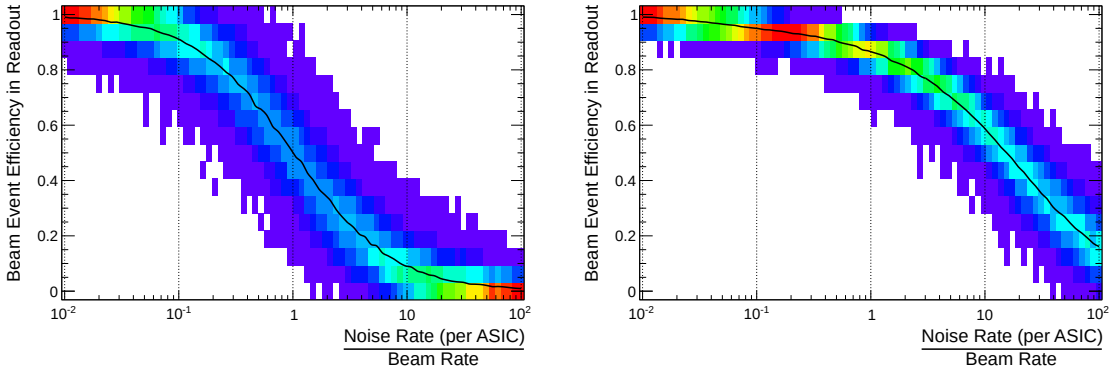

(a) *With OR36 Logic* **(b)** *Without OR36 Logic*

Figure 3.9.: *Simulated beam event efficiencies for a single readout ASIC, scanned over simulated noise-to-beam ratios for a simulation with and without the OR36 trigger logic of the SPIROC2 ASIC. The colored boxes indicate the number of results per simulation configuration on a linear scale. The black curve indicates the mean readout efficiency for a given noise-to-beam ratio.*

be immense. Instead a simple estimation shows that SiPM noise occupancy will not be a primary concern in the design and operation of the ILD AHCAL.

Modern trenched SiPMs (see section 2.1) show dark noise rates above 0.5 px threshold of around $f_{\text{noise}}^{0.5\,\text{px}} = 20\,\text{kHz}$ with pixel crosstalk probabilities $p_{\text{xt}} < 1\,\%$ [77]. Assuming a tile lightyield of 15 $\frac{\text{px}}{\text{MIP}}$ and a conservative (for the purpose of this estimation) channel trigger threshold of 0.3 MIP, corresponding to 4.5 px, the noise rate above threshold of such a SiPM is

$$\begin{aligned} f_{\text{noise}}^{4.5\,\text{px}} &= f_{\text{noise}}^{0.5\,\text{px}} \times (p_{\text{xt}})^4 \\ &\leq 2 \times 10^4\,\text{Hz} \times (1\,\%)^4 \\ &\leq 2 \times 10^{-4}\,\text{Hz}. \end{aligned} \tag{3.5}$$

Assuming $N_{\text{AHCAL}} = 1 \times 10^7$ channels in the full ILD AHCAL and an ILC bunch train length of $t_{\text{train}} = 1\,\text{ms}$, the mean number of expected SiPM noise hits in the full ILD AHCAL per ILC bunch train is

$$\begin{aligned} \langle n_{\text{noise}} \rangle &\leq N_{\text{AHCAL}} \times t_{\text{train}} \times f_{\text{noise}}^{4.5\,\text{px}} \\ &\leq 1 \times 10^7 \times 1\,\text{ms} \times 2 \times 10^{-4}\,\text{Hz} \\ &\leq 2 \end{aligned} \tag{3.6}$$

and thus fully negligible.

Even though SiPM dark noise is likely irrelevant, the buffer depth for an ILD AHCAL readout chip still has to be optimised with similar considerations as given in the toy simulation above, ideally using physics simulations to estimate the expected calorimeter cell occupancies for one bunch train.

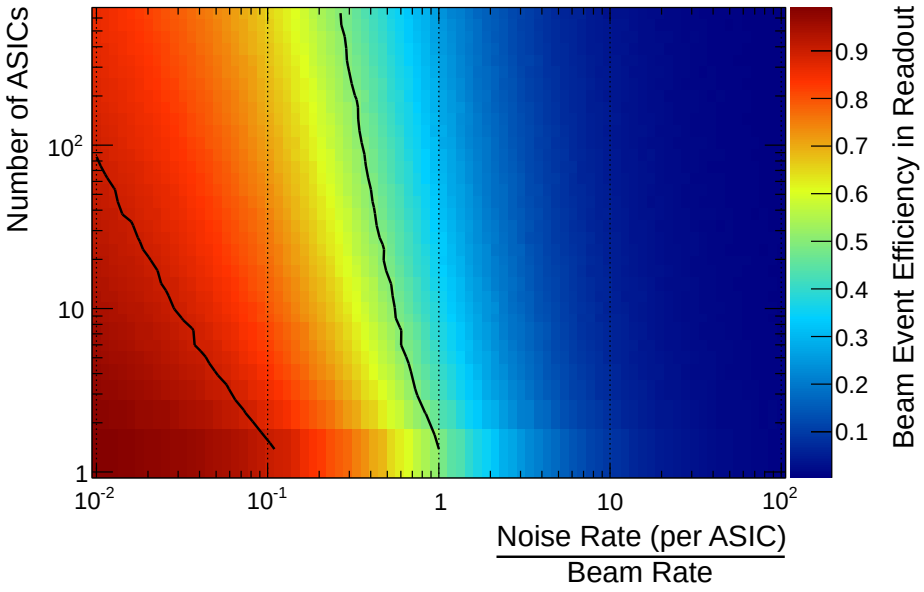

(a) *With OR36 Logic*

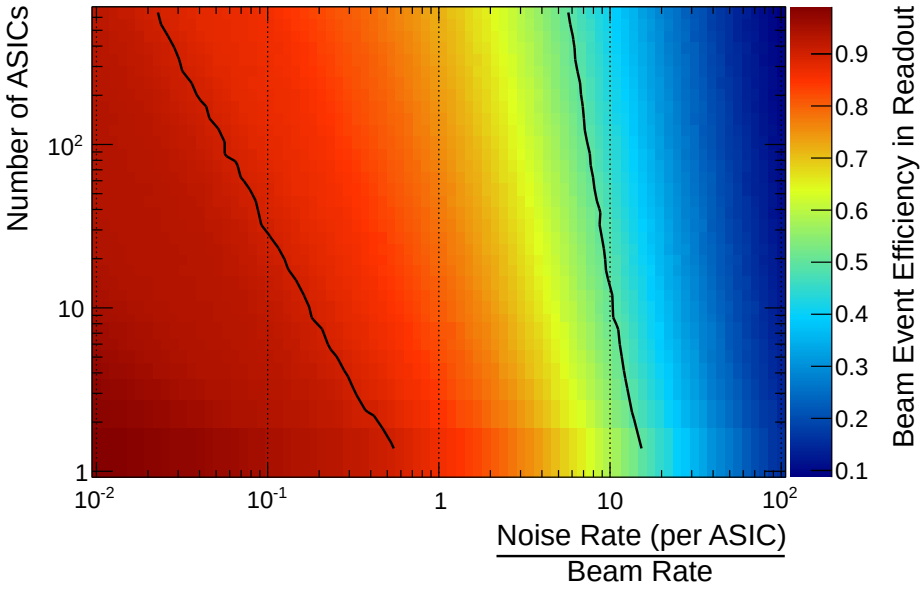

(b) *Without OR36 Logic*

Figure 3.10.: *Simulated mean beam event efficiencies for a parameter space in r and N_{chips}, for simulations with and without the OR36 trigger logic of the SPIROC2 ASIC. The black lines indicate beam event efficiencies of 50 % and 90 %, respectively.*

4. Energy Resolution of the Combined Scintillator Calorimeter System

Different combinations of CALICE calorimeter prototypes were operated in measurement campaigns at the *Fermilab Testbeam Facility* (FTBF) in 2008 and 2009. The datasets analysed in this thesis have been acquired with the combined scintillator-SiPM calorimeter system consisting of the ScECAL, AHCAL and TCMT (as described in chapter 2) in May 2009.

This chapter first discusses the setup of the testbeam and the corresponding simulation model before elaborating on the reconstruction algorithms used and implemented for this study. These reconstruction algorithms are used in the following description of the applied event selections.

The main goal of the analysis presented here is the determination of the single pion energy resolution for the combined calorimeter system, as an important ingredient to the particle flow jet energy resolution of a full linear collider detector. All steps of the parallel validation of the dataset and the accompanying simulations are presented, starting from validating the ScECAL calibration and simulation model with electromagnetic interactions and showers up to its full electromagnetic energy response and resolution. Furthermore longitudinal shower profiles of electrons and pions are compared in data and simulations. Finally two different energy reconstruction schemes for the combined calorimeter system are presented and their results discussed.

The key results of this chapter have been approved by the CALICE collaboration for presentation at conferences with the label *CALICE Preliminary* and have been published on the CALICE website [66] as *CALICE Analysis Note 056: Pion Response and Resolution in a Combined Scintillator Calorimeter System in the FNAL Testbeam* (CAN-056) [108]. All figures and tables taken directly from the note are referenced as such. The text of CAN-056 was used as the basis for this chapter and is not referenced separately.

4.1. The FTBF MTest Beamline

The experimental setup was installed in sector MT6-2B of the FTBF MTest beamline. The MTest beamline offers particle beams in the energy range 1 GeV to 120 GeV, with different particle compositions and polarities depending on the selected beamline configuration. All datasets analysed in this thesis have been acquired using the *low energy pion mode* of the MTest beamline, generating negative polarity beams in the energy range 1 GeV to 32 GeV from the primary 120 GeV proton beam via conversion in a 30 cm Al target 145 m upstream of the beam area. The primary proton beam induces a hadron shower in the target, producing multiple secondary particles of various particle types and energies. These secondaries are then selected for momentum and polarity by a configurable dipole and collimator setup. The momentum of the secondary particles passing through to the beam

area is selected by the dipole field strength, while the momentum spread depends on the collimator settings. The secondary particles are mostly charged and neutral pions, and protons. Kaons are assumed to be produced rarely as the QCD production of the needed s-quark is kinematically disfavoured compared to u/d-quarks. Antiprotons are produced very rarely, as the absorber material is made up exclusively of quarks, so all three required anti-quarks would have to be produced from the QCD processes in the hadronic interaction. The geometric beam profile of the secondary particle beam is typically rather narrow (see subsection 4.3.2). However, muons can punch through the collimator and thus result in a wide profile beam halo. Additional muons in beam events can thus be distributed over the whole AHCAL cross-sectional area.

A more detailed description of the accelerator layout and the secondary beam generation is given in [34, 109, 110].

Apart from polarity and energy, the beamline does not offer any further selection of particle types in the secondary beam. The beam is primarily composed of electrons, pions and muons. Additionally a significant fraction of events contains more than one incident particle. Approximated fractions of particle types and multi particle events as a function of beam energy are given in Figure 4.1.

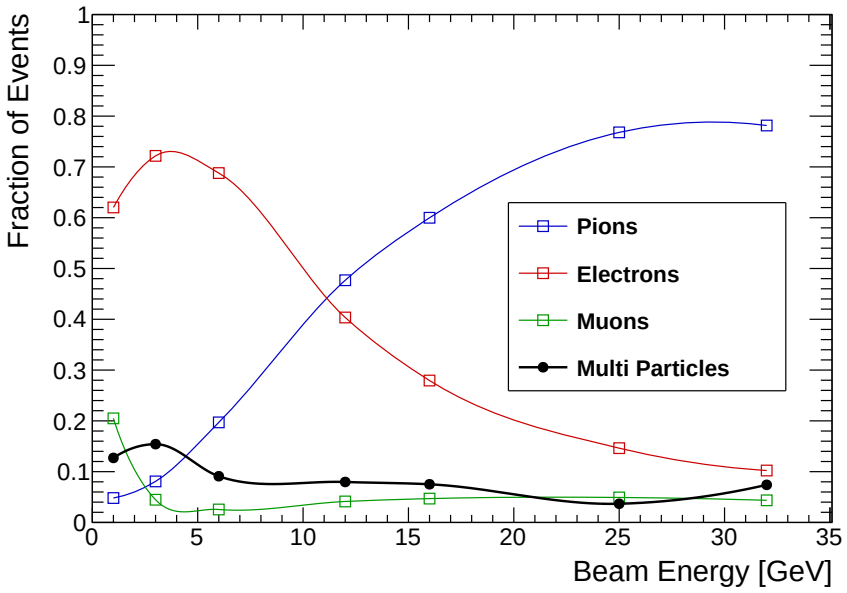

Figure 4.1.: *Beam composition as a function of beam energy in the FNAL MTest beamline. Adapted from [34, 110].*

4.2. Testbeam Setup

Starting downstream of the final beam energy selection dipole and collimator, the MT6 beamline is instrumented with a differential Cherenkov detector, various trigger scintillators and wire chambers, and finally the calorimeter prototypes installed in the order ScECAL,

AHCAL and then TCMT. The coordinate system used throughout all analyses from the beam period at FTBF is right handed with the Z axis pointing in the direction of the beam and the Y axis pointing upwards. A schematic view of the beamline setup, approximately to scale, is given in Figure 4.2.

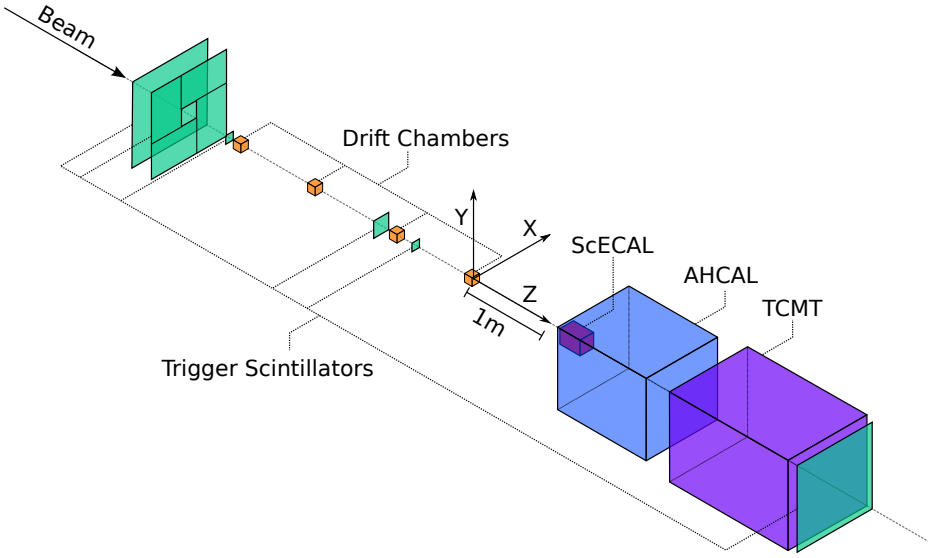

Figure 4.2.: *Schematic sketch of the beamline setup as used during the data taking period at FNAL in 2009, starting from the first trigger scintillator. The Cherenkov tube upstream of the first trigger scintillator is not shown.*

The differential Cherenkov counter installed in the MT6 beamline consists of an 18.5 m long pressure tank filled with either N or He gas at adjustable pressures up to 1.4 bar, a primary mirror to reflect generated Cherenkov light out of the pressure tank and two PMTs, C1 and C2, as sketched in Figure 4.3.

Cherenkov light is emitted by charged particles traversing a medium with refractive index n when the particle velocity is larger than the phase speed $\frac{c}{n}$ of light in this medium [26]. The generated Cherenkov photons are emitted in a cone of the angle

$$\cos\left(\theta_{\text{cone}}\right) = \frac{1}{n\beta} \tag{4.1}$$

with respect to the direction of motion of the particle. Given particles of the same momentum, only particles below a threshold mass

$$m_{\text{thr}} = \frac{p}{c}\sqrt{n^2 - 1} \tag{4.2}$$

generate Cherenkov radiation [111] with

$$\theta_{\text{cone}} \propto \Delta M = m_{\text{thr}} - m. \tag{4.3}$$

As n is proportional to the gas pressure in the Cherenkov tube, both θ_{cone} and m_{thr} directly depend on the selected gas pressure.

Narrow angle Cherenkov light is detected by C1, while wider angle Cherenkov light is reflected by the secondary mirror onto C2. The gas pressure is typically set up such that ideally Cherenkov photons generated from pions only hit C1, Cherenkov photons generated from electrons only hit C2 and hadrons heavier than pions do not generate Cherenkov light at all [34]. For beam energies $\leq$4 GeV the gas pressure cannot be increased enough to generate Cherenkov light from pions. At such low beam energies the Cherenkov detector can thus only be used to tag electrons.

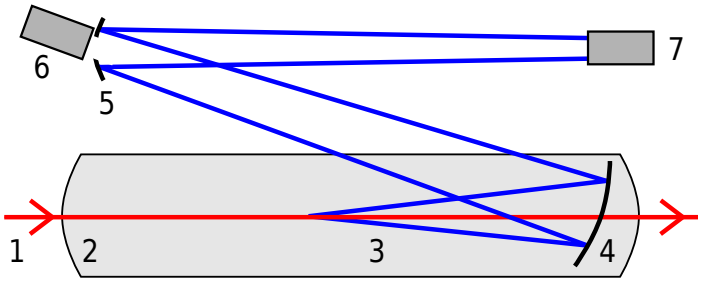

Figure 4.3.: *Schematic sketch of the differential Cherenkov counter installed in the MTest beamline. 1: incident particle, 2: gas tank, 3: Cherenkov light cone, 4: primary mirror, 5: secondary mirror with hole, 6: inner PMT C1, 7: outer PMT C2. [34]*

The trigger scintillators set up in the testbeam area are typically plastic scintillator paddles coupled to a PMT, read out by a binary single-threshold comparator connected to the DAQ system.

The coincidence of two large 1 m $\times$ 1 m triggers installed as the first trigger downstream of the Cherenkov tube and the last trigger downstream of the TCMT is used to trigger muons traversing the whole calorimeter system in MIP calibration runs. The upstream trigger is removed during electron and pion runs to minimise material upstream of the calorimeters. A 1 m $\times$ 1 m veto wall with a central 20 cm $\times$ 20 cm hole, made up of 4 scintillator plates of 60 cm $\times$ 40 cm each with individual PMT readout, is used to veto additional particles in the beam halo originating from the beam collimation. The coincidence of two 10 cm $\times$ 10 cm scintillators placed 2.5 m apart is used to trigger beam events in pion and electron runs. The PMT of an additional 20 cm $\times$ 20 cm plastic scintillator is connected to a 16 bit readout, enabling the suppression of events with more than one particle traversing the scintillator from the amplitude measured by the PMT.

The drift chambers installed in the beamline did not work properly and are not used in the analyses presented here.

In electron and pion beam runs the coincidence of the two 10 cm $\times$ 10 cm scintillator paddles is used in the DAQ online trigger decision. In addition to the beam triggers, information from one of the Cherenkov channels is included in the trigger decision, typically tagging the desired particle type (C1 for pion runs, C2 for electron runs). The information of all installed beam triggers and both Cherenkov channels as well as the beam spill status is recorded for each event and can be used for further event selection in the offline analysis.

4.3. Simulation Setup

The simulation of the combined prototype setup is based on the MOKKA framework v08-05 [36], which provides full GEANT 4 simulations of detector implementations with detailed geometry and material descriptions. This analysis uses the beamline model *TBFnal0508*, including basic trigger scintillators but no further detailed beam instrumentation. The detector models used for each subdetector are *TBscint04* for the ScECAL, *TBhcal08* for the AHCAL and *TBcatcher08* for the TCMT. The distances between simulated subdetectors are 63 mm between ScECAL and AHCAL and 402 mm between AHCAL and TCMT as given in [79]. The axial alignment of the ScECAL and AHCAL is described in subsection 4.3.3. The simulation models of the AHCAL and TCMT are well understood and have been validated in various published studies [88, 112, 113]. A full validation of the ScECAL simulation model is presented in section 4.6.

Depending on the pressure in the Cherenkov gas tube, the material between the final beam energy selection magnet and collimator of the MT6 beamline and the ScECAL front face amounts to $0.08\,X_0$ to $0.16\,X_0$ distributed over around 30 m, as estimated in [34]. As the He filled beam transport tubes and most of the beam instrumentation is not represented in the simulation model, a similar amount of material between beam generation and calorimeter front face is achieved in the simulations for this analysis by filling the world volume with air, setting the simulated beam gun at 6 m from the calorimeter front face and adding 5 mm of Al directly in front of the ScECAL, amounting to around $0.1\,X_0$ in total.

The beam gun is configured to generate single particles with mean momentum equal to the corresponding data run. The beam energy and beam momentum are practically identical for the particle types and beam momenta considered here. The beam momentum spread is set to 2.7 % for runs with beam energy $\leq$4 GeV and 2.3 % for runs with higher beam energies, following [81]. The beam profile is extracted from data and transferred into the simulation for each run individually as discussed in subsection 4.3.2.

All electron simulations discussed in this analysis are simulated with GEANT 4 10.1p2 using the QGSP_BERT physics list, as no significant differences have been found to any other tested physics list. Usage of the _EMY type physics lists does not significantly change the description of the electromagnetic shower variables discussed in this analysis.

Pion showers are simulated using the QGSP_BERT_HP and FTFP_BERT_HP physics lists in GEANT 4 10.1p2, as those two physics lists are well validated and generally recommended in the simulation of high energy particle interactions with matter. To better understand the differences in the behaviour of the FTFP_BERT_HP physics list to the previous GEANT 4 version, all pion runs are also simulated using FTFP_BERT_HP in GEANT 4 9.6p3.

For each used data run 100 000 simulated π^-, e^-, p^- and μ^-events are generated, using identical simulation setups apart from the particle type. The simulations with particle types different from the primary particle type of the data run are used to study selection efficiencies and beam purities.

4.3.1. ScECAL Absorber Composition

In order to precisely simulate the ScECAL response to particle showers, the material composition of the ScECAL absorber plates has to be well known and implemented correctly

into the simulation model. The dimensions and weights of the used absorber plates are measured precisely, yielding an averaged density of $(14.25 \pm 0.04)\ \frac{\mathrm{g}}{\mathrm{cm}^3}$ [114].

Analyses of the absorber material composition have been performed with *X-ray diffraction* (XRD) and *energy-dispersive X-ray spectroscopy* (EDX) methods, using samples of the absorber plates used in the ScECAL prototype [114]. The XRD measurements show that the ScECAL absorber plates consist of WC[1)] and Co, negligible amounts of Cr, but no significant amount of elementary W. Combined with the mass fractions of W, Cr and Co obtained from the EDX analysis, the *analysed* composition of the absorber plates is determined to be (81.8 ± 0.3) % W, (5.4 ± 0.0) % C, (0.5 ± 0.5) % Cr and (12.4 ± 0.5) % Co in mass fractions [114]. The calculated density of such a compound would be $(14.76 \pm 0.07)\ \frac{\mathrm{g}}{\mathrm{cm}^3}$, which is 3.5 % higher than the measured density of the absorber plates. Tungsten carbide plates are typically produced in powder sintering processes, which can result in porous materials with significant inclusions of vacuum or air bubbles, effectively decreasing the density of the material. However in cobalt cemented tungsten carbide only up to 1 % porosity is considered typical [115], and no obvious bubble inclusions are visible in *backscattered electron imaging* (BSEI) pictures of the ScECAL absorber sample. To make the simulated absorber density match up with the measured value, the density is superficially set to the measured density, effectively assuming a 3.5 % porosity in the simulation.

Assuming zero porosity of the material and disregarding the minor possible amounts of Cr present, the absorber composition can also be *calculated* directly from the measured plate density and the known densities of WC and Co to be (74.6 ± 0.1) % W, (4.9 ± 0.0) % C and (20.5 ± 0.0) % Co in mass fractions.

Comparing the longitudinal electron shower profiles of the ScECAL simulations with the analysed absorber composition and the calculated absorber composition shows a small but significant difference between the compositions, see Figure 4.4.

As simulations using the calculated absorber composition generally show better agreement with data, the analysed absorber composition is not used in this analysis. However, the effective differences in results, especially for pions, are very small. The question of the correct absorber composition will be addressed further in an upcoming paper on the ScECAL construction and electromagnetic performance currently in preparation [116].

4.3.2. Beam Profiles

The geometric position and shape of the beam spot on the ScECAL front face (the *beam profile*) of data runs has to be well modelled in simulations to ensure the same averaged impact of dead channels, possible transverse leakage and systematic effects due to the used scintillator geometries in data and simulations. This is achieved by setting up the position of the simulated beam gun and its (typically Gaussian) position smearing according to the beam profiles extracted from data runs. In principle the angular distribution of the beam particles is relevant as well, however due to the wire chamber trackers not working in the FNAL 2009 beam period, no data on this is available. Depending on the particle type, different definitions of the beam profile are used.

For electrons, the distribution of the ScECAL shower centers of gravity in X and Y is used as an estimate of the beam profile. The shower center of gravity is calculated as the

[1)] tungsten carbide

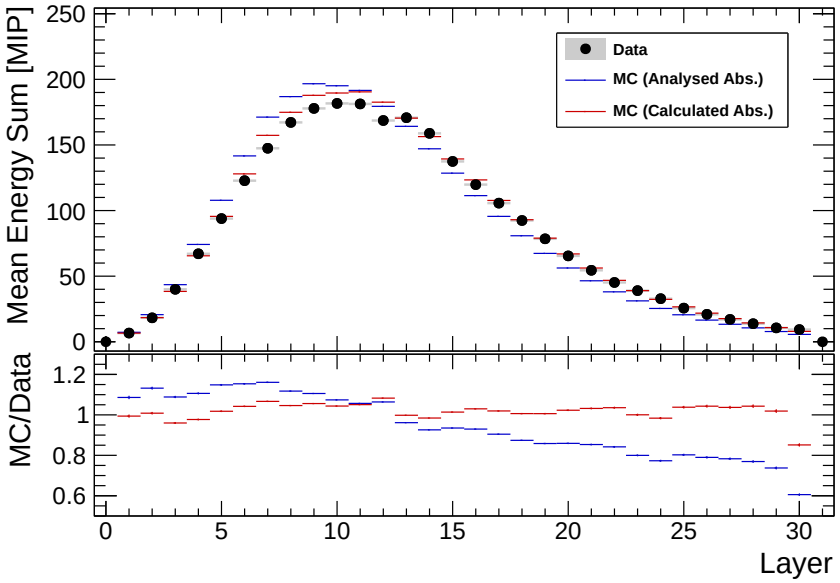

Figure 4.4.: *Longitudinal shower profile for 20 GeV electrons in the ScECAL for data and simulations with the analysed and calculated absorber compositions. The lower plot shows the ratio between data and both simulations. The calculated absorber compositions gives a much better description of the measured longitudinal profile.*

energy weighted mean position of all shower hits. To calculate an accurate center of gravity in the strip geometry of the ScECAL, only depositions in the vertically oriented layers are used to calculate the center of gravity in X and only depositions in the horizontally oriented layers are used to calculate the center of gravity in Y. The distribution of centers of gravity in one dimension shows peaks with a distance of the ScECAL strip width 10 mm as shown in Figure 4.7.(a). The position and shape of the beam profile are extracted from a two-dimensional Gaussian fit to the distribution of centers of gravity, binned in the inherent 10 mm $\times$ 10 mm layout of the ScECAL strip overlaps, see Figure 4.7.(b).

The pion beam profile is extracted from the positions of tracks generated by pions which traverse the ScECAL as a MIP, without a hard hadronic interaction in the ScECAL volume. For this the single pion event selection as detailed in subsection 4.5.2 is extended by additionally requiring the first hadronic interaction layer (see subsection 4.4.2) to be reconstructed in the AHCAL. The distribution of XY-positions of the identified primary track in the ScECAL (with the inherent position quantisation of the effective 10 mm $\times$ 10 mm grid of ScECAL strip overlaps) is used as an estimation of the beam profile. The beam position and shape are extracted from a two-dimensional Gaussian fit to the distribution of primary track coordinates.

In simulated muon runs, flat beam profiles covering the full ScECAL or full AHCAL are configured in the simulation. Reproducing the exact beam profile of data muon runs, which is very close to flat, is not expected to influence the MIP response crosschecks performed with such simulations.

The beam profiles extracted from both electron and pion data runs are generally very close to Gaussian in shape, with the axes of the Gaussian ellipse well aligned with the X and Y axis of the beamline coordinate system. Typically the beam spot is wider in X than in Y. For beam sizes close to (or larger than) the size of the 10 cm $\times$ 10 cm beam trigger scintillator, which is typical for runs at $\leq$4 GeV, its acceptance has to be taken into account in fitting the beam profile. This is approximated by multiplying a two dimensional 10 cm $\times$ 10 cm rectangular function onto the Gaussian beam profile fit. A rectangular function with slightly smeared edges is used to account for multiple scattering between the trigger scintillator and the calorimeter front face.

The mean beam position $\mu_{\text{fit}}^{\text{data}}$ fitted from the beam profile is directly used to setup the simulation beam gun. To obtain the correct beam spread from simulated events, multiple scattering has to be taken into account. Multiple elastic scattering of the primary particle in the air and material between the beam gun and the ScECAL front face causes an effective widening of the beam profile added in quadrature to the beam position smearing configured in the beam gun. To extract the magnitude of this effect for pions, different beam gun position spread setups were simulated for all used beam energies. Figure 4.5 shows the effective widening of the beam $\sigma_{\text{eff.}} = \sqrt{{\sigma_{\text{fit}}^{\text{MC}}}^2 - {\sigma_{\text{gun}}}^2}$ with the fitted beam profile width in the ScECAL $\sigma_{\text{fit}}^{\text{MC}}$ and the configured beam gun spread σ_{gun} as a function of beam energy. The different points at the same beam energy correspond to different configured beam gun position spreads in X and Y.

The RMS beam angle smearing from multiple scattering is expected to scale as $\sigma_{\theta_0} \propto \frac{1}{\beta p}$, with the velocity β and the momentum p of the initial particle [26]. Assuming a relativistic primary particle, a homogeneous traversed medium density and small total scattering angle, which is reasonably satisfied in the setup and beam energies discussed here, this corresponds to an effective widening of the beam profile proportional to $\approx \frac{1}{E_{\text{beam}}}$. The fitted function shown in Figure 4.5 additionally accounts for a constant increase in the fitted beam profile width from the 10 mm $\times$ 10 mm quantisation of the track position measurement. The full fit function

$$\sigma_{\text{eff.}}(E) = \sqrt{\left(\frac{a}{E[\text{GeV}]}\right)^2 + \left(\frac{10\,\text{mm}}{\sqrt{12}}\right)^2}. \tag{4.4}$$

describes the simulated beam spot widening very well with the fitted parameter $a = (68.2 \pm 0.4)$ mm.

To extract the beam gun position and position smearing parameters for an ideal reproduction of the pion beam profile, the data beam profile fit parameters $\mu_{\text{fit}}^{\text{data}}$, $\sigma_{\text{fit}}^{\text{data}}$ are inserted into

$$\mu_{\text{gun}} = \mu_{\text{fit}}^{\text{data}} \tag{4.5}$$

$$\sigma_{\text{gun}} = \sqrt{\left(\sigma_{\text{fit}}^{\text{data}}\right)^2 - \left(\sigma_{\text{eff.}}(E)\right)^2}. \tag{4.6}$$

for X and Y coordinates separately. The resulting beam gun configurations reproduce the data pion beam profiles very well, as is shown for an exemplary energy point in Figure 4.6.

This approach gives a reasonable estimate of the beam gun configuration for electron runs as well, but the results are significantly improved by retuning the obtained parameters

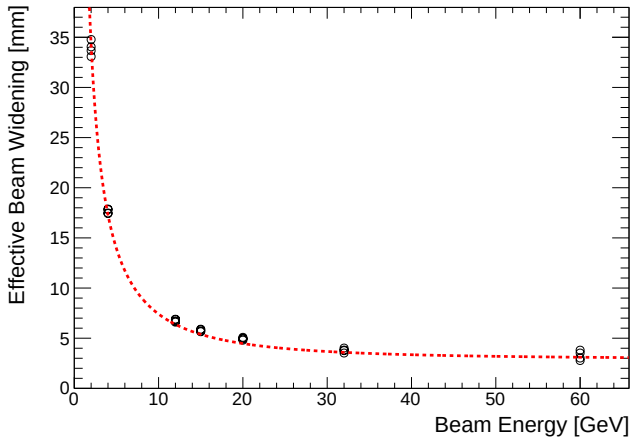

Figure 4.5.: *Effective widening of the pion beam profile from the beam position spread configured in the simulation beam gun as a function of beam energy, including a fit of the expected behaviour from multiple elastic scattering and a constant term from the finite strip granularity. Simulated using QGSP_BERT_HP with GEANT 4 10.1p2.*

manually. This is likely due to additional systematic effects from the definition of the electron beam profile, as the distribution of electromagnetic shower center of gravities has a, possibly energy dependent, inherent spread which might even by systematically different in X and Y coordinates due to the center of gravity calculation method. An example electron run beam profile in data and simulation is shown in Figure 4.7. The apparent difference between data and simulation in width of the individual peaks in the beamprofile projected in the X coordinate is consistent with the difference in observed shower radii in data and simulation as discussed in subsection 4.6.2.

The particle gun configuration applied to reproduce all data runs used in this thesis are given in Table 4.1

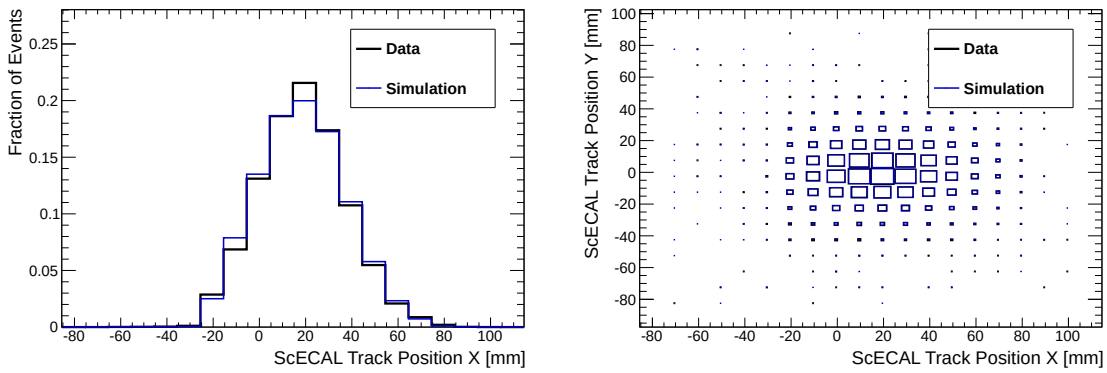

(a) *Beam Profile X* ***(b)*** *Beam Profile XY*

Figure 4.6.: *Beam profiles for 12 GeV pions in data and simulation. Simulated using QGSP_BERT_HP with GEANT 4 10.1p2.*

Table 4.1.: *Simulated particle gun settings applied to reproduce the beamprofile of the data runs used in this thesis.*

Run/Type	p_{beam} $\left[\frac{\text{GeV}}{c}\right]$	$\sigma_{p_{\text{beam}}}$ $\left[\frac{\text{GeV}}{c}\right]$	μ_X [mm]	μ_Y [mm]	σ_X [mm]	σ_Y [mm]
560339, e^-	1.0	0.027	−14.5	7.4	68.1	55.6
560337, e^-	2.0	0.054	−3.4	7.6	46.2	40.2
560330, e^-	4.0	0.108	20.7	6.9	28.2	28.7
560306, e^-	8.0	0.184	16.7	7.0	20.9	14.7
560294, e^-	12.0	0.276	12.4	6.6	16.1	10.0
560291, e^-	15.0	0.345	5.0	6.9	15.0	8.7
560284, e^-	20.0	0.460	25.2	4.6	15.5	7.5
560378, e^-	30.0	0.690	9.2	6.1	10.5	5.8
560390, e^-	32.0	0.736	10.6	2.0	9.8	5.4
560506, π^-	4.0	0.108	12.4	−1.6	49.6	36.9
560498, π^-	12.0	0.276	17.5	0.9	19.6	11.9
560496, π^-	15.0	0.345	5.5	1.3	17.6	9.6
560481, π^-	20.0	0.460	9.5	0.8	14.4	7.8
560474, π^-	32.0	0.736	8.1	−2.7	11.7	5.4

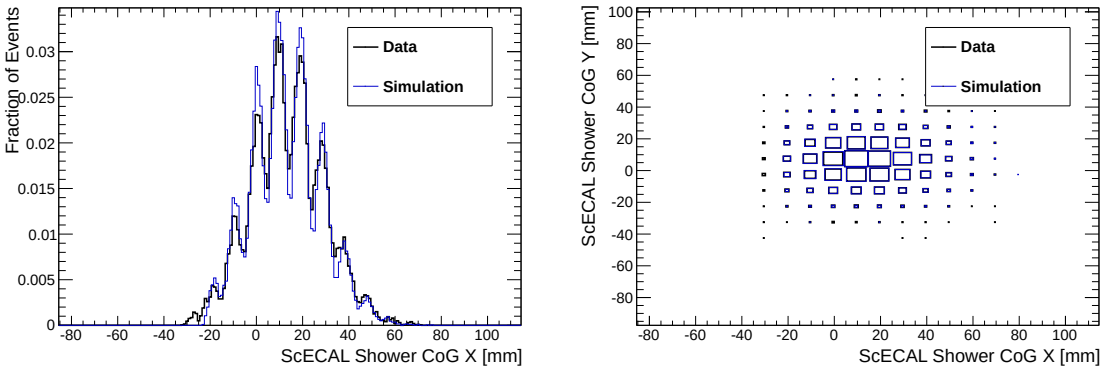

(a) *Beam Profile X* **(b)** *Beam Profile XY*

Figure 4.7.: *Beam profiles for 12 GeV electrons in data and simulation. Simulated using QGSP_BERT with GEANT 4 10.1p2.*

4.3.3. Relative Alignment of the Subdetectors

Ideally the central axes of the ScECAL, AHCAL and TCMT would be perfectly aligned during the FNAL data taking. In practice this is never fully achieved. To correctly reflect the relative alignment between the subdetectors, the misalignment is measured from data and accounted for in the reconstruction and simulation. The procedure to measure the misalignment in the XY plane between the ScECAL and the AHCAL is described here. The axial alignment of the TCMT cannot be measured reliably with the procedures described here, as it is lacking the required readout granularity. As the mean energy deposition in the TCMT is small in the considered beam energy range, misalignments are assumed to be negligible for the results of this study.

The relative alignment between the ScECAL and the AHCAL is extracted from events in which a single MIP-like particle traverses both the ScECAL and the AHCAL, leaving an isolated track in both subdetectors. Such events are extracted from a high statistics muon data run using the MIP event selection criteria detailed in subsection 4.5.1. The comparison of the reconstructed track XY-coordinates in the ScECAL and AHCAL then yields the average misalignment, as the mapping used to look up the position coordinates for each calorimeter cell in data assumes perfect alignment of the subdetectors.

Tracks parallel to the beam axis can be reconstructed with a spatial granularity of 10 mm $\times$ 10 mm in the ScECAL (see subsection 4.4.3) and 30 mm $\times$ 30 mm in the central part of the AHCAL. The distribution of reconstructed track position differences is thus expected to show a structure of size up to 40 mm $\times$ 40 mm with substructures around the size of the ScECAL track granularity of 10 mm $\times$ 10 mm, as is visible in Figure 4.8.

The mean of the acquired distribution in X and Y coordinates yields the measured misalignment of $\Delta X = \left\langle \text{track}_X^{\text{AHCAL}} - \text{track}_X^{\text{ScECAL}} \right\rangle = 14.5\,\text{mm}, \Delta Y = 2.5\,\text{mm}$. The alignment is crosschecked for each used pion and electron run, utilising the beam contamination muons and punch-through pions, confirming the misalignment within the statistical uncertainties.

To correct for the misalignment in data, the ScECAL hit positions are shifted by ΔX and ΔY in the mapping phase of the hit reconstruction. In the simulation the position of the whole ScECAL geometry is shifted by ΔX and ΔY.

The track position difference distributions for data and simulation after correction are shown in Figure 4.8. The remaining measured mean misalignments are <1 mm in data. As in simulation the hit position for each ScECAL strip is extracted directly from the simulated hit, the track position difference plot will always be centered around zero. The residuals extracted from the simulationare thus a rough estimate of the systematic uncertainty of the method.

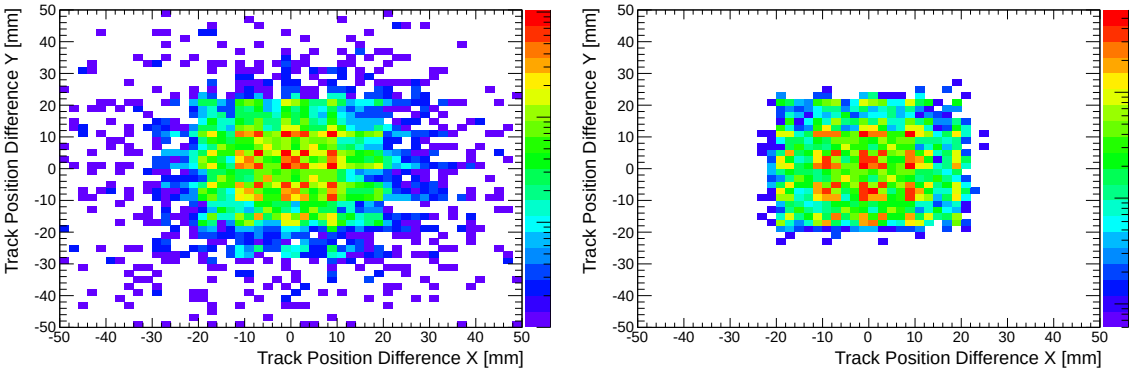

(a) *Data* **(b)** *Simulation*

Figure 4.8.: *Distribution of differences in matched ScECAL and AHCAL tracks from a muon run after correcting for the misalignment. The remaining mean misalignment residuals are* $\langle \Delta\ X \rangle_{Data} = -0.19\,\text{mm}$, $\langle \Delta\ Y \rangle_{Data} = 0.98\,\text{mm}$, $\langle \Delta\ X \rangle_{Sim} = -0.07\,\text{mm}$, $\langle \Delta\ Y \rangle_{Sim} = -0.22\,\text{mm}$.

4.4. Reconstruction

Reconstruction denotes the conversion of the raw recorded data into hits into the calibrated MIP scale and higher level objects derived from the spatial relations of these hits.

The simulation digitisation procedure (see section 2.7) is designed such that its output is fully compatible with raw testbeam data amplitudes. The reconstruction procedures used for data and simulated events are thus exactly identical except for the one difference that no in-situ pedestal correction is performed in the reconstruction of digitised simulation events, as the noise overlaid in the digitisation step is already pedestal subtracted (see subsection 2.7.5).

4.4.1. Deposited Energy

The conversion of the raw ADC input to the MIP scale makes use of the appropriate calibration factors for the channel as described in section 2.6.

To suppress noise in the detectors only hits above 0.5 MIP reconstructed amplitude are used in the analysis.

Each hit is assigned a position in the world reference coordinate system. In data this position is generated from a look-up database which maps the hardware address of each sensor into the appropriate XYZ-coordinates (*mapping*). The simulation models are configured to reproduce these coordinates, and thus use the position of the simulated scintillator cells directly.

4.4.2. Layer of First Interaction

The layer of *first hadronic interaction* (FHI) is defined as the calorimeter layer in which the first hard interaction between the primary hadron and a nucleus in the detector takes place, indicating the start of the hadronic cascade (see subsection 1.3.3). Before the first hadronic interaction, the primary hadron typically behaves MIP-like and only deposits very small amounts of its energy. In the first hadronic interaction, typically several secondary particles are generated, causing a steep increase in deposited energy in the next active layer. The reconstruction of the FHI layer is based on detecting this sudden increase in deposited enery per layer.

Definition of the First Hadronic Interaction MC Truth

In simulated events, the *true* first hadronic interaction layer can be extracted from the detailed informations available on each interaction. Each simulated interaction in GEANT 4 outputs the type of interaction (hadronic, electromagnetic, decay, optical...), the parameters (particle ID, momentum, kinetic energy) of the initial particle before the interaction, of all particles generated in the interaction and of the initial particle after the interaction. However, simply using the initial hadron's first interaction flagged as hadronic as the true FHI is not satisfactory. Many of these interactions are elastic, with very small energy transfer off the initial hadron. Generally there is no reliable distinction between the initial particle after the interaction and particles generated in the interaction, as sometimes the initial particle has vanished after the interaction and a single particle with nearly identical features as the initial particle is generated. The separation by GEANT 4 of initial particle after the interaction and generated particles is thus not used in this study. Instead, the union of particles generated in the interaction and the initial particle after the interaction is referred to as *secondary particles*. The initial hadron before the interaction is referred to as *primary particle*.

To remove elastic and soft inelastic first hadronic interaction events from the FHI reconstruction optimisation, only events with reasonably hard first hadronic interactions are used. The hardness of a hadronic interaction is classified by the kinetic energy sum of the secondary particles generated in the interaction

$$E_{\text{kin}}^{\text{gen}} = \sum E_{\text{kin}}^{\text{sec}} - E_{\text{kin}}^{h_{\text{lead}}}. \tag{4.7}$$

$\sum E_{\text{kin}}^{\text{sec}}$ is the sum of the kinetic energies of all secondary particles generated in the interaction. $E_{\text{kin}}^{h_{\text{lead}}}$ is the kinetic energy of the leading secondary hadron, the one secondary hadron of the same particle type as the primary hadron with highest momentum projected onto the primary hadron's momentum. Subtracting these two quantities effectively removes the

primary hadron's kinetic energy from the secondary particles, yielding an estimate of the sum of kinetic energies of the secondary particles generated in the interaction.

Correlation plots of the number of secondary particles versus the sum of kinetic energies of the secondary particles generated in the interaction are shown in Figure 4.9. The very high density points around $E_{\text{kin}}^{\text{gen}} = 0$ and 0 to 3 secondary particles in both plots correspond to elastic interactions. Rejecting events with $E_{\text{kin}}^{\text{gen}}$ less than one third of the kinetic energy of the primary hadron $E_{\text{kin}}^{h_{\text{prim}}}$ effectively ensures that only first hadronic interactions in which a sizeable fraction of the primary hadron's energy went into the generation of new particles are flagged as such. Events that do not fit the elastic interaction criteria described above but do not pass the cut on $E_{\text{kin}}^{\text{gen}}$ are termed soft inelastic interactions.

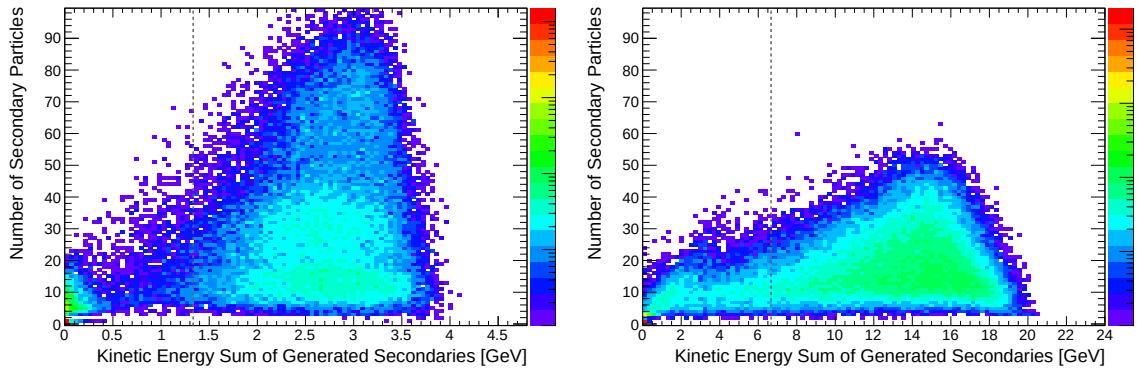

(a) 4 GeV π^- **(b)** 20 GeV π^-

Figure 4.9.: *Correlation of the sum of kinetic energies of the secondary particles (excluding the leading secondary pion) versus the number of secondary particles created in the first hadronic-flagged interaction of the initial particle. The frequency of occurrence is color coded on a logarithmic scale. The dashed grey line indicates the applied threshold to be included in the benchmark sample. Simulated using QGSP_BERT_HP with GEANT 4 10.1p2.*

At 4 GeV beam energy 40 % of the simulated events are rejected due to the first hadronic interaction being considered elastic, lowering to 25 % for 32 GeV pions. Out of the remaining first hadronic interactions 5 % to 15 % are rejected due to being too soft.

The corresponding layer of the first hadronic interaction is calculated from the Z-position of the interaction. Events where the first hadronic interaction occurs outside the prototype system volume, e.g. in the air volume between beam gun and prototype or simulated beam instrumentation, are also rejected for the optimisation of the FHI reconstruction.

Reconstruction of the FHI Layer

The layer of first hadronic interaction is reconstructed by successive comparison of the deposited energy and number of hits per layer to given thresholds. This is done separately for the ScECAL and the AHCAL with slightly different algorithms. The individual results are then combined into the reconstructed FHI layer of the event.

In the AHCAL, the FHI layer is reconstructed using the algorithm detailed in [113]. The earliest layer in which both the moving average of deposited energy in the previous ten layers up to the current and the following layer is above a given energy threshold $E_{\text{thr}}^{\text{HCAL}}$ and the number of hits in the current and the following layer is above a given threshold $N_{\text{thr}}^{\text{HCAL}}$ is identified as the AHCAL FHI layer. The averaging of layer depositions over ten layers is needed to suppress noise hits misrepresenting a first hadronic interaction. The parameters $E_{\text{thr}}^{\text{HCAL}}$ and $N_{\text{thr}}^{\text{HCAL}}$ are optimised as a function of the beam energy, ranging from $E_{\text{thr}}^{\text{HCAL}} = 6.4\,\text{MIP}$, $N_{\text{thr}}^{\text{HCAL}} = 5$ at 4 GeV to $E_{\text{thr}}^{\text{HCAL}} = 9.2\,\text{MIP}$, $N_{\text{thr}}^{\text{HCAL}} = 7$ at 32 GeV [113].

The FHI reconstruction in the ScECAL was developed for this analysis. It is similarly based on thresholds in layer deposition $E_{\text{thr}}^{\text{ECAL}}$ and layer number of hits $N_{\text{thr}}^{\text{ECAL}}$. The algorithm iterates through the ScECAL layers, starting from the first layer. If the current layer deposition is above $E_{\text{thr}}^{\text{ECAL}}$, the mean deposition in the following three layers is also above $E_{\text{thr}}^{\text{ECAL}}$ and the mean number of hits in the following three layers is above $N_{\text{thr}}^{\text{ECAL}}$, the current layer is identified as the FHI layer. If one of the last three layers of the ScECAL is inspected, the information of up to the first three layers in the AHCAL are used for comparison to the given thresholds.

$E_{\text{thr}}^{\text{ECAL}}$ and $N_{\text{thr}}^{\text{ECAL}}$ are optimised based on the achieved resolution and inefficiency of the FHI layer reconstruction. Here inefficiency is defined as the fraction of events in which no layer satisfies the FHI conditions although the true first hadronic interaction is located within the ScECAL volume. Lower thresholds typically give worse resolutions due to too early reconstructed FHI layers from noise or delta electrons, while higher thresholds increase the inefficiency of the reconstruction.

Compared to the AHCAL, pure noise hits are less of a problem in the ScECAL, so $N_{\text{thr}}^{\text{ECAL}} = 2$ is used for all beam energies. For beam energies of 12 GeV and above, $E_{\text{thr}}^{\text{ECAL}} = 13.0\,\text{MIP}$ yields inefficiencies $\leq 1\,\%$ with good accuracies. The beam energy point at 4 GeV is more problematic, as the FHI is generally quite soft due to the low initial particle energy. The best trade-off between resolution and inefficiency is reached at $E_{\text{thr}}^{\text{ECAL}} = 5.5\,\text{MIP}$, yielding a reasonable resolution with an inefficiency of 12 %.

The separate outputs of the FHI reconstruction in ScECAL and AHCAL are combined by prioritising the ScECAL output. Only if the ScECAL FHI algorithm does not detect any FHI layer, the AHCAL algorithm result is used. If no layer satisfying the FHI criteria is found in neither ScECAL nor AHCAL, the found FHI layer number is output as zero, indicating no reconstructed FHI layer. In around 90 % of simulated muon events, no reconstructed FHI layer is found. The 10 % of muons misreconstructing an FHI layer are likely due to delta-electrons with enough energy to initiate a small electromagnetic subshower which is above the FHI reconstruction threshold.

The correlations of true and reconstructed FHI layer, as well as the distribution of differences in true and reconstructed FHI layer are shown in Figure 4.10. The high number of entries on the diagonal of the correlations show that the FHI layer is generally well reconstructed. It is apparent that the efficiency of reconstructing the FHI in the ScECAL is not ideal for 4 GeV pions, resulting in the visibly significant number of events where the true FHI is located in the ScECAL, while the reconstructed FHI layer is located in one of the first layers of the AHCAL. In the FHI resolution plot of the 4 GeV simulation this is also visible as the shoulder to the right side of the central peak. As is tabulated in detail for all beam energies in Table 4.2, the FHI layer is well reconstructed for beam energies higher

than 4 GeV, with RMS of the distribution around 2.2 and about 90 % of the reconstructed FHI layers within ± 2 layers of the true FHI layer, similar to the performance achieved in the standalone AHCAL [113].

The distribution of reconstructed FHI layers in pion events is shown in Figure 4.41 for data and simulated events, indicating a similar performance of the reconstruction in data and all examined simulation physics lists, including the 5 % to 15 % of too soft first hadronic interactions not included in the reconstruction optimisation.

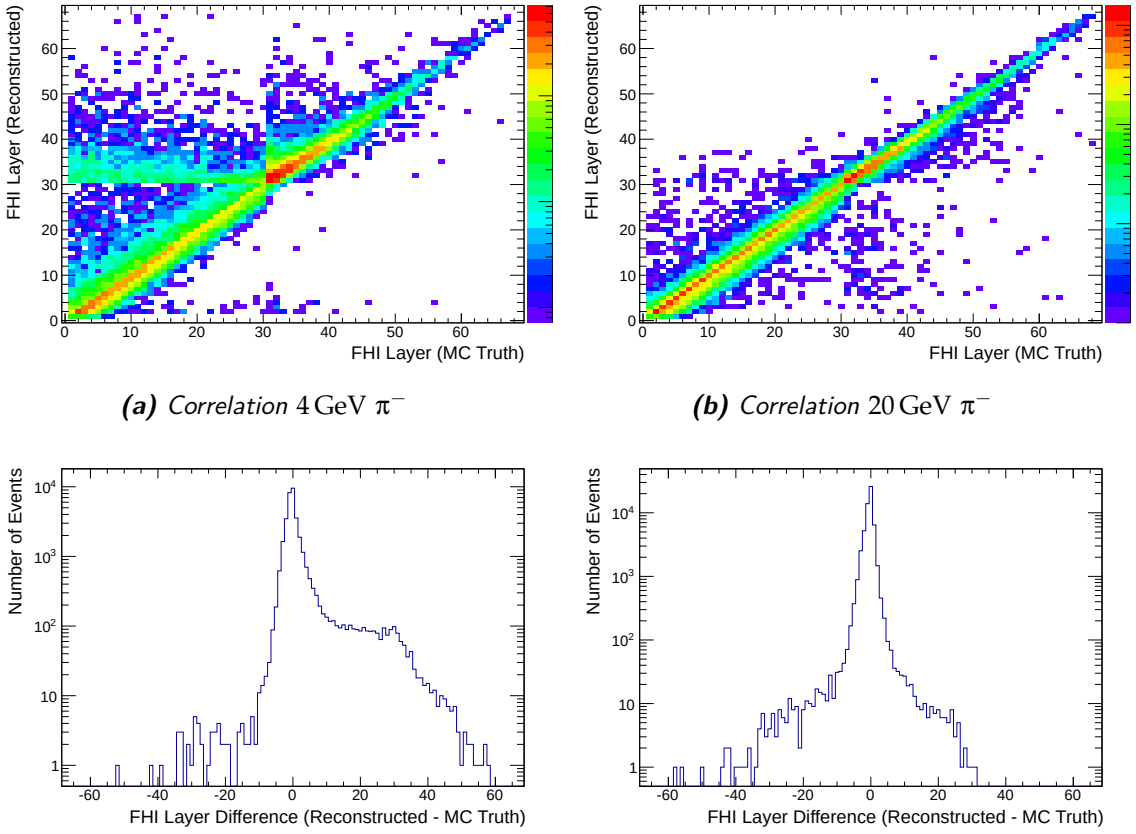

(a) *Correlation* 4 GeV π^- **(b)** *Correlation* 20 GeV π^-

(c) *FHI Difference* 4 GeV π^- **(d)** *FHI Difference* 20 GeV π^-

Figure 4.10.: *Correlation of true FHI layer versus reconstructed FHI layer (a, b) and difference between true and reconstructed FHI layer (c, d) for events with sufficiently hard first hadronic interaction at 4 GeV (a, c) and 20 GeV (b, d). Layers 1 to 30 are part of the ScECAL, layers 31 to 68 are the AHCAL layers. The frequency of occurrence in the correlation plots is color coded on a logarithmic scale. The statistical indexes for the residual spectra are given in Table 4.2. Simulated using QGSP_BERT_HP with GEANT 4 10.1p2.*

Table 4.2.: *Statistical indexes for the distributions of difference between true and reconstructed FHI layer Δ_{FHI} as shown in Figure 4.9 (c, d). Simulated using QGSP_BERT_HP with GEANT 4 10.1p2.*

Energy	μ	RMS	$\lvert\Delta_{\mathrm{FHI}}\rvert \leq 0$ [%]	$\lvert\Delta_{\mathrm{FHI}}\rvert \leq 1$ [%]	$\lvert\Delta_{\mathrm{FHI}}\rvert \leq 2$ [%]	$\not\epsilon_{\mathrm{FHI}}^{\mathrm{ECAL}}$ [%]
4 GeV	1.5	6.6	27	61	76	11.8
12 GeV	−0.35	2.2	48	81	92	<0.1
15 GeV	−0.44	2.1	46	80	91	<0.1
20 GeV	−0.49	2.2	46	79	90	<0.1
32 GeV	−0.60	2.2	44	78	90	<0.1

4.4.3. Track Reconstruction

The reconstruction of tracks from minimum ionising particles in the calorimeter system is an important part of the event selections described in section 4.5 and the selection of hits in MIP calibration studies as discussed in subsection 4.6.1.

The algorithm described in [104] is used to reconstruct tracks and track segments in the AHCAL. It is capable of reconstructing sequences of hits resembling MIP track segments in all orientations (except for tracks parallel to the AHCAL absorber plates). Its output consists of a list of hits on the found track segment and the angular orientation of the reconstructed track. In this analysis only tracks parallel to the beam axis are used for event selection purposes. In this case track segments can easily be merged into longer tracks by combining tracks that have consistent starting points and end points in the XY plane.

Implementing the track reconstruction algorithm used in [104] on the ScECAL is difficult due to the strip geometry of the ScECAL. Efficient algorithms for the reconstruction of strips hits into virtual square cells in the context of high granularity calorimeters are available [117] and have been implemented for the ScECAL [118]. In principle this enables the implementation of a general purpose track segment reconstruction, although the effect of ghost hits generated in the strip splitting would have to be considered carefully. However, only tracks from primary beam particles are of interest in this analysis, and as the geometric configuration of the testbeam prototype is fixed with the absorber plates perpendicular to the beam axis, a simpler approach to track reconstruction is utilised.

For an idealised track perpendicular to the absorber structure, each ScECAL layer has exactly one hit, which is in the same strip for each respective vertical and horizontal layer. The hit strips in the vertically and horizontally oriented layers are necessarily overlapping. There are only 20×20 (18 strips per row + two extra from the non-integer aspect ratio of the strips as shown in Figure 4.11) of such possible strip overlaps. It is thus feasible to check each possible idealised track hypothesis versus the distribution of hits in the event.

All possible track candidates are built from hits in overlapping strips of one event. Each such track candidate is accepted or rejected based on observables which are reconstructed for each track candidate. In the analysis presented here two sets of criteria are applied, depending on the use of the reconstructed tracks.

To extract hits from MIP tracks in the ScECAL for MIP calibration crosschecks (see subsections4.5.1 and 4.6.1) the *simple track* definition is used. As muon events are preselected to mostly contain single MIP track events, the track reconstruction is only needed to extract which hits in the event are part of the track and includes no requirement on isolation. The only requirement for a simple track is at least 14 hits on one track candidate, at least seven in each layer orientation. The efficiency to reconstruct a simple track in a simulated sample of single muon events is 98 %, which is sufficient for MIP calibration crosschecks. The misreconstructed events most likely contain muons which, within the ScECAL volume or in the air and beam instrumentation upstream of the ScECAL, were scattered enough to fall outside of the angular acceptance of the simple track reconstruction.

The selection of pion events is based on reconstructing an isolated primary track segment of the incident particle (see subsection 4.5.2). For this a reasonable efficiency to reconstruct at least the initial segment of the primary track is needed. As a segment of a few tracks hits is enough to define the shower axis, the efficiency of reconstructing a track for its full length

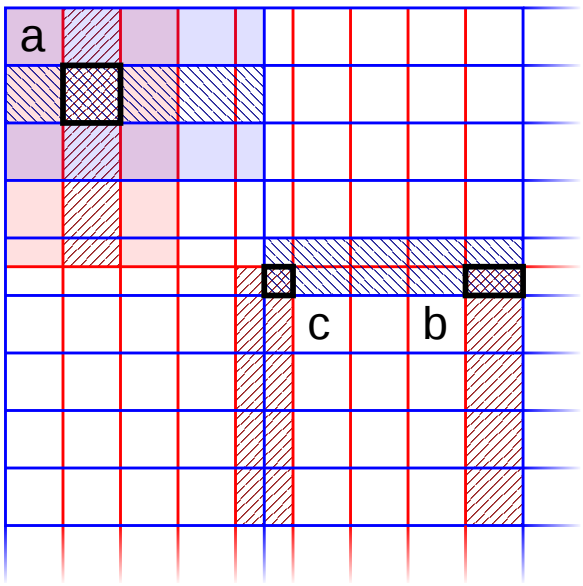

Figure 4.11.: *Schematic view of one quarter of two ScECAL layers. Horizontal strips are shown in blue, vertical strips in red. The hatched areas show example strips. The black bordered areas are overlaps between the hatched example strips. (a) shows a full overlap of two strips, (b) shows a half overlap between strips caused by the non-integer aspect ratio of the strips, (c) shows a quarter overlap between the strips. The shaded strips next to the overlapping strips in (a) are the adjacent strips used for the calculation of the halo deposition. Note that even though there are only nine rows of strips shown for each orientation, there are* 10×10 *possible overlapping strip areas in this drawing.*

is of secondary importance. For a track candidate to be considered as a *primary track*, the starting layer of the track has to be the first or second layer of the ScECAL. Assuming a (conservative, see subsection 3.2.1) 90 % MIP hit efficiency at the applied 0.5 MIP threshold, the chance of a true track being rejected from this requirement is below 1 %. Each remaining track candidate is iteratively shortened by removing its last hit until it fulfills a requirement on the hit efficiency of 85 %, defined as the number of hits on the track divided by the last track hit layer. All remaining candidates which have a track length larger than four layers are tagged as *primary* track segment.

Primary track segments might further qualify as *clean*, based on the *halo deposition* of its track hits, defined as the energy deposition sum of the strip hit by the track in a given layer plus the two strips adjacent to its longer side, as shown in the shaded strips around overlap (a) in Figure 4.11. A primary track segment is tagged as clean until the first layer in which the halo deposition of the two following layers exceed 3 MIP each.

The efficiency of reconstructing a *clean primary track* of a given length from a simulated sample of single muon events is shown in Figure 4.12. Ideally all single muon tracks would be classified as clean primary tracks of length 30, however, for each layer there is a chance of around 1 % to be misreconstructed as the last clean layer. This is mostly due to delta electrons from muon interactions, generating small local electromagnetic showers which cause significant spikes in the local energy deposition.

In the TCMT a conceptually similar track reconstruction as in the ScECAL is applied. However, the algorithm simplifies considerably due to all horizontal strips in the TCMT

overlapping with all vertical strips. A TCMT track is identified as the strip overlap region with the highest number of hits in the event.

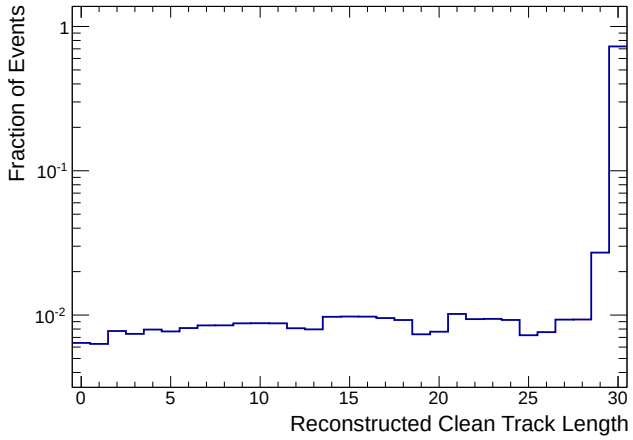

Figure 4.12.: *Distribution of reconstructed clean track lengths for a simulated sample of single 32 GeV muons evenly distributed over the ScECAL cross section area. In each layer around 1 % of the events are mistakenly tagged* unclean, *leading to around 75 % of the events being reconstructed as clean tracks with the full ScECAL length.*

4.5. Event Selection

In order to perform the analyses described later in this chapter, the ability to efficiently select events containing a single particle of the right particle type from the recorded beam data sample is essential. As is shown in Figure 4.1, beam runs recorded in the MTest beamline typically yield a mixture of particle types, often containing event contaminations of additional particles. Utilising the beamline instrumentation both in the online selection of recorded events as well as in the offline selection yields a substantially cleaned event sample. However there are still significant fractions of events of the wrong particle type left.

The event selection can thus be further improved by utilising the shower topology information available due to the high granularity of the combined calorimeter system. Representative examples of event displays for a simulated muon, electron and pion are given in Figure 4.13. Muons typically deposit long straight track signatures with only around one hit per calorimeter layer. Electrons produce dense showers, which are mostly contained within the ScECAL. Pions deposit MIP-like tracks until their first hadronic interaction, after which a shower extends through the whole calorimeter system.

This section describes the criteria applied to select single MIPs, electrons and pions out of the recorded data events, including a discussion of the selection efficiencies and an estimation of the selection bias on the reconstructed response and resolution for pions. Apart from information only available from the testbeam setup (Cherenkov triggers, multi particle trigger) all selections are applied identically on data and simulated runs.

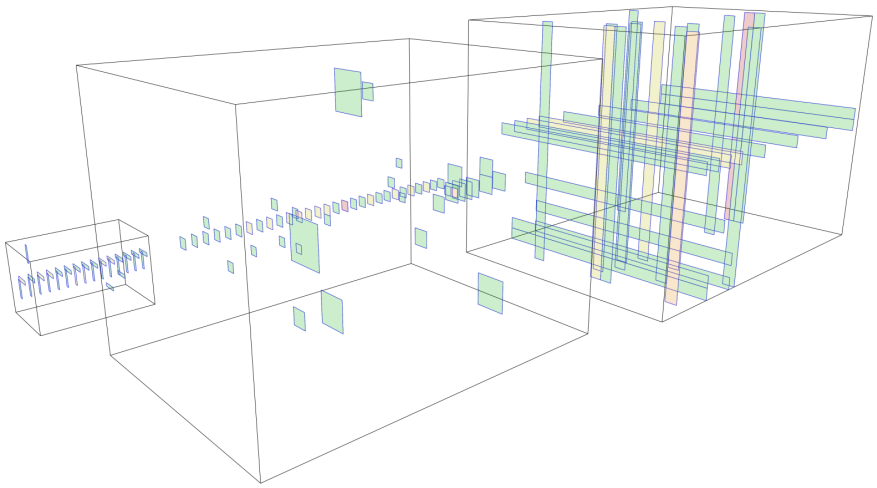

(a) 32 GeV μ^-

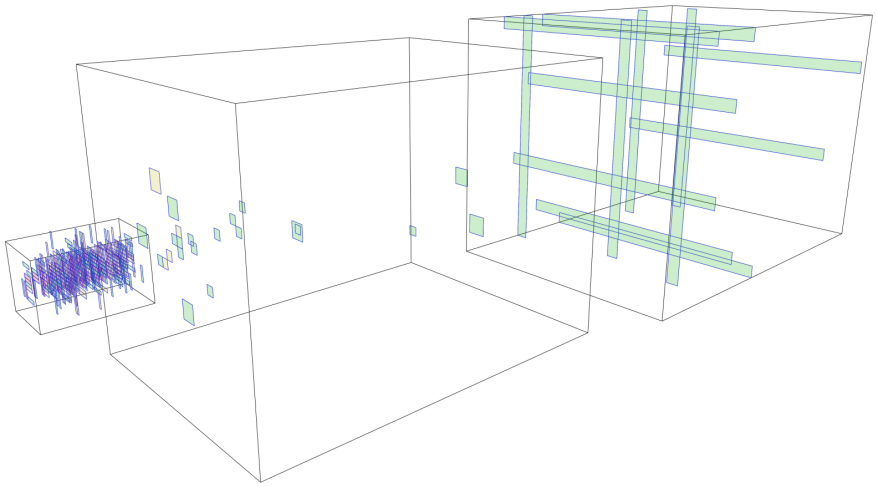

(b) 32 GeV e^-

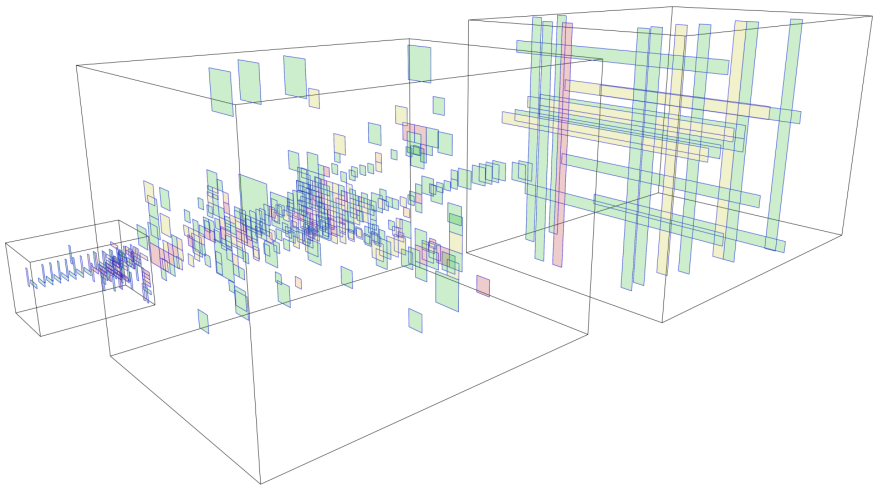

(c) 32 GeV π^-

Figure 4.13.: *Exemplary simulated event displays for a muon, electron and pion of 32 GeV each in the CALICE combined scintillator-SiPM calorimeter system. The simulation is fully digitised and thus includes noise hits overlaid from real data pedestal events, visible as isolated hit cells in the detectors.*

4.5.1. MIP Selection

The selection of hits on MIP tracks is essential to obtain and crosscheck MIP calibration factors for single cells of the calorimeter system. As such, the selection is designed to first preselect events consistent with a single MIP-like particle traversing the full detector. In a second step, the generated track is reconstructed and all hits which are part of the MIP track identified.

The MIP event pre-selections are independent for the ScECAL, AHCAL and TCMT. The MIP-like track deposited by a charged pion punching through the whole ScECAL without hadronic interaction can be used for MIP calibration crosschecks independent of whether it initiates a hadron shower in the AHCAL or not. Similarly, the continuation of an identified ScECAL muon track might not be suitable for MIP calibration in the AHCAL due to additional particles entering the AHCAL outside of the geometric ScECAL coverage. Due to the large beam spot size of the FTBF muon beam, most of the muons seen in the AHCAL are not traversing the ScECAL first.

The preselection is based on the energy weighted center of gravity along the Z-axis cog_Z and the number of hits n_{hits}. A MIP track traversing a whole subdetector should deposit roughly the same energy in each layer, and thus yield cog_Z close to the subdetector center in the Z-coordinate. The number of hits of a single MIP track event should be around one hit per layer plus the mean number of noise hits expected per event for the respective subdetector.

The ScECAL and AHCAL distributions in the cog_Z:n_{hits} plane obtained for simulated 32 GeV muons, electrons and pions, as well as the applied event preselection cut are shown in Figure 4.14. The preselection efficiency in the ScECAL is 92 % for muons, <0.1 % for electrons and 37 % for pions. The pion efficiency is well compatible with the fraction of pions traversing the ScECAL without hadronic interaction, as shown in Figure 4.41. The preselection efficiency in the AHCAL is 88 % for muons, <0.1 % for electrons and 1.2 % for pions. All efficiencies are reasonably constant over the beam energy range relevant for this analysis, except for the pion selection efficiency in the AHCAL, which increases from the given 1.2 % at 32 GeV to 10 % in 4 GeV events.

The selection of hits on MIP tracks is based on the track reconstructions described in subsection 4.4.3. In the ScECAL all hits reconstructed on a *simple track* with length ≥14 are selected as MIP hits. The ScECAL simple track definition is sufficient here, as the preselection effectively suppresses all events containing significant showers. In the AHCAL, hits on reconstructed track segments with length >10 and $\cos\phi > 0.99$ are selected as MIP hits. In the TCMT only tracks of length ≥12 are used as MIP tracks.

A detailed overview of the applied cuts is given in Table C.1, Table C.2 and Table C.3 in the Appendix.

4.5.2. Pion Selection

The analysis of pion showers in the combined calorimeter is the most important aspect of this analysis. In order to minimise the influence of beam contaminations on the results, the applied pion event selection needs to efficiently extract events containing a single pion shower in the detector system from the recorded data sets. To determine the intrinsic resolution of single pion showers in the calorimeter system, the applied event selection must

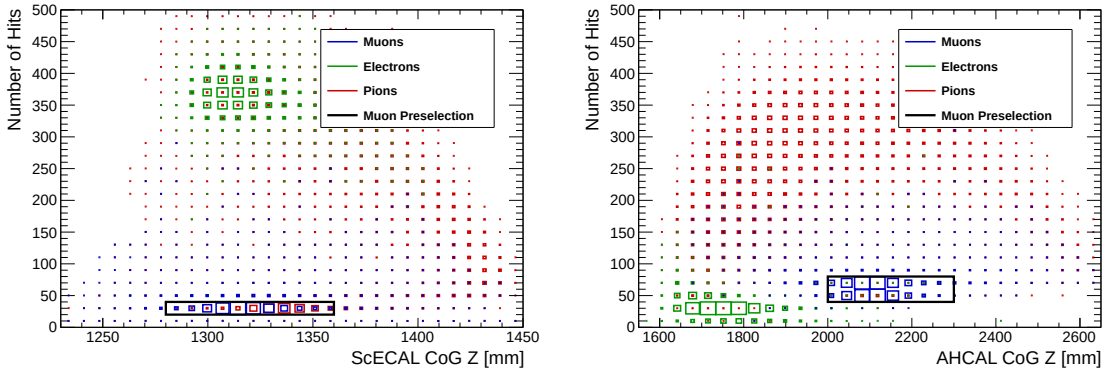

(a) *ScECAL* **(b)** *AHCAL*

Figure 4.14.: *Distribution of event frequencies in the cog_Z:n_{hits} plane for 32 GeV muons, electrons and pions including the applied MIP preselection. Simulated with QGSP_BERT_HP in GEANT4 10.1p2.*

not bias the composition of selected pion showers (e.g. electromagnetic fraction), while ensuring a high shower containment on average.

A preselection yields *Raw* events by requiring hit beam triggers to exclude pedestal and gain calibration events from the analysis. The first selection step evaluates information from the DAQ and external beam instrumentation, differential Cherenkov counters, the multi-particle counter and other trigger scintillators and excludes empty events (*Event Quality*).

The cut on the multi-particle counter amplitude is set to accept events within 2000 ADC to 3800 ADC according to [84], as shown in Figure 4.15. The selection range corresponds to around 0.4 MIP to 1.4 MIP, rejecting around 20 % of all data events.

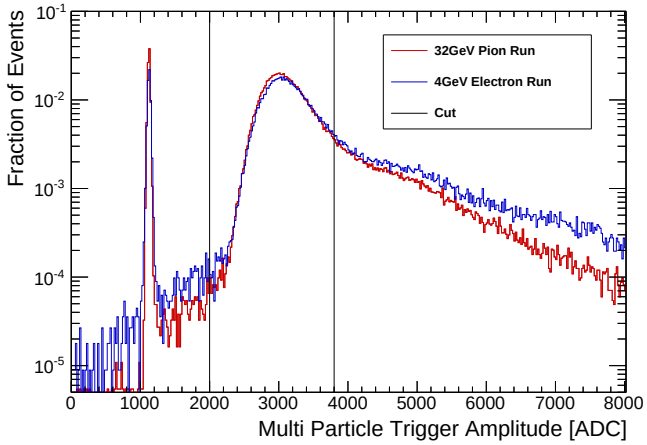

Figure 4.15.: *Measured multi-particle counter ADC spectra for an exemplary 4 GeV electron run and 32 GeV pion run. The sharp peak around 1200 ADC is the pedestal of the readout system. The long tail towards high amplitude hits corresponds to multi-particle events.*

As discussed in section 4.2, the Cherenkov pressure is configured such that C1 tags pions and C2 tags electrons of the given beam energy in runs with beam energy >4 GeV. C1 is typically included into the online trigger decision of pion runs and thus does not yield any further information in the offline selection. The electron tag C2 could be used to reduce the electron contamination of the event sample, however it also rejects pions with an inefficiency of around 50 % (up to 85 % in the 15 GeV pion run). As the electron suppression from the following pion selection is excellent, no offline selection on the Cherenkov information is performed for beam energies >4 GeV. For the 4 GeV beam energy run, both Cherenkov channels C1 and C2 are required to not have triggered to pass the event quality selection.

The *Pion Selection* step is performed to suppress electron and muon events in the sample. Single muons and punch-through pions are suppressed by rejecting events based on the muon selection discussed in the previous section. Electrons are suppressed by requiring the reconstructed layer of first hadronic interaction (FHI layer) (see subsection 4.4.2) to be $\geq$5, which also removes events that have started showering upstream of the calorimeters by effectively using the first four ScECAL layers as an integrated pre-shower detector. The distributions of reconstructed FHI layers for electrons and pions at beam energies 4 GeV and 32 GeV, as well as their selection efficiencies as a function of the FHI layer cut are shown in Figure 4.16. The efficiency of the FHI based pion selection is 89 % for pions and 0.4 % for

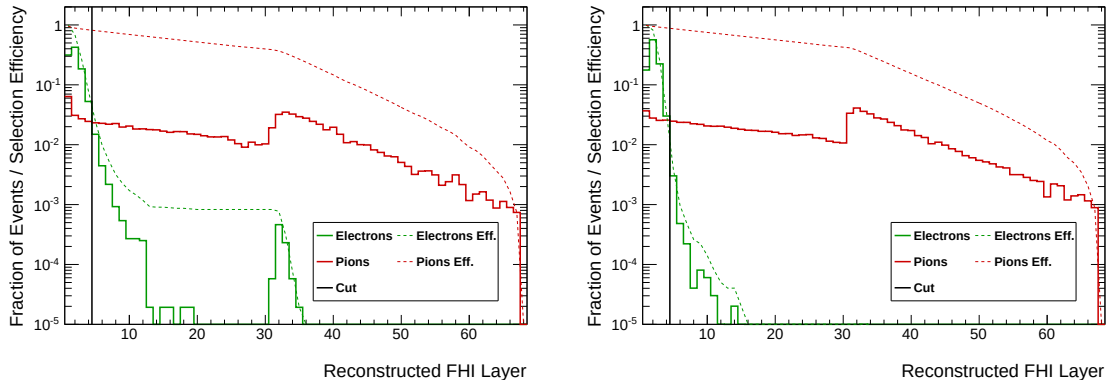

(a) 4 GeV **(b)** 32 GeV

Figure 4.16.: *Reconstructed first hadronic interaction layer for electrons and pions at 4 GeV and 32 GeV, as well as their selection efficiencies for a cut FHI >X. The events with FHI layer around 30 to 35 in the 4 GeV simulation correspond to electrons which were scattered between the simulated beam trigger and the ScECAL front face, hitting the AHCAL directly. Simulated with QGSP_BERT_HP in GEANT4 10.1p2.*

electrons at 32 GeV beam energy. In 4 GeV simulations, the selection efficiency for pions is 94 % and 2.5 % for electrons. The bias introduced by the cut on the reconstructed FHI layer is described later in this section.

Manual inspection of event displays of the highest few percent of reconstructed energy events per run is helpful to understand the characteristics of potentially remaining multi-particle contamination events after the event quality selection. Two close-up examples of such event displays are given in Figure 4.17. Figure 4.17(a) shows two pions (or a pion and a muon) traversing the ScECAL and generating at least one particle shower in the

AHCAL. Figure 4.17(b) shows a shower in the ScECAL, extending into the AHCAL with an additional muon track in the AHCAL, just outside of the geometric ScECAL acceptance.

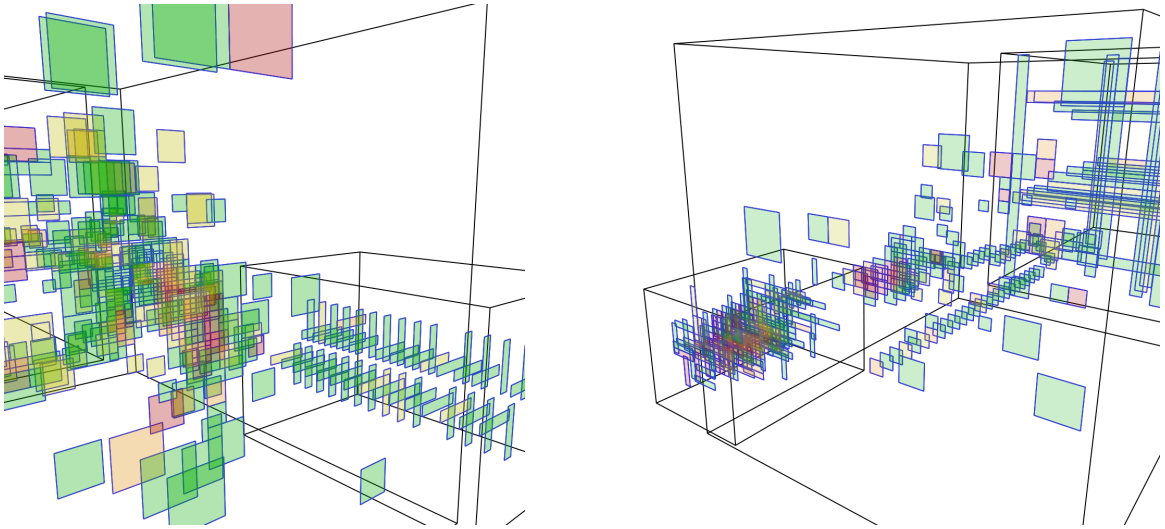

(a) *Two pions traversing the ScECAL and showering in the AHCAL.*

(b) *Shower in the ScECAL extending into the AHCAL. Additional muon in the AHCAL extending through to the TCMT.*

Figure 4.17.: *Event displays with at least two primary particles in the calorimeter system. Taken from run 560498 (12 GeV π^-) before multi particle suppression cuts.*

The suppression of events with multiple primary particles in the detector is achieved by reconstructing the primary MIP-like track a pion is depositing in the ScECAL before its first hard interaction. Since the previous selection step requires a reconstructed FHI layer $\geq$5, a *clean primary track* (as defined in subsection 4.4.3) should be reconstructable in each single pion event. Events with an additional spatially separated pion or muon in the ScECAL should yield two reconstructed clean primary tracks and can thus be identified. Events with an additional electron in the ScECAL should give a reconstructed FHI layer $<$5 due to the electron and thus be excluded already in the previous step. The inefficiencies in reconstructing full length *isolated primary tracks* are no issue in the pion selection, since only a track segment of minimum length is required.

The distribution of number of reconstructed clean primary tracks in data and simulation is shown in Figure 4.18. Across the whole beam energy range, $\geq$90 % of simulated pion events yield one reconstructed clean primary track. All examined simulation physics lists agree in their predictions within statistic uncertainties. An excess of data over simulation in the zero reconstructed clean primary track bin would point towards a contamination with electrons. An excess of data over simulation in the number of reconstructed clean primary track bins two and higher would point towards contaminations with one or more pions or muons.

A clear excess of data in the bins of zero and two reconstructed clean primary tracks is seen at energies $>$4 GeV. The 4 GeV data show an excess only in the zero tracks bin. Thus only events with exactly one reconstructed clean primary track are selected.

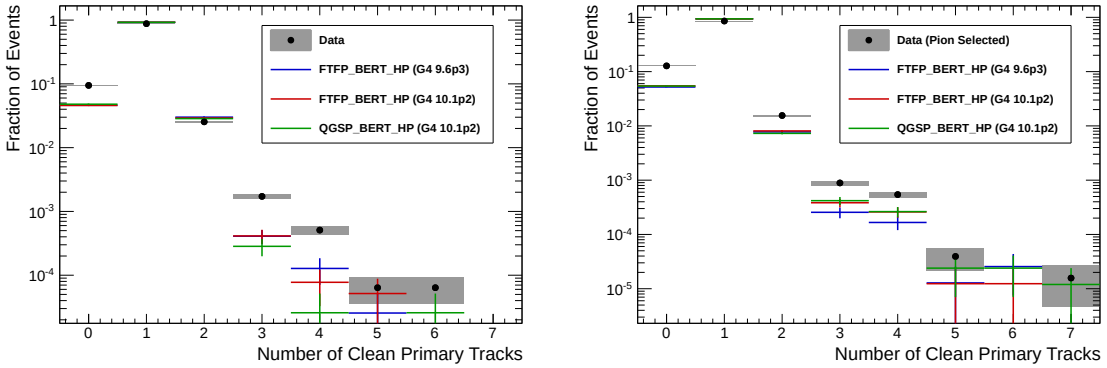

(a) *4 GeV* **(b)** *32 GeV*

Figure 4.18.: *Number of reconstructed clean primary tracks in data and simulations.*

Due to the much wider beam profile of muons compared to the primary beam, additional muons can be distributed across the whole AHCAL front face. Such events should be suppressed by the beam halo veto scintillator, which is however found to be largely inefficient [34]. To suppress such events with additional muons entering the AHCAL outside of the coverage of the ScECAL and multi particle counter, all events with tracks parallel to the beam axis longer than five layers in the outer parts of the AHCAL are rejected. Events with additional electrons or showering pions entering the AHCAL outside of the ScECAL coverage are not reliably suppressed by this selection. However, the primary beam profile on the ScECAL front face is typically narrow, making additional primary particles that pass by the ScECAL and hit the AHCAL directly unlikely.

The combination of the cut on the number of clean primary tracks in the ScECAL and beam-parallel tracks in the AHCAL is referred to as *Multi particle suppression*. Apart from inefficiencies in the reconstructions used to select single particle events, exactly overlapping particles cannot be disentangled by the methods described here. However, manual inspection of the event displays in the highest few percent of reconstructed energy per run did not show any more events with visually identifiable multi-particle content. An estimation and further discussion of the remaining contaminations is given in subsection 4.5.4.

Finally, to select for showers that are reasonably well contained laterally and longitudinally, only events with the primary pion track around the center of the ScECAL and reconstructed FHI layer at the latest in the fifth layer of the AHCAL are accepted into the analysis (*Containment*), consistent with previous AHCAL + TCMT analyses [88].

A detailed table of cuts performed is given in Table C.5 in the Appendix. An example of the full step-by-step event selection in data and simulation is shown in Figure 4.19. The event quality preselection excludes most of the obvious beam contamination events at reconstructed energies above the clearly visible single pion peak. The contaminations are significantly suppressed further by the applied multi particle selection. The containment selection reduces the tail to lower reconstructed energies due to longitudinal and, to a lesser extent, transverse shower energy leakage.

Applying the event selection to simulated events does not visibly distort the reconstructed energy spectrum, except for a similar reduction of the leakage tail as in data. The few events around double the reconstructed beam energy originate from the noise overlay, in which at least one event containing a pion shower (of the same energy as the simulated beam energy, as the overlaid noise events are extracted from the respective data run) seems to have passed the pedestal event selection. Out of the around ten events before the selection, only one event remains after the multi particle selection. This indicates (at limited significance due to the low statistics) the performance of the event-topology based multi particle suppression.

A detailed list of selection efficiencies of the pion selection is given in Table 4.3. 45 % to 50 % of simulated pion events pass the pion selection across all examined physics lists. Most of the excluded pion events are rejected by the FHI layer requirements for electron suppression and shower containment. From the selection requirements of FHI layer and isolated primary track an excellent electron suppression of $\gtrsim$ 99.9% is achieved. The selection efficiencies for the multi particle suppression $\frac{\epsilon_{\text{mult}}}{\epsilon_{\pi\text{Sel}}}$ are around 90 % (4 GeV) to 80 % (32 GeV) on simulated events, similar between the used physics lists. In data the efficiency for the same selection varies from around 80 % (4 GeV) to 70 % (32 GeV), indicating around 10 % remaining multi particle contamination in data before the selection.

Possible biases by the event selection on the reconstructed response and resolution of the calorimeter system are studied from simulated event samples. This is done both for a minimal selection (*FHI*) and the full pion selection (*sel.*). The minimal selection contains the lower and upper cuts on FHI layer to roughly preserve sampling fractions and average containment between the selections. By applying the minimal selection, an inherent bias is introduced compared to using the full set of simulated events. The cut on maximum reconstructed FHI layer does not influence the shower composition and only effects the mean shower containment. The lower FHI layer cut is needed to suppress electrons in the data event sample and effectively removes the first four layers of the ScECAL from the fiducial shower volume. The resolutions obtained with this pion event selection are thus the intrinsic resolutions of a combined calorimeter system consisting of an effectively 26 layer deep ScECAL, the AHCAL and the TCMT.

The biases on single pion response and resolution, as given in Table 4.4, are $\lesssim$ 1% for all examined beam energies and physics lists.

The pion selection described in this section selects single, contained pion showers without significantly biasing the extracted intrinsic energy resolution with an event efficiency of around 50 %. An estimation of the remaining contaminations and their systematic influence on the extracted results is given in subsection 4.5.4.

4.5.3. Electron Selection

The electron selection aims to extract a sample of single electrons in the calorimeter system. Such events are needed to compare electromagnetic shower observables in data and simulation in order to validate the ScECAL simulation model.

Similar to the pion selection, an *Event Quality* preselection is performed on data, utilising the beam instrumentation. Only events in which the electron-tag Cherenkov channel C2 has triggered, while no signal was measured in the pion tag C1, are used in the electron analyses. The *Electron Selection* rejects events based on their reconstructed FHI layer and

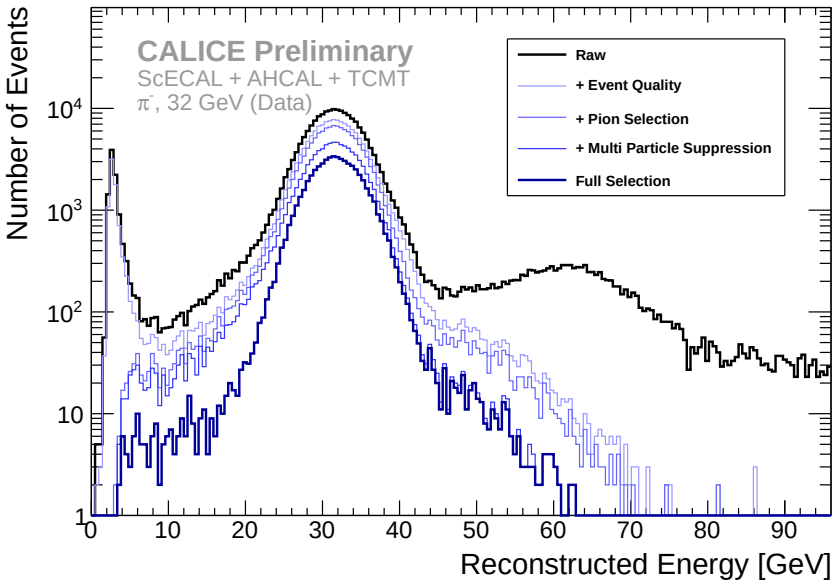

(a) *Data [108]*

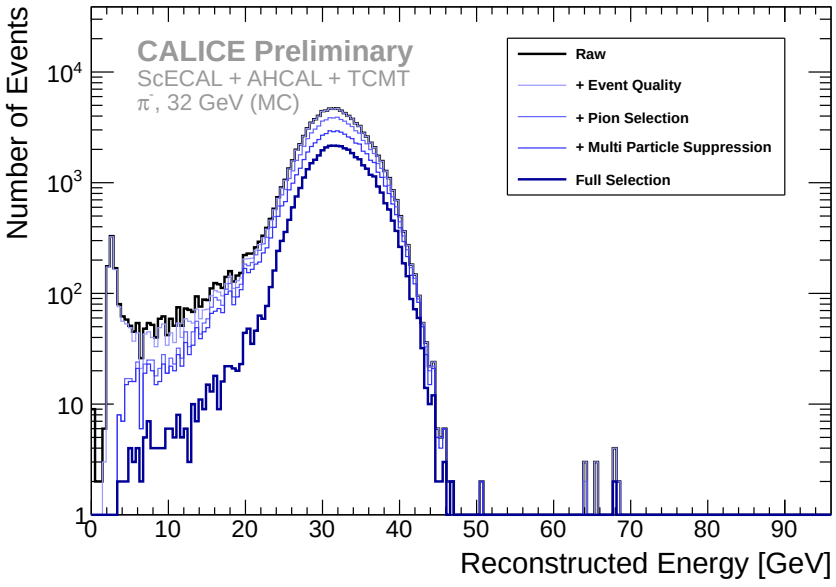

(b) *FTFP_BERT_HP (G4 10.1p2) [108]*

Figure 4.19.: *Reconstructed energy spectrum (using the standard energy reconstruction as described in section 4.7) of run 560474 (32 GeV π^-) in data and simulation for different steps of the applied event selection. Plots of all other beam energies are given in section D of the Appendix.*

Table 4.3.: *Stepwise selection efficiencies of the single pion selection for data and different simulation physics lists and particle types. The event quality efficiency ϵ_{evQ} is normalised to the number of remaining events after the raw cut. Efficiencies marked with † are normalised to the number of remaining events after the event quality cut to enable comparison of data and simulation results and are given as cumulative fractions of events passing the selections up to the currently shown step. The raw preselection efficiency of the 4 GeV simulations is low, as the simulated beam profile is wider than the ScECAL geometry, see Table 4.1. All simulations are generated with GEANT 4 10.1p2 except lines marked with $^{(*)}$, which are GEANT 4 9.6p3.*

Run/Energy		Type	$\frac{n_{\text{raw}}}{n_{\text{evts}}}$ [%]	ϵ_{evQ} [%]	$\epsilon_{\pi\text{Sel}}{}^{\dagger}$ [%]	$\epsilon_{\text{mult}}{}^{\dagger}$ [%]	$\epsilon_{\text{cont}}{}^{\dagger}$ [%]	$\frac{n_{\text{sel}}}{n_{\text{raw}}}$ [%]
560506 (4 GeV)	π^-	Data	87.1	66.9	66.4	52.8	38.5	25.8
	π^-	FTFP_BERT_HP	54.0	96.9	74.0	66.7	47.5	46.1
	π^-	FTFP_BERT_HP$^{(*)}$	54.2	96.7	74.7	67.3	48.1	46.5
	π^-	QGSP_BERT_HP	54.0	96.9	74.1	66.6	47.4	45.9
	e^-	QGSP_BERT	51.9	99.9	2.4	0.3	0.2	0.2
560498 (12 GeV)	π^-	Data	91.1	70.2	80.3	61.3	43.8	30.8
	π^-	FTFP_BERT_HP	97.7	98.0	82.4	70.7	50.5	49.5
	π^-	FTFP_BERT_HP$^{(*)}$	97.8	97.9	83.1	71.0	50.7	49.6
	π^-	QGSP_BERT_HP	97.8	98.0	82.4	70.8	50.4	49.4
	e^-	QGSP_BERT	96.7	100.0	1.7	< 0.1	< 0.1	< 0.1
560496 (15 GeV)	π^-	Data	90.3	70.8	81.2	60.9	43.4	30.7
	π^-	FTFP_BERT_HP	94.2	98.2	82.8	70.2	49.7	48.8
	π^-	FTFP_BERT_HP$^{(*)}$	94.2	98.2	83.5	70.2	50.0	49.1
	π^-	QGSP_BERT_HP	94.2	98.2	83.5	70.8	50.1	49.2
	e^-	QGSP_BERT	93.0	100.0	1.2	< 0.1	< 0.1	< 0.1
560481 (20 GeV)	π^-	Data	91.1	73.0	80.4	57.8	41.0	29.9
	π^-	FTFP_BERT_HP	98.6	98.6	83.0	68.6	48.2	47.5
	π^-	FTFP_BERT_HP$^{(*)}$	98.6	98.4	83.6	68.8	48.3	47.6
	π^-	QGSP_BERT_HP	98.6	98.5	84.8	69.6	48.7	48.0
	e^-	QGSP_BERT	98.3	100.0	0.8	< 0.1	< 0.1	< 0.1
560474 (32 GeV)	π^-	Data	90.7	72.9	80.8	55.2	38.5	28.0
	π^-	FTFP_BERT_HP	99.5	99.0	83.1	64.7	44.8	44.3
	π^-	FTFP_BERT_HP$^{(*)}$	99.5	98.8	83.7	64.9	44.8	44.3
	π^-	QGSP_BERT_HP	99.5	98.9	85.4	66.3	45.5	45.0
	e^-	QGSP_BERT	99.4	100.0	0.4	< 0.1	< 0.1	< 0.1

Table 4.4.: *Biases on the response and resolution for a minimal selection and the full pion selection for different physics list and particle types. The* FHI *sample is selected for scintillator trigger and FHI layer cuts only,* sel. *contains the full pion selection. Statistical errors on fit are negligibly small and thus not quoted. The biases on the response* $\delta_\mu = \left|1 - \frac{\mu_{FHI}}{\mu_{sel.}}\right|$ *and resolution* $\delta_{\sigma/\mu} = \left|1 - \frac{\sigma_{FHI}/\mu_{FHI}}{\sigma_{sel.}/\mu_{sel.}}\right|$ *are given as well. All simulations are done with GEANT 4 10.1p2 except lines marked with* $^{(*)}$*, which are GEANT 4 9.6p3.*

Run/Energy		Type	μ_{FHI} [GeV]	$\sigma_{\text{FHI}}/\mu_{\text{FHI}}$ [%]	$\mu_{\text{sel.}}$ [GeV]	$\sigma_{\text{sel.}}/\mu_{\text{sel.}}$ [%]	δ_μ [%]	$\delta_{\sigma/\mu}$ [%]
560506 (4 GeV)	π^-	FTFP_BERT_HP	3.82	22.92	3.83	22.86	0.3	0.3
	π^-	FTFP_BERT_HP$^{(*)}$	3.81	22.64	3.82	22.59	0.3	0.2
	π^-	QGSP_BERT_HP	3.80	22.95	3.81	22.87	0.3	0.3
560498 (12 GeV)	π^-	FTFP_BERT_HP	11.62	15.49	11.67	15.37	0.4	0.8
	π^-	FTFP_BERT_HP$^{(*)}$	11.68	14.73	11.71	14.65	0.3	0.5
	π^-	QGSP_BERT_HP	11.54	15.54	11.59	15.45	0.4	0.6
560496 (15 GeV)	π^-	FTFP_BERT_HP	14.64	14.43	14.70	14.30	0.4	0.9
	π^-	FTFP_BERT_HP$^{(*)}$	14.69	13.59	14.74	13.49	0.3	0.7
	π^-	QGSP_BERT_HP	14.66	14.30	14.71	14.20	0.3	0.7
560481 (20 GeV)	π^-	FTFP_BERT_HP	19.69	13.25	19.78	13.19	0.5	0.5
	π^-	FTFP_BERT_HP$^{(*)}$	19.70	12.35	19.77	12.28	0.4	0.6
	π^-	QGSP_BERT_HP	19.78	12.74	19.86	12.66	0.4	0.6
560474 (32 GeV)	π^-	FTFP_BERT_HP	31.97	11.59	32.15	11.58	0.6	0.1
	π^-	FTFP_BERT_HP$^{(*)}$	31.97	10.66	32.12	10.60	0.5	0.6
	π^-	QGSP_BERT_HP	31.92	10.96	32.08	10.82	0.5	1.3

measured shower containment in the ScECAL. The ScECAL shower energy containment $f_c = \frac{E_{\text{sum}}^{\text{ScECAL}}}{E_{\text{sum}}^{\text{ScECAL}} + E_{\text{sum}}^{\text{AHCAL}}}$ characterises the fraction of total event energy deposited in the ScECAL. As electrons are expected to be mostly contained in the ScECAL, electron events should cluster around large values of f_c. Most pion showers extend into the AHCAL and thus result in lower values of f_c. The event frequency distributions in the FHI : f_c plane for simulated electrons, pions and muons with the cuts performed to select electrons is given in Figure 4.20.

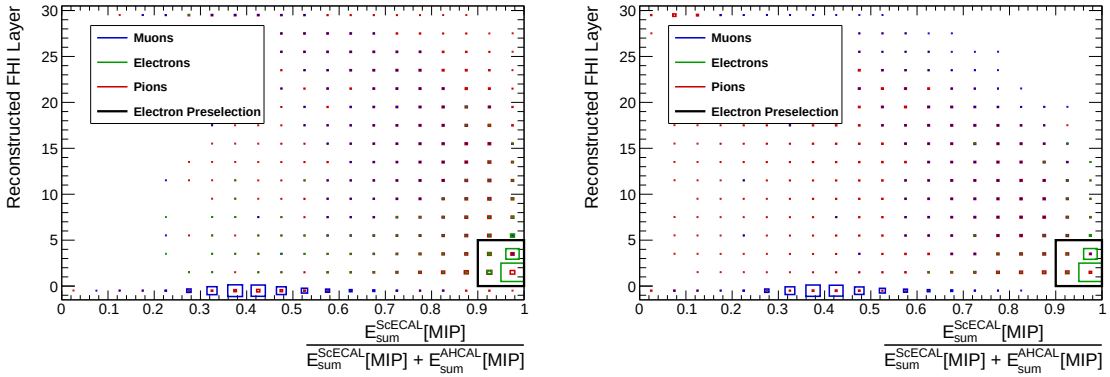

(a) *4 GeV* **(b)** *32 GeV*

Figure 4.20.: *Distribution of event frequencies in the FHI: $\frac{E_{sum}^{ScECAL}}{E_{sum}^{ScECAL} + E_{sum}^{AHCAL}}$ plane for 4 GeV and 32 GeV electrons, pions and muons, including the applied electron selection. Events with FHI layer <1 do not have a reconstructed FHI layer. Simulated with QGSP_BERT_HP in GEANT4 10.1p2.*

The selection efficiency at 4 GeV beam energy is 96 % for electrons, 7.3 % for pions and <0.1 % for muons. For 32 GeV runs the efficiencies are 99 % for electrons, 3.6 % for pions and <0.1 % for muons.

The *Multi Particle Suppression* rejects events with additional particles entering the ScECAL, utilising the same reconstruction of clean primary tracks as used in the pion selection. Only events with no reconstructed clean primary tracks pass the multi particle selection. To suppress electron events with one or more additional muons traversing the ScECAL, all events are required to not yield any reconstructed tracks in the AHCAL.

The transverse shower leakage is minimised by requiring the hit energy weighted ScECAL shower center of gravity in X and Y coordinates to be within the central quarter of the ScECAL.

A detailed table of cuts performed is given in Table C.4 in the Appendix. The selection efficiency of the full electron selection on simulated single electron events varies between around 95 % at 4 GeV to around 85 % at 32 GeV. Two examples of the full step-by-step event selection on data are shown in Figure 4.21.

The electron selection described here yields clean single particle event samples across the whole examined energy range. The purity of the selected electron sample is improved significantly over the ScECAL electron selection described in [81], as is visible from comparing the spectra in ScECAL energy sum for both selections as shown in Figure 4.22. The electron selection is thus considered adequate for the purpose of electron analyses in this thesis.

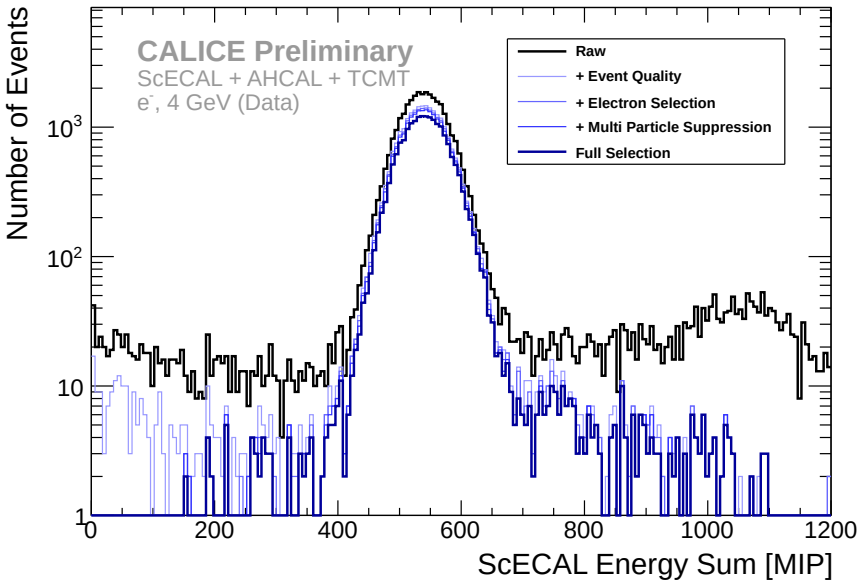

(a) *4 GeV [108]*

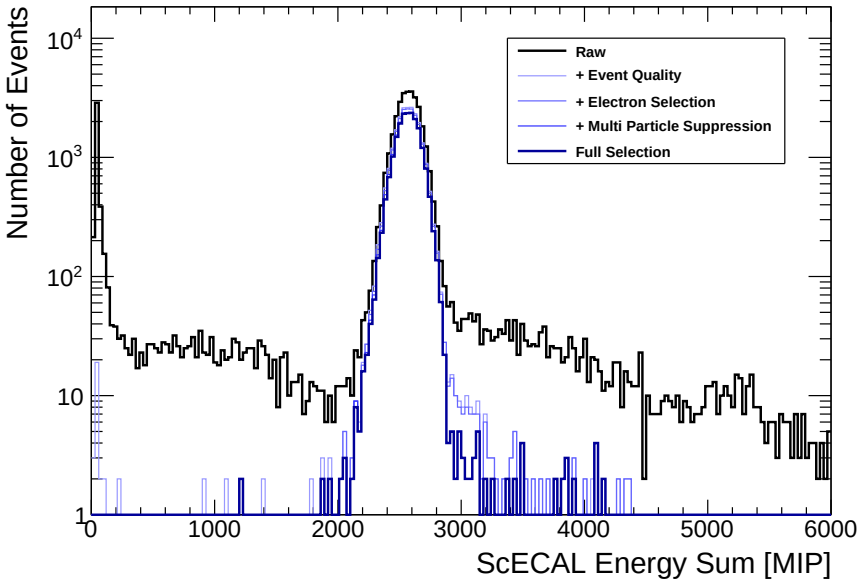

(b) *32 GeV*

Figure 4.21.: *Reconstructed energy spectrum of data runs 560332 (4 GeV e^-) and 560284 (20 GeV e^-) for different steps of the applied electron event selection.*

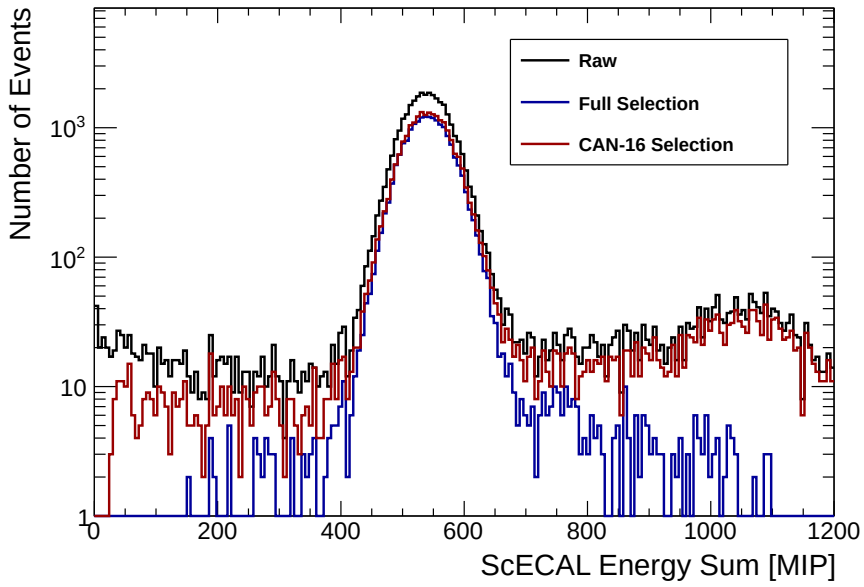

Figure 4.22.: *Comparison of the full electron selection presented here and the electron selection described in [81] for a 4 GeV electron data run.*

4.5.4. Pion Event Contaminations

After the selection of pion events from data as explained in the previous section, small fractions of contaminations are still left in the dataset. This section explains the methods used to quantify the electron and proton contamination of the selected pion sample as well as a general estimation of remaining beam impurities.

Electron Contamination

To estimate the remaining fraction of electrons in data events passing the pion selection, the distribution of the energy fraction reconstructed in the ScECAL $f = \frac{E_{\text{rec}}^{\text{ScECAL}}}{E_{\text{rec}}}$, using the standard energy reconstruction as discussed in subsection 4.7.1, is fitted with a linear combination of templates extracted from electrons and pions in simulation. Electron showers are typically fully contained in the ScECAL and thus result in f values around unity. Pions that start showering in the AHCAL deposit only little energy in the ScECAL and thus tend to cluster at low f, which pions which start showering in the ScECAL can generate values of f in the full range of 0 to 1.

The template distribution for pions is extracted from simulated events passing the pion event selection. The template distribution for electrons ideally would be obtained in the same way, however due to the requirements on minimum reconstructed FHI layer and a reconstructed isolated primary track of the pion selection, leading to a strong electron suppression $\geq$99.8 % (see Table 4.3), the statistics in the electron template would be very small even when using large simulation statistics. As electron showers that deposit very few energy in the first 5 layers of the ScECAL are nevertheless expected to be contained

within its volume, events merely passing the event quality pre-selection are used to generate the electron template. This makes most of the simulated electron events usable in the template but could possibly bias its shape. A comparison of the ScECAL energy fraction distributions of 4 GeV electrons passing the full pion selection and the event quality pre-selection is shown in Figure 4.23. Both distributions agree with each other within statistical uncertainties, supporting the use of the event quality pre-selected electron events for the electron template.

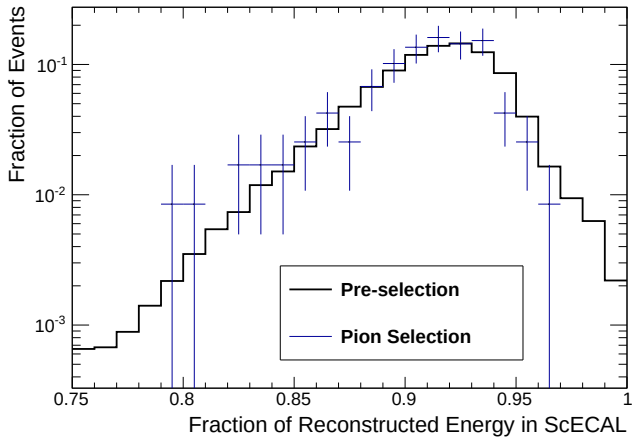

Figure 4.23.: *Comparison of the reconstructed energy fraction in the ScECAL for 4 GeV electrons for simulated events passing the full single pion selection and the event quality pre-selection. Both distributions agree within their statistical uncertainties.*

Due to even lower remaining statistics, this distribution shape comparison is not possible for higher beam energies than 4 GeV. But as the fraction of electrons in the beam generally reduces with beam energy (see Figure 4.1) and the electron suppression of the pion selection improves with beam energy (see Table 4.3), the electron contamination at high beam energies is expected to be very small anyhow, so a precise estimation of the contamination is not as important.

The data distribution, electron template and pion template are all normalised to unity. The fit is a linear combination of the two template distributions

$$f_i^{\text{fit}} = a \times f_i^{\text{e}} + (1 - a) \times f_i^{\pi} \tag{4.8}$$

with the unconstrained free parameter a representing the fitted pion fraction, the bin number i and the template distributions of electrons f^{e} and pions f^{π}, respectively.

Examples of the data distribution, the fit result and its underlying template distributions are shown in Figure 4.24. Even after accounting for the remaining electron contamination, the fitted distribution does not perfectly describe the data, although the description is improved over the pure pion case. This is possibly related to imperfect modelling of hadronic showers in the simulation or further remaining beam contaminations beyond electrons, such as multi-particle events.

The resulting fitted electron contamination of the data pion runs used in this analysis are 2.3 % at 4 GeV, 0.2 % at 12 GeV and $\leq$0.1 % for all beam energies $\geq$15 GeV. All fits result in

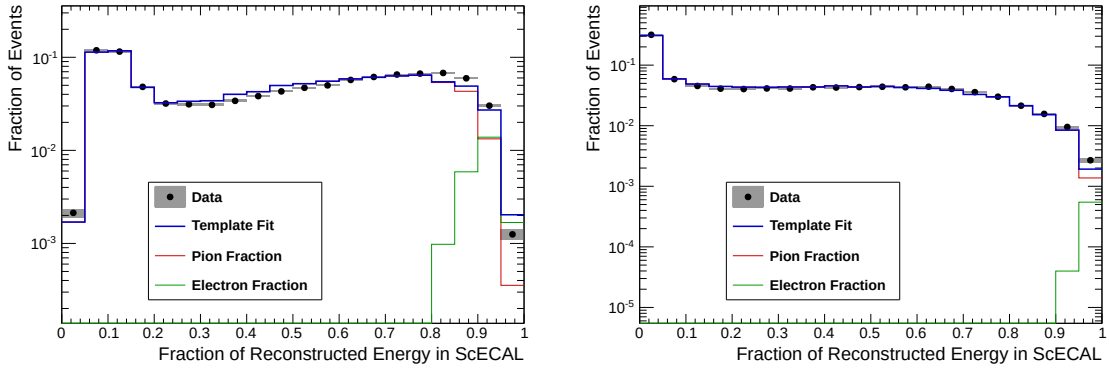

(a) 4 GeV **(b)** 20 GeV

Figure 4.24.: *Distribution of the standard reconstructed energy fraction in the ScECAL in data. The fit is performed as a linear combination of templates for pions and electrons, extracted from simulations using Geant 4 10.1p2 with QGSP_BERT_HP. The binning used for fitting is five times finer than shown in the plot.*

a <1 without any parameter constraints. These results are to be interpreted as upper limits on the single electron contamination fraction, as other possible beam contaminations are not accounted for in the fit.

Proton Contamination

The proton contamination in the beam runs used for this analysis is expected to be small, as exclusively negative beam polarity pion runs were recorded. Only antiprotons, which are expected to be produced very rarely, could possibly contaminate the beam.

The (anti-)proton contamination of the data samples can be estimated from the fitted slope of the reconstructed FHI layer spectrum in the AHCAL separately. This is due to the nuclear interaction length λ_n being smaller than the pion interaction length λ_π and thus protons generating steeper FHI layer spectra compared to pions. As the FHI layer spectra are well described in simulations, see Figure 4.41, the FHI slopes from data can be compared to FHI slopes from pion and proton simulations.

The events used to estimate the proton contamination are selected using the pion selection excluding the containment cut to obtain reconstructed FHI spectra extending up to the last layer of the AHCAL. The resulting reconstructed FHI layer spectrum is fitted in the range of AHCAL layers 3 to 30 with an exponential function of the form $f(x) = a \times e^{-\frac{x}{\tau}}$ with the free parameter decay constant τ and the normalisation nuisance parameter a. The first AHCAL layers are omitted due to increased uncertainties and inefficiencies in the FHI reconstruction around the transition region between ScECAL and AHCAL. The last eight AHCAL layers are excluded due to possible systematic effects of the FHI reconstruction from the different granularity in these layers. The fitted parameter τ can then be compared between data and both pion and proton simulations. This method is insensitive to possible additional electron contamination, as the very most electron showers will result in a reconstructed FHI layer in the first layers of the ScECAL.

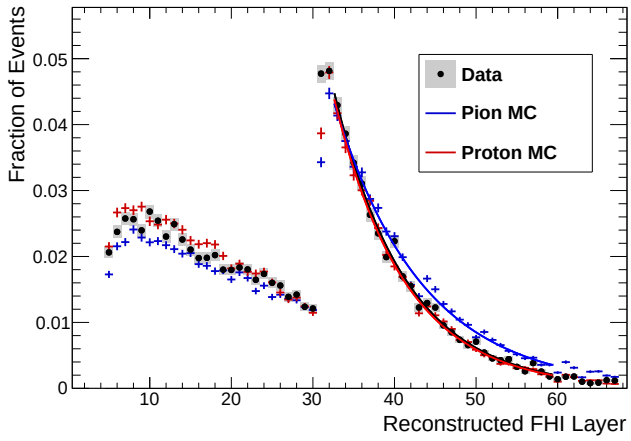

Figure 4.25.: *Comparison of the reconstructed first hadronic interaction layer for a run of positive polarity and unknown beam composition at 60 GeV beam energy compared to simulated runs with pions and anti-protons including exponential fits to the AHCAL part of the spectrum. Simulations done with Geant 4 10.1p2 using QGSP_BERT_HP*

As a benchmark of this method, the fit is performed on a positive polarity data run at 60 GeV beam energy of unknown beam composition[2)]. As the setup of the Cherenkov counter is also not known for this run, no offline selection on the Cherenkov information is performed. As the selected beam energy is a significant fraction of the primary beam energy and the chosen beam polarity is positive, it is expected that the beam consists primarily of protons. Figure 4.25 shows the reconstructed FHI spectrum with fits to the AHCAL part for data and simulations with 60 GeV protons and pions. The fitted results are $\tau_{\text{data}} = 8.74 \pm 0.01$ in data, $\tau_{\pi} = 10.69 \pm 0.11$ for simulated pions and $\tau_{\text{p}} = 8.66 \pm 0.09$ for simulated protons. The ratio of fitted proton and pion slopes $\frac{\tau_{\text{p}}}{\tau_{\pi}} = 0.81 \pm 0.01$ is in good agreement with the ratio $\frac{\lambda_{\text{n}}}{\lambda_{\pi}} = \frac{16.77\,\text{cm}}{20.42\,\text{cm}} = 0.82$ of pure Fe [26]. The fit results from data and the simulated proton sample are compatible within uncertainties, while the fits from pions are incompatible with the fits from data, indicating an approximately pure proton beam in the observed run.

No significant deviations from the AHCAL FHI slope predicted by simulated pions are found in the data runs used in this analysis. Therefore all data runs used in this analysis are fully consistent with no significant proton contamination within the systematic uncertainties of this method.

The same procedure could be performed on the reconstructed FHI slope in the ScECAL for an independent measurement. However due to unknown efficiency effects of the isolated primary track requirement in the pion selection and possible remaining uncertainties from the ScECAL absorber composition this is much less precise, as the expected difference in τ between pions and protons is lower in the ScECAL than in the AHCAL due to the smaller difference of λ_{n} and λ_{π} in W.

[2)] Run 560540 was recorded with an additional 60 mm steel absorber 185 cm upstream of the ScECAL front face to generate π^0 particles for testing di-photon reconstruction in the ScECAL.

General Contamination

A general estimate of the remaining fraction of contaminated data events after the pion selection can be obtained from the distribution of reconstructed energies in data runs as shown for the 32 GeV run in Figure 4.19(a). Events that are clearly not part of the main reconstructed energy peak are seen above around 44 GeV reconstructed energy. Depending on the chosen integration starting point between 43 GeV to 45 GeV around 0.5 % to 0.7 % of all events are clearly contaminated. Assuming some of these events as also being hidden in the fitted response, the remaining contamination fraction is estimated as 1 % to 2 %.

In previous analyses based on the cleaner testbeam at CERN [84, 88, 119], no such entries above the main reconstructed energy peak are observed. Hardware effects are thus disfavoured as an explanation of thes events. It is known that the MTest beamline delivers a significant fraction of events with more than one beam particle, which are not perfectly suppressed in the analysis, see Figure 4.1 and subsection 4.5.2. The observed remaining contaminations are unlikely to be events with two beam energy pions or one beam energy pion and an additional electron of the same energy, as such events would form a peak around twice the reconstructed energy, which is not visible. The distribution of reconstructed energies rather shows a continuous contamination tail towards higher reconstructed energies. This could be caused by additional contamination particles lower than the beam energy, as might be punching through the final beam collimator. The observed behaviour cannot be explained by remaining additional muons in the beam halo, as such muons would deposit far less energy than the additional depositions needed to explain the observed contamination tail. The visible tail towards lower reconstructed energies is part of the signal, caused by pion showers that are not fully contained in the calorimeter system. An estimation of contaminations is thus not possible in this region.

The behaviour discussed above for the 32 GeV run is similar for the data runs at beam energies of 12 GeV and higher (see Figure D.2 in the Appendix). A study of the systematic influence and uncertainty on the reconstructed energy response and resolution is given in Appendix B.

As the reconstructed energy spectrum of the 4 GeV run is asymmetric with a tail to higher energies, the fraction of contamination events would be well hidden below the signal and cannot be estimated in this way.

4.6. Validation Studies

In order to be able to do meaningful comparisons of recorded data and simulation, accurate data calibration factors as well as a realistic simulation model of the detector are essential.

This section first describes crosschecks performed to validate the pre-existing cell-wise energy calibration for the data runs used in this analysis. The ScECAL simulation model, which was not used in published analyses before, is then fully validated by comparing electromagnetic shower observables in data and simulations. To validate the ScECAL simulation and digitisation model, comparisons of electromagnetic interactions within the ScECAL are preferred as such interactions should be well described in simulations and subject to less modeling uncertainties than hadronic showers. The simulation models of the

AHCAL and TCMT are not validated separately, as they are considered well understood and have been used in various recently published analyses [88, 113, 119].

4.6.1. MIP Calibration

The MIP calibration defines the energy scale on which energy depositions are measured in the CALICE calorimeter prototypes. It is thus imperative to carefully setup and validate the MIP calibration in data and simulated runs in order to obtain comparable results.

The combined ScECAL+AHCAL+TCMT pion dataset used in this study has not been analysed in detail before, however data taken immediately before and after the pion runs has been used in previous analyses [34, 81]. Calibration factors for the FNAL testbeam are thus available in the CALICE database and it is sufficient to crosscheck the existing MIP calibration of the calorimeter system for that beam period.

Dedicated MIP calibration muon beam runs are fully reconstructed into hits on the MIP scale. Applying the MIP event and hit selections described in subsection 4.5.1 yields distributions of single MIP hit amplitudes for all channels. The comparison of a MIP spectrum of a single ScECAL strip, obtained from data and simulations in Figure 4.26 shows that the shape of the hit energy spectrum is well described in the digitised ScECAL simulation. This validates the implemented scintillator-SiPM digitisation at the lowest hit energies.

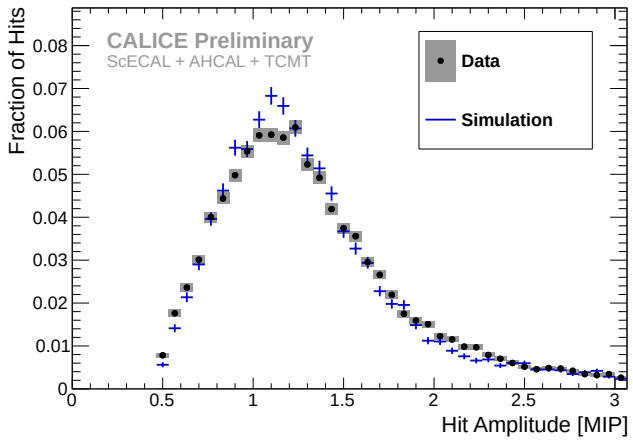

Figure 4.26.: *Hit energy spectrum of a single ScECAL cell in run 560474 (32 GeV π^-) for hits consistent with a MIP like track [108].*

Fitting these spectra individually for each calorimeter cell and extracting the MIP value[3)] yields the distribution of MIP responses shown in Figure 4.27. For a perfectly calibrated detector, the extracted MIP values would be exactly at unity for all channels. In practice, miscalibrations and limited statistics per channel result in a widening of the distribution, ideally without shifting its mean.

[3)] The definition how to extract the MIP value from a fitted MIP spectrum differs slightly between ScECAL and AHCAL, see subsection 2.6.3.

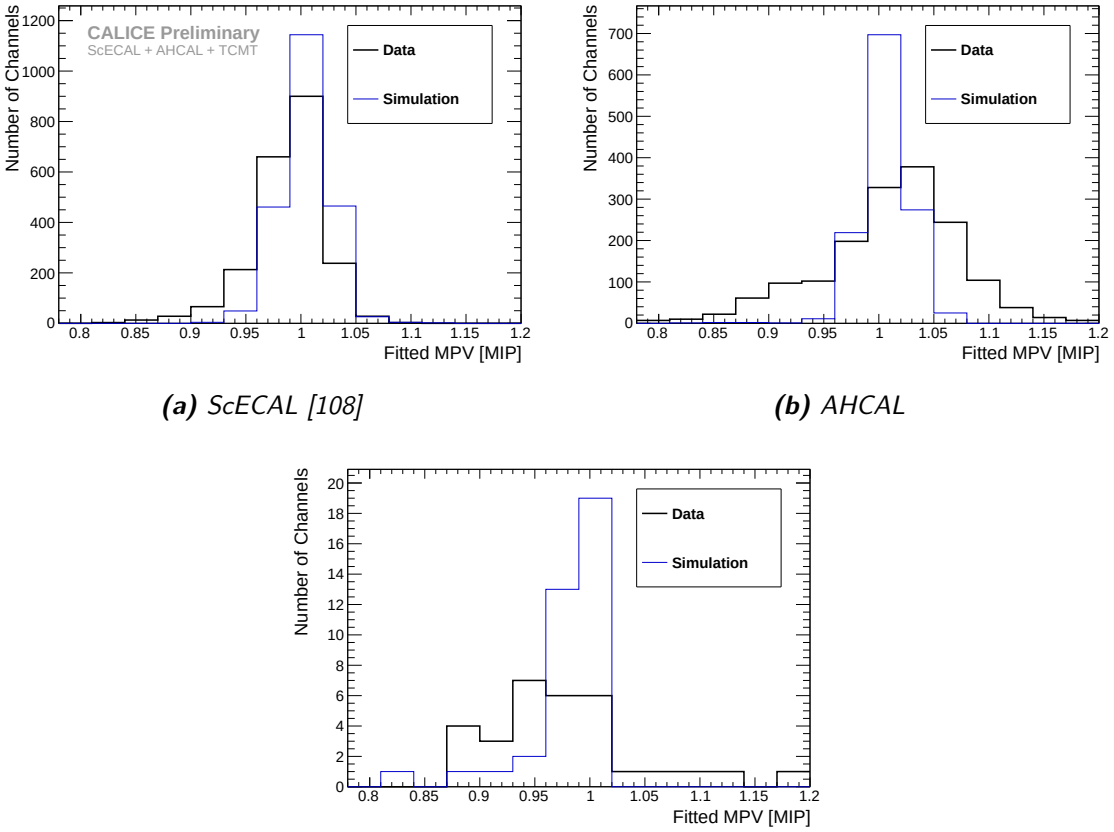

(a) *ScECAL [108]*

(b) *AHCAL*

(c) *TCMT (First eight layers)*

Figure 4.27.: *Distribution of fitted MIP responses in single cells from Run 560269 (32 GeV μ^-).*
(a): ScECAL: $\mu_{data} = 0.99, RMS_{data} = 0.040, \mu_{MC} = 1.00, RMS_{MC} = 0.022$.
(b): AHCAL: $\mu_{data} = 1.01, RMS_{data} = 0.066, \mu_{MC} = 1.00, RMS_{MC} = 0.044$
(c): TCMT: $\mu_{data} = 0.98, RMS_{data} = 0.069, \mu_{MC} = 0.98, RMS_{MC} = 0.037$

Both the ScECAL and AHCAL give mean fitted MIP values of very close to unity in data and simulations, indicating a good average cell energy calibration. The AHCAL data distribution is slightly skewed towards higher values, with its most probable value a few percent above unity. This might be related to the up to 6 % shift in MIP calibration observed in data runs obtained at FTBF in a previous thesis [84]. No clear conclusion on this can be drawn, but the effect is most likely negligible as the mean AHCAL MIP calibration is still reasonably close to one.

The distribution of fitted data MIP values in the TCMT suffers from general issues in its calibration and operational stability, due to the rather low lightyield of the used scintillator strips and high noise rates in the used SiPMs. In order to shift the TCMT MIP values extracted from data towards unity, all measured TCMT depositions in data runs are scaled by a constant factor of 1.2 in all analyses presented in this thesis. The number of fitted TCMT channels is small, as the used muon run mostly contains particles going through the ScECAL, the area of which is covered by only four TCMT strips per TCMT layer. Additionally only

the first eight layers of the TCMT are used in the analyses presented here, leading to only around 32 TCMT channels in the shown distributions.

For all subdetectors, the reconstructed MIP values distributions from data are wider than in simulations, as channel-wise miscalibrations are not modeled as part of the digitisation. The ScECAL data distribution gives a lower RMS than the AHCAL distribution, indicating a generally better calibration in the ScECAL due to the different SiPMs used.

4.6.2. Hit Energy Spectra and Shower Profiles

From the comparison of electromagnetic shower observables in the ScECAL in data and simulations, the simulation and reconstruction of deposition amplitudes and their geometric distribution can be validated across the whole beam energy range. This allows insights into the modelling quality of the ScECAL material composition in the simulation, as well as effects of uncertainties in the SiPM saturation unfolding and the general ScECAL calibration.

The comparison of hit energy distributions in Figure 4.28 shows a significantly longer tail towards higher hit energies in simulated events than in data. Assuming a perfect description of the physics of electron showers in the simulation, this could be either caused by a wrong or incomplete treatment of SiPM saturation effects in data, or a wrong material description in the simulation model.

The unfolding of the SiPM saturation in ScECAL data is performed by assuming a single calibration factor representing the effective number of pixels per sensor for all cells, using the mean of the number of effective pixels measured from a subset of ScECAL strips (see section 2.6). Re-reconstructing the dataset with this parameter reduced by 20% (corresponding to around 2σ of the measured distribution) yields the spectra and profiles labelled as *Data (Sat. Scale)* in the following. This leads to slightly longer tails in the hit energy distribution in data for all beam energies, although not enough to make data and simulation agree, as shown in Figure 4.28. The specific saturation behaviour observed in the type of SiPM used in the ScECAL (see section 2.6) is not included into the desaturation calculation during reconstruction and is still under active investigation [85]. However a correct description of the ScECAL SiPM saturation behaviour in the hit energy reconstruction would lead to an even softer hit energy spectrum and can thus not be the sole explanation here.

An incorrect description of the materials in the simulation model would lead to an additional discrepancy in observed shower profiles between data and simulation. The transverse shower profiles in Figure 4.29 indeed show a significantly narrower shower core in simulations compared to data for all beam energies, leading to higher energy deposition densities and thus potentially explaining the harder hit energy spectra. The longitudinal profiles in Figure 4.30 are however well described, indicating that the amount of absorber material in X_0/Layer is well modelled in simulation. The only way to increase the effective *Molière Radius* R_M nearly without influencing X_0/Layer is increasing the thickness of air between individual ScECAL layers. Separate simulations with modified air gap between individual ScECAL layers (doubled from 1.24 mm to 2.48 mm) labelled *MC (Airgap*2)* are shown in the figures below. The wider air gap slightly increases R_M and reduces the tail in the hit energy spectra, but not enough to make the simulation agree with data. A further increase of the air gap is entirely unphysical, as the doubled air gap already

makes the modified ScECAL simulation model $30 \times 1.24\,\text{mm} \approx 3.7\,\text{cm}$ longer than the measured length of the ScECAL prototype. Thus, the possibility should be considered that the simulation used in this study indeed produces slightly too narrow electromagnetic showers. Shifting the saturation scale in data reconstruction has a small influence on the measured transverse shower profile, but does not improve the agreement with simulations.

The studied effects produce shifts in the order of the observed discrepancies between data and simulation in the hit energy spectra while keeping the longitudinal profiles compatible to data, but the description of the transverse shower profiles does not improve in the same way. No final conclusion whether the discrepancies between data and simulation can be attributed to the shower simulation or the geometry modelling and SiPM saturation can be drawn. The datasets obtained with modified simulations and reconstruction parameters are thus used as estimates on the systematic uncertainties on shower simulation, geometry modelling and SiPM desaturation.

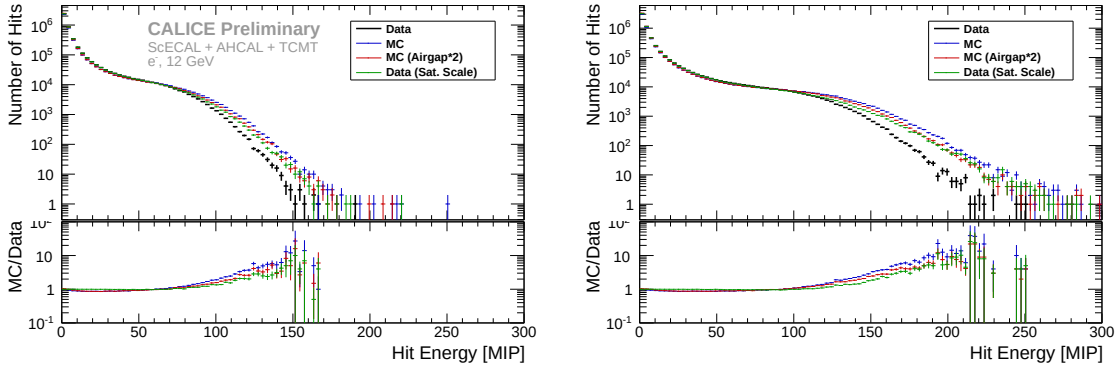

(a) *12 GeV [108]* **(b)** *20 GeV*

Figure 4.28.: *Electron shower hit energy distributions for data, simulation and possible systematic effects in simulation and reconstruction.* MC (Airgap*2) *are simulated events obtained from a simulation model with doubled amount of air between ScECAL layers.* Data (Sat. Scale) *is the same raw data set as* Data, *but with the effective number of SiPM pixels used for saturation unfolding reduced by 20% in reconstruction.*

The longitudinal profiles of electron showers are generally well described by simulations in both shape and amplitude, see Figure 4.30. The remaining fluctuations from layer to layer are accounted to channel-wise miscalibrations (which are not fully included in the simulation), in combination with most energy being deposited in few cells per layer. The systematic effects described in the previous paragraphs show very small influence within the existing fluctuations. Generally the measured response calibrated to the MIP scale in data and simulations agrees within a few percent, and the description of electromagnetic showers in simulation is satisfactory for the following study of hadron showers.

4.6.3. ScECAL Electron Response & Resolution

To further validate the ScECAL simulation and reconstruction, initial results of the ScECAL electromagnetic shower response and resolution in data and simulation are presented here.

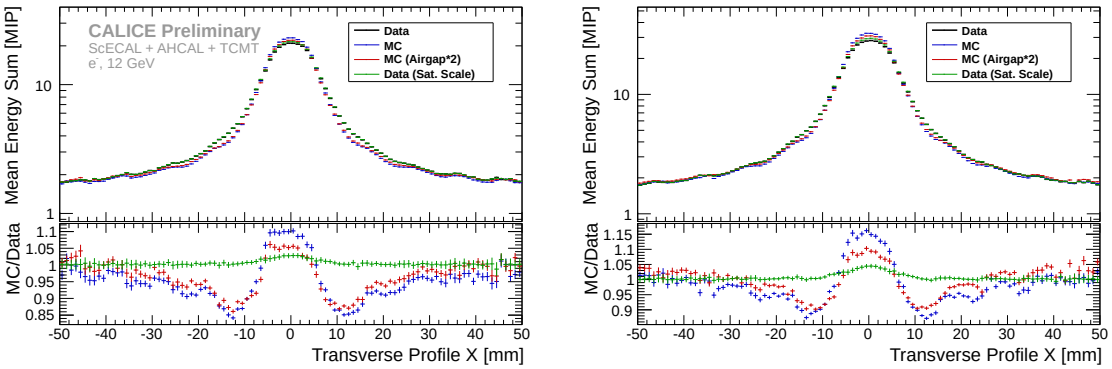

(a) *12 GeV [108]* **(b)** *20 GeV*

Figure 4.29.: *Transverse electron shower profiles for data, simulation and possible systematic effects in simulation and reconstruction.* MC (Airgap*2) *are simulated events obtained from a simulation model with doubled amount of air between ScECAL layers.* Data (Sat. Scale) *is the same raw data set as* Data, *but with the effective number of SiPM pixels used for saturation unfolding reduced by 20% in reconstruction.*

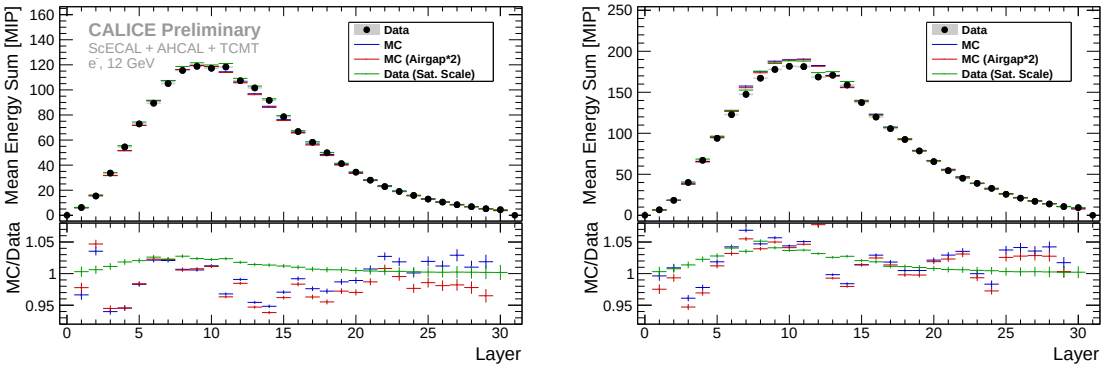

(a) *12 GeV [108]* **(b)** *20 GeV*

Figure 4.30.: *Transverse electron shower profiles for data, simulation and possible systematic effects in simulation and reconstruction.* MC (Airgap*2) *are simulated events obtained from a simulation model with doubled amount of air between ScECAL layers.* Data (Sat. Scale) *is the same raw data set as* Data, *but with the effective number of SiPM pixels used for saturation unfolding reduced by 20% in reconstruction.*

The results given in this section are based on a simplified analysis, using only one out of several available electron data runs per beam energy. No additional systematic uncertainties resulting from run-to-run variations and uncertainties on the ScECAL absorber composition, desaturation calibration parameters etc. are taken into account. A comprehensive analysis of the electromagnetic response and resolution of the ScECAL physics prototype, based on the already published preliminary results [79–82], is currently in preparation [116].

For each used electron run, the response and resolution is extracted from a Gaussian fit to the ScECAL energy sum spectra of events passing the electron selection. The extracted responses of data and simulations are shown as a function of beam energy in Figure 4.31. The responses obtained from each set of runs are fitted with a linear function

$$f(E_{\text{beam}}) = a \times E_{\text{beam}} + b, \tag{4.9}$$

with the electromagnetic scale factor a in $\frac{\text{MIP}}{\text{GeV}}$ and the offset b in MIP. Both the slope and offset parameter of the fit function must be free fit parameters, as threshold and noise effects can shift the function away from the origin. The results of all such fits are given in Table 4.5. The standard simulation yields a good agreement in the scale factor of only around 2 % difference compared to data. The apparent differences in the constant response offset between data and simulation have been observed similarly in electron analyses of the AHCAL with both Fe and W absorbers [112, 119]. The difference in scales factors between both simulations is small, as the effective sampling fraction does practically not change from the added air between the layers.

The deviations shown in Figure 4.31 are given relative to the fitted data response, assuming a 1 % relative response uncertainty from the precision of the ScECAL MIP calibration. The linearity of the data points is good, with $\leq$2 % deviation from the fit. The difference between the standard reconstruction and the reconstruction with shifted SiPM saturation scale yields upwards deviations especially for the highest two energy points where saturation effects are expected to result in the strongest impact.

Table 4.5.: *Electromagnetic shower response fit results obtained from a linear fit over the energy range 2 GeV to 32 GeV.* Simulation (Airgap*2) *are simulated events obtained from a simulation model with doubled amount of air between ScECAL layers.* Data (Sat. Scale) *is the same raw data set as* Data, *but with the effective number of SiPM pixels used for saturation unfolding reduced by 20% in reconstruction.*

Run Type	a $\left[\frac{\text{MIP}}{\text{GeV}}\right]$	Δa $\left[\frac{\text{MIP}}{\text{GeV}}\right]$	b [MIP]	Δb [MIP]
Data	129.8	0.0	22.2	0.2
Simulation	132.4	0.0	0.0	0.2
Simulation (Airgap*2)	131.7	0.0	−1.0	0.2
Data (Sat. scale)	134.4	0.0	9.5	0.2

The resolutions extracted from all examined datasets are shown in Figure 4.32. Both the standard and modified geometry simulations give a reasonable agreement with the

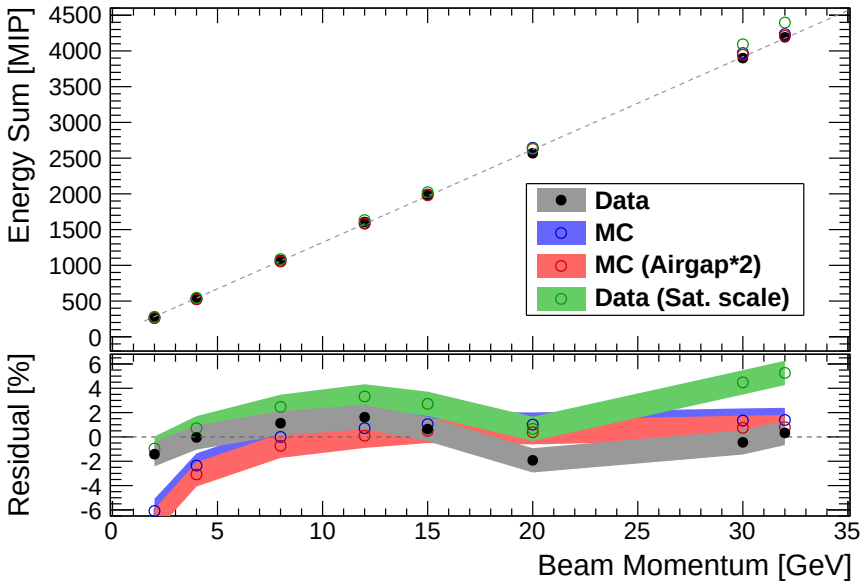

Figure 4.31.: *ScECAL electron shower response for data, simulation and possible effects in simulation and reconstruction. The deviation is given compared to the linear fit of the data points, shown as the dashed grey line.*

resolutions extracted from data runs, without any specific trend or pattern visible in their deviations. The data points reconstructed with a shifted saturation scale give significantly worse resolutions at the two highest energy points, indicating that the saturation scale used in the standard reconstruction is reasonably close to the ideal value.

The dashed resolution curve shown in Figure 4.32 is the resolution curve fitted from a preliminary full analysis of all electron runs available per beam energy [82] and thus *not* a fit to any of the shown data points. As the fit given in [82] is performed after subtracting the assumed beam energy spread from each extracted resolution, which is not done in this analysis, an additional constant term of 2.4 % is added in quadrature to the drawn resolution function. Data and both simulations agree well with the given resolution function.

The responses and resolutions obtained from data in this study are very similar to the published preliminary values [82]. The simulation results are in good agreement with the data points across the whole energy range. No strong effects due to mis-modelling of the electromagnetic resolution of the ScECAL are expected in the following hadron analysis.

4.7. Energy Reconstruction in a Combined Calorimeter System

Hadron showers can deposit significant amounts of their energy in all sub-detectors of the combined calorimeter system. The measured depositions of all sub-detectors have to be combined into a common reconstructed energy. This section describes the general formalism in which the parameters of energy reconstruction schemes can be obtained, as well as two different approaches to calorimeter energy reconstruction.

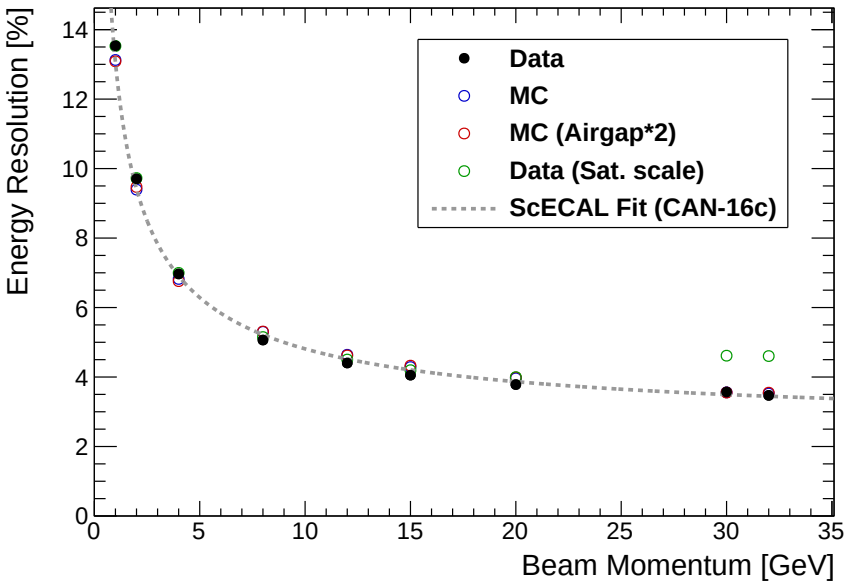

Figure 4.32.: *ScECAL electron shower energy resolution for data, simulation and possible effects in simulation and reconstruction, including the published fit to the full ScECAL electron data set given in [82] (adapted to account for the beam energy spread) for comparison.*

Typically, the full shower energy is obtained by applying a weight to each deposition. All weighted depositions are then summed up into the reconstructed energy. In more complicated energy reconstruction schemes the reconstructed energy can depend on any number of measured event quantities and external parameters (*weighting*). For any chosen energy reconstruction algorithm, external parameters can be optimised by minimising the sum of quadratic distances of the reconstructed event energy to the known beam energy, resembling a χ^2 function:

$$\chi^2 = \sum_{events} \frac{\left(E_{\text{rec}}^{\text{event}} - E_{\text{beam}}^{\text{event}}\right)^2}{(55\%)^2 \cdot E_{\text{beam}}^{\text{event}}} \tag{4.10}$$

In this formalism parameters can be estimated for multiple runs at multiple beam energies in one procedure, optimising the detector resolution and response linearity simultaneously.

In the energy range considered here, the variance of the reconstructed energy spectrum is expected to scale proportionally to the beam energy (according to the $1/\sqrt{E}$ stochastic term resolution dependence). To normalise contributions to χ^2 between different beam energies, each event is thus de-weighted by its known beam energy. The constant factor in the denominator is approximating the expected stochastic term of the calorimeter to enable correct parameter uncertainty estimation by the optimisation algorithm, but does not influence the estimated parameter values.

The χ^2-optimisation described above only gives ideal results for Gaussian distributions. The reconstructed energy spectra obtained from the used calorimeter setup can exhibit non-Gaussian features from fluctuations in the electromagnetic fraction of pion showers,

leakage effects and remaining sample impurities in data. The optimisation of weights is thus performed iteratively on the central 90% of reconstructed energies per run.

In order not to bias the parameter estimation towards a specific beam energy, the same number of events are added to χ^2 for each run. The first 40,000 selected events of each data run (20,000 in simulated runs) are used in the parameter optimisation. No significant difference in reconstructed energy resolution is observed whether the events used for parameter optimisation are excluded in the reconstruction or not, for both energy reconstruction schemes discussed here.

4.7.1. Standard Weighting

In an idealised sampling calorimeter, the reconstructed energy for an incoming particle is directly proportional to the measured sum of depositions. For a calorimeter system consisting of several different sampling ratios, the reconstructed energy is the sum of all hit energies weighted by a constant factor, typically close to the inverse sampling fraction $\frac{1}{f_s}$, for each calorimeter. As the sampling fraction within the ScECAL is constant and the AHCAL and first eight layers of the TCMT have identical sampling fractions, the standard energy reconstruction only has two parameters w_{ECAL} and w_{HCAL}:

$$E_{\mathrm{rec}}^{\mathrm{classic}} = w_{\mathrm{ECAL}} \cdot E_{\mathrm{sum}}^{\mathrm{ScECAL}} + w_{\mathrm{HCAL}} \cdot \left(E_{\mathrm{sum}}^{\mathrm{AHCAL}} + E_{\mathrm{sum}}^{\mathrm{TCMT}} \right) \tag{4.11}$$

Figure 4.33 shows the weights optimised for each beam energy run on its own and all runs at once. The weight dependence on beam energy is flat, with the smallest beam energy point at 4 GeV preferring slightly different weights. The weights optimised for all beam energies are close to the values obtained for single beam energies. All used physics lists produce very similar weights. The weights obtained from data have slightly ($\approx 5\,\%$) higher values than the weights obtained from simulations. This hints to a general overestimation of depositions in simulations, as is also observed in the longitudinal shower profile (Figure 4.42 in subsection 4.8.1).

The reconstructed energy resolution and response linearity only depend on the ratio of weights, which is very similar between data and simulations. Using weights obtained from simulation to reconstruct data events (or vice versa) would thus not notably influence the resulting resolution, but only result in a shifted energy scale.

The ratio of mean contribution to the reconstructed energy of pion showers in ScECAL and AHCAL $r = E_{\mathrm{rec}}^{\mathrm{AHCAL}} / E_{\mathrm{rec}}^{\mathrm{ScECAL}}$ varies from around unity (at 4 GeV) to around three (at 32 GeV).

4.7.2. Software Compensation Weighting

As is explained in more detail in section 1.5, most calorimeters give a distinctly different measurable response to electromagnetic showers and hadron showers of the same initial energy. The calorimeter system used in this analysis gives a higher measured response to electrons than to hadrons and is thus undercompensating with $\frac{e}{h} > 1$ in each subdetector. However, the exact value of $\frac{e}{h}$ may differ between the ScECAL and AHCAL.

If it is possible to identify electromagnetic sub-shower contributions within hadron showers, reweighting them down to the purely hadronic deposition scale should lead to an

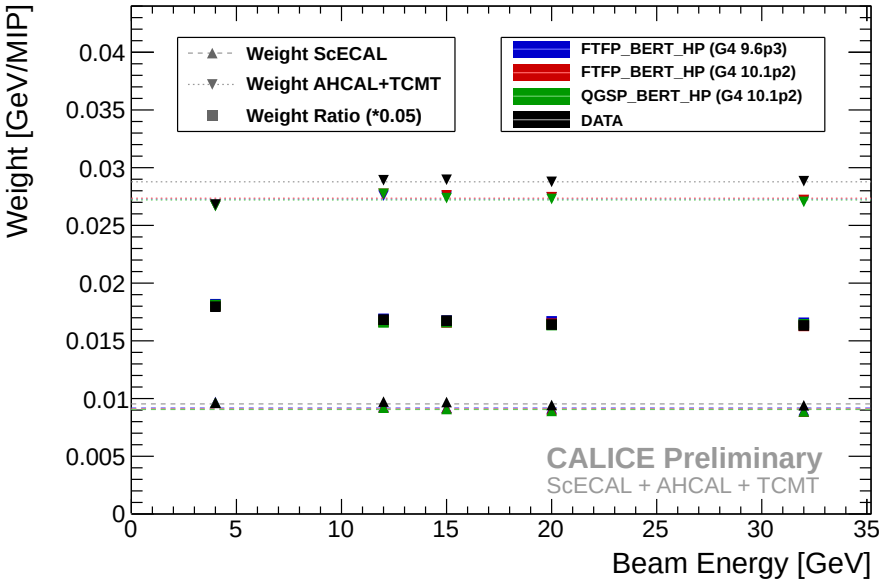

Figure 4.33.: *Standard energy reconstruction weights obtained from data and simulations. Markers indicate weights optimised for single beam energies, lines represent weights optimised for all available beam energy runs at once. All statistical uncertainties are smaller than the used markers. [108]*

improvement in resolution and linearity of the reconstructed energy. Such reconstruction techniques are termed *Software Compensation* (SC).

With the materials used in this setup, the length scales of hadron showers and electromagnetic showers are notably different ($X_0/\text{layer} \gg \lambda_\pi/\text{layer}$ in both ScECAL and AHCAL). In combination with the high readout granularity of around the feature size of electromagnetic showers, this enables the differentiation between electromagnetic and hadronic shower components by the deposited energy density. Each measured cell deposition is thus weighted as a function $w(\rho, E_{\text{est.}})$ of the local deposition density ρ and an estimate of the full shower energy $E_{\text{est.}}$.

In the software compensation implementation devised for this thesis, instead of fully parametrising $w(\rho, E_{\text{est.}})$, the dependence in ρ is divided into fixed bins, while the dependence on $E_{\text{est.}}$ is parametrised over the used energy range for each such bin. This scheme differs from the *local software compensation* implementation in [88] by not enforcing any functional dependence on ρ, as ρ is only ever evaluated in the chosen bins of deposition density. The scheme presented here leads to more free parameters and thus more degrees of freedom while improving the stability of the parameter optimisation.

Instead of using the deposition density as the hit amplitude divided by the cell size, the hit energy for each hit is used directly, disregarding the differently sized tiles in the AHCAL, slightly improving the performance of the full algorithm. This is due to energy depositions of around 1 MIP in a single tile being most likely generated by a single traversing particle, regardless of the given tile size. Most hit energies are in the lower range around a few MIPs, as shown in Figure 4.34. If the true measured hit energy density was used to assign a hit energy bin instead of the hit energy, most hits in the larger cell sizes would be assigned into

the first hit energy bin, leading to a loss of information and thus potentially degradation of the resolution.

This analysis uses eight hit energy bins as given in Table 4.6. The obtained resolutions do not critically depend on the number of bins or exact bin boundaries [120].

Table 4.6.: *Software compensation bin boundaries used in the ScECAL and AHCAL in this analysis.*

Bin	ScECAL [MIP]	AHCAL [MIP]
1	0.0 – 2.0	0.0 – 2.0
2	2.0 – 4.0	2.0 – 4.0
3	4.0 – 7.6	4.0 – 6.6
4	7.6 – 14.5	6.6 – 11.0
5	14.5 – 27.6	11.0 – 18.2
6	27.6 – 52.5	18.2 – 30.2
7	52.5 – 100.0	30.2 – 50.0
8	100.0 – ∞	50.0 – ∞

For the two lowest hit energy bins in the ScECAL and AHCAL, instead of summing up hit energies, only the number of hits falling into these bins are counted. This counting of hits, which is similar to the SDHCAL reconstruction [121], effectively suppresses sampling fluctuations stemming from the tail of the Landau distribution in low particle multiplicity hits, slightly improving the resulting energy resolution of the algorithm. All TCMT depositions are treated as falling into the same hit energy bin, effectively parametrising the relative TCMT weight as a function of the beam energy only.

The lowest hit energy bin has significant contributions from the primary track before the first hard interaction, which show nearly no dependence on beam energy. To exclude biasing of the parameter optimisation towards weighting up the primary track hits to the full beam energy, hits on the primary track are excluded from the software compensation weighting. All hits on the axis of the reconstructed clean primary track (as described in subsection 4.5.2) from the first ScECAL layer up to two layers before the reconstructed FHI layer are included into the energy reconstruction without hit energy or shower energy dependent weighting. To exclude Landau fluctuations, only the number of such hits is used and multiplied by the mean energy deposition of a MIP-like particle in a single cell of the given calorimeter section.

An example of the distribution of hits into hit energy bins is given in Figure 4.34. It is apparent that in the lowest hit energy bin in the ScECAL around one quarter of all contributions would come from the primary track if not identified and excluded. The contribution of primary track hits to the AHCAL hit energy spectrum is small, as around 70% of selected events start showering in the ScECAL (see Figure 4.41).

The full formula to reconstruct the energy in the combined system, with the sampling weights w, the bin weights for the ith bin α_i, β_i as well as the TCMT weight γ, as a function

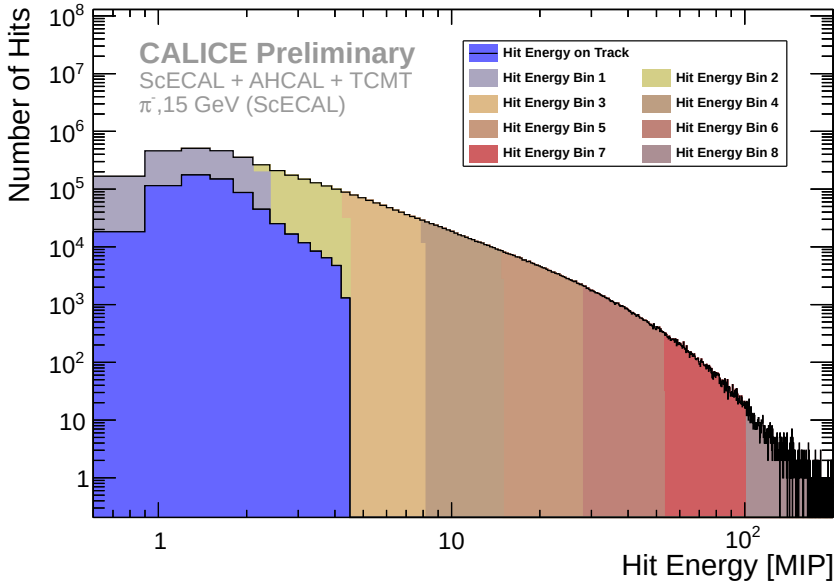

(a) *ScECAL [108]*

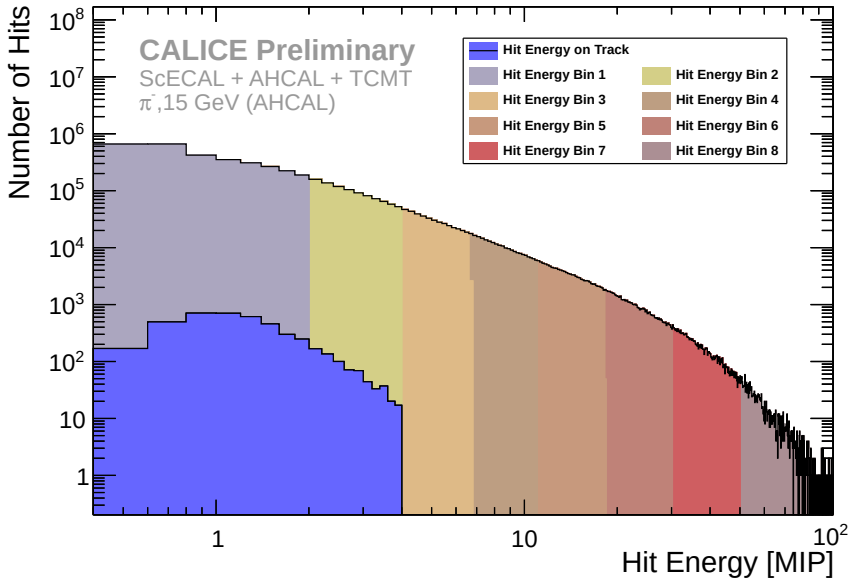

(b) *AHCAL [108]*

Figure 4.34.: *Hit energy spectra of data run 560496 (15 GeV π^-), colours assigned to track hits and by software compensation bin.*

of the estimated particle energy $E_{\text{est.}}$, the sum (or count) of energy depositions in the ith bin E_i and the energy depositions on the primary track E_{track}, is:

$$E_{\text{rec}}^{\text{SC}} = w_{\text{ECAL}} \cdot \left(\sum_{i}^{\text{bins}} \alpha_i \left(E_{\text{est.}}\right) \cdot E_i^{\text{ECAL}} + E_{\text{track}}^{\text{ECAL}} \right) + w_{\text{HCAL}} \cdot \left(\sum_{i}^{\text{bins}} \beta_i \left(E_{\text{est.}}\right) \cdot E_i^{\text{HCAL}} + E_{\text{track}}^{\text{HCAL}} + \gamma \left(E_{\text{est.}}\right) \cdot E_{\text{sum}}^{\text{TCMT}} \right) \quad (4.12)$$

Each relative bin weight in the ScECAL α_i, in the AHCAL β_i and the TCMT weight γ is parametrised as a second order Chebyshev polynomial of the form

$$f\left(E_{\text{est.}}\right) = a \times T_0\left(\frac{E_{\text{est.}}}{S}\right) + b \times T_1\left(\frac{E_{\text{est.}}}{S}\right) + c \times T_2\left(\frac{E_{\text{est.}}}{S}\right) \quad (4.13)$$

$$= a + b \times \frac{E_{\text{est.}}}{S} + c \times \left(2 \times \left(\frac{E_{\text{est.}}}{S}\right)^2 + 1\right) \quad (4.14)$$

With the parameters a, b, c separate for each bin and subdetector, and the scale factor $S = 35\,\text{GeV}$, introduced to scale most events into the function domain $[0, 1]$, to preserve the orthogonality properties of the Chebyshev polynomials.

The software compensation reconstruction is thus defined by 51 parameters in total (8 bins in the ScECAL $\times$ 3 parameters per bin, 8×3 parameters for the AHCAL and 3 parameters for the TCMT). In the optimisation of the parameters the known beam energy is used for $E_{\text{est.}}$, while during reconstruction the standard reconstruction result is used as an estimate. Using the known beam energy for the parameter optimisation does not introduce a bias, as the parameter optimisation is completely independent of the energy reconstruction.

Figure 4.35 shows the beam energy dependence of the bin weights for the ScECAL and the AHCAL. The slope in the first two bins in Figure 4.35 (c), (d) corresponds to a $1/E$ dependence and thus a constant contribution to the reconstructed energy of each hit in these bins, regardless of the hit energy. Assuming a shower of $E_{\text{est.}} = 4\,\text{GeV}$, a hit in the AHCAL with a measured hit energy $E_{\text{hit}} = 1\,\text{MIP}$ would be weighted with a factor of around 1.5 (as given by the blue lines in Figure 4.35(d)) for a contribution to the reconstructed shower energy of $1.5 \times 1\,\text{MIP} = 1.5\,\text{MIP}$. A hit of measured energy $E_{\text{hit}} = 0.5\,\text{MIP}$ would be weighted with the double weight, due to the $1/E$ dependence of the first two hit energy bins, for the identical contribution of $3 \times 0.5\,\text{MIP} = 1.5\,\text{MIP}$ to the reconstructed shower energy. In hit energy bins ≥ 3, two hits of different hit energy within the same hit energy bin would contribute to the reconstructed shower energy proportional to their hit energy.

Higher energy bins tend to be weighted below unity, indicating a high energy hit to belong more likely to an electromagnetic sub-shower. Especially in the ScECAL is it clearly visible that bin weights are not monotonically decreasing for increasing hit energies, as is enforced in the *local software compensation* scheme used in [88]. However, the hit energy of the bin with minimal weight is increasing with energy, indicating that the typical hit energy scale for electromagnetic sub-showers increases with the incident pion energy.

Applying the weights shown in Figure 4.35 to the dataset yields an improvement in energy resolution as shown in Figure 4.36. Iterations of software compensation reconstruction

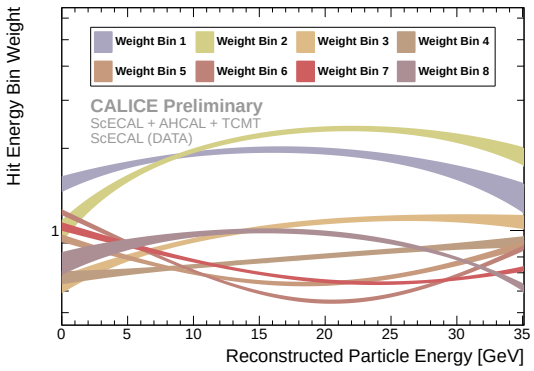

(a) *ScECAL bin weights as a function of energy [108]*

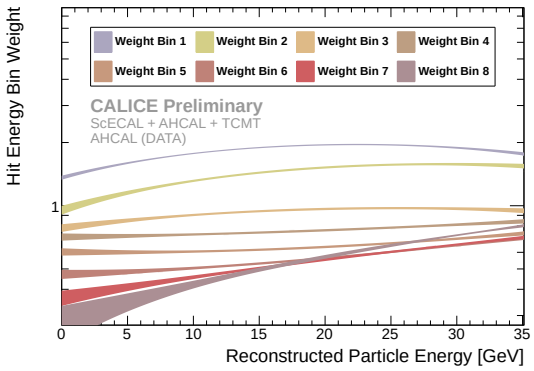

(b) *AHCAL bin weights as a function of energy [108]*

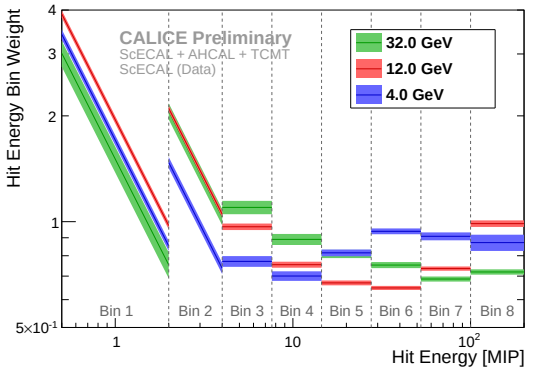

(c) *ScECAL bin weights for selected energies [108]*

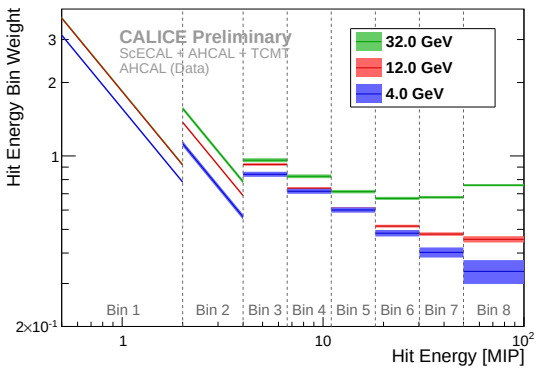

(d) *AHCAL bin weights for selected energies [108]*

Figure 4.35.: *Hit energy bin weights as a function of beam energy, optimised from data runs. In* ***(c)*** *and* ***(d)****, the hit energy dependent weights of the first two bins correspond to a* $1/E$ *dependence and thus a counting of hits in these bins. The width of each plotted line indicates the weight uncertainty propagated from the parameter errors.*

using the previous result as $E_{\text{est.}}$ do not further improve the energy resolution. The correlation between the reconstructed energies from the standard and software compensation reconstruction shows a clear non-linearity in the central part of the reconstructed energies, causing events with a high hadronic fraction, and thus lower standard reconstructed energy, to be shifted up in software compensation reconstruction. Likewise events with above average electromagnetic shower content, and thus too high standard reconstructed energy, are shifted down when reconstructed with the software compensation reconstruction.

The identical procedure of reconstructing energies and optimising weight parameter is applied on simulated events. The dependence of bin weight to beam energy compared between data and simulation is shown in Figure 4.37 for selected bins. All used simulation physics lists agree with each other within the parameter uncertainties. While the AHCAL generally shows reasonable agreement between weights derived from data and simulations in all bins, the ScECAL shows discrepancies especially for the first two bins and the highest hit energy bin. The TCMT weight also has a large discrepancy between data and simulations, likely due to the numerous outliers in the TCMT calibration.

Optimising the software compensation weights on data runs reconstructed with a shifted saturation scale in the ScECAL (as described in subsection 4.6.2) shows only a very small influence on the optimised weights. Optimising weights from simulations with adjusted air gaps between ScECAL layers yields bin weights with small but significant differences to the standard simulation.

The ScECAL pion hit energy spectra show similar behaviour to the electron hit spectra discussed in subsection 4.6.2, as in high tails of the ScECAL hit energy spectrum being overestimated in simulation, which could explain the differences in optimised software compensation weights in data and simulations for the highest ScECAL hit energy bin. The AHCAL hit energy spectra generally show less discrepancy between data and simulations.

The averaged summed deposition per event for each bin is investigated further in order to understand the observed differences in the weights, as shown in Figure 4.39. The highest hit energy bin in the ScECAL has around twice of the mean deposition in simulation compared to data, in accordance with the observed mis-description in hit energy spectra, with significant differences showing from the sixth bin. For lower energies the effect is less pronounced. In the AHCAL all bins show reasonable agreement between data and simulation, with smaller overestimations in the highest hit energy bin.

The observed differences in mean hit energy per bin (and thus hit energy spectra) do not sufficiently explain the differences in optimised software compensation weights on their own. Although the highest ScECAL hit energy bin shows discrepancies between data and simulation for all beam energies, its bin weight is only different in the central part of the beam energies (see Figure 4.37(c)). Likewise the mean energy sum in the first ScECAL hit energy bin is well described for all energies, but the corresponding bin weights are not (see Figure 4.37(a)).

If remaining instrumental and shower modelling effects would affect the optimised weights even in hit energy ranges where the observed hit energy spectra match reasonably between data and simulation, such effects would likely show up in the parameter correlations. The parameter correlations obtained from the optimisations for data and the QGSP_BERT_HP simulation are given in Figure 4.40 and do not differ strongly in their general shape, although most correlations in simulation are found to be around 10 % lower

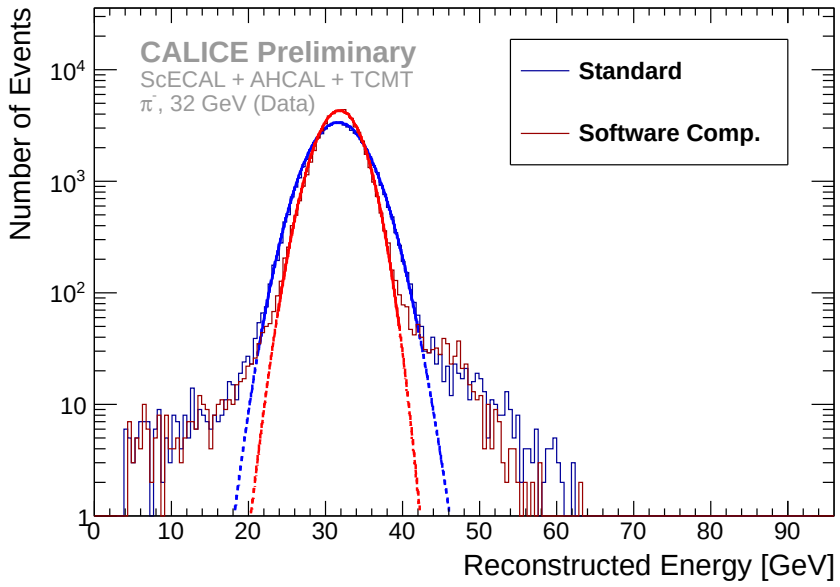

(a) *Reconstructed energy spectra for standard and software compensation reconstruction.*

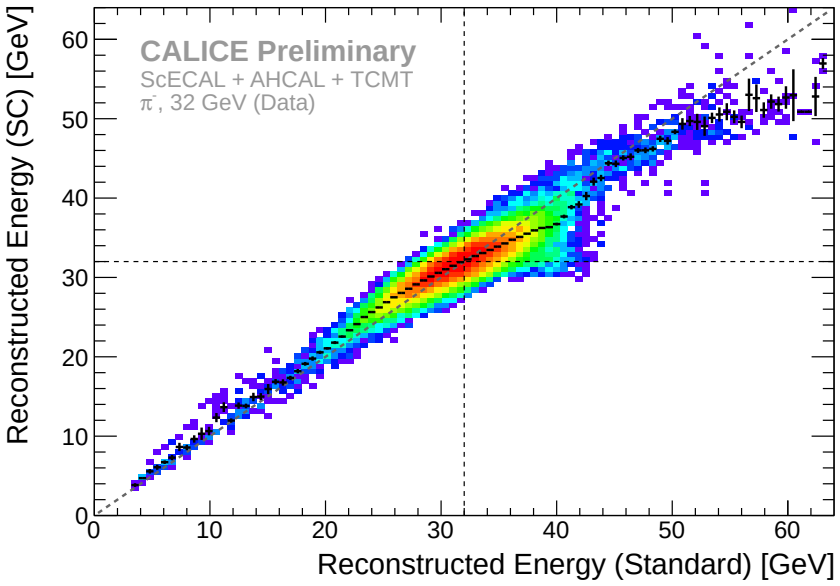

(b) *Correlation standard vs. software compensation reconstructed energy.*

Figure 4.36.: *Reconstructed energy in standard and software compensation reconstruction for data run 560474 (32 GeV π^-). The black markers in the correlation plot show the profile of mean software compensation reconstructed energy for bins in standard reconstruction energy. The black dashed lines in the correlation plot indicate the beam energy of the run. The plots for all other used data runs are given in section D in the Appendix.*

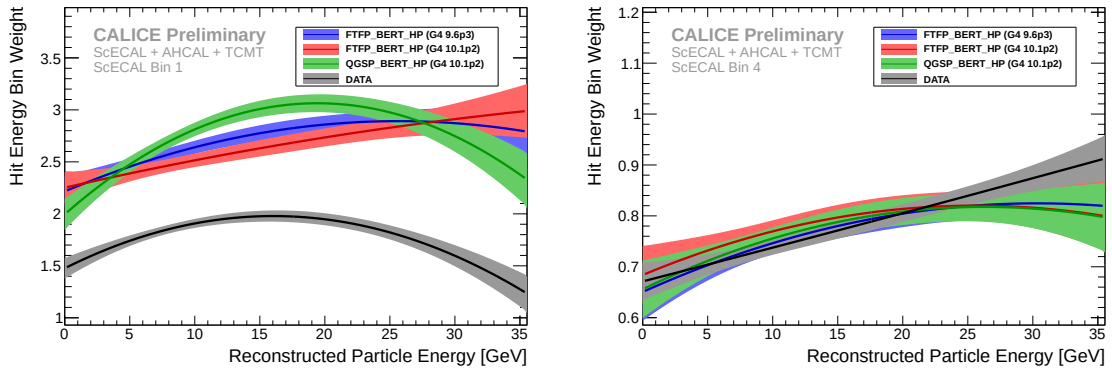

(a) *ScEcal Bin 1 [108]*

(b) *ScEcal Bin 4 [108]*

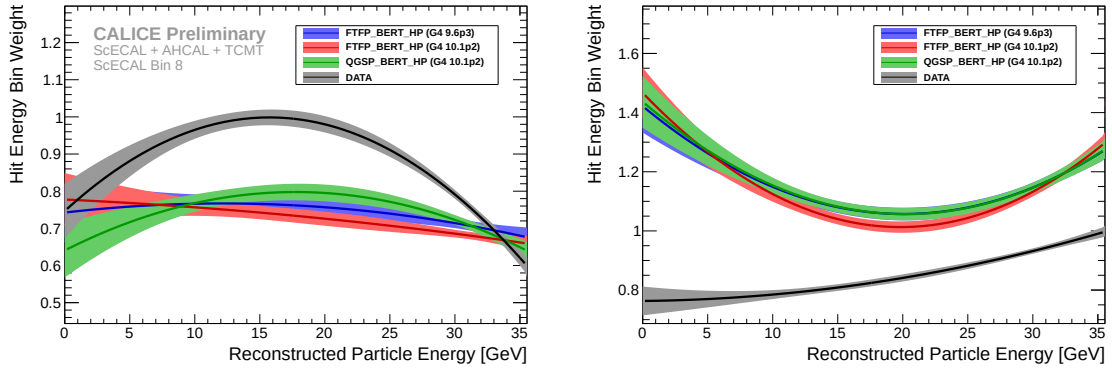

(c) *ScEcal Bin 8 [108]*

(d) *TCMT Weight*

Figure 4.37.: *Hit energy bin weights as a function of beam energy for data and different simulations. The width of each plotted line indicates the weight uncertainty propagated from the parameter errors. Low and high hit energy bin weights are not well reproduced in the ScECAL. The plots for all hit energy bin weights are given in section D in the Appendix.*

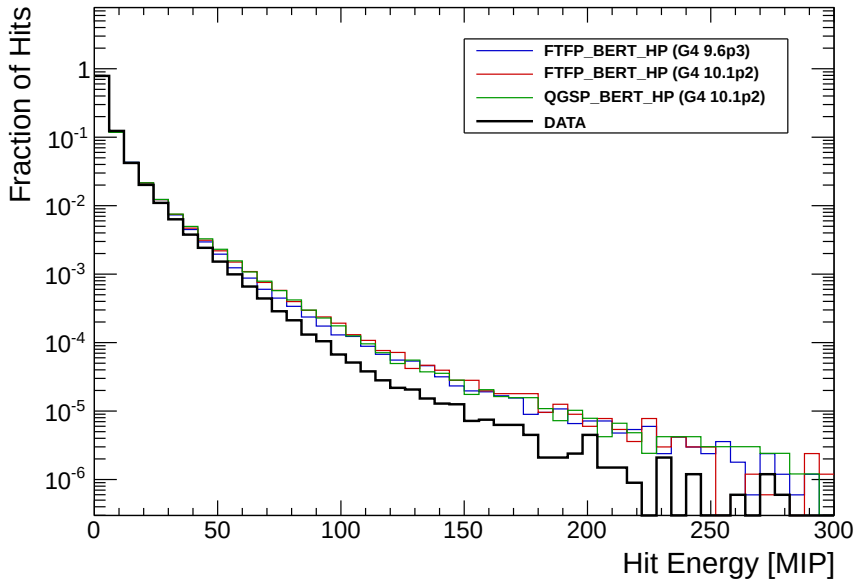

(a) *ScECAL, Run 560498 (12 GeV) [108]*

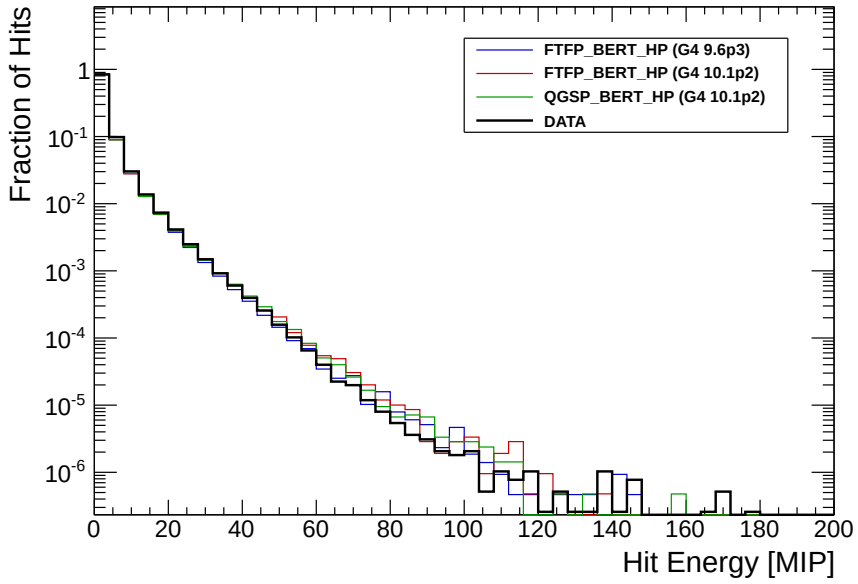

(b) *AHCAL, Run 560498 (12 GeV) [108]*

Figure 4.38.: *Pion shower hit energy spectra of the ScECAL and AHCAL for data and simulations. The discrepancies between data and simulations observed in the ScECAL are similar to the hit energy mis-description in electromagnetic showers, see section 4.6.*

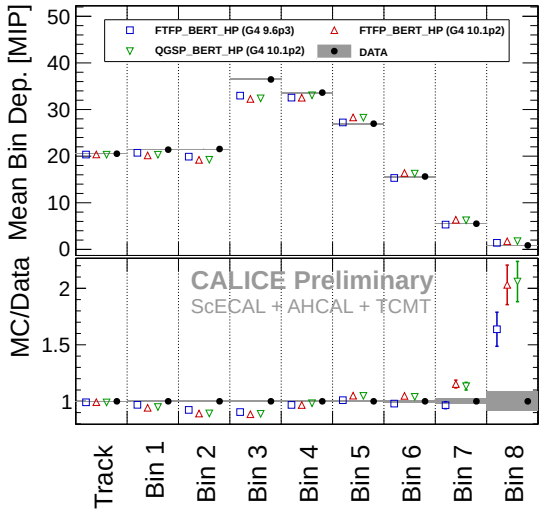

(a) *ScECAL, Run 560506 (4 GeV) [108]*

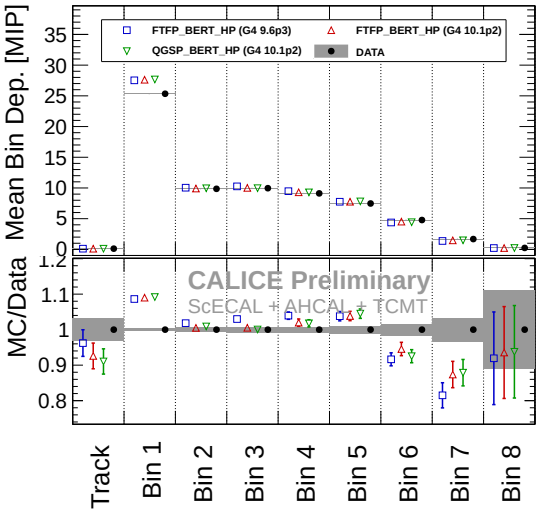

(b) *AHCAL, Run 560506 (4 GeV) [108]*

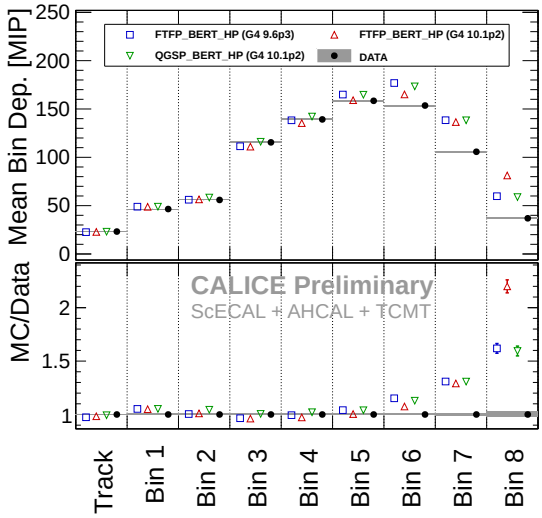

(c) *ScECAL, Run 560474 (32 GeV) [108]*

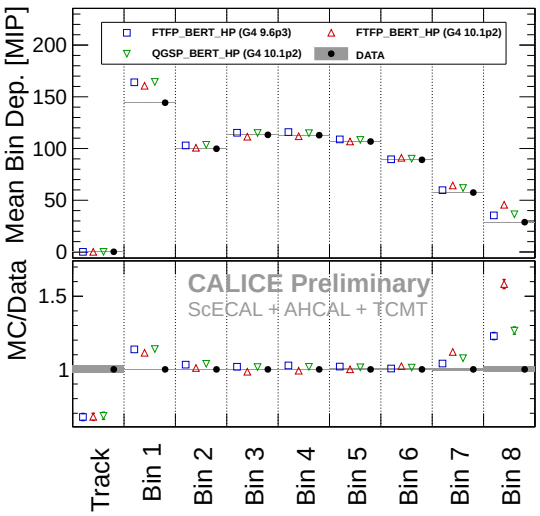

(d) *AHCAL, Run 560474 (32 GeV) [108]*

Figure 4.39.: *Averaged energy deposition sum per hit energy bin per event for data and simulations in the ScECAL and AHCAL. For most entries the statistical error is smaller than the used markers.*

than in data. However the strongest (anti-)correlation observed is between the first and second hit energy bin in the ScECAL, indicating that the observed difference in the first two ScECAL bin weights does not strongly influence the reconstructed energy, as is discussed further in subsection 4.8.4.

Possible instrumental effects are covered by the systematic uncertainties given, so all remaining differences in data and simulation are attributed to imperfect modelling of hadronic shower processes, especially in high-Z absorbers and on the granularity scale that is studied here.

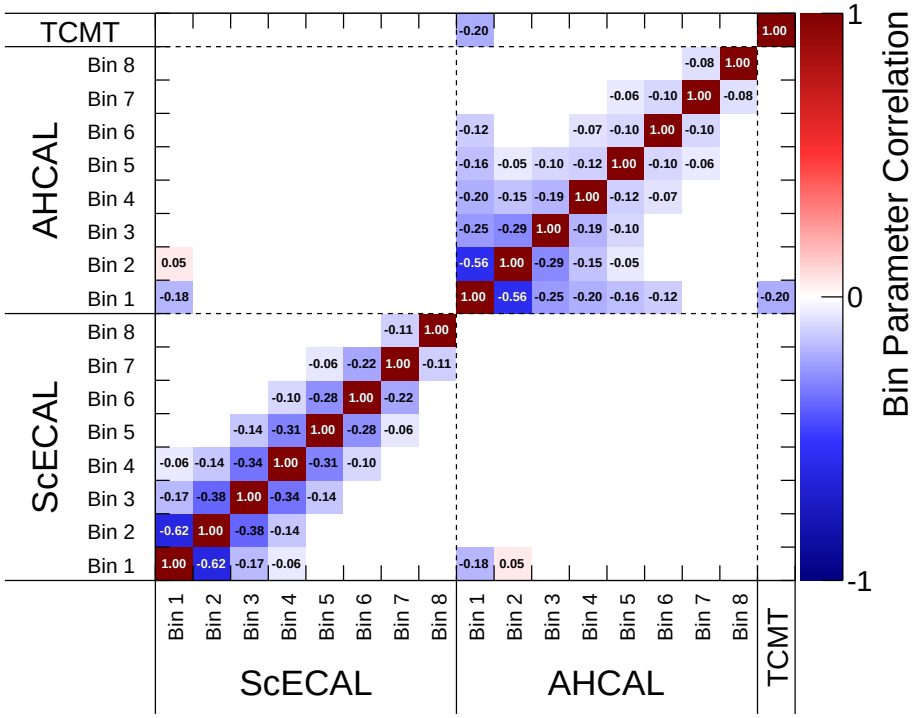

(a) *Data*

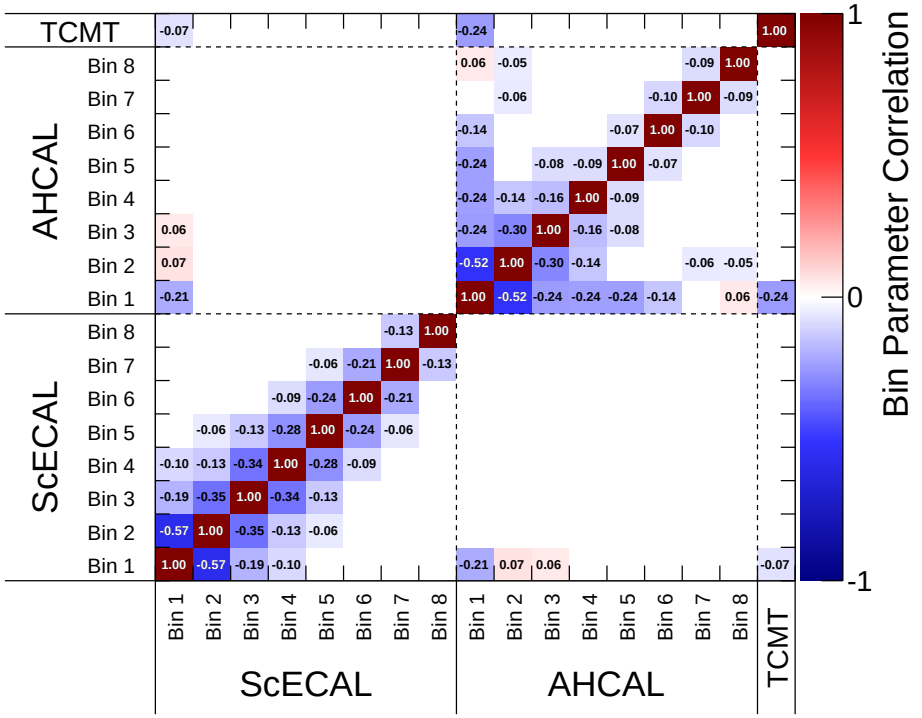

(b) *QGSP_BERT_HP*

Figure 4.40.: *Parameter correlations of the software compensation bin weight parameters. Only the correlations between the b parameters of the weight parametrisations are shown, as the correlation matrix for any 3×3 segment is found to be* $\begin{pmatrix} b & -b & b \\ -b & b & -b \\ b & -b & b \end{pmatrix}$.

4.8. Pion Analysis

During the FNAL testbeam period in 2009 at FNAL, π^--runs were recorded with beam momenta ranging from 2 GeV to 32 GeV. Typically two separate runs were recorded in immediate succession for each beam energy, one shorter run of up to 50 000 events and one longer run of 200 000 to 250 000 events. As the increased statistics from the smaller run is negligible and the possible systematic effects from using two separate runs of the same beam energy are small due to the minimal time gap between the runs, this analysis only considers the one high statistics run per beam energy. The 2 GeV energy point is omitted for containing a large admixture of electrons and multi-particle events as shown in Figure 4.1, a very wide beam profile due to multiple scattering in beam instrumentation and air downstream of the final selection magnet (see subsection 4.3.2) as well as inefficient and imprecise determination of the layer of first hard interaction, leading to an impure selection of pions for further analysis.

For each run, averaged longitudinal shower profiles are compared in data and simulations to assess the accuracy of the simulation models. Furthermore, the energy response, linearity and energy resolution of the combined calorimeter system is extracted from data and compared to simulations, using both the standard energy reconstruction as well as the software compensation scheme presented in the previous section.

4.8.1. Pion Shower Profiles

The comparison of pion shower profiles in data and simulations gives insights into the general deposition scale as well as the modelling of the geometries of the sub-detectors and their longitudinal alignment. The quality of the description of pion shower profiles is a direct measure of the validity of the simulation model.

The distribution of reconstructed FHI layers (see subsection 4.4.2) for 32 GeV pion events in data and simulations is shown in Figure 4.41. The upper FHI layer containment cut of the pion selection is not applied in this plot, to show the full range of reconstructed FHI layers. A reduction of efficiency in selecting events with shower start early in the ScECAL (around layers 5–8) is seen as a tapered off lower edge of the FHI spectrum. This is most likely due to shower albedo, causing inefficiencies in reconstructing a clean primary track up to the FHI layer.

The mean longitudinal profile of all pion shower events passing the event selection for 32 GeV beam energy is shown in Figure 4.42. The low mean deposition in the first around five layers is a consequence of the pion event selection (FHI layer $\geq$5). The low mean deposition in the last AHCAL layers points to good average shower containment even without including the TCMT layers. The general shape of the profile is well described by all physics lists, including the dip in response from lateral leakage in the ScECAL around the transition region between the ScECAL and AHCAL. Simulations with the FTFP_BERT_HP physics lists show a peak in the ratio to data around layer 5 which is not present for QGSP_BERT_HP. All studied simulations overestimate the mean depositions by around 5% regardless of beam energy, as already noted in subsection 4.7.1. This difference is larger than the systematic uncertainty on the full response from the MIP calibration or saturation effects.

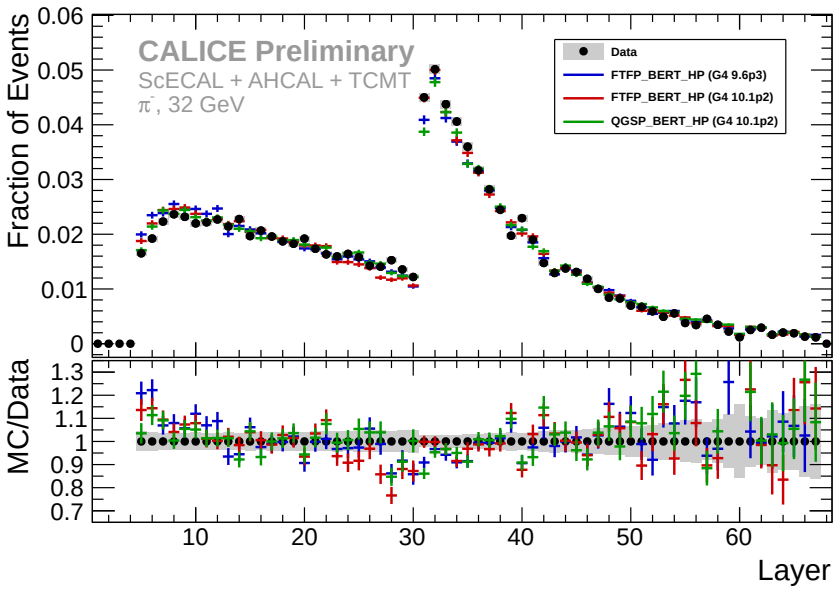

Figure 4.41.: *Reconstructed FHI layer for 32 GeV π^- (Run 560474) in data and different simulation physics lists [108]. The distributions for all beam energies are shown in section D in the Appendix.*

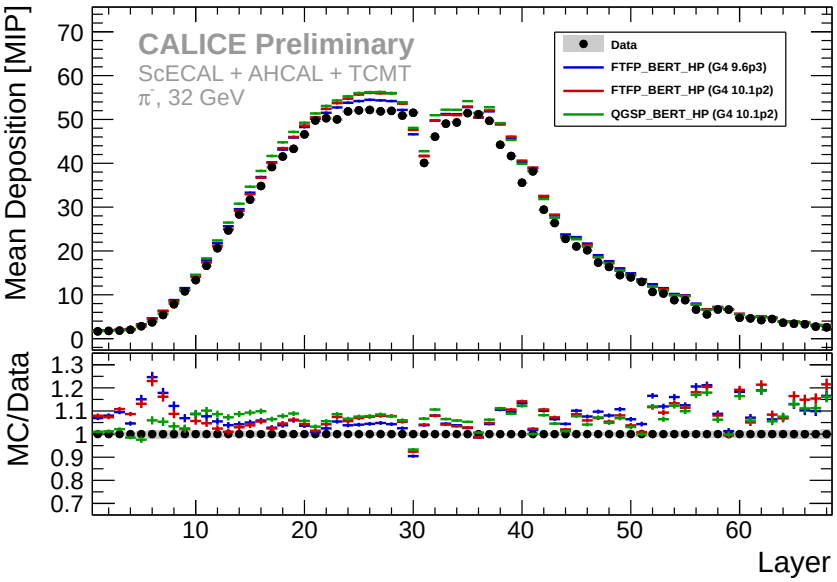

Figure 4.42.: *Averaged longitudinal shower profile for 32 GeV π^- events in data and different simulation physics lists [108]. Depositions in the ScECAL are shown in layers 1–30, layers 31–68 are AHCAL layers. The distributions for all beam energies are shown in section D in the Appendix.*

Further insight into the longitudinal development of pion showers is gained by plotting the shower profile as a function of distance to the reconstructed shower start layer. Such shower profiles are shown in Figure 4.43, separately for showers starting in the ScECAL and in the AHCAL. For events with reconstructed shower start in the ScECAL, the shower profiles predicted by the FTFP_BERT and QGSP_BERT simulation models vary significantly, under and overestimating depositions compared to data in different layers, especially for high beam energies. Most of the data points lie between the predictions of the different physics lists used. FTFP_BERT_HP in GEANT 4 10.1p2 shows slightly longer showers than GEANT 4 9.6p3.

In events with reconstructed FHI layer in the AHCAL, the examined simulation models agree well with each other. The agreement between data and simulation is on a similar level, with similar features in the ratio, as in a dedicated study [122]. In the AHCAL, FTFP_BERT_HP shows slightly shorter showers in GEANT 4 10.1p2 than in GEANT 4 9.6p3, opposite to the behaviour in the ScECAL.

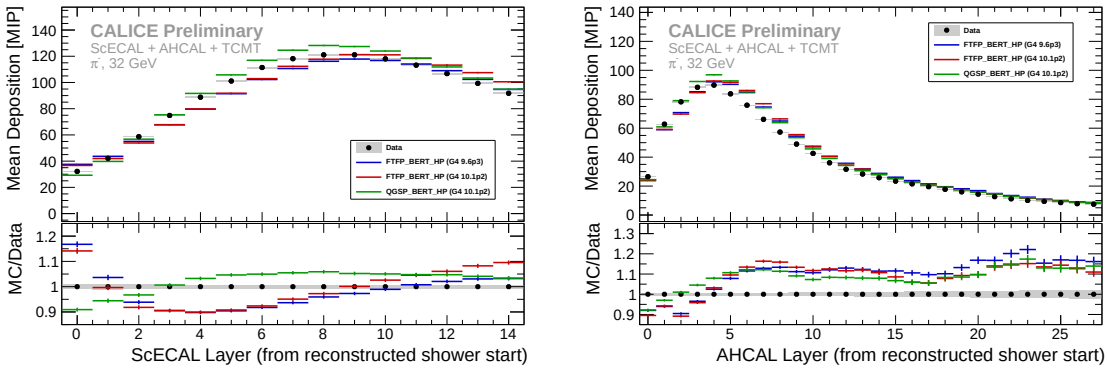

(a) *Shower start in ScECAL layer 5–16.* ***(b)*** *Shower start in AHCAL layer 0–10.*

Figure 4.43.: *Averaged longitudinal shower profile for 32 GeV π^- events in data and different simulation physics lists [108]. Depositions are plotted as function of distance to reconstructed FHI layer. The distributions for all beam energies are shown in section D in the Appendix.*

All longitudinal pion shower profiles are reasonably well described by simulations, with significant discrepancies showing between simulation models for the higher end of beam energies in the high-Z absorber of the ScECAL. A general overestimation of depositions by around 5 % is observed in simulations, which should not influence the energy reconstruction, as it is absorbed into the individually optimised energy reconstruction weights.

4.8.2. Energy reconstruction and linearity

For each event the particle energy is reconstructed with the techniques described in section 4.7, without use of the known beam energy. For each run the spectrum of obtained reconstructed energies is fitted with a Novosibirsk function (see Figure 4.36, Figure D.2 in the Appendix), which is better suited than a Gaussian to describe the obtained partially asymmetric energy distributions as explained in [123]. The energy response and resolution

are extracted from the fitted function as its mean and RMS, calculated using Monte-Carlo integration.

The energy reconstruction of data and all simulation physics lists is performed with the parameters optimised from their own datasets. A systematic uncertainty of 1% on the MIP scale is added in quadrature to the negligible statistical error of the response. The effects from the modified air gap in simulations and the shifted saturation scales in data show negligible impact here. The plotted residual is defined as the relative deviation of the mean reconstructed energy from the known beam energy.

The mean reconstructed energies in data agree very well with the beam energy with all deviations better than 3%, as shown in Figure 4.44. The linearity observed in simulations shows a small non-linearity with no deviation from the beam energy exceeding 5%.

Reconstructing the particle energy using the software compensation scheme described in subsection 4.7.2, the linearity of data and simulated events is better than 3%.

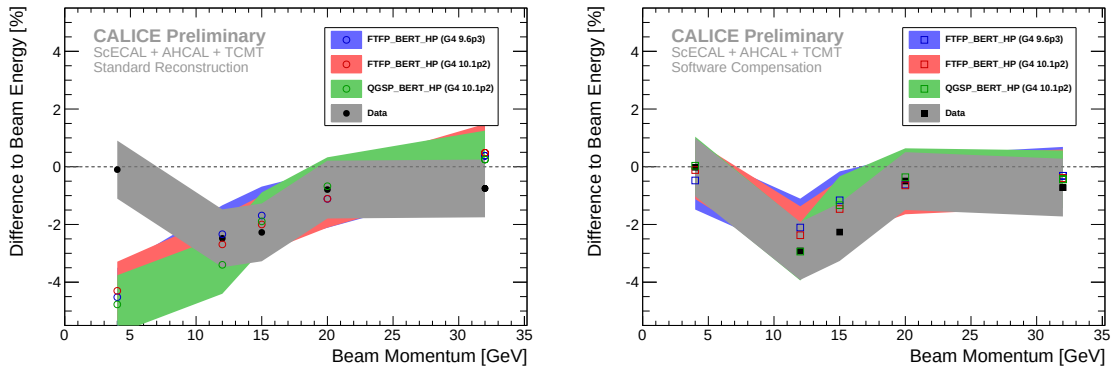

(a) *Standard Reconstruction* **(b)** *Software Compensation Reconstruction*

Figure 4.44.: *Residual of mean fitted reconstructed energy over beam energy in data and different simulation physics lists [108].*

4.8.3. Energy resolution

The single pion energy resolution of the combined scintillator-SiPM calorimeter system for both discussed energy reconstruction schemes is the central result of this analysis, especially in comparison to the results of a previously published analysis of only the AHCAL and TCMT [88].

The relative energy resolution of each run is calculated from the RMS and mean of the Novosibirsk function fitted to the reconstructed energy spectrum for standard and software compensation reconstruction . In simulated runs, the difference in resolution between the standard simulation and the simulation with modified airgap is used as fully correlated systematic uncertainty. Shifting the saturation scale has no significant effect on the reconstructed single energy resolution in data and is thus omitted as a systematic uncertainty. The systematic uncertainty due to the remaining contaminations in the selected

beam events are also considered negligible, as discussed in section B of the Appendix. The statistical uncertainty on each resolution point is small.

Using the standard energy reconstruction, the data points are generally very well described by the simulations, as shown in Figure 4.45(a). QGSP_BERT_HP produces the best agreement with data while the FTFP_BERT_HP samples show small deviations either in the low or high beam energy region of the sample.

The software compensation reconstruction leads to a relative improvement of the energy resolutions in data runs between 10 % to 20 % (2 % to 3 % absolute), depending on the beam energy, see Figure 4.45(a). The resolution of the simulated samples agrees between physics lists when using software compensation reconstruction, but generally and significantly overestimates the achievable resolution improvements by relative 5 % to 10 % compared to data, as shown in Figure 4.45(b).

The distribution of the ratio in reconstructed energy between the standard and software compensation reconstruction $r = \frac{E_{\text{rec}}^{\text{SC}}}{E_{\text{rec}}^{\text{Standard}}}$ is shown in Figure 4.46 for 32 GeV pions. In all simulation models an overestimation of events around $r \approx 0.85$ is observed, corresponding to events with too high standard reconstructed energy and thus likely a large electromagnetic fraction in the event. This hints towards an overestimated production of π^0/η particles in the simulated pion showers. The observed shoulder in the spectra from simulation is more pronounced in the FTFP_BERT_HP physics lists when running on GEANT 4 10.1p2, in line with the increased π^0 production compared to the previous version GEANT 4 9.6p3 [50].

The combined scintillator-SiPM calorimeter system of several readout granularities, samplings and absorber materials is reasonably described in simulations, even when complex energy reconstructions, utilising the detailed structure of individual showers, are employed, although discrepancies are seen when using the software compensation energy reconstruction.

Figure 4.47 compares the energy resolutions obtained in this analysis from data to the energy resolutions obtained from [88], in which only pion showers with reconstructed FHI layer in the AHCAL are considered. The resolutions obtained for both analyses are in good agreement, indicating that the energy reconstruction in the combined system with different absorber materials and sampling fractions maintains the good single pion energy resolution of the AHCAL of around $\frac{57.6\,\%}{\sqrt{E[\text{GeV}]}} \oplus 1.6\,\%$ using the standard reconstruction and $\frac{44.3\,\%}{\sqrt{E[\text{GeV}]}} \oplus 1.8\,\%$ using the local software compensation reconstruction [88].

4.8.4. Applying the Software Compensation Weights from Simulation to Data

To estimate the influence of the deviations in optimised software compensation weights between data and simulations, and to test whether software compensation weights obtained from simulated events can be used to reconstruct data events, Figure 4.48 shows the energy resolution and linearity of data runs reconstructed using weights optimised from both data and simulation. Only the simulation weights optimised from QGSP_BERT_HP in Geant 4 10.2p1 are used for this comparison, as the difference between weights of different simulation physics lists is small. Furthermore only the software compensation specific weights $\alpha_i, \beta_i, \gamma$ are used from simulation, while the standard reconstruction weights $w_{\text{ECAL}}, w_{\text{HCAL}}$ are used from data to set the correct energy reconstruction scale (see subsection 4.7.1).

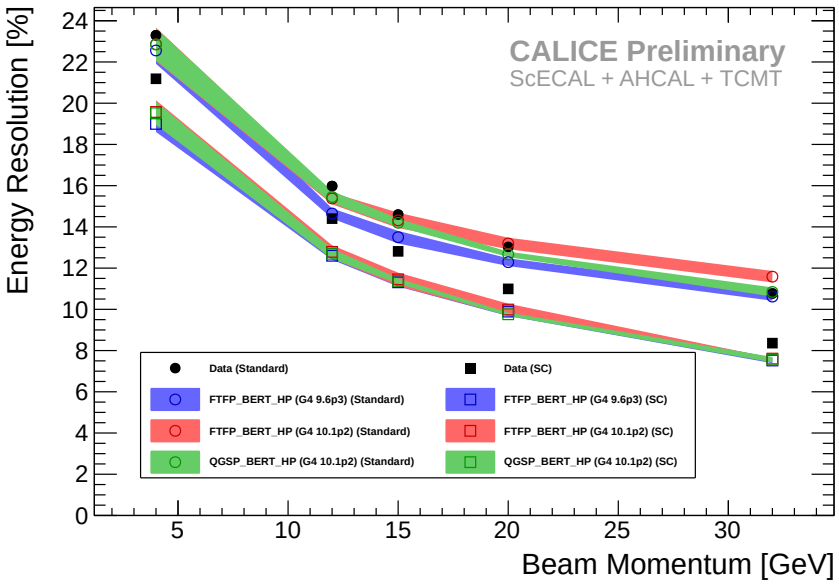

(a) *Energy Resolutions [108]*

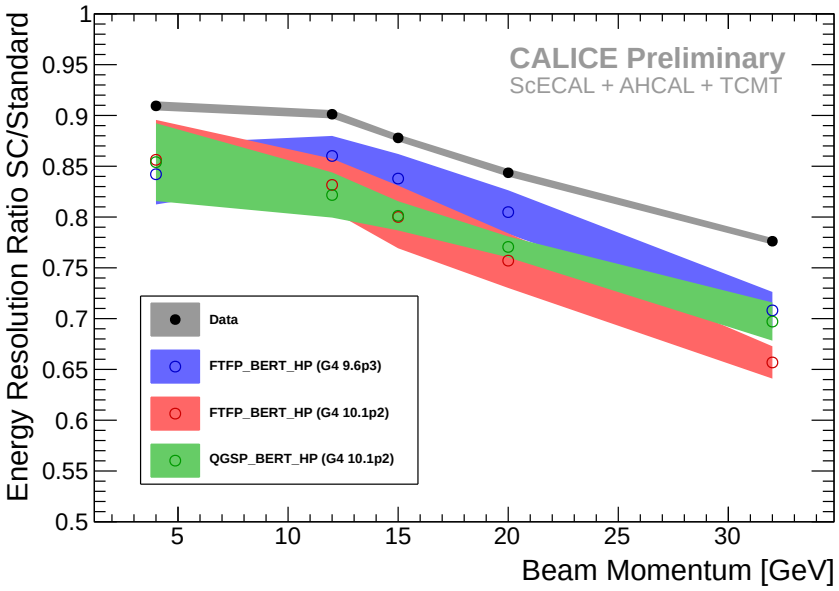

(b) *Resolution improvement with software compensation [108]*

Figure 4.45.: *Reconstructed energy resolution as a function of beam energy in data and different simulation physics lists for the standard and software compensation energy reconstruction. All plotted values are tabulated in Table D.1 in the Appendix.*

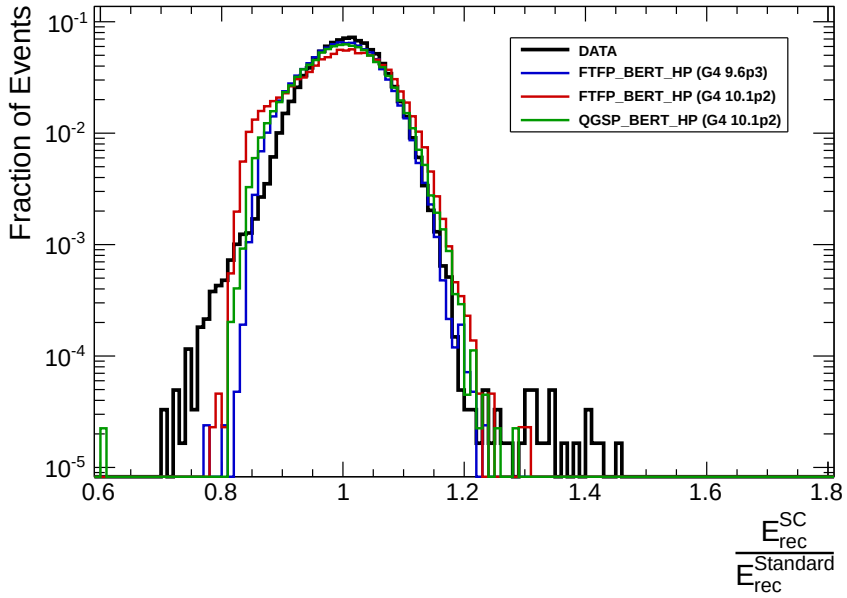

Figure 4.46.: *Distribution of ratios between reconstructed energy in standard and software compensation reconstruction in data and simulations for 32 GeV pion events. The observed shoulder around $r \approx 0.85$ hints at an overestimated production of π^0/η particles in the simulated pion showers.*

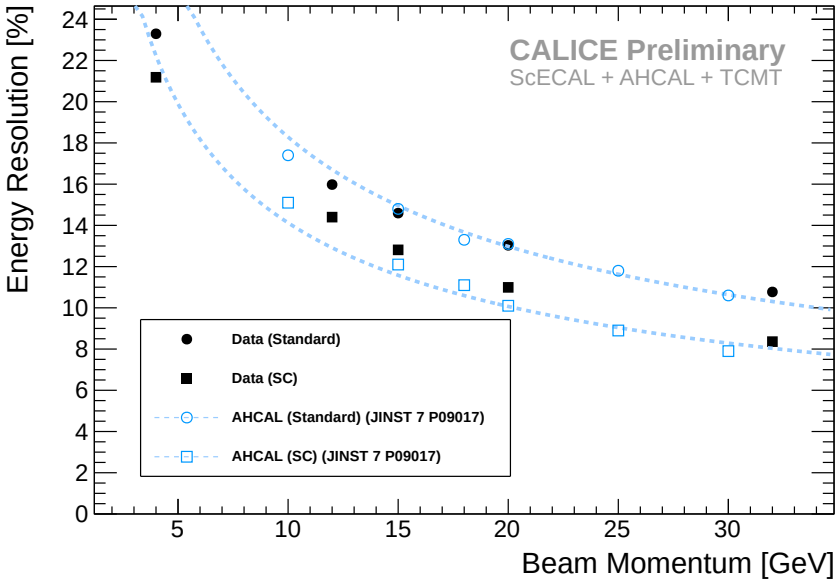

Figure 4.47.: *Single pion energy resolutions with standard and software compensation reconstruction from the combined ScECAL+AHCAL+TCMT system compared to resolutions obtained from AHCAL+TCMT in [88]. Plot taken from [108].*

Applying the software compensation weights obtained from simulations to data events improves the energy resolution slightly by relative 1 % to 3 %. However, the achieved linearity is deteriorated, showing generally larger deviations than for weights derived from data, with additional fluctuations of magnitude similar as seen in the resolution of 1 % to 4 %. Although there are significant differences in the first two and last ScECAL hit energy bin weights between data and simulation, applying weights optimised from simulation onto data events does not deteriorate the energy resolution of the combined system and only very slightly worsens the deviations from linearity to still acceptable $\leq$4 % in the energy range examined in this analysis.

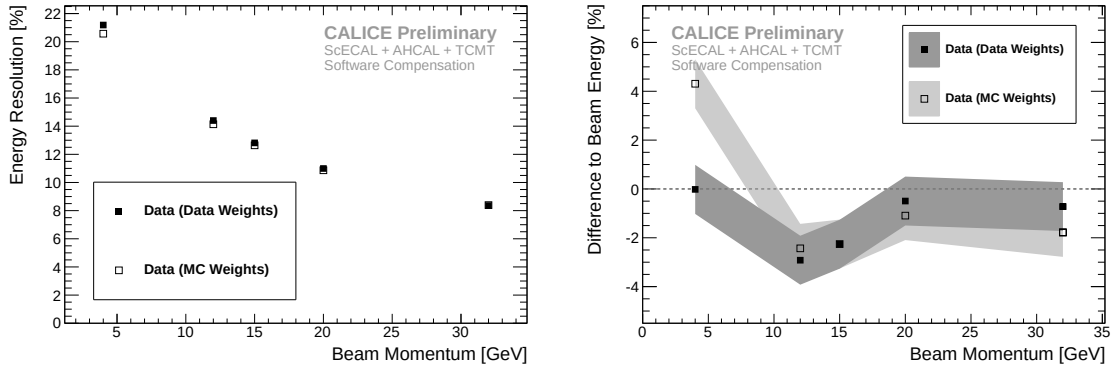

(a) *Energy Resolutions* ***(b)*** *Linearity Residual*

Figure 4.48.: *Reconstructed energy resolutions and linearity for the data sample when using software compensation weights derived from data and simulation (QGSP_BERT_HP in Geant 4 10.2p1) for energy reconstruction [108]. Reconstructing the data sample with software compensation weights derived from simulations, the energy resolution is marginally improved while the linearity is slightly deteriorated.*

4.9. Summary and Outlook

This chapter presents results obtained with the combined scintillator-SiPM calorimeter system consisting of the ScECAL, AHCAL and TCMT in the energy range 4 GeV to 32 GeV.

The simulation model of the ScECAL is validated with electromagnetic interactions from MIP signals in single cells up to full shower profiles. All observables show good agreement between data and simulation except for the hit energy spectra which show differences in the high end tails. This is likely due to a combination of underestimated shower radii in simulation and imperfect saturation correction in data. The resulting influence on pion measurements is expected to be small. The systematic uncertainties from these effects are propagated into the pion results. The ScECAL response and resolution to electron showers is well described in the simulation model.

A clean selection of single particle events is obtained by using the information from the beam instrumentation installed in the beam line and additional reconstruction of features of the shower topology to identify additional particles entering the detectors. Possible

biases introduced by the pion selection are checked in simulated samples and found to be negligibly small. A detailed estimation of different possible remaining beam contaminations and their influence on the extracted energy response and resolution are given and found to be similarly negligible.

Longitudinal profiles of pion showers show good agreement between data and simulation, with a general deposition overestimation of around 5 % in all tested simulation physics lists. In the ScECAL, the longitudinal shower profile as a function of distance to reconstructed FHI layer shows considerable differences between simulation models, especially for high beam energies.

The weights for the standard energy reconstruction agree well in data and simulation, apart from the generally slightly overestimated depositions. The linearity deviation of the pion standard energy reconstruction is <5 % in simulation and <3 % in data. The energy resolution of the standard reconstruction is well described by all simulation models.

The novel implementation of a local software compensation scheme devised for this analysis does not enforce any functional dependence of weights between bins in hit energy density. The weight dependence on particle energy is parametrised per hit energy bin. Counting hits instead of summing up depositions in the first two bins suppresses Landau fluctuations and slightly improves the energy resolution. The hit energy and beam energy dependent weights used for the software compensation reconstruction are well described in the AHCAL. Significant discrepancies of these weights are observed in some ScECAL bins. This is potentially connected to, but not adequately explained by, the observed deviations in the hit energy spectra. Using the software compensation reconstruction, the response linearity deviation improves for data and simulation to <3 %. In data, the energy resolution improves by 10 % to 20 % from applying software compensation. Energy resolution improvements from software compensation are overestimated in simulation by 5 % to 10 % for all beam energies and simulation models.

Both the standard and software compensation energy resolutions in data are in good agreement with resolutions obtained from a similar analysis in which only showers starting in the AHCAL are considered. The good single pion energy resolution of the AHCAL is thus maintained when including the ScECAL into the calorimeter system.

Applying the software compensation weights obtained from simulations to data runs results in practically identical performance numbers, slightly improving the achieved energy resolution while similarly slightly deteriorating the linearity.

The software compensation implementation developed for this study solely relies on the channel hit energy to statistically identify electromagnetic sub-showers in pion showers, which is possible due to the small cell size of the used calorimeter prototypes. However the topology of the measured energy depositions is not at all incorporated into this classification. A modern approach to efficiently decide classification problems are multi variate methods such as support vector machines (SVMs) [124], which take multiple inputs into account to form their output. To classify hits in a shower into electromagnetic and hadronic sub-showers, the hit energy, local hit energy density (taking into account the surrounding calorimeter cells), distance to the reconstructed FHI layer, radial distance to the reconstructed showers axis and more could be used. The weighting factor for each hit could then be parametrised as a function of the SVM output and possibly a limited number of extra parameters such as the shower energy estimate, possibly improving the recon-

structed energy resolution beyond what is achieved with the current software compensation implementation.

5. Validation of the HCAL Simulation for ILD

The full detector simulation of the *International Large Detector* (ILD) is used as a basis for performance studies and contains realistic models of each planned subdetector system. All key geometry parameters are adjustable in software to allow for comparative studies of different geometries and cost optimisation.

To ensure the reliability of the results obtained with the ILD full simulation model, each subdetector has to be modelled as realistically as possible in both geometry and specific readout effects. Ideally each simulated subdetector shows the same performance in the full simulation as in testbeam measurements of prototypes.

This chapter discusses the implementation of the scintillator-SiPM digitisation model described in section 2.7 into the ILD full simulation model and the influence of the digitisation steps on energy depositions and resolutions in the ILD scintillator-SiPM hadron calorimeter. The calorimetric energy resolutions obtained from the ILD model are compared with simulations and data of the AHCAL testbeam prototype.

5.1. Simulation Setup

The study presented here is based on the full ILD detector simulation framework[1)]. As only the HCAL is of interest here, all other subdetectors are removed from the simulation. Digitisation effects are included by using the current version[2)] of the ILDCaloDigi processor (see subsection 5.1.2). All results are obtained using the simulation physics list QGSP_BERT_HP.

In this study two models are set up within the ILD simulation framework. The *ILD baseline model* uses the default ILD HCAL geometry and sampling, with digitisation parameters chosen comparable to what is achieved in the current AHCAL engineering prototype. The *ILD testbeam model* uses geometry parameters and sampling fraction as similar as possible to the AHCAL physics prototype, with digitisation parameters resembling what has been measured in the AHCAL physics prototype. Still some specifics of the AHCAL prototype, such as exact cassette material and composition, cabling material estimations and geometry details, which are included in the dedicated AHCAL testbeam simulation model, cannot be configured in the ILD testbeam model. The ILD testbeam model is used to compare to testbeam data and simulations, while the ILD baseline model extrapolates these results to the performance of a realistic ILD HCAL.

5.1.1. Model Geometry Modifications

The baseline geometry and sampling ratio of the ILD HCAL differs from the sampling ratio of the CALICE AHCAL physics prototype. In order to directly compare measurements

[1)] iLCsoft v01-17-06, Mokka v08-03, ILD model version ILD_o1_v06 and GEANT 4 9.5p2

[2)] as of 03.02.2016, SVN revision 5159

and simulations from the CALICE testbeam campaigns to simulations of the ILD model, its geometry and sampling are adjusted to correspond to the AHCAL testbeam prototype. The ILD baseline sampling consists of 3 mm of scintillator and 20 mm steel per layer, while the AHCAL physics prototype has 5 mm thick scintillator tiles and 21 mm steel absorber plates [76]. As the AHCAL reference pion analysis includes the TCMT, effectively doubling the instrumented calorimeter depth, the number of layers in the ILD testbeam model is increased from 48 to 64. This does not fully cover the added depth of the TCMT and disregards its longitudinally varying sampling, but the depositions in that depth and their influence on the resolution are expected to be small for the shower energies discussed here, so the results should not crucially depend on the TCMT modelling.

The AHCAL testbeam measurements used for comparison [88] are recorded with the beam perpendicular to the layer structure of the prototype. In all simulations with the ILD model the beam gun is thus aimed at the center of an HCAL barrel segment, perpendicular to its front face as sketched in Figure 5.1.

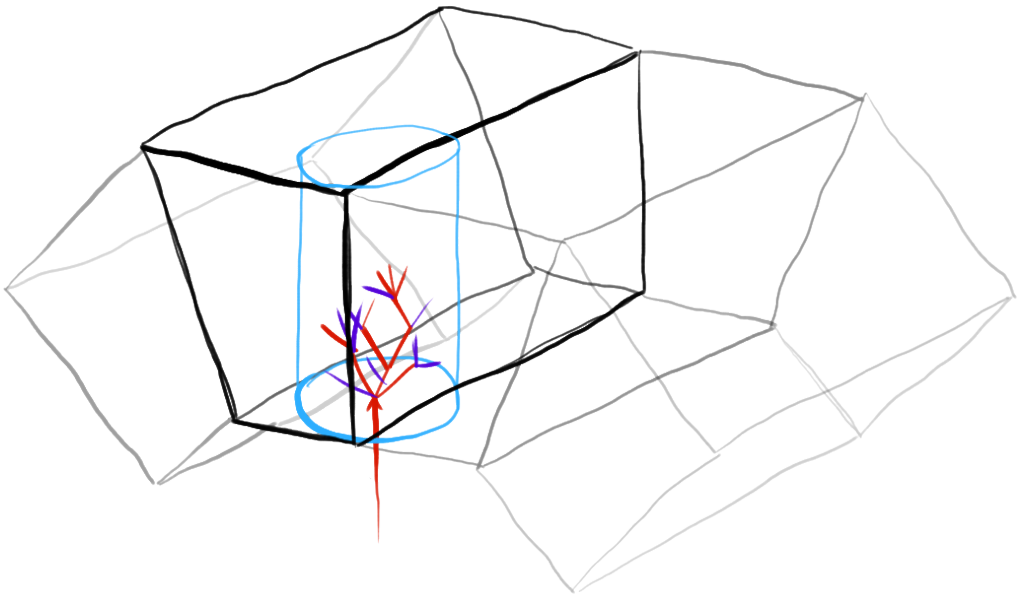

Figure 5.1.: *Sketch of a hadron shower in the ILD HCAL barrel. The HCAL barrel structure is drawn in black, the incident particle in red. The light blue cylinder corresponds to the range cut applied to maintain a similar fiducial volume to the AHCAL testbeam prototype.*

5.1.2. ILDCaloDigi

ILDCaloDigi is a Marlin processor for realistic digitisation and reconstruction of simulated hits in the ILD calorimeters, implementing technology specific effects for both scintillator-SiPM readout as well as pure silicon readout [125]. The scintillator-SiPM digitisation (as discussed in subsection 2.7.4) was implemented into ILDCaloDigi as part of this thesis. Irrespective of readout technology, ILDCaloDigi is capable of applying thresholds in hit energy and hit timing, simulation of dead cells, correlated and uncorrelated miscalibrations per cell as well as Gaussian electronics noise contributions. For scintillator-SiPM calorimeters

the same statistical treatment as described in section 2.7 is used. Additionally, gain non-uniformities between SiPM pixels on the same sensor are be modelled as additional Gaussian smearing proportional to the square root of the number of fired pixels. The conversion factors from deposited energy to the MIP scale (*MIP2GeV*) and MIP scale to SiPM pixel scale (*lightyield*) have to be set up manually.

The MIP2GeV factors are extracted individually for both models from a sample of muons traversing the HCAL barrel perpendicular to the layer structure. The lightyield is assumed to be 15 $\frac{\text{px}}{\text{MIP}}$ for a realistic ILD detector (see subsection 3.2.1) and set up as 13.7 $\frac{\text{px}}{\text{MIP}}$ as measured for the AHCAL physics prototype [76]. Energy depositions more than 150 ns after the propagation time corrected initial particle incidence are excluded to be able to directly compare with the AHCAL prototype. The electronics noise of 0.3 px is larger than what is measured from the current hardware of the AHCAL engineering prototype [94, 97], but does not significantly influence the overall performance and simplifies fits to the MIP spectra by smearing the single photon peaks. The used pixel non-uniformity of 10 % is a conservative estimate, modern SiPMs typically show pixel uniformities better than 5 % [126]. The optical crosstalk between adjacent AHCAL tiles scintillator is not modelled in ILDCaloDigi as most investigated tile concepts for the AHCAL engineering prototype tiles plan to individually wrap each tile in reflective foil, eliminating optical crosstalk. The effect of optical crosstalk on the energy resolution is expected to be small for standard reconstruction schemes (see subsection 4.7.1) and thus should not notably influence the comparison to testbeam results.

5.2. Digitisation Effects on Shower Measurement

The used digitisation parameters are grouped into steps of increasing realism as tabulated in Table 5.1. The *fiducial cut* is excluding depositions outside of a cylinder of 1 m diameter centered around the particle incidence position to approximately equalise the fiducial volume of the ILD simulation and the AHCAL prototype.

The effects of the digitisation steps on a muon hit energy spectrum are shown in Figure 5.2. The width of the raw spectrum is much narrower than after realistic digitisation. This is due to the Poissonian fluctuations in detected photons as described in section 2.7. The application of the SiPM digitisation model without any noise effects results in a hit energy spectrum quantised to integer numbers of fired SiPM pixels, which is smoothed out by the inclusion of electronic noise and pixel non-uniformity in the final step.

In order to study the effects of the digitisation model on particle shower measurements, data sets with electrons and pions of various energies are simulated. Their response and resolution are extracted from Gaussian fits to the spectra obtained by summing up all energy depositions (within timing and fiducial volume cuts, if applicable) for each simulated beam energy. Figure 5.3 shows the response and resolution obtained for electrons and pions at 30 GeV for both the ILD baseline model and the ILD testbeam model.

The electron response is not significantly influenced by the cuts on timing and fiducial volume. This is expected as the development of electron showers is quasi-instantaneous and electron showers are well contained in the fiducial volume of the AHCAL prototype. The application of the hit energy threshold is reducing the energy sum by a few percent. This reduction in response is slightly smaller with the ILD baseline model than in the ILD testbeam model, because of the slightly higher MIP efficiency of the 15.0 $\frac{\text{px}}{\text{MIP}}$ lightyield

Table 5.1.: *Simulation and digitisation parameters for the ILD baseline model and ILD testbeam model.*

	ILD Baseline	Testbeam	
Scintillator Thickness	3 mm	5 mm	
Absorber Thickness	20 mm	21 mm	
Layers	48	64	
MIP2GeV Factor	489.6 $\frac{\text{keV}}{\text{MIP}}$	817.0 $\frac{\text{keV}}{\text{MIP}}$	Raw
Fiducial Cut	yes	yes	+Fiducial
Timing Cut	−10 ns..150 ns	−10 ns..150 ns	+Timing
Hit Energy Threshold	0.5 MIP	0.5 MIP	+Threshold
Lightyield	15.0 $\frac{\text{px}}{\text{MIP}}$	13.7 $\frac{\text{px}}{\text{MIP}}$	
Number of SiPM Pixels	2000 px	1156 px	+SiPM statistics
Electronic Noise	0.3 px	0.3 px	
Pixel Non-uniformity	10 %	10 %	Realistic

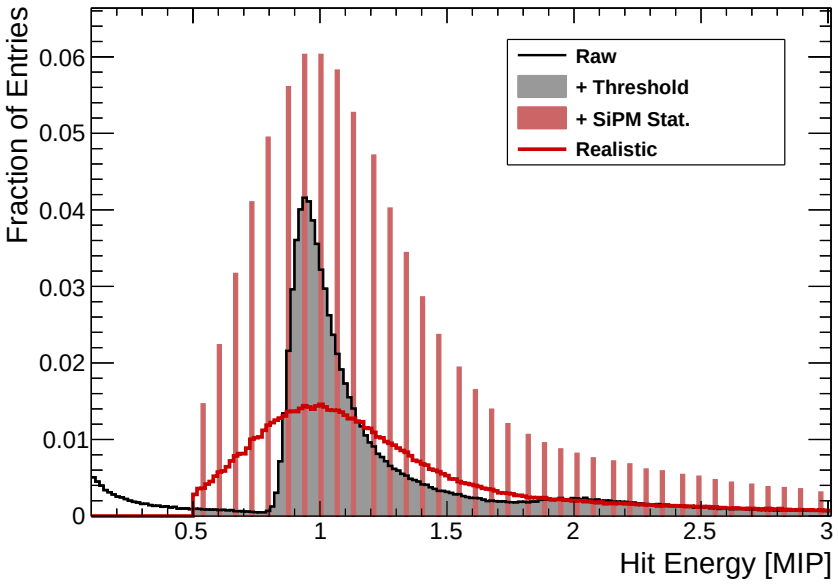

Figure 5.2.: *Hit energy spectrum of a 50 GeV muon for the different steps of the digitisation as tabulated in Table 5.1. The fiducial and timing cuts are not shown separately as they do not influence the spectrum.*

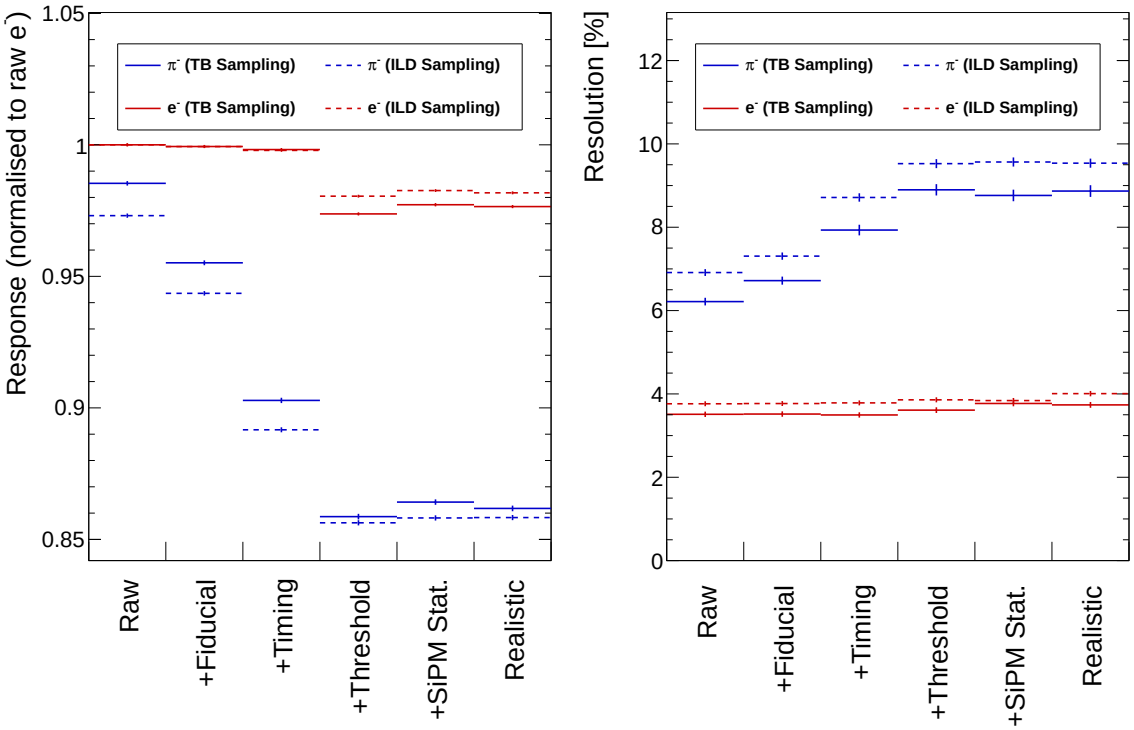

(a) *Response* ***(b)*** *Resolution*

Figure 5.3.: *Response and resolution of* 30 GeV *electrons and pions for different steps in the digitisation as explained in Table 5.1, for both the ILD baseline model and the ILD testbeam model (TB).*

assumed for the ILD baseline model compared to the 13.7 $\frac{px}{MIP}$ for the ILD testbeam model. The steps of including the SiPM statistics model and noise effects do not further alter the electron response.

The raw response of pions, normalised to the electron response, is higher for the ILD testbeam model than for the ILD baseline model. This is likely due to the increased calorimeter depth in the ILD testbeam model, causing relatively more longitudinal leakage in the ILD baseline model, although influences on $\frac{e}{h}$ from the different samplings are also possible (see section 1.5). Excluding depositions outside of the defined fiducial volume reduces the response by a few percent from transverse leakage. The timing cut further reduces the pion response by around 5 % in both models. Application of the hit energy threshold lowers the energy sum by further 5 %. Similar to the effect in electron showers, the response reduction by the hit energy threshold is slightly larger for the ILD testbeam model than with the ILD baseline model. The relative loss in response from the hit energy threshold is larger for pions than for electrons, which is explained by the larger extension of pion showers compared to electron showers. A similar total energy deposition in a significantly larger volume reduces the average deposition density and thus hit energy, increasing the relative loss of response from the constant hit energy threshold.

After the hit energy threshold step the response relative to electrons is coincidentally very similar between ILD testbeam model and ILD baseline model. The influence of SiPM and noise effects on the pion response are negligible. Notably the $\frac{e}{\pi}$-ratio is nearly compensating in raw hits at 30 GeV. With the ILD baseline model the $\frac{e}{\pi}$-ratio is slightly higher for raw hits. It is unclear whether this is solely due to longitudinal leakage, or also caused by a different invisible energy fraction due to surface effects arising from the specific geometry. Further studies would be needed to conclude on this matter.

The resolution of electrons, as shown in Figure 5.3(b), is barely influenced by any of the digitisation steps. This is expected from the timing cut, fiducial cut and SiPM effects, as they do not significantly influence the response. It is however remarkable that the hit energy threshold does not significantly influence the energy resolution, hinting that the energy information carried from the lowest energy hits in electromagnetic showers is small. The difference in sampling fraction shows in form of a slightly worse energy resolution of the ILD baseline model. A small loss of resolution is observed from the last step of adding noise contributions, especially for very high electron energies $\gtrsim$ 80 GeV. This is explained by the very highest amplitude hits in the core of such showers generating high SiPM saturation. The functional dependence of the reconstructed hit energy on number of hit SiPM pixels in that region of hit energies is very steep (see section 2.7) and thus the influence of noise addition, although mostly irrelevant for the full energy resolution, is amplified. However this effect is likely of no relevance in realistic applications, as the occurrence of single electrons above 50 GeV in the HCAL is expected to be very rare at a future e^+e^--collider. Single electrons generated in the primary collision will shower in the ECAL, with only minor fractions of deposited energy expected in the HCAL. Electromagnetic sub-showers that are initiated in the HCAL from π^0/η decay (see subsection 1.3.3) only carry fractions of the initial particle's energy. Furthermore each initial particle itself only carries a fraction of the full jet energy. With the jet energy effectively being limited to half the center-of-mass energy of the collider ($\approx$ 500 GeV for ILC), this makes high energy electromagnetic sub-showers in the HCAL extremely uncommon.

The energy resolution of pions is affected about equally by the fiducial cut, timing and the application of the hit energy threshold. The influence of SiPM statistics and noise effects is negligible. The resolution of the ILD baseline model is worse by around 1 % (absolute) for all steps of digitisation at 30 GeV, which is expected from the lower sampling fraction. The full loss of energy resolution from the digitisation steps is around 3% absolute (60% relative). The relative loss of resolution is thus several times larger than the relative loss of response.

5.3. Testbeam Comparison

The resolution dependence on beam energy for both studied ILD model configurations is compared to the published values obtained with the CALICE AHCAL for electrons in Figure 5.4 and for pions in Figure 5.5.

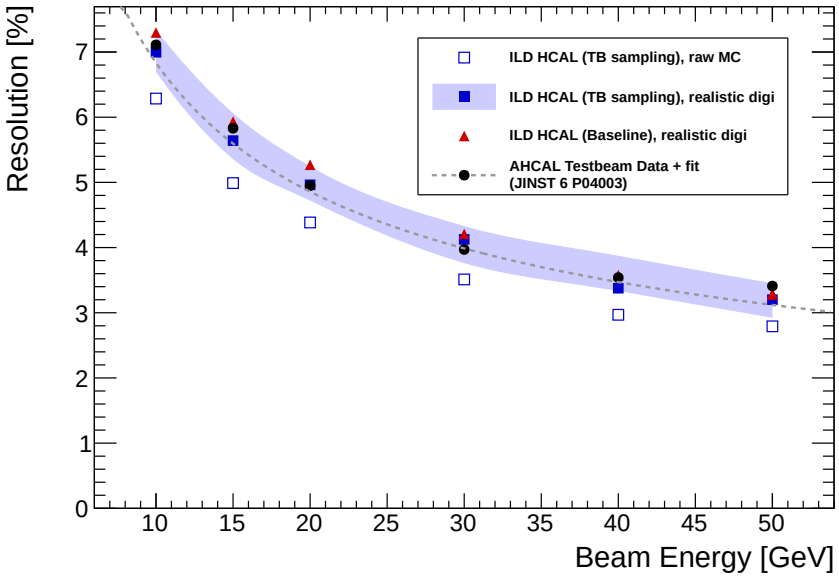

Figure 5.4.: *Electron energy resolution comparison of AHCAL prototype data, ILD testbeam model and ILD baseline model.*

Cells that are identified as unusable (see section 2.6) in the AHCAL data are disabled in the AHCAL testbeam simulations. As the exact pattern of dead cells in the AHCAL cannot be transferred to the ILD model, only the fraction of dead cells is used to make the ILD simulation results comparable to the published AHCAL results.

The fraction of dead AHCAL cells in the electron analysis is taken as 2 % [112]. To estimate the systematic uncertainties from the unmodelled exact distribution of dead cells in the ILD simulations, digitisations with 0% and 4% dead cells are used to define the systematic error band. The statistical errors on the fits are smaller than the used markers.

The electron shower resolution from the ILD testbeam model agrees very well with the data points from [112]. The influence of the digitisation is divided equally between the dead

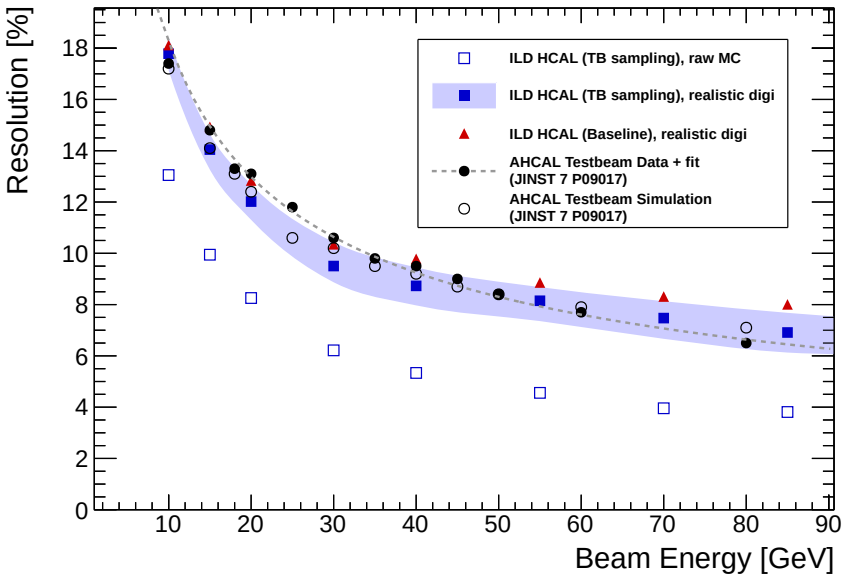

Figure 5.5.: *Pion energy resolution comparison of AHCAL prototype data, AHCAL prototype simulation, ILD testbeam model and ILD baseline model.*

channel fraction and the other digitisation effects, shifting all observed resolutions up by around 1%. The ILD baseline model simulation shows less than 0.5% worse resolutions from the reduced sampling fraction.

Depending on the beam period, the fraction of dead cells in pion beam runs is reported between 2 % to 7 % [34, 76, 84]. The fraction of dead cells in the ILD simulation is thus set to 5 %, using 0 % to 10 % to cover systematic uncertainties in the dead cell fraction and exact dead cell distribution. In the published AHCAL pion energy resolution analysis a cut on the layer of the first hadron interaction (see subsection 4.4.2) is performed, reducing the average longitudinal leakage of the sample. This event selection is not applied on the simulation shown in this chapter, as currently no reconstruction of the first hadron interaction layer is available for the ILD model, possibly biasing the results of the ILD simulation towards worse resolutions for high beam energies.

The agreement between AHCAL testbeam data and the ILD testbeam model simulation is reasonable considering the general inaccuracies of hadron shower simulations. The influence of digitisation effects on the pion energy resolution is much larger than for electrons, worsening the resolution by an absolute 4 % (absolute) across the full studied energy range. The ILD testbeam model simulation however matches the AHCAL testbeam simulation very well.

5.4. Conclusions

The good agreement between the results obtained from the AHCAL testbeam data and the ILD testbeam model simulation indicates a sufficient modelling of all relevant aspects of a scintillator-SiPM hadron calorimeter in the ILD simulation model. This is the first study using a realistic scintillator-SiPM digitisation model in the ILD HCAL simulations. However the influence of this digitisation is small, so the ILD full simulation physics samples simulated before the implementation of these effects can still be considered valid, as timing and hit energy threshold cuts with reasonable parameters were already contained in the simulation before.

Summary

Future e^+e^--collider experiments as the *International Large Detector* (ILD) at the *International Linear Collider* (ILC) will require unprecedented jet energy resolutions to reach their ambitious goals in the precision measurement of Standard Model parameters. In order to reach the required jet energy resolution of 3 % to 4 %, *Particle Flow Algorithms* aim to combine the measurements of the tracking system and calorimeters into an optimal jet energy measurement, by reconstructing every particle in a given jet and using the best resolution sub-detector measurement to determine the energy of each particle individually.

Particle Flow Algorithms need to efficiently assign particle tracks from the tracking system to calorimeter depositions, which needs unparallelled spatial granularities in the calorimeter systems. The CALICE collaboration develops prototypes for such novel high-granularity calorimeters. One of the pursued readout technologies consists of plastic scintillator tiles or strips of few cm^2 area, read out individually by *Silicon Photomultipliers* (SiPMs). Several prototypes using this scintillator-SiPM technology have been built and operated in various testbeam campaigns.

This thesis presents the first analysis of a full calorimeter system based on the scintillator-SiPM technology. In the testbeam campaign at the Fermilab testbeam facility in May 2009, the combined scintillator-SiPM prototype calorimeter system consisting of the CALICE *Scintillator Electromagnetic Calorimeter* (ScECAL), the CALICE *Analogue Hadronic Calorimeter* (AHCAL) and the CALICE *Tail Catcher & Muon Tracker* (TCMT) were operated in particle beams of electrons, pions and muons in the energy range up to 32 GeV. The absorber material and sampling fraction of the ScECAL is different from the AHCAL and TCMT, which complicates the reconstruction of shower energies and potentially impacts the achievable energy resolution of showers extending through the whole calorimeter system.

The main challenge in the analysis of data obtained from the Fermilab testbeam facility is the large contamination of beam events with additional particles or particles of different types. A clean selection of single particle events of a given particle type is obtained using the information from the beam instrumentation installed in the beam line and from the reconstruction of features of the shower topology to identify additional particles entering the detectors. The remaining contaminations are found to be small enough to not significantly bias the results. Possible selection biases on the energy response or resolution are found to be negligible in simulation studies.

The study presented here is the first study using the ScECAL simulation model. A detailed validation of the ScECAL model is performed with electromagnetic showers and interactions, ranging from the single cell spectra of MIP particles up to full electromagnetic shower profile and their response and resolution. The agreement between data and simulation is satisfactory apart from a small but significant discrepancy in the hit energy spectra and shower radii. Systematic studies of these deviations show it to be unlikely due to misreconstructed SiPM saturation effects. Adapting the geometry of the ScECAL simulation

model can reduce the observed discrepancies, however not within reasonable ranges of modification.

The analysis of pion data recorded with the combined scintillator-SiPM system aims to extract the energy resolution for single, contained pion showers, both in comparison to different simulations and to the resolutions obtained from a similar setup without the ScECAL.

The longitudinal profiles of pion showers show a good agreement between data and simulation, with a general deposition overestimation of around 5 % in all tested simulation physics lists. In the ScECAL the longitudinal shower profile as a function of distance to shower start shows considerable differences between physics lists, especially for the higher end of beam energies available in this analysis.

Two separate energy reconstruction algorithms are presented in this thesis. The standard reconstruction uses constant weights per sub-detector to reconstruct the primary pion energy. The energy resolutions obtained from the standard reconstruction are well described by all tested simulation models.

The implementation of a software compensation reconstruction developed for this analysis aims to distinguish electromagnetic sub-shower depositions in hadronic showers by the deposited energy in each hit. The implementation differs from a previous software compensation scheme used within CALICE by forcing less dependencies on the shapes of the optimised weights, increasing the number of free parameters but ultimately resulting in a more stable parameter optimisation. The software compensation reconstruction improves the energy resolution of data events by 10 % to 20 %. The improvement in resolution from the software compensation reconstruction is overestimated by around 5 % to 10 % in simulations. Applying the software compensation weights obtained from simulations to data events yields a similar performance compared to the native data weights, slightly degrading the response linearity while even slightly improving the energy resolution.

The single pion energy resolution of the ScECAL+AHCAL+TCMT calorimeter system is very similar to the energy resolution obtained from a previous AHCAL+TCMT analysis in both the standard energy reconstruction ($\approx {}^{58\,\%}/\sqrt{E[\mathrm{GeV}]}$) and the software compensation energy reconstruction ($\approx {}^{44\,\%}/\sqrt{E[\mathrm{GeV}]}$), indicating that the excellent pion energy resolution of the AHCAL is maintained when adding the ScECAL with its different sampling ratio, different absorber material and different $\frac{\mathrm{e}}{\mathrm{h}}$ ratio.

The calorimeter prototypes used in the testbeam analysis presented in this thesis were built to prove the general feasibility of high granularity scintillator-SiPM calorimeters, which they fully accomplished. To demonstrate the scalability of such calorimeters to the size and requirements of a full-scale particle physics experiment as ILD, second generation prototypes with fully integrated readout electronics are developed within the CALICE collaboration. The efficient operation of a second generation scintillator-SiPM calorimeter prototype relies on the careful setup and validation of the operation parameters. A toy-simulation study performed for this thesis shows that the development of scintillator-SiPM tile systems should target a lightyield of 15 $\frac{\mathrm{px}}{\mathrm{MIP}}$ in order to maintain a 95 % MIP efficiency even for 2σ outliers, when assuming a hit energy threshold of 0.5 MIP. An efficient method to extract and validate trigger thresholds positions for all cells of the detector system is presented, requiring only minimal additional data taking during gain calibration runs with the integrated LED calibration system.

A toy simulation of the testbeam readout efficiency of the second generation AHCAL prototype as a function of the ratio of noise rate to beam rate and total system size is described in this thesis. For large testbeam setups consisting of many readout chips, the noise rate to beam rate ratio is not equivalent to the beam data readout efficiency. For a $1\,m^3$ testbeam prototype, a beam rate of five times higher than the noise rate is required in order to reach a 50 % fraction of beam events in the recorded data. This readout specific behaviour is likely not relevant for a full ILD calorimeter, as the number of total noise hits in the full ILD HCAL barrel is expected to be very small, assuming the noise rates of currently available SiPMs as a basis for the calculation.

As part of this thesis, the digitisation algorithm used to efficiently and realistically model the statistical behaviour of single scintillator cells read out by SiPMs is fully validated analytically and in toy model simulations. It is found to be mathematically equivalent to a more accessible but less efficient algorithm. The validated digitisation model is implemented into the ILD HCAL full simulation model. The energy resolutions obtained from the ILD HCAL simulations are in good agreement with the testbeam data obtained with the CALICE AHCAL pysics prototype, when the sampling of the ILD HCAL is properly adjusted to be directly comparable, validating the ILD HCAL full simulation model.

The analyses performed in this thesis showcase that scintillator-SiPM calorimeter systems fulfil the requirements of a future linear collider detector in both granularity and energy resolution. The continuously growing ScECAL and AHCAL engineering prototype will demonstrate the scalability of the concept to the full size needed for ILD or similar multi-purpose particle physics experiments.

Acknowledgements

This thesis and everything leading up to it would not have been possible without the continuous support of many people. I would like to thank these people here, although I am sure I will have forgotten about someone.

First I would like to thank my thesis supervisors and referees. Prof. Christian Zeitnitz always gave me maximum freedom in pursuing my research under his tutelage. Dr. Felix Sefkow always reassured me of his trust in my abilities and enabled all the opportunities I was given during my time at DESY. I profited so much from your guidance and advice about calorimetry, physics and the politics of science, up to how to give a wedding speech and how to prepare a proper Bouillabaisse. You door was always open for questions and discussions of any kind, for which I am truly grateful.

I would also like to thank the other members of my defense committee, Prof. Knechtli and Prof. Helbing, for participating and showing great flexibility in their schedules. A special thank you is in order to Dr. Christian Hölbling for answering my many novice questions about LQFT, which greatly contributed to my successful defense exam.

This thesis would probably not have been finished without the tremendous efforts of Dr. Katja Krüger in personal supervision and proof-reading of presentations, abstracts, paper drafts and this thesis. The countless questions and ideas you discussed with me at all (typically late) times of the day really formed the results of this thesis. Your encyclopaedic knowledge of previous experiments and analyses (especially how things were done "back in H1") and broad interest in all of particle physics really shaped me as a young scientist, for which I will be thankful forever.

I would like to thank the many more DESY seniors for teaching, mentoring and supporting me over the years, especially Marcel "Someday, and that day may never come" Stanitzki, Karsten Buesser, Ralf Diener, Mathias Reinecke, Erika Garutti, Ingrid-Maria Gregor, Karsten Gadow, Vasiliy Morgunov (†), Jenny List, Ties Behnke and others.

The people in the AHCAL project, Ambra, Benjamin, Coralie, Ali, Eldwan, Jiri, Lan, Shaojun, Sebastian and Sarah as well as the DESY FLC group in general, especially Moritz, Felix and Claude, made my work at DESY an unforgettable experience. Over the time I had the pleasure to work with some people that have left DESY in the meantime, especially Mark Terwort, without whom I would probably not have started to work at DESY at all, and Marco Ramilli.

Apart from the FLC group, I would like to thank my friends from other DESY groups, especially Özgür, Tuğba, Artur, Ksenia, Engin, Jasone, Carsten and Masha for pulling me out of the office for dinner and other activities from time to time.

Even though I was in Hamburg for most of the time, my friends and former colleagues in Wuppertal never forgot about me. Especially Mathias was a great help in producing all of the simulations used in the testbeam data analysis and acquainting me to the CALICE

software. Julia made sure to keep me updated about every bit of BUW gossip, making me feel like I never left the group.

Matteo, Kalle and Ralf sparked my interest in bouldering, which really helped me in balancing my life, keeping a level head most of the time.

Last but not least I would like to thank my parents and my brother. You always supported my in every way imaginable and without you I certainly would not be here today. I am deeply grateful for all the advice and strength you gave me over the past 29 years.

Appendix

A. Analytical Resolution of the Binomial SiPM-Model

Mean Response

Starting with the expectation value of the binomial distribution

$$\mathrm{E}\left[B(n_B, p_B)\right] = n_B p_B \tag{A.1}$$

and substituting $n_B = m$, $p_B = \frac{\langle n \rangle}{m} = \frac{f_{\mathrm{sat}}(a,m)}{m}$ as given in subsection 2.7.4 yields

$$\begin{aligned} \langle n \rangle_{\mathrm{binomial}} &= \mathrm{E}\left[B(n_B, p_B)\right] && \text{(A.2)} \\ &= \cancel{m} \frac{f_{\mathrm{sat}}(a,m)}{\cancel{m}} && \text{(A.3)} \\ &= \langle n \rangle_{\text{photon-by-photon}} . \quad \square && \text{(A.4)} \end{aligned}$$

Resolution

Beginning with the variance of the binomial distribution on the saturated scale

$$\begin{aligned} \mathrm{Var}\left[B(n_B, p_B)\right] &= n_B p_B \left(1 - p_B\right) && \text{(A.5)} \\ &= m \left(e^{-\frac{a}{m}}\right) \left(1 - e^{-\frac{a}{m}}\right), && \text{(A.6)} \end{aligned}$$

converting to the unsaturated scale following [87]

$$\begin{aligned} \mathrm{Var}\left[a_{\mathrm{rec}}\right] &= \mathrm{Var}\left[B(n_B, p_B)\right] \left(\frac{d f_{\mathrm{sat}}^{-1}(n,m)}{dn}\right)^2 && \text{(A.7)} \\ &= m \left(e^{\frac{a}{m}} - 1\right) && \text{(A.8)} \end{aligned}$$

yields the resolution of the binomial SiPM model

$$\frac{\sqrt{\mathrm{Var}\left[a_{\mathrm{rec}}\right]}}{a} = \frac{\sqrt{m\left(e^{\frac{a}{m}} - 1\right)}}{a}, \tag{A.9}$$

which is identical to the resolution of the photon-by-photon model in Equation 2.6. $\square$

B. Systematic Influence of the Observed Beam Contamination in Pion Runs

To investigate the systematic influence of the remaining beam contaminations on the fitted responses and resolutions obtained from pion data runs, a simple toy model accounting for the single pion signal and a partially underlying contamination is implemented. The 32 GeV π^- run is used as an example for modelling here, but the results are assumed to be universal for all runs with $\geq$12 GeV beam energy, as the contamination visible in the reconstructed energy spectrum is similar in all these runs.

The toy model consists of a single pion signal model, parametrised as a normalised Gaussian with $\mu_{\text{sig}} = 32\,\text{GeV}, \sigma_{\text{sig}} = 3.5\,\text{GeV}$, corresponding to the around 11 % standard reconstruction energy resolution for 32 GeV pions. The contamination fraction is modelled by adding a Gaussian with $\mu_{\text{bkg}} = 43\,\text{GeV}, \sigma_{\text{bkg}} = 7\,\text{GeV}$, normalised to 2 % of the signal integral as a conservative estimate of the contamination fraction. The assumed signal and contamination shape is shown in Figure B.1 together with the reconstructed energy distribution from the 32 GeV pion data run.

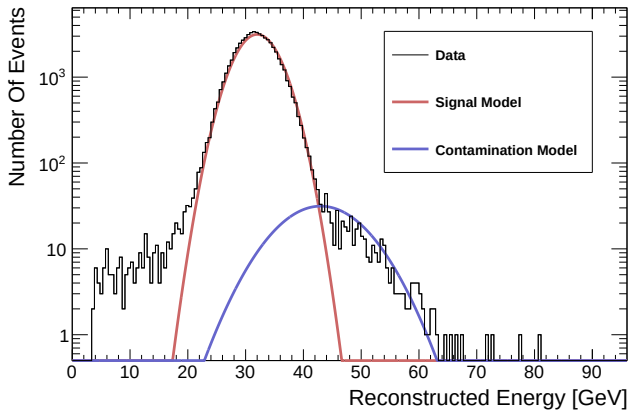

Figure B.1.: *Reconstructed energy distribution of the* 32 GeV *pion data run overlaid with the signal and contamination model assuming a* 2 % *contamination fraction.*

55 000 random numbers (roughly matching the statistics of the data sample) are generated according to the combined signal + contamination toy model. The resulting distribution is fitted with a Gaussian in the fit range used in the data set (around 20 GeV to 44 GeV). The response and resolution are extracted from the fit and are compared to the known true values of the toy signal model. As a crosscheck, the same statistics is generated from the pure signal component of the toy model. This procedure is repeated 5000 times. The resulting distributions of reconstructed toy model energy response and resolution are shown in Figure B.2.

The mean systematic shift in response for the full toy model is very small with below 0.2 %. The systematic shift in resolution is relative 1.3 %, only slightly larger than the statistical fit uncertainty with the statistics in a typical data run after the event selection and on a similar scale as the small possible biases introduced by the event selection given in Table 4.4.

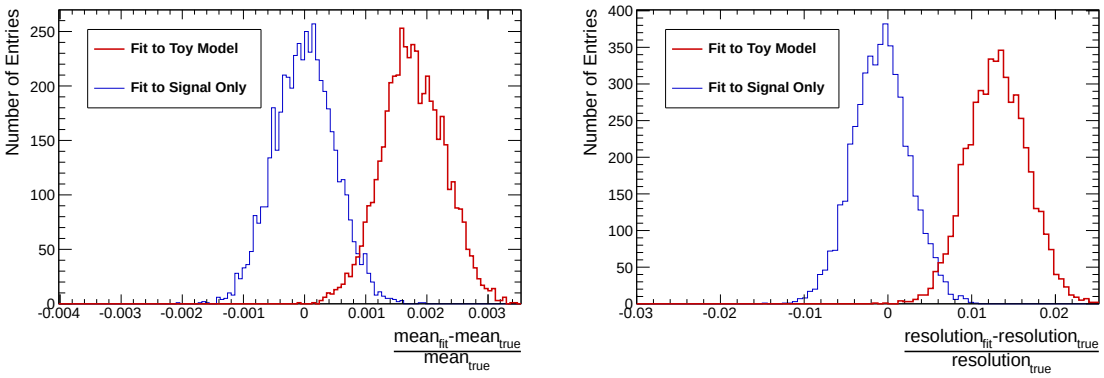

(a) *Fitted Toy Model Response*
$\mu_{full} = 0.0018, \sigma_{full} = 0.0005$
$\mu_{sig} = 0.0000, \sigma_{sig} = 0.0005$

(b) *Fitted Toy Model Resolution*
$\mu_{full} = 0.013, \sigma_{full} = 0.004$
$\mu_{sig} = 0.000, \sigma_{sig} = 0.003$

Figure B.2.: *Distribution of fitted responses and resolutions obtained for the full toy MC model and the signal model only, assuming a 2 % contamination fraction.*

No systematic shifts are observed in the signal-only model as expected. The widths of the distributions are similar for both models, indicating no significant additional systematic fitting uncertainty due to the added contamination.

As the exact contamination fraction and shape of the contamination energy distribution is not known exactly, the extracted systematic shift in resolution of relative 1.3 % is interpreted as an upper limit on the systematic resolution uncertainty due to remaining beam contaminations.

C. Event Selections

Table C.1.: *Cuts applied to select single MIP events and hits from MIP tracks in the ScECAL.*

Name	Beam Energy	Cut
Preselection	All	$1280\,\text{mm} < cog_Z < 1360\,\text{mm}$
	All	$20 < n_{\text{hits}} < 40$
Track Selection	All	Reconstructed ScECAL simple track

Table C.2.: *Cuts applied to select single MIP events and hits from MIP tracks in the AHCAL.*

Name	Beam Energy	Cut
Preselection	All	$2000\,\text{mm} < cog_Z < 2300\,\text{mm}$
	All	$40 < n_{\text{hits}} < 80$
Track Selection	All	Track segment $\cos\phi > 0.99$
	All	Track segment length >10

Table C.3.: *Cuts applied to select single MIP events and hits from MIP tracks in the TCMT.*

Name	Beam Energy	Cut
Preselection	All	$3500\,\text{mm} < cog_Z < 3900\,\text{mm}$
	All	$15 < n_{\text{hits}} < 30$
Track Selection	All	Reconstruced track length ≥12

Table C.4.: *Cuts applied to select single electrons. Cuts marked with $^{(*)}$ are applied only on data, cuts marked with $^{(\dagger)}$ are applied only on simulated events.*

Name	Beam Energy	Cut
Raw	All	beamBit = 1 $^{(*)}$
	All	a10x10Bit = 1 $^{(\dagger)}$
Event Quality	All	vetoBit = 0 $^{(*)}$
	All	2000 < multiADC < 3800 $^{(*)}$
	All	Energy in first 5 ScECAL layers >3.5 MIP
	All	cherenkowBit = 0 $^{(*)}$
	All	cherenkow2Bit = 1 $^{(*)}$
Electron Selection	All	Reconstructed FHI layer ≤ 4
	All	$\frac{E_{\text{sum}}^{\text{ScECAL}}[\text{MIP}]}{E_{\text{sum}}^{\text{ScECAL}}[\text{MIP}]+E_{\text{sum}}^{\text{AHCAL}}[\text{MIP}]} > 0.9$
	All	Reject events passing AHCAL MIP preselection
Multi Particle Suppr.	All	nTracks in AHCAL = 0
	All	nTracks (isolated) in ScECAL = 0
Containment	All	Shower CoG in central quarter of the ScECAL

Table C.5.: *Cuts applied to select single pions. Cuts marked with $^{(*)}$ are applied only on data, cuts marked with $^{(\dagger)}$ are applied only on simulated events.*

Name	Beam Energy	Cut
Raw	All	beamBit = 1 $^{(*)}$
	All	a10x10Bit = 1 $^{(\dagger)}$
Event Quality	All	vetoBit = 0 $^{(*)}$
	All	2000 < multiADC < 3800 $^{(*)}$
	All	Energy in first 5 ScECAL layers >3.5 MIP
	$\leq$4 GeV	cherenkowBit = 0 $^{(*)}$
	$\leq$4 GeV	cherenkow2Bit = 0 $^{(*)}$
Pion Selection	All	Reconstructed FHI layer $\geq$ 5
	All	Reject events passing AHCAL MIP preselection
Multi Particle Suppr.	All	nTracks parallel to beam in outer AHCAL = 0
	All	nTracks (isolated) in ScECAL = 1
Containment	All	reconstructed FHI layer $\leq$ 35
	All	Isolated track in central quarter of ScECAL

D. Additional Information FNAL Testbeam Analysis

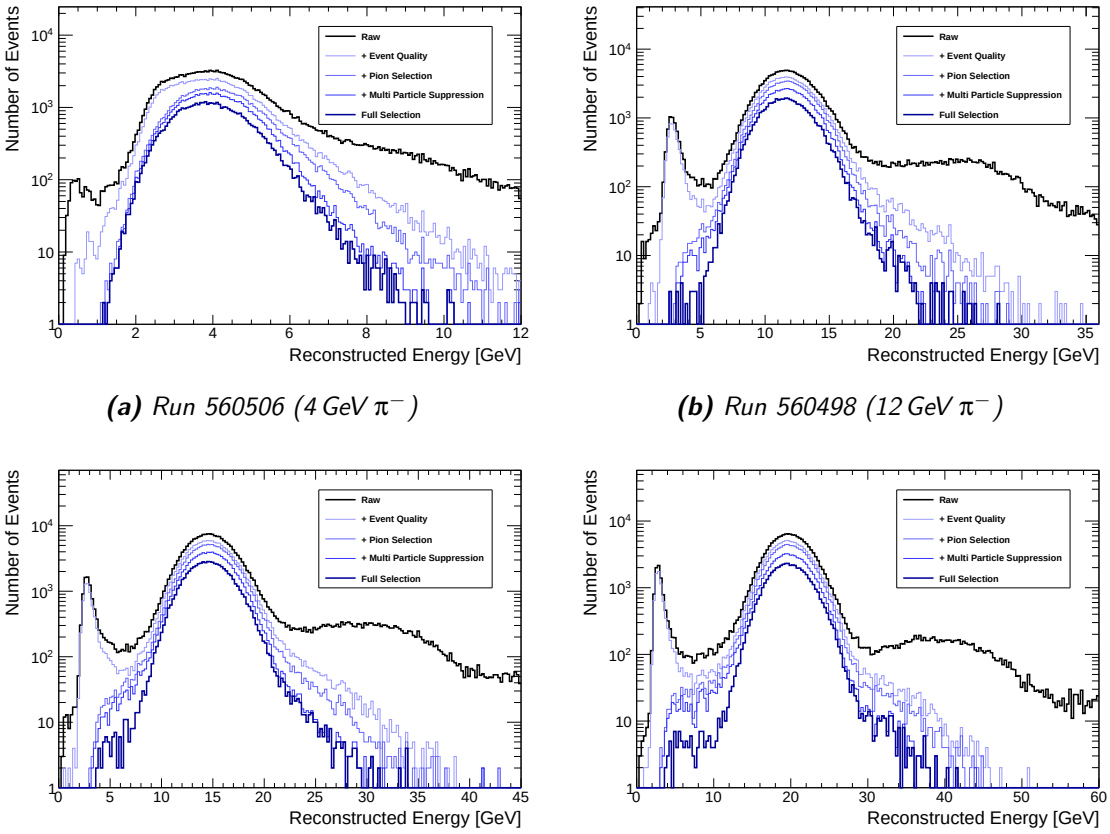

(a) *Run 560506 (4 GeV π^-)*

(b) *Run 560498 (12 GeV π^-)*

(c) *Run 560496 (15 GeV π^-)*

(d) *Run 560481 (20 GeV π^-)*

Figure D.1.: *Reconstructed energy spectra of pion data runs for different steps of the applied event selection.*

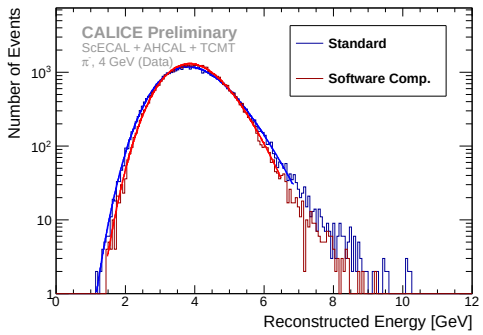

(a) *E_{rec} (4 GeV π^-) [108]*

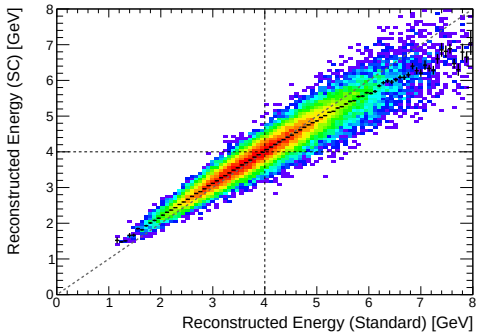

(b) *Correlation (4 GeV π^-)*

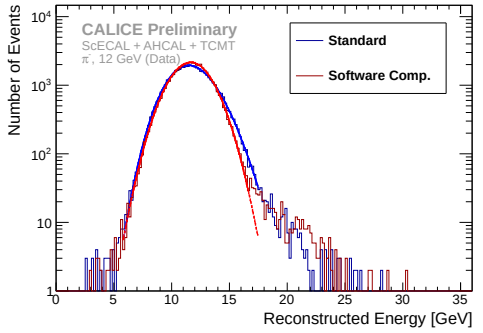

(c) *E_{rec} (12 GeV π^-) [108]*

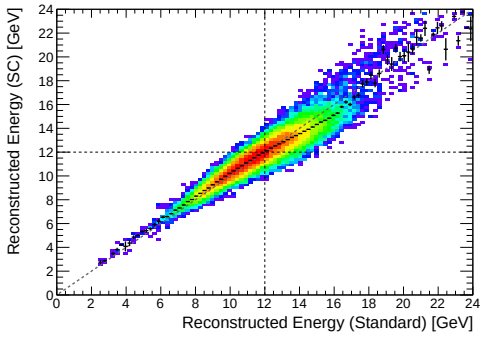

(d) *Correlation (12 GeV π^-)*

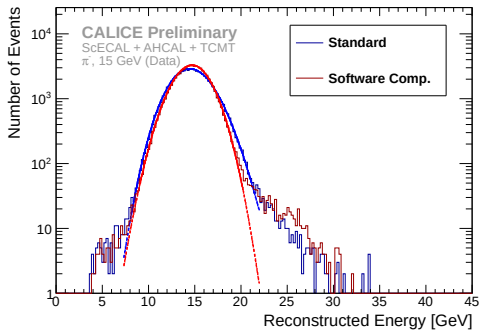

(e) *E_{rec} (15 GeV π^-) [108]*

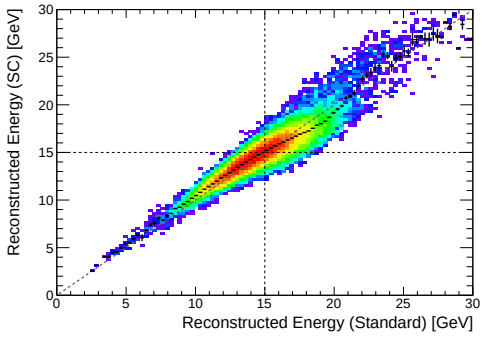

(f) *Correlation (15 GeV π^-)*

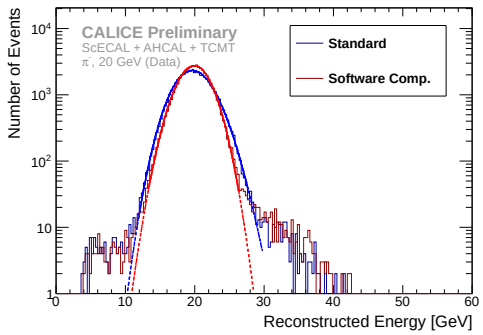

(g) *E_{rec} (20 GeV π^-) [108]*

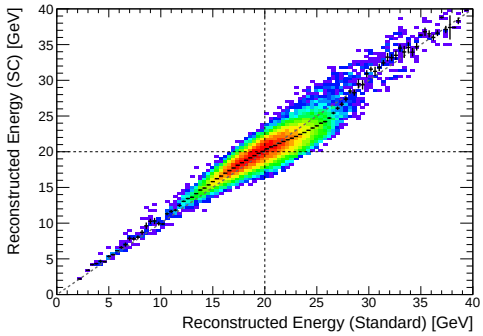

(h) *Correlation (20 GeV π^-)*

Figure D.2.: *Reconstructed energy in standard and software compensation reconstruction for pion data runs as well as their correlation. The black markers in the correlation plot show the profile of mean software compensation reconstructed energy for bins in standard reconstruction energy. The black dashed lines in the correlation plot indicate the beam energy of the run.*

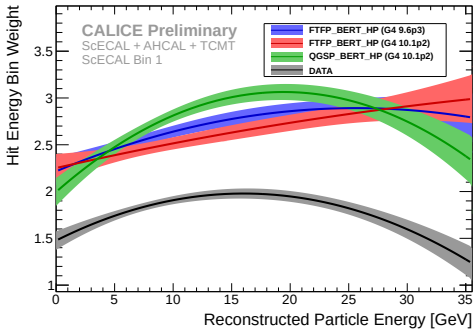

(a) *ScEcal Bin 1 [108]*

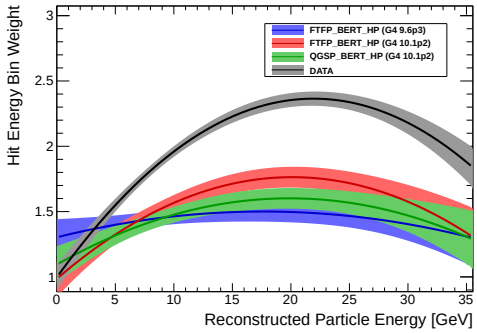

(b) *ScEcal Bin 2*

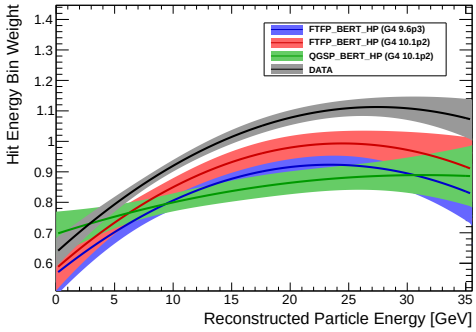

(c) *ScEcal Bin 3*

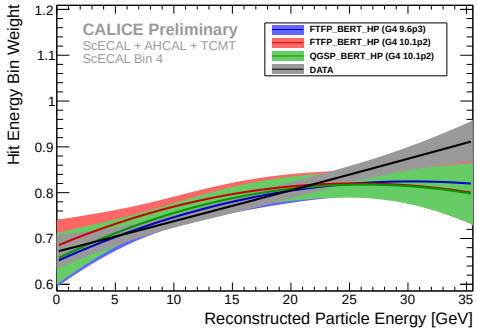

(d) *ScEcal Bin 4 [108]*

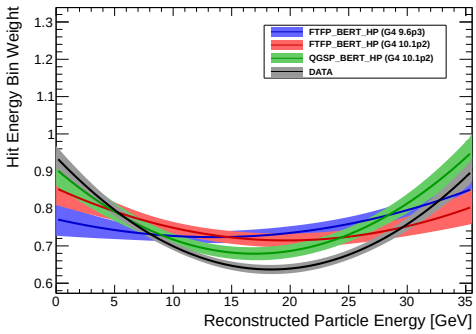

(e) *ScEcal Bin 5*

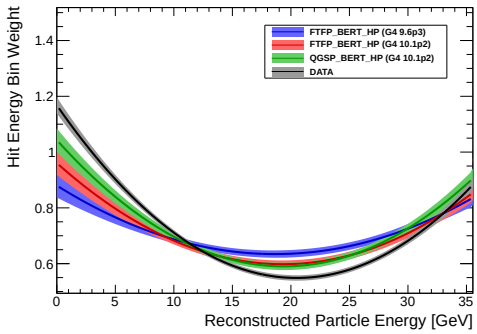

(f) *ScEcal Bin 6*

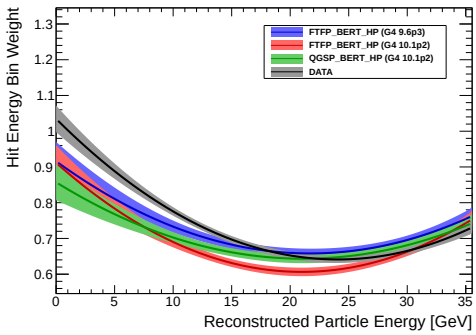

(g) *ScEcal Bin 7*

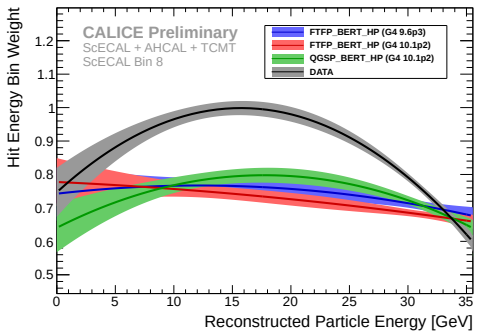

(h) *ScEcal Bin 8 [108]*

Figure D.3.: *ScECAL hit energy bin weights as a function of beam energy for data and different simulations. The width of each plotted line indicates the weight uncertainty propagated from the parameter errors.*

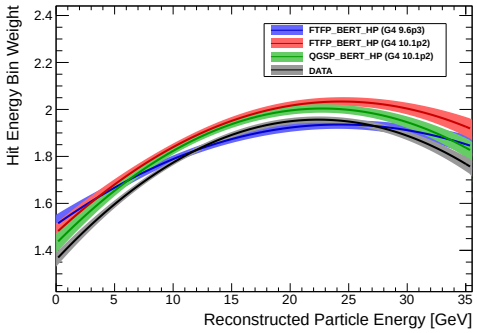

(a) *AHCAL Bin 1*

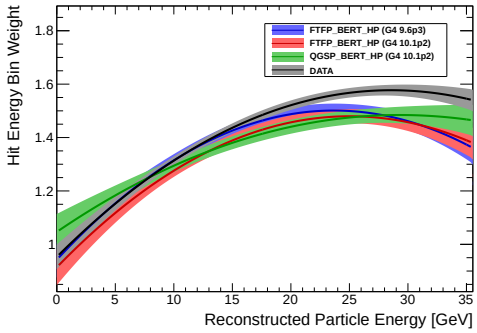

(b) *AHCAL Bin 2*

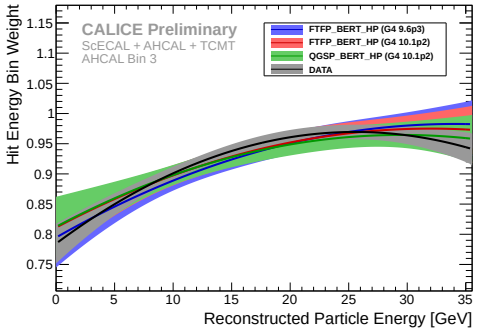

(c) *AHCAL Bin 3 [108]*

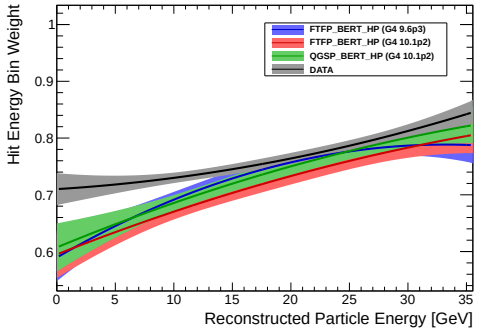

(d) *AHCAL Bin 4*

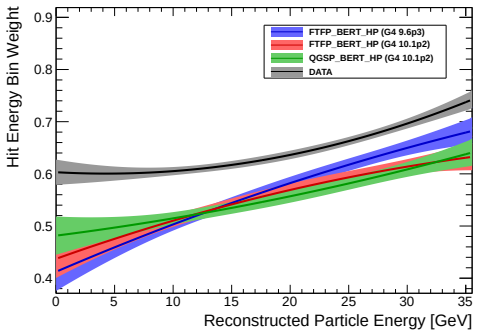

(e) *AHCAL Bin 5*

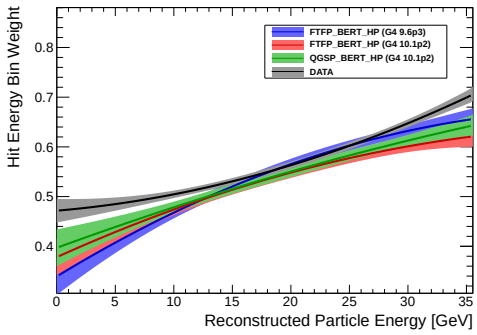

(f) *AHCAL Bin 6*

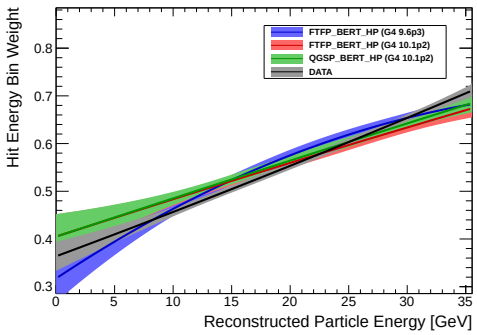

(g) *AHCAL Bin 7*

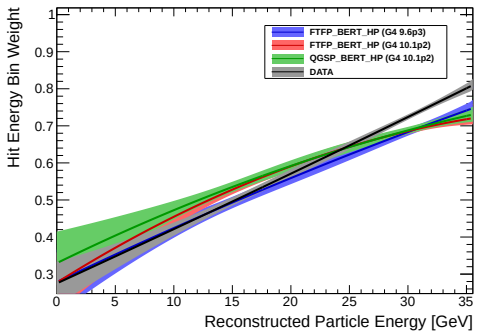

(h) *AHCAL Bin 8*

Figure D.4.: *AHCAL hit energy bin weights as a function of beam energy for data and different simulations. The width of each plotted line indicates the weight uncertainty propagated from the parameter errors.*

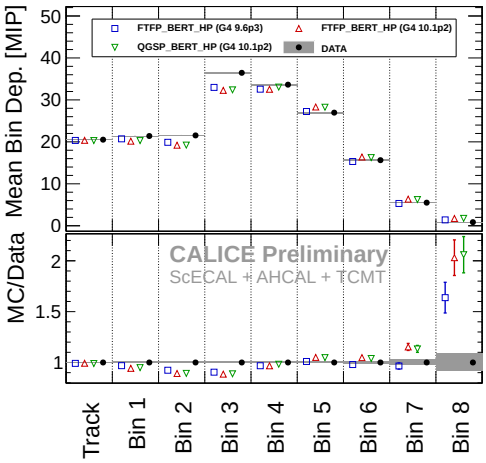

(a) *Run 560506 (4 GeV π^-) [108]*

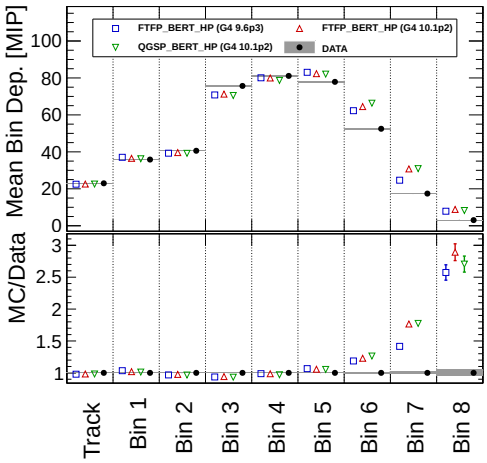

(b) *Run 560498 (12 GeV π^-)*

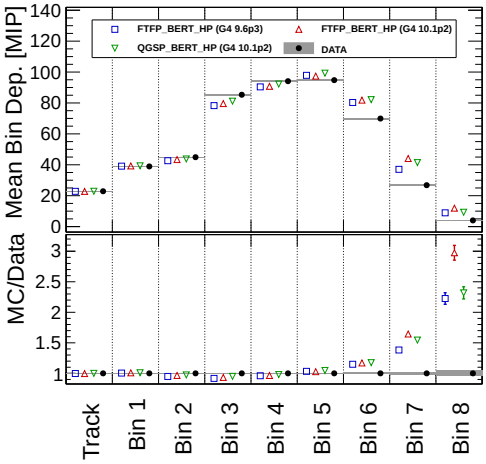

(c) *Run 560496 (15 GeV π^-)*

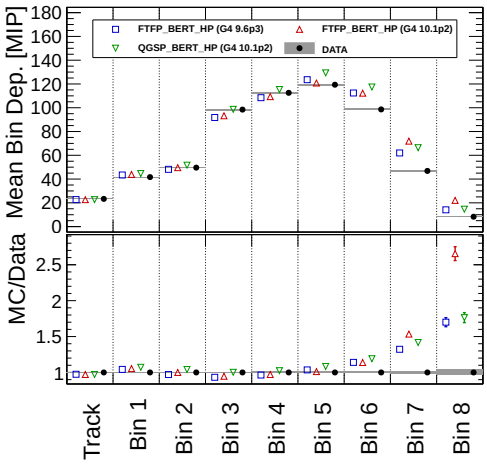

(d) *Run 560481 (20 GeV π^-)*

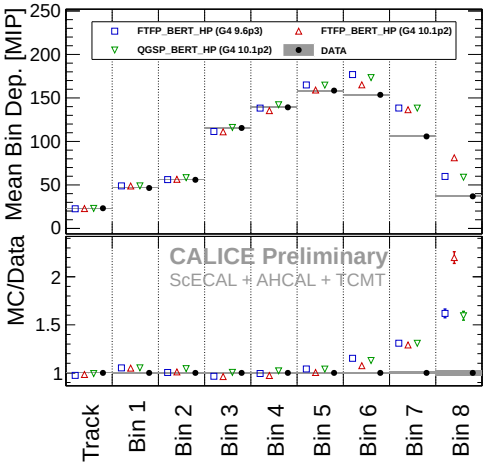

(e) *Run 560474 (32 GeV π^-) [108]*

Figure D.5.: *Averaged energy deposition sum per hit energy bin per event for data and simulations in the ScECAL. For most entries the statistical error is smaller than the used markers.*

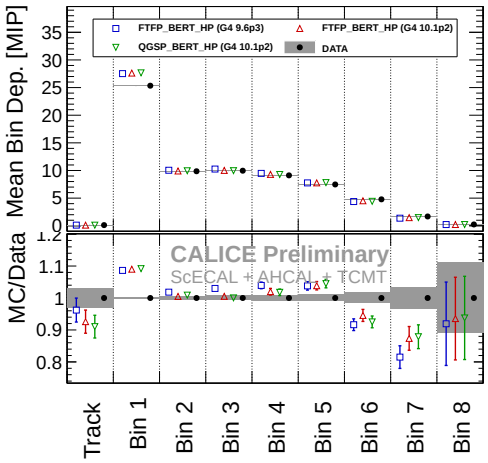

(a) *Run 560506 (4 GeV π^-) [108]*

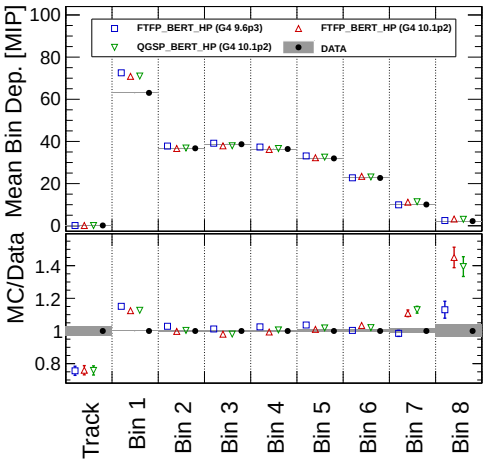

(b) *Run 560498 (12 GeV π^-)*

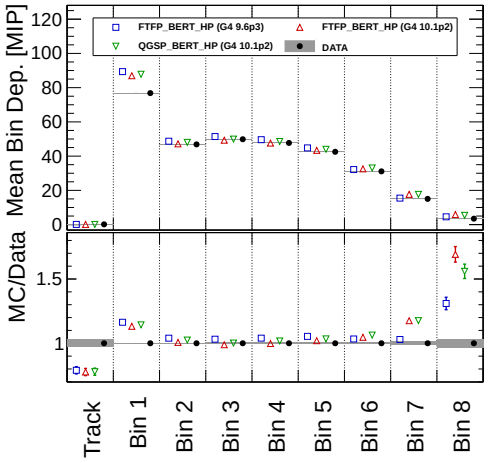

(c) *Run 560496 (15 GeV π^-)*

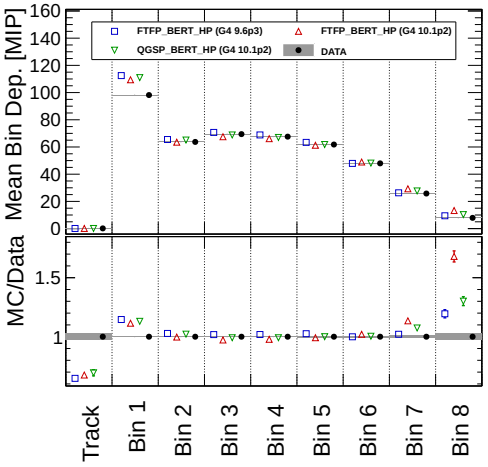

(d) *Run 560481 (20 GeV π^-)*

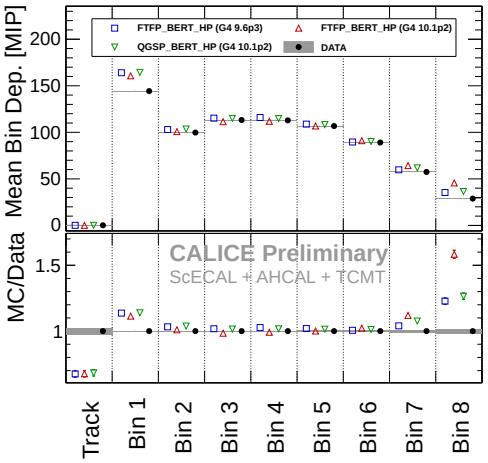

(e) *Run 560474 (32 GeV π^-) [108]*

Figure D.6.: *Averaged energy deposition sum per hit energy bin per event for data and simulations in the AHCAL. For most entries the statistical error is smaller than the used markers.*

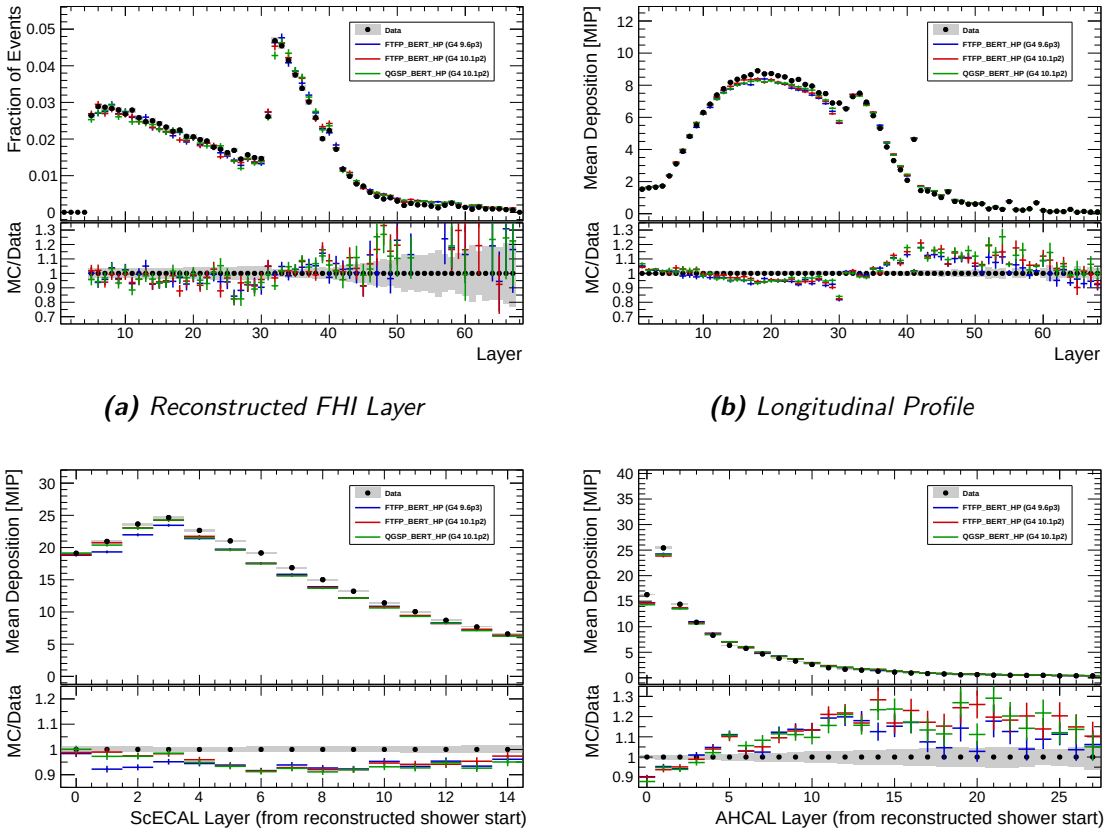

(a) *Reconstructed FHI Layer*

(b) *Longitudinal Profile*

(c) *Longitudinal Profile ScECAL (from FHI)*

(d) *Longitudinal Profile AHCAL (from FHI)*

Figure D.7.: *Longitudinal shower profiles for run 560506 (4 GeV π^-).*

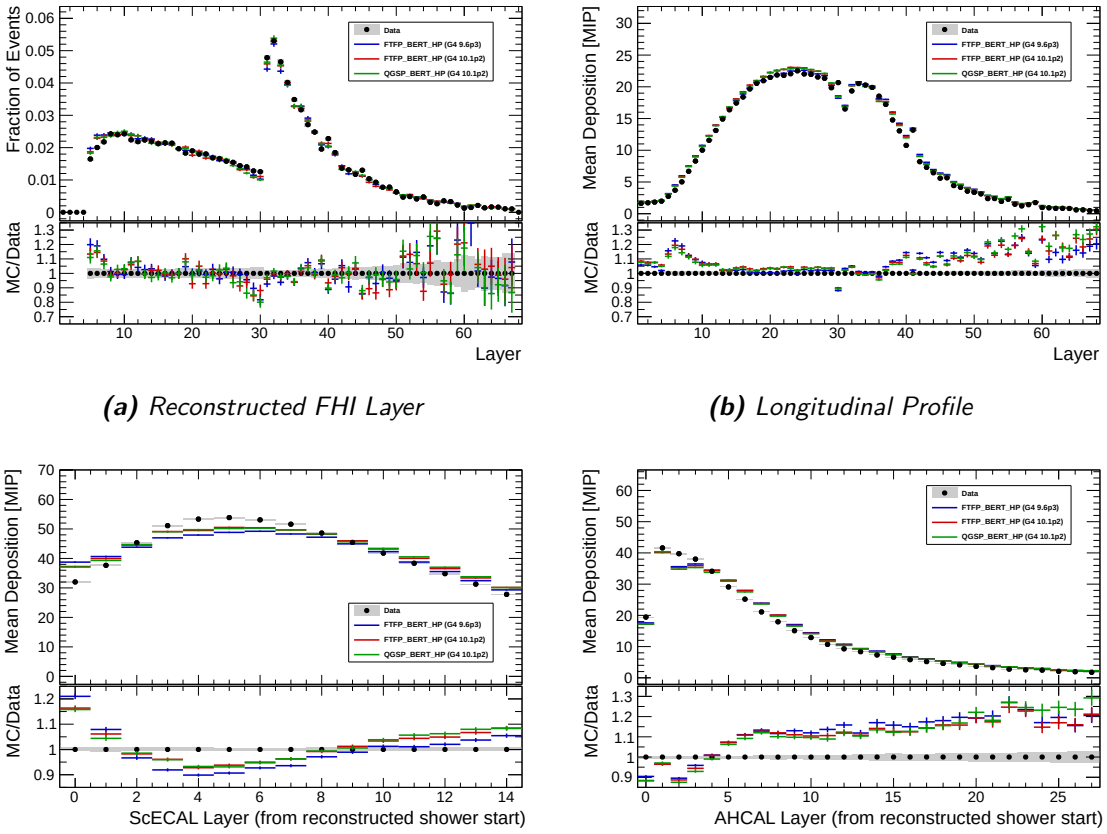

(a) *Reconstructed FHI Layer*

(b) *Longitudinal Profile*

(c) *Longitudinal Profile ScECAL (from FHI)*

(d) *Longitudinal Profile AHCAL (from FHI)*

Figure D.8.: *Longitudinal shower profiles for run 560498 (12 GeV π^-).*

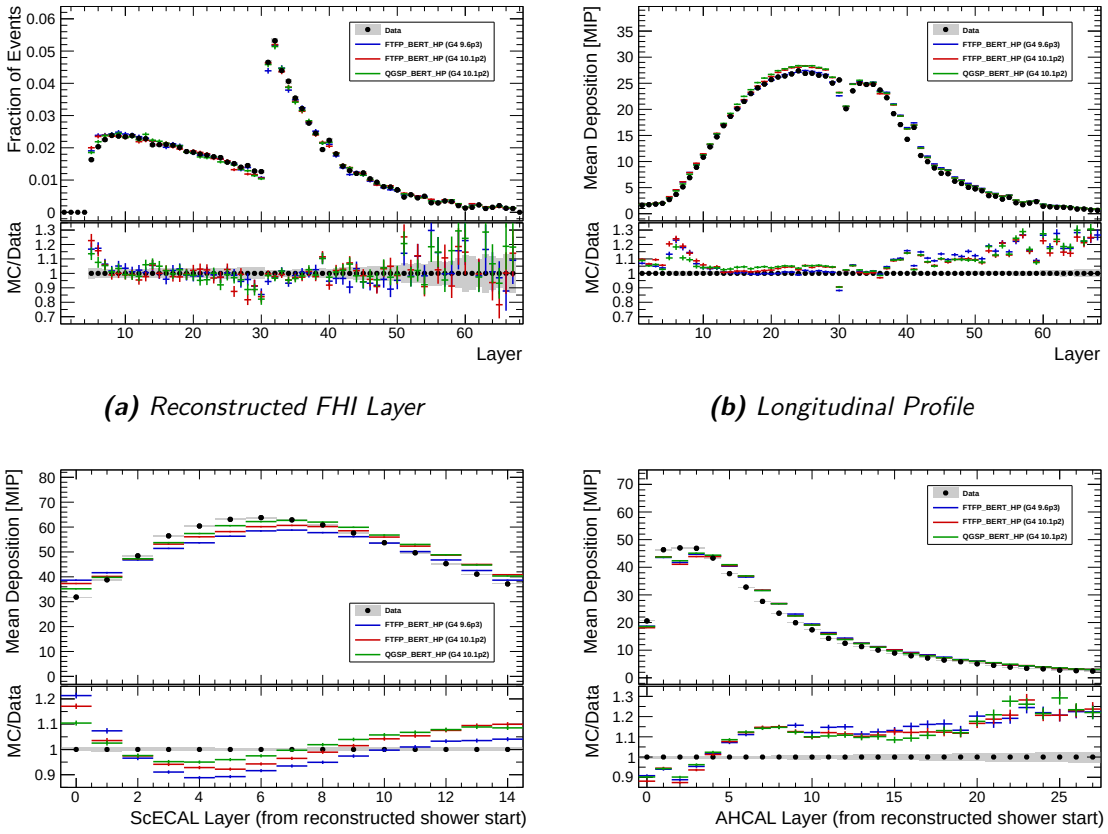

(a) *Reconstructed FHI Layer*

(b) *Longitudinal Profile*

(c) *Longitudinal Profile ScECAL (from FHI)*

(d) *Longitudinal Profile AHCAL (from FHI)*

Figure D.9.: *Longitudinal shower profiles for run 560496 (15 GeV π^-).*

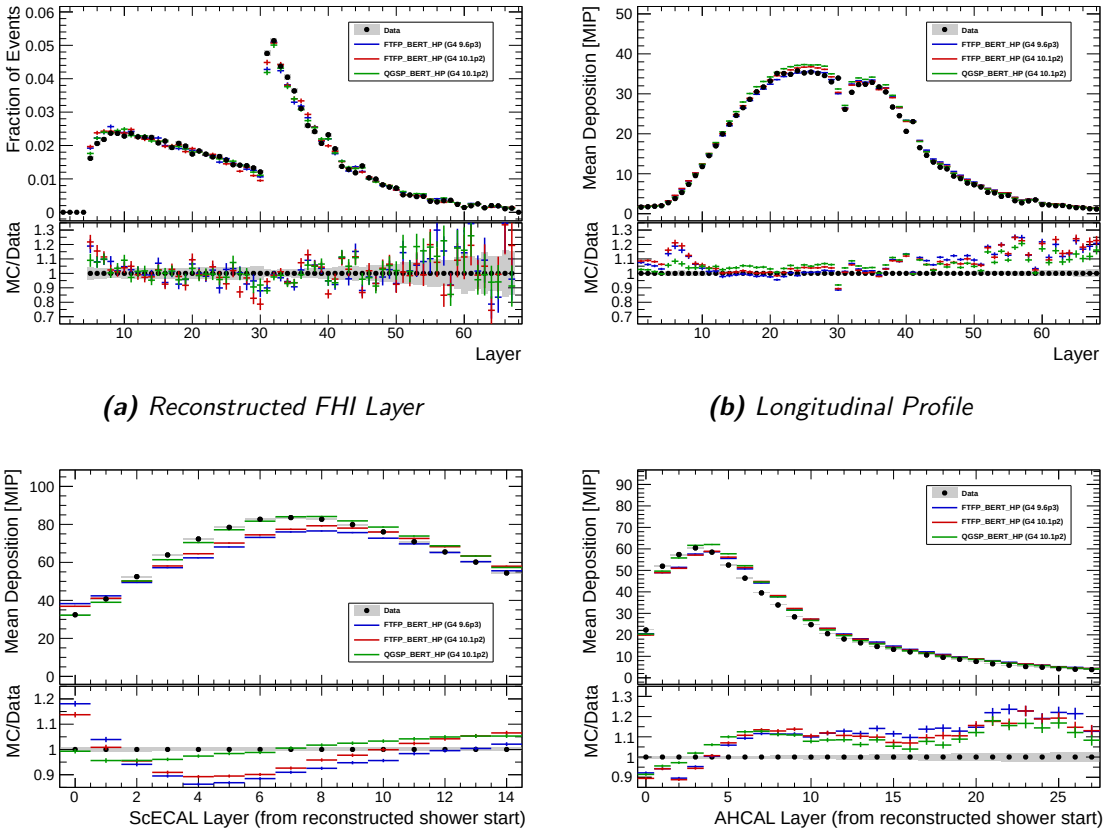

(a) *Reconstructed FHI Layer*

(b) *Longitudinal Profile*

(c) *Longitudinal Profile ScECAL (from FHI)*

(d) *Longitudinal Profile AHCAL (from FHI)*

Figure D.10.: *Longitudinal shower profiles for run 560481 (20 GeV π^-).*

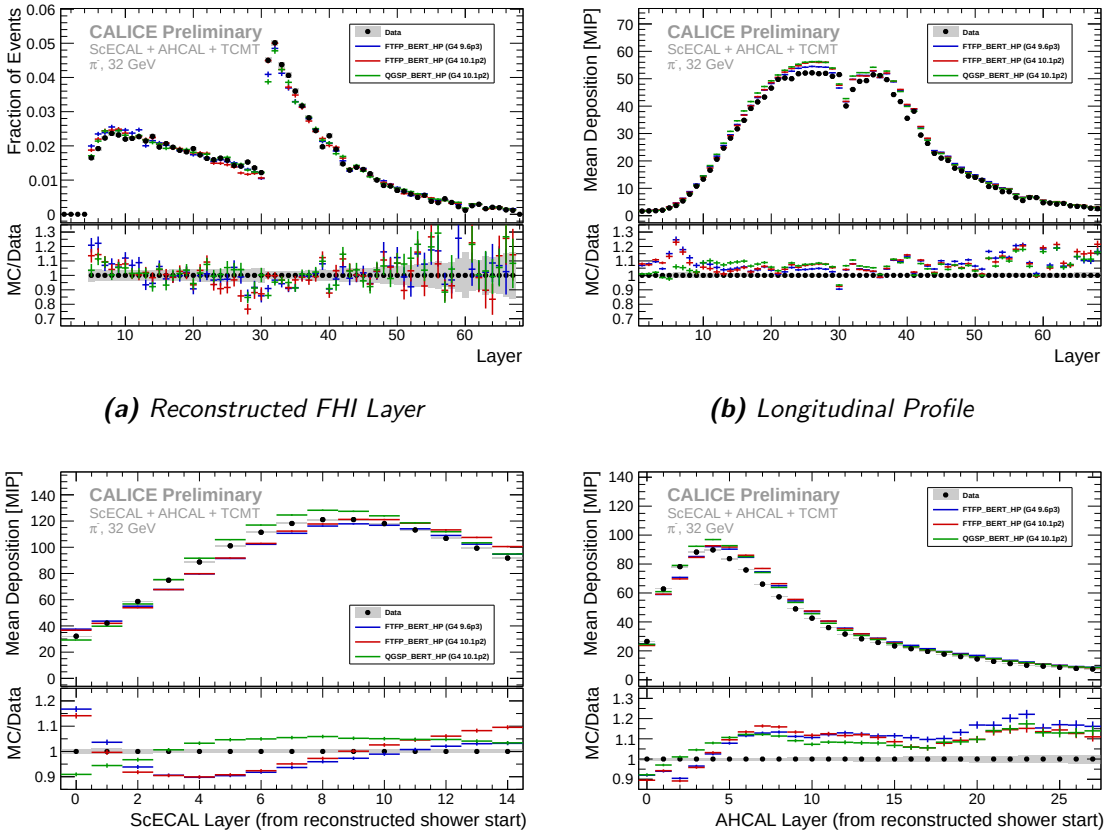

(a) *Reconstructed FHI Layer*

(b) *Longitudinal Profile*

(c) *Longitudinal Profile ScECAL (from FHI)*

(d) *Longitudinal Profile AHCAL (from FHI)*

Figure D.11.: *Longitudinal shower profiles for run 560474 (32 GeV π^-).*

Table D.1.: *Energy resolutions extracted from pion runs in data and simulations, using the standard energy reconstruction (Std.) and the software compensation reconstruction (SC) as plotted in Figure 4.45. Errors on data are purely statistical, errors on simulation include systematic modelling uncertainties as explained in subsection 4.8.2. All simulations are generated with GEANT 4 10.1p2 except lines marked with $^{(*)}$, which are GEANT 4 9.6p3.*

Run/Energy		Type	$(\sigma/\mu)_{\text{Std.}}$		$(\sigma/\mu)_{\text{SC}}$		$\frac{(\sigma/\mu)_{\text{SC}}}{(\sigma/\mu)_{\text{Std.}}}$	
			[%]	Δ[%]	[%]	Δ[%]	[%]	Δ[%]
560506 (4 GeV)	π^-	Data	23.30	0.08	21.19	0.07	0.91	0.00
	π^-	FTFP_BERT_HP	22.56	0.65	19.00	0.39	0.84	0.03
	π^-	FTFP_BERT_HP$^{(*)}$	22.86	0.81	19.57	0.57	0.86	0.04
	π^-	QGSP_BERT_HP	22.85	0.78	19.51	0.56	0.85	0.04
560498 (12 GeV)	π^-	Data	15.98	0.05	14.40	0.05	0.90	0.00
	π^-	FTFP_BERT_HP	14.65	0.25	12.60	0.20	0.86	0.02
	π^-	FTFP_BERT_HP$^{(*)}$	15.38	0.28	12.79	0.32	0.83	0.03
	π^-	QGSP_BERT_HP	15.45	0.29	12.69	0.25	0.82	0.02
560496 (15 GeV)	π^-	Data	14.59	0.04	12.81	0.04	0.88	0.00
	π^-	FTFP_BERT_HP	13.50	0.30	11.31	0.20	0.84	0.02
	π^-	FTFP_BERT_HP$^{(*)}$	14.32	0.37	11.45	0.33	0.80	0.03
	π^-	QGSP_BERT_HP	14.20	0.20	11.38	0.13	0.80	0.01
560481 (20 GeV)	π^-	Data	13.03	0.04	10.99	0.04	0.84	0.00
	π^-	FTFP_BERT_HP	12.29	0.19	9.89	0.22	0.80	0.02
	π^-	FTFP_BERT_HP$^{(*)}$	13.19	0.28	9.99	0.28	0.76	0.03
	π^-	QGSP_BERT_HP	12.67	0.13	9.76	0.08	0.77	0.01
560474 (32 GeV)	π^-	Data	10.77	0.03	8.36	0.02	0.78	0.00
	π^-	FTFP_BERT_HP	10.62	0.20	7.52	0.13	0.71	0.02
	π^-	FTFP_BERT_HP$^{(*)}$	11.59	0.28	7.61	0.03	0.66	0.02
	π^-	QGSP_BERT_HP	10.84	0.22	7.56	0.13	0.70	0.02

Bibliography

[1] H Geiger and E Marsden. "On a Diffuse Reflection of the alpha particles". In: *Proc. Royal Soc.* 82 (1909), pages 495–500. ISSN: 1364-5021. DOI: 10.1098/rspa.1909.0054 (cited on page 9).

[2] E. Rutherford. "The scattering of α and β particles by matter and the structure of the atom". In: *Philosophical Magazine Series 6* 21.125 (1911), pages 669–688. ISSN: 1478-6435. DOI: 10.1080/14786435.2011.617037 (cited on page 9).

[3] Sheldon L. Glashow. "Partial-symmetries of weak interactions". In: *Nuclear Physics* 22.4 (Feb. 1961), pages 579–588. ISSN: 00295582. DOI: 10.1016/0029-5582(61)90469-2 (cited on page 9).

[4] A. Salam and J.C. Ward. "Electromagnetic and weak interactions". In: *Physics Letters* 13.2 (Nov. 1964), pages 168–171. ISSN: 00319163. DOI: 10.1016/0031-9163(64)90711-5 (cited on page 9).

[5] Steven Weinberg. "A Model of Leptons". In: *Physical Review Letters* 19.21 (Nov. 1967), pages 1264–1266. ISSN: 0031-9007. DOI: 10.1103/PhysRevLett.19.1264 (cited on page 9).

[6] ATLAS Collaboration. "Observation of a new particle in the search for the Standard Model Higgs boson with the ATLAS detector at the LHC". In: *Physics Letters B* 716.1 (2012), pages 1–29. ISSN: 03702693. DOI: 10.1016/j.physletb.2012.08.020. arXiv: 1207.7214 (cited on page 9).

[7] CMS Collaboration. "Observation of a new boson at a mass of 125GeV with the CMS experiment at the LHC". In: *Phys. Lett. B* 716 (2012), pages 30–61. ISSN: 03702693. DOI: 10.1016/j.physletb.2012.08.021. arXiv: 1207.7235 [hep-ex] (cited on page 9).

[8] MissMJ. *Standard Model of Elementary Particles*. Licensed under CC BY 3.0. URL: https://en.wikipedia.org/wiki/Standard_Model%5C#/media/File:Standard%5C_Model%5C_of%5C_Elementary_Particles.svg (cited on page 10).

[9] Hideki Yukawa. "On the Interaction of Elementary Particles. I". In: *Proceedings of the Physico-Mathematical Society of Japan. 3rd Series* 17 (1935), pages 48–57 (cited on page 10).

[10] Peter W. Higgs. "Broken Symmetries and the Masses of Gauge Bosons". In: *Physical Review Letters* 13.16 (Oct. 1964), pages 508–509. ISSN: 0031-9007. DOI: 10.1103/PhysRevLett.13.508 (cited on page 11).

[11] F. Englert and R. Brout. "Broken Symmetry and the Mass of Gauge Vector Mesons". In: *Physical Review Letters* 13.9 (Aug. 1964), pages 321–323. ISSN: 0031-9007. DOI: 10.1103/PhysRevLett.13.321 (cited on page 11).

[12] CERN. *The Large Hadron Collider*. Apr. 2016. URL: http://home.cern/topics/large-hadron-collider (cited on page 11).

[13] ATLAS Collaboration. *Search for the Standard Model Higgs boson in produced in association with a vector boson and decaying to bottom quarks with the ATLAS detector*. Technical report ATLAS-CONF-2012-161. Geneva: CERN, Nov. 2012 (cited on page 12).

[14] Ties Behnke et al. "The International Linear Collider Technical Design Report - Volume 1: Executive Summary". In: (June 2013). arXiv: 1306.6327 (cited on pages 11–13, 15).

[15] Howard Baer et al. "The International Linear Collider Technical Design Report - Volume 2: Physics". In: (June 2013). arXiv: 1306.6352 (cited on pages 11, 17).

[16] Chris Adolphsen et al. "The International Linear Collider Technical Design Report - Volume 3.I: Accelerator R&D in the Technical Design Phase". In: (June 2013). arXiv: 1306.6353 (cited on pages 11, 14).

[17] Chris Adolphsen et al. "The International Linear Collider Technical Design Report - Volume 3.II: Accelerator Baseline Design". In: (June 2013). arXiv: 1306.6328 (cited on pages 11, 14).

[18] Ties Behnke et al. "The International Linear Collider Technical Design Report - Volume 4: Detectors". In: (June 2013). arXiv: 1306.6329 (cited on pages 11, 15, 57).

[19] T. Barklow et al. "ILC Operating Scenarios". In: (June 2015). arXiv: 1506.07830 (cited on page 14).

[20] V. Ayvazyan et al. "First operation of a free-electron laser generating GW power radiation at 32 nm wavelength". In: *European Physical Journal D* 37.2 (2006), pages 297–303. ISSN: 14346060. DOI: 10.1140/epjd/e2005-00308-1 (cited on page 14).

[21] Massimo Altarelli et al. *The European XFEL Technical Design Report*. Technical report. 2007 (cited on page 14).

[22] M Aicheler et al. *A Multi-TeV Linear Collider Based on CLIC Technology: CLIC Conceptual Design Report*. Technical report CERN-2012-007. SLAC-R-985. KEK-Report-2012-1. PSI-12-01. JAI-2012-001. Geneva, 2012 (cited on page 14).

[23] M. A. Thomson. "Particle flow calorimetry and the PandoraPFA algorithm". In: *Nuclear Instruments and Methods in Physics Research, Section A: Accelerators, Spectrometers, Detectors and Associated Equipment* 611.1 (2009), pages 25–40. ISSN: 01689002. DOI: 10.1016/j.nima.2009.09.009. arXiv: 0907.3577 (cited on pages 16, 39–40).

[24] Keisuke Fujii et al. "Physics Case for the International Linear Collider". In: *arXiv* (June 2015), page 37. arXiv: 1506.05992 (cited on pages 17–20, 22).

[25] G Moortgat-Pick et al. "Physics at the e+e- linear collider." In: *The European physical journal. C, Particles and fields* 75.8 (), page 371. ISSN: 1434-6044. DOI: 10.1140/epjc/s10052-015-3511-9 (cited on page 17).

[26] K A Olive and Particle Data Group. "Review of Particle Physics". In: *Chinese Physics C* 38.9 (2014) (cited on pages 18, 25–29, 35, 73, 78, 106).

[27] CERN Higgs Cross Section Working Group. *LHCHXSWGCrossSectionsFigures*. URL: https://twiki.cern.ch/twiki/bin/view/LHCPhysics/LHCHXSWGCrossSectionsFigures (cited on page 18).

[28] Ian Low, Riccardo Rattazzi, and Alessandro Vichi. "Theoretical constraints on the Higgs effective couplings". In: *Journal of High Energy Physics* 2010.4 (Apr. 2010), page 126. ISSN: 1029-8479. DOI: 10.1007/JHEP04(2010)126. arXiv: 0907.5413 (cited on page 19).

[29] Marco Farina, Maxim Perelstein, and Nicolas Rey-Le Lorier. "Higgs couplings and naturalness". In: *Physical Review D* 90.1 (July 2014), page 015014. ISSN: 1550-7998. DOI: 10.1103/PhysRevD.90.015014. arXiv: 1305.6068 (cited on page 19).

[30] Claude Dürig. "Determination of the Higgs decay width at the ILC". Master Thesis. Universität Bonn, 2012 (cited on page 20).

[31] M. A. Thomson. "Model-independent measurement of the e+ e- → HZ cross section at a future e+ e- linear collider using hadronic Z decays". In: *The European Physical Journal C* 76.2 (Feb. 2016), page 72. ISSN: 1434-6044. DOI: 10.1140/epjc/s10052-016-3911-5 (cited on pages 21, 24).

[32] Richard Wigmans. *Calorimetry, Energy Measurement in Particle Physics*. Oxford Science Publications, Oxford University Press, 2000 (cited on pages 25, 27, 30, 35).

[33] Ian C. Brock and Thomas Schörner-Sadenius. *Physics at the Terascale*. 2011. ISBN: 9783527410019. DOI: 10.1002/9783527634965 (cited on page 29).

[34] Nils Feege. "Low-Energetic Hadron Interactions in a Highly Granular Calorimeter". PhD thesis. 2011 (cited on pages 30, 32–34, 39, 48–49, 52, 72, 74–75, 96, 108, 146).

[35] S. Agostinelli and Et Al. "Geant4 - a simulation toolkit". In: *Nuclear Instruments and Methods in Physics Research Section A: Accelerators, Spectrometers, Detectors and Associated Equipment* 506.3 (2003), pages 250–303. ISSN: 01689002. DOI: 10.1016/S0168-9002(03)01368-8. arXiv: 1005.0727v1 (cited on page 31).

[36] *Mokka - a GEANT4 Application to Simulate the Full ILD Geometry*. URL: http://polzope.in2p3.fr:8081/MOKKA (cited on pages 31, 75).

[37] V N Ivanchenko, O Kadri, M Maire, and L Urban. "Geant4 models for simulation of multiple scattering". In: *Journal of Physics: Conference Series* 219.3 (2010), page 032045. ISSN: 1742-6596. DOI: 10.1088/1742-6596/219/3/032045 (cited on page 31).

[38] V. Ivanchenko et al. "Recent Improvements in Geant4 Electromagnetic Physics Models and Interfaces". In: *3th Monte Carlo Conference MC2010* 2 (2011), pages 898–903 (cited on page 31).

[39] The CALICE Collaboration et al. "DHCAL with Minimal Absorber: Measurements with Positrons". In: (Mar. 2016). arXiv: 1603.01652 (cited on page 31).

[40] Aatos Heikkinen, Nikita Stepanov, and J. P. Wellisch. "Bertini intra-nuclear cascade implementation in Geant4". In: (June 2003). arXiv: 0306008 [nucl-th] (cited on page 32).

[41] *GEANT4 Physics Reference Manual*. URL: http://geant4.web.cern.ch/geant4/G4UsersDocuments/UsersGuides/PhysicsReferenceManual/html/PhysicsReferenceManual.html (cited on pages 32–33).

[42] G. Folger and J. P. Wellisch. "String Parton Models in Geant4". In: *Computing in High Energy and Nuclear Physics*. 2003. arXiv: 0306007 [nucl-th] (cited on page 33).

[43] Bo Andersson. "THE FRITIOF DYNAMICS". In: *2nd International Workshop on Correlation and Fluctuation in Multiparticle Production (IWCF 1997) Jinan, Shandong, China, June 28-July 6, 1987*. 1987 (cited on page 33).

[44] N. S. Amelin, E. F. Staubo, and L. P. Csernai. "Semihard collisions in Monte Carlo quark-gluon string model". In: *Physical Review D* 46.11 (Dec. 1992), pages 4873–4881. ISSN: 0556-2821. DOI: 10.1103/PhysRevD.46.4873 (cited on page 33).

[45] B. Andersson, G. Gustafson, and B. Nilsson-Almqvist. "A model for low-pT hadronic reactions with generalizations to hadron-nucleus and nucleus-nucleus collisions". In: *Nuclear Physics, Section B* 281.1-2 (1987), pages 289–309. ISSN: 05503213. DOI: 10.1016/0550-3213(87)90257-4 (cited on page 33).

[46] Jose Manuel Quesada et al. "Recent developments in pre-equilibrium and de-excitation models in Geant4". English. In: () (cited on page 33).

[47] H. Fesefeldt. "The Simulation of Hadronic Showers: Physics and Applications". In: (1985) (cited on page 33).

[48] J. Apostolakis et al. "GEANT4 Physics lists for HEP". In: *IEEE Nuclear Science Symposium Conference Record*. 2008, pages 833–836. ISBN: 9781424427154. DOI: 10.1109/NSSMIC.2008.4774655 (cited on page 33).

[49] A. Ribon et al. *Status of Geant4 hadronic physics for the simulation of LHC experiments at the start of LHC physics program*. Technical report. 2010 (cited on page 33).

[50] Andrea Dotti. "Geant4 Updates". CALICE Collaboration Meeting, Munich 2015. 2015 (cited on pages 34, 133).

[51] Christian W. Fabjan and Fabiola Gianotti. "Calorimetry for particle physics". In: *Reviews of Modern Physics* 75.4 (2003), pages 1243–1246. ISSN: 00346861. DOI: 10.1103/RevModPhys.75.1243 (cited on pages 35, 37).

[52] P. Adzic et al. "Energy resolution of the barrel of the CMS Electromagnetic Calorimeter". In: *Journal of Instrumentation* 2.04 (2007), P04004–P04004. ISSN: 1748-0221. DOI: 10.1088/1748-0221/2/04/P04004 (cited on page 36).

[53] B. Aubert et al. "Development and construction of large size signal electrodes for the ATLAS electromagnetic calorimeter". In: *Nuclear Instruments and Methods in Physics Research, Section A: Accelerators, Spectrometers, Detectors and Associated Equipment* 539.3 (2005), pages 558–594. ISSN: 01689002. DOI: 10.1016/j.nima.2004.11.005 (cited on page 36).

[54] J. Pinfold et al. "Performance of the ATLAS liquid argon endcap calorimeter in the pseudorapidity region $2.5 < | \eta | < 4.0$ in beam tests". In: *Nuclear Instruments and Methods in Physics Research, Section A: Accelerators, Spectrometers, Detectors and Associated Equipment* 593.3 (2008), pages 324–342. ISSN: 01689002. DOI: 10.1016/j.nima.2008.05.033. arXiv: 0407009v1 [physics] (cited on page 36).

[55] Richard Wigmans. "High resolution hadron calorimetry". In: *Nuclear Instruments and Methods in Physics Research Section A: Accelerators, Spectrometers, Detectors and Associated Equipment* 265.1-2 (Mar. 1988), pages 273–290. ISSN: 01689002. DOI: 10.1016/0168-9002(88)91081-9 (cited on page 37).

[56] Robert Klanner. "Test program for the ZEUS calorimeter". In: *Nuclear Inst. and Methods in Physics Research, A* 265.1-2 (1988), pages 200–209. ISSN: 01689002. DOI: 10.1016/0168-9002(88)91072-8 (cited on page 37).

[57] A. Bernstein et al. "Beam tests of the ZEUS barrel calorimeter". In: *Nuclear Inst. and Methods in Physics Research, A* 336.1-2 (1993), pages 23–52. ISSN: 01689002. DOI: 10.1016/0168-9002(93)91078-2 (cited on page 37).

[58] P. Adragna et al. "Testbeam studies of production modules of the ATLAS Tile Calorimeter". In: *Nuclear Instruments and Methods in Physics Research Section A: Accelerators, Spectrometers, Detectors and Associated Equipment* 606.3 (July 2009), pages 362–394. ISSN: 01689002. DOI: 10.1016/j.nima.2009.04.009 (cited on page 37).

[59] Richard Wigmans. "The DREAM project—Towards the ultimate in calorimetry". In: *Nuclear Instruments and Methods in Physics Research Section A: Accelerators, Spectrometers, Detectors and Associated Equipment* 617.1-3 (May 2010), pages 129–133. ISSN: 01689002. DOI: 10.1016/j.nima.2009.09.118 (cited on page 37).

[60] Richard Wigmans. "The dual-readout approach to calorimetry". In: *Nuclear Instruments and Methods in Physics Research, Section A: Accelerators, Spectrometers, Detectors and Associated Equipment* 732 (2013), pages 475–479. ISSN: 01689002. DOI: 10.1016/j.nima.2013.04.005 (cited on page 37).

[61] W. Braunschweig et al. "Results from a test of a PbCu liquid argon calorimeter". In: *Nuclear Inst. and Methods in Physics Research, A* 265.3 (1988), pages 419–434. ISSN: 01689002. DOI: 10.1016/S0168-9002(98)90008-0 (cited on page 37).

[62] D Buskulic et al. "Performance of the ALEPH detector at LEP". In: *Nuclear Instruments and Methods in Physics Research Section A: Accelerators, Spectrometers, Detectors and Associated Equipment* 360.3 (June 1995), pages 481–506. ISSN: 01689002. DOI: 10.1016/0168-9002(95)00138-7 (cited on page 38).

[63] Matti Peez. "Search for deviations from the Standard Model in high transverse energy processes at the electron-proton collider HERA". PhD Thesis. Universite Claude Bernard - Lyon 1, 2003 (cited on page 38).

[64] Benjamin Portheault. "Determination of electroweak parameters at HERA with the H1 experiment". In: *AIP Conference Proceedings*. Volume 792. AIP, July 2005, pages 563–566. DOI: 10.1063/1.2122100. arXiv: 0507309 [hep-ph] (cited on page 38).

[65] The CMS Collaboration. "Particle-Flow Event Reconstruction in CMS and Performance for Jets, Taus, and ETmiss". In: *Cms Pas Bph-10-002* July (2013), pages –5. ISSN: 1098-5530. DOI: CMS-PAS-PFT-09-001 (cited on page 38).

[66] The CALICE Collaboration. *CALICE Website*. Feb. 2016. URL: https://twiki.cern.ch/twiki/bin/view/CALICE/WebHome (cited on pages 41, 71).

[67] C Adloff et al. "MICROMEGAS chambers for hadronic calorimetry at a future linear collider". en. In: *Journal of Instrumentation* 4.11 (Nov. 2009), P11023–P11023. ISSN: 1748-0221. DOI: 10.1088/1748-0221/4/11/P11023 (cited on page 41).

[68] B Bilki et al. "Hadron showers in a digital hadron calorimeter". en. In: *Journal of Instrumentation* 4.10 (Oct. 2009), P10008–P10008. ISSN: 1748-0221. DOI: 10.1088/1748-0221/4/10/P10008 (cited on page 41).

[69] The CALICE Collaboration. *CAN-039: Analysis of Tungsten-DHCAL Data from the CERN Test Beam* (cited on pages 41, 46).

[70] G. Baulieu et al. "Construction and commissioning of a technological prototype of a high-granularity semi-digital hadronic calorimeter". en. In: *Journal of Instrumentation* 10.10 (Oct. 2015), P10039–P10039. ISSN: 1748-0221. DOI: 10.1088/1748-0221/10/10/P10039 (cited on pages 41, 46).

[71] P Buzhan, B Dolgoshein, and A Ilyin. "An advanced study of Silicon Photomultiplier". In: *ICFA Inst.* 23 (2001), pages 28–41. DOI: 10.1142/9789812776464{_}0101 (cited on page 41).

[72] D Renker and E Lorenz. "Advances in solid state photon detectors". In: *Journal of Instrumentation* 4.04 (2009), page 6. ISSN: 1748-0221. DOI: 10.1088/1748-0221/4/04/P04004 (cited on page 41).

[73] V. Andreev et al. "A high-granularity scintillator calorimeter readout with silicon photomultipliers". In: *Nuclear Instruments and Methods in Physics Research, Section A: Accelerators, Spectrometers, Detectors and Associated Equipment* 540.2-3 (2005), pages 368–380. ISSN: 01689002. DOI: 10.1016/j.nima.2004.12.002 (cited on pages 41, 44).

[74] Erika Garutti. "Silicon photomultipliers for high energy physics detectors". In: *Journal of Instrumentation* 6.10 (2011), pages C10003–C10003. ISSN: 1748-0221. DOI: 10.1088/1748-0221/6/10/C10003. arXiv: 1108.3166 (cited on page 43).

[75] Patrick Eckert et al. "Characterisation studies of silicon photomultipliers". In: *Nuclear Instruments and Methods in Physics Research, Section A: Accelerators, Spectrometers, Detectors and Associated Equipment* 620.2-3 (2010), pages 217–226. ISSN: 01689002. DOI: 10.1016/j.nima.2010.03.169. arXiv: 1003.6071 (cited on page 43).

[76] The Calice Collaboration et al. "Construction and commissioning of the CALICE analog hadron calorimeter prototype". In: *Journal of Instrumentation* 5.05 (2010), P05004–P05004. ISSN: 1748-0221. DOI: 10.1088/1748-0221/5/05/P05004. arXiv: 1003.2662 (cited on pages 44–46, 48–49, 56, 140–141, 146).

[77] Frank Simon. "AHCAL status - focus on simulations". ILD Meeting, KEK, April 2015. 2015 (cited on pages 44, 63, 69).

[78] K. Francis et al. "Performance of the first prototype of the CALICE scintillator strip electromagnetic calorimeter". In: *Nuclear Instruments and Methods in Physics Research Section A: Accelerators, Spectrometers, Detectors and Associated Equipment* 763 (Nov. 2014), pages 278–289. ISSN: 01689002. DOI: 10.1016/j.nima.2014.06.039 (cited on page 44).

[79] The CALICE Collaboration. *CAN-016: First Stage Analysis of the Energy Response and Resolution of the Scintillator ECAL in the Beam Test at FNAL, 2008* (cited on pages 44, 51, 75, 113).

[80] The CALICE Collaboration. *CAN-016a: Temperature Correction on ADC/MIP Conversion Factors for September 2009 Data of ScECAL FNAL Test Beam Module* (cited on pages 44, 49, 113).

[81] The CALICE Collaboration. *CAN-016b: Update of the Analysis of the Test Beam Experiment of the CALICE ScECAL Physics Prototype* (cited on pages 44, 48, 75, 101, 103, 108, 113).

[82] The CALICE Collaboration. *CAN-016c: Erratum to CAN-016b, corrected calibration* (cited on pages 44, 113–115).

[83] C Adloff et al. "Construction and performance of a silicon photomultiplier/extruded scintillator tail-catcher and muon-tracker". en. In: *Journal of Instrumentation* 7.04 (Apr. 2012), P04015–P04015. ISSN: 1748-0221. DOI: 10.1088/1748-0221/7/04/P04015 (cited on pages 45, 48).

[84] Clemens Günter. "Comparison of Iron and Tungsten Absorber Structures for an Analog Hadron Calorimeter". PhD Thesis. Universität Hamburg, 2014 (cited on pages 48–52, 93, 107, 109, 146).

[85] Katsushige Kotera, Weonseok Choi, and Tohru Takeshita. "SiPM Response Functions Representing Wide Range Including Linear Behavior After Saturation". In: (Oct. 2015), page 10. arXiv: 1510.01102 (cited on pages 49, 110).

[86] C Adloff et al. "The time structure of hadronic showers in highly granular calorimeters with tungsten and steel absorbers". en. In: *Journal of Instrumentation* 9.07 (July 2014), P07022–P07022. ISSN: 1748-0221. DOI: 10.1088/1748-0221/9/07/P07022 (cited on page 50).

[87] A Stoykov et al. "On the limited amplitude resolution of multipixel Geiger-mode APDs". In: *Journal of Instrumentation* 2.06 (June 2007), P06005–P06005. ISSN: 1748-0221. DOI: 10.1088/1748-0221/2/06/P06005. arXiv: 0706.0746 (cited on pages 52, 155).

[88] C Adloff et al. "Hadronic energy resolution of a highly granular scintillator-steel hadron calorimeter using software compensation techniques". en. In: *Journal of Instrumentation* 7.09 (Sept. 2012), P09017–P09017. ISSN: 1748-0221. DOI: 10.1088/1748-0221/7/09/P09017 (cited on pages 52, 75, 96, 107–108, 117, 120, 132–133, 135, 140).

[89] A. C. Atkinson. "The Computer Generation of Poisson Random Variables". In: *Journal of the Royal Statistical Society. Series C (Applied Statistics)* 28.1 (1979), pages 29–35 (cited on page 53).

[90] A. C. Atkinson. "Recent Developments in the Computer Generation of Poisson Random Variables on JSTOR". In: *Journal of the Royal Statistical Society. Series C (Applied Statistics)* 28.3 (1979), pages 260–263 (cited on page 53).

[91] Luc Devroye. *Non-Uniform Random Variate Generation*. Springer, 1986, page 843. ISBN: 3-540-96305-7 (cited on page 53).

[92] The Ild Concept Group. "The International Large Detector: Letter of Intent". In: *Arxiv preprint arXiv10063396* (2010), page 163. arXiv: 1006.3396 (cited on page 57).

[93] Peter Göttlicher. "A Concept for Power Cycling the Electronics of CALICE-AHCAL with the Train Structure of ILC". In: *Physics Procedia* 37 (2012), pages 1586–1593. ISSN: 18753892. DOI: 10.1016/j.phpro.2012.02.489 (cited on page 57).

[94] Oskar Hartbrich. "Commissioning and LED System Tests of the Engineering Prototype of the Analog Hadronic Calorimeter of the CALICE Collaboration". Master Thesis. Bergische Universität Wuppertal, 2012, page 99 (cited on pages 58–59, 64, 141).

[95] Sebastian Weber. *Entwicklung eines integrierten LED-Kalibrationssystems und Studien zur Ortsauflösung für das szintillatorbasierte hadronische CALICE Kalorimeter*. deu. Aug. 2012 (cited on pages 58, 64).

[96] Mathias Goetze. "Systematische Untersuchungen zum LED Kalibrationssystem des analogen hadronischen Kalorimeters der CALICE Kollaboration". Diploma Thesis. 2011 (cited on pages 58, 64).

[97] Benjamin Hermberg. "Measuring Hadronic Jets at the ILC - From Particle Flow Calorimetry to the Higgs Self-Coupling". Universität Hamburg, Diss., 2015. Dr. Hamburg: Universität Hamburg, 2015, page 211 (cited on pages 58–60, 64, 66, 141).

[98] M Bouchel et al. "SPIROC (SiPM Integrated Read-Out Chip): dedicated very front-end electronics for an ILC prototype hadronic calorimeter with SiPM read-out". In: *Journal of Instrumentation* 6.01 (Jan. 2011), pages C01098–C01098. ISSN: 1748-0221. DOI: 10.1088/1748-0221/6/01/C01098 (cited on page 58).

[99] S Conforti Di Lorenzo et al. "SPIROC: design and performances of a dedicated very front-end electronics for an ILC Analog Hadronic CALorimeter (AHCAL) prototype with SiPM read-out". In: *Journal of Instrumentation* 8.01 (Jan. 2013), pages C01027–C01027. ISSN: 1748-0221. DOI: 10.1088/1748-0221/8/01/C01027 (cited on page 58).

[100] Omega. "SPIROC2 User Guide". Draft. 2009 (cited on page 60).

[101] Phi Chau. "Towards 2nd generation of SMD HBU: Assembly preparations and tests of white solder mask performance". AHCAL main meeting 2015, DESY, 10.12.2015. 2015 (cited on page 60).

[102] Aliakbar Ebrahimi. "Commissioning of the New Multilayer Integration Prototype with SiPM Readout of the CALICE Tile Hadron Calorimeter". Poster at IEEE NSS-MIC 2014, Seattle, 9.-13.11.2014. 2014 (cited on page 60).

[103] E Corrin. "EUDAQ Software User Manual". In: *EUDET Memos* June (2010), pages 1–69 (cited on page 60).

[104] C Adloff et al. "Track segments in hadronic showers in a highly granular scintillator-steel hadron calorimeter". en. In: *Journal of Instrumentation* 8.09 (Sept. 2013), P09001–P09001. ISSN: 1748-0221. DOI: 10.1088/1748-0221/8/09/P09001 (cited on pages 62, 88).

[105] Huong Lan Tran. "New ITEP tiles study". Internal note. 2014 (cited on page 62).

[106] Sarah Schröder. "Commissioning of a prototype hadronic calorimeter". Master. Universität Hamburg, 2016 (cited on page 63).

[107] Lloyd Teh Tzer Tong. "Trigger Threshold Verification for the Hadronic Calorimeter Prototype for the ILC". Summer Student Report. 2014 (cited on page 66).

[108] The CALICE Collaboration and Oskar Hartbrich. "CAN-056: Pion Response and Resolution in a Combined Scintillator Calorimeter System in the FNAL Testbeam" (cited on pages 71, 98, 102, 108–109, 111–112, 117, 119, 121, 124–126, 130–132, 134–136, 162–166).

[109] E. Ramberg. "A broad energy range detector test beam facility at fermilab". In: *2007 IEEE Nuclear Science Symposium Conference Record*. Volume 3. IEEE, 2007, pages 2349–2350. ISBN: 978-1-4244-0922-8. DOI: 10.1109/NSSMIC.2007.4436616 (cited on page 72).

[110] FNAL Testbeam Facility. *FTBF Website*. Feb. 2016. URL: http://ftbf.fnal.gov/beam-delivery-path/ (cited on page 72).

[111] J Litt and R Meunier. "Cerenkov Counter Technique in High-Energy Physics". en. In: *Annual Review of Nuclear Science* 23.1 (Dec. 1973), pages 1–44. ISSN: 0066-4243. DOI: 10.1146/annurev.ns.23.120173.000245 (cited on page 73).

[112] The CALICE Collaboration et al. "Electromagnetic response of a highly granular hadronic calorimeter". en. In: *Journal of Instrumentation* 6.04 (Apr. 2011), P04003–P04003. ISSN: 1748-0221. DOI: 10.1088/1748-0221/6/04/P04003 (cited on pages 75, 113, 145).

[113] B. Bilki et al. "Pion and proton showers in the CALICE scintillator-steel analogue hadron calorimeter". en. In: *Journal of Instrumentation* 10.04 (Apr. 2015), P04014–P04014. ISSN: 1748-0221. DOI: 10.1088/1748-0221/10/04/P04014 (cited on pages 75, 85–86, 108).

[114] Katsushige Kotera. *Tungsten Absorber for the CALICE ScECAL Prototype*. Technical report. 2016 (cited on page 76).

[115] Xiaoyong Ren, Hezhuo Miao, and Zhijian Peng. *A review of cemented carbides for rock drilling: An old but still tough challenge in geo-engineering*. 2013. DOI: 10.1016/j.ijrmhm.2013.01.003 (cited on page 76).

[116] The CALICE Collaboration. "Construction and Electromagnetic Response of a Highly Granular Scintillator-based Electromagnetic Calorimeter". (in preparation) (cited on pages 76, 113).

[117] Katsushige Kotera, Daniel Jeans, Akiya Miyamoto, and Tohru Takeshita. "A novel strip energy splitting algorithm for the fine granular readout of a scintillator strip electromagnetic calorimeter". In: *Nuclear Instruments and Methods in Physics Research Section A: Accelerators, Spectrometers, Detectors and Associated Equipment* 789 (July 2015), pages 158–164. ISSN: 01689002. DOI: 10.1016/j.nima.2015.04.001. arXiv: 1405.4456 (cited on page 88).

[118] Mathias Götze. "Working Title". (in preparation). PhD thesis. 2016 (cited on page 88).

[119] M. Chefdeville et al. “Shower development of particles with momenta from 15 GeV to 150 GeV in the CALICE scintillator-tungsten hadronic calorimeter”. en. In: *Journal of Instrumentation* 10.12 (Dec. 2015), P12006–P12006. ISSN: 1748-0221. DOI: 10.1088/1748-0221/10/12/P12006 (cited on pages 107–108, 113).

[120] The CALICE Collaboration and Coralie Neubüser. “CAN-049a: Comparison of Energy Reconstruction Schemes and Different Granularities in the CALICE AHCAL”. Draft in collaboration review (cited on page 118).

[121] The CALICE Collaboration. “First results of the CALICE SDHCAL technological prototype”. en. In: *Journal of Instrumentation* 11.04 (Apr. 2016), P04001–P04001. ISSN: 1748-0221. DOI: 10.1088/1748-0221/11/04/P04001 (cited on page 118).

[122] The CALICE Collaboration et al. “Hadron shower decomposition in the highly granular CALICE analogue hadron calorimeter”. In: (Feb. 2016), page 38. arXiv: 1602.08578 (cited on page 131).

[123] The CALICE Collaboration and Coralie Neubüser. “CAN-049: Analogue, Digital and Semi-Digital Energy Reconstruction in the CALICE AHCAL” (cited on page 131).

[124] Mehmet Özgür Sahin, Dirk Krücker, and Isabell-Alissandra Melzer-Pellmann. “Performance and optimization of support vector machines in high-energy physics classification problems”. In: (Jan. 2016), page 20. arXiv: 1601.02809 (cited on page 137).

[125] Daniel Jeans and Oskar Hartbrich. “Realistic calorimeter hit digitisation in the ILD-CaloDigi processor”. In: (2015) (cited on page 140).

[126] Chen Xu. “Study of the Silicon Photomultipliers and Their Applications in Positron Emission Tomography”. PhD Thesis. University of Hamburg, 2014, page 119 (cited on page 141).